CENTRO DE INVESTIGACION Y DE ESTUDIOS AVANZADOS DEL INSTITUTO POLITECNICO NACIONAL

UNIDAD ZACATENCO
DEPARTAMENTO DE INGENIERÍA ELÉCTRICA
SECCIÓN DE ELECTRÓNICA DEL ESTADO SÓLIDO

Depósito y caracterización de películas de $Cu(In_{1-x}Ga_x)Se_2$ mediante multiples técnicas de depósito

Tesis que presenta

Pablo Itzam Reyes Figueroa

para obtener el grado de
Doctorado en Ciencias

en la Especialidad de
Ingeniería Eléctrica

Director de tesis: **Dr. Velumani Subramaniam**
Dr. Nicolas Barreau

Mexico, Ciudad de México.

CENTRO DE INVESTIGACION Y DE ESTUDIOS AVANZADOS DEL INSTITUTO POLITECNICO NACIONAL

ZACATENCO UNIT
DEPARTMENT OF ELECTRICAL ENGINEERING
SECTION OF SOLID STATE ELECTRONICS

Deposition and characterization of $Cu(In_{1-x}Ga_x)Se_2$ films by multiple deposition techniques

Thesis Presented by

Pablo Itzam Reyes Figueroa

To obtain the grade of

Doctorate in Sciences

Specialty in

Electrical Engineering

Thesis Directors: **Dr. Velumani Subramaniam**
Dr. Nicolas Barreau

Mexico City, December 2016

Resumen

En la tecnología fotovoltaica, la correspondiente a las película delgadas de $Cu(In,Ga)Se_2$ (CIGSe) es una de las más prometedoras para cumplir con el desafío actual de producción de energía. El desarrollo de nuevos procesos de crecimiento de CIGSe es un tema importante tanto para la investigación como para las aplicaciones industriales. En este trabajo se ha investigado el crecimiento de CIGSe por el proceso de “3-etapas” e híbrido. La primera parte de este trabajo aborda el depósito de películas absorbentes de $CuInSe_2$ (CISe) crecidas por el proceso de co-evaporación en 3-etapas, el fenómeno de recristalización y el efecto de la temperatura del substrato durante la primera etapa. El fenómeno de recristalización ocurre cuando el contenido de cobre dentro de la capa de CISe alcanza la sur-estequiometria, es decir, y =[Cu]/[In]>1.Este fenómeno se activa térmicamente y da como resultado la reducción tanto de la densidad de los límites de grano como de la densidad de defectos intragranulares. La temperatura más alta de substrato en la primera etapa (400 ° C) conduce al rendimiento más alto de las celdas solares con un 12% de eficiencia (Voc = 460mV, Jsc = 37 mA / cm^2, FF = 78.3%). Además, se investiga el efecto que el oxígeno y el sodio tienen sobre los absorbentes de CISe y las celdas solares correspondientes. La exposición prolongada al oxígeno de las películas de precursores In2Se3 resultan en valores bajos de los parámetros de las celdas solares. Las celdas solares de CISe sin sodio fueron altamente degradadas después de la oxidación, con una caída de Voc y FF del 72% y 45%, respectivamente (en comparación con las muestras no expuestas al oxígeno).

La segunda parte del trabajo trata sobre el crecimiento de películas CISe mediante un proceso híbrido que implica dos técnicas de depósito, a saber, spray pirolítico y co-evaporación. El proceso se basa en la técnica de co-evaporación de 3-etapas, pero reemplazando la película precursora de la 1ª-etapa por una capa precursora de In2Se3 depositada por spray pirolítico. Con este proceso se demostró que se pueden obtener películas CISe de alta calidad. La optimización de las condiciones de crecimiento del proceso híbrido (principalmente el régimen de Cu) permitió celdas solares con eficiencias

de 11.1% (Voc = 438mV, Jsc = 37 mA/cm^2, FF = 67.5%). Se podría lograr una mejora adicional del proceso mediante la disminución de la recombinación en las interfaces (por ejemplo, las producidas en el contacto posterior CISe / Mo).

Palabras clave

$CuInSe_2$, $Cu(In,Ga)Se_2$, Celdas solares, Co-evaporación, spray pirolítico, Depósito híbrido, Oxidación, Sodio.

ABSTRACT

In photovoltaics, the thin film Cu(In,Ga)Se_2 (CIGSe) technology is one of the most promising technology to keep up with today's energy production challenge. The development of new CIGSe growth processes is an important issue for both, research and industrial applications. In order to achieve this target, the CIGSe growth by 3-stage and hybrid process have been investigated. The first part of this work addresses the deposition of $CuInSe_2$ (CISe) absorbers films by the 3-stage co-evaporation process and the effect of the growth substrate temperature during the 1st stage. The recrystallization phenomenon is underlined when the copper content within the CISe layer reaches the sur-stoichiometry, i.e. y = [Cu]/[In]>1. This phenomenon is thermally activated and results in the reduction of both the grain boundaries density and intra-granular defects density. The highest 1st-stage substrate temperature (400°C) leads to the highest efficiency of 12% (V_{oc}=460mV, J_{sc}=37 mA/cm^2, FF=78.3%). Furthermore, the effect of the oxygen along with sodium on the CISe absorbers and solar cells is investigated. The exposure to oxygen of the In_2Se_3 precursors films showed that long time exposures resulted in low solar cell parameters. The CISe cells without sodium were highly degraded after oxidation, with a drop in V_{oc} and FF of 72% and 45%, respectively (compared to samples not exposed to oxygen). The second part of the work deals with the growth of CISe films by a hybrid process which involves two deposition techniques, namely spray pyrolysis and co-evaporation. The process is based on a 3-stage co-evaporation process but replacing the 1st-stage film with an In_2Se_3 spray pyrolyzed precursor layer. It was shown that high-quality CISe films can be obtained. Optimization of the hybrid process growth conditions (mostly Cu regime) allowed solar cells with efficiencies of 11.1% (V_{oc}=438mV, J_{sc}=37 mA/cm^2, FF=67.5%). Further improvement could be achieved by the decrease of recombination at the interfaces (e.g. CISe/Mo back contact). The third part deals with the deposition of Cu(In,Ga)Se_2 films by 3-stage co-evaporation and hybrid processes (similar to the proposed above). The 3-stage CIGSe devices showed efficiencies of 16.5% (V_{oc}=670mV, J_{sc}=33 mA/cm^2, FF=75%). The efficiency obtained for the CIGSe devices grown by the hybrid process was 9.3% (V_{oc}=524mV, J_{sc}=29.7 mA/cm^2, FF=60%). It was found that these last devices have a variable Ga/([In]+[Ga]) ratio through out the absorber

layer, with a minimum value at the CdS/CIGSe interface. This variation in Ga content directly impacts the band gap of the CIGSe along its thickness. The developed band gap gradient in this samples are such that promotes the recombination of charge carriers at the CIGSe/Mo interface and thus, lower performances are obtained. Future scope of the work lie on further improvement of growth processes by taking in consideration the effects that the oxygen and sodium have on the growth and final properties of the absorber films.

Keywords

$CuInSe_2$, $Cu(In,Ga)Se_2$, Solar cells, Co-evaporation, Spray pyrolysis, Hybrid deposition, Oxidation, Sodium.

Acknowledgement

.

This doctoral thesis was possible with the support of several people. I would like to dedicate few words to express my sincere gratitude to all of them.

Firstly, I would like to thank my advisors Dr. Velumani Subramaniam and Dr. Nicolas Barreau for all their support and constant motivation throughout this period of my life. I also would like to thank to Dr. Ludovic Arzel for all the support and the help.

I express my warm thanks to my thesis committee members: Dr. José Chávez, Dr. Arturo Maldonado, Dr. Arturo Morales, Dr. John Kessler, Dr. Olivier Briot, Dr. Pawel Zabierowski and Dr. Guy Ouvrard for spending their valuable time to make my thesis perfect in all aspects. Their comments were always a motivation to improve in my research work and in life itself. My sincere thanks to Dr. Mauricio Ortega, Dr. Gabriel Romero, Dra. María de la Luz for always welcome me for discussion and advice. My gratitude is also dedicated to Dr. Yuriy Koudriavtsev for his help in SIMS profiles measurements and discussions.

My particular thanks to the technicians in SEES and in IMN for all their support and advanced skills. Special thanks to Ing. Miguel Galván, M. en C. Miguel Avendaño, M. en C. Adolfo Fuentes. Also a special gratitude to Álvaro Guzman for his support in lab activities.

I would like to give special recognition to Dr. Thomas Painchaud for all his dedication to train me in the skills required for the solar cells fabrication. I also want to thank to François Couzinie, Edouard Leonard, Thomas Lepetit for their friendship and good research advice. All of them made me feel like home during my stay in France.

I thank all my lab mates, Latha Marasamy, Aruna Devi, Victor Israyelu, Ravi Chandran and Goldie Oza, in Mexico for their kind help offered during these years. Also my thanks are due to my seniors Vidhya Bhojan and Jagadeesh Babu who helped and trained me during my first steps in research.

I thank Jeny Salazar and Yessika Solis for their friendship and support offered through all these long years.

Last but not least, I would like to thank my parents for all their love, encouragement and support in all my activities and decisions.

I acknowledge to CONACYT (grant 219494) and CEMIE-Sol “Proyecto 26” for the financial assistance. Without this support, my project would never have taken place.

List of contents

Chapter 1 Introduction

This introductory chapter discloses the importance that electricity generated by solar cells has in the quality of life of human beings. This importance is presented through the impact that the consumption and production of energy have on several indicators such as quality of life index, life expectancy, mean years of schooling, water access, among others. Moreover, this chapter presents the principal means of energy production through non-renewable fossil fuels (e.g. carbon, coal, gas) and its impact on the climate change and quality of life of human race. Additionally, the chapter gives an overview of the photovoltaic market in different regions of the world such as Europe and Latin America. Further, a survey of the various photovoltaic technologies is given, focusing on the $Cu(In,Ga)Se_2$ (CIGSe) thin film technology. Finally, the scope of the research work along with a brief summary of all the chapters of this thesis are presented.

1.1 Importance of energy

Historically, the energy production and its consumption has been a keystone factor in the development of our civilization. The improvements in life expectancy, water access, mean years of schooling, infant mortality rate, electrification level, which are characteristic of our modern society, show a high correlation with the energy consumption. To have an idea of this relation, Pasten et al. [1] propose the use of a simple quality of life index (QL) mainly involving the life expectancy (LE) and mean years of schooling (MYS). A LE=100 (30) years and MYS=16 (0) years correspond to a maximum (minimum) quality of life index of 10 (0). Figure 1.1 shows the historical evolution and predictions of the global quality of life index (QL_{global}) and global energy consumption rate per capita (ECR_{global}, TW) [1-3]. It is possible to observe a strong correlation between the ECR_{global} and QL_{global}, with a predicted increase of 50% and 26%, respectively, from 2010 to 2040 [1,2]. These tendencies indicate that water access, life expectancy, electrification level and mean years of schooling increase with the energy consumption rate, highlighting the importance of energy production and distribution to an always increasing population.

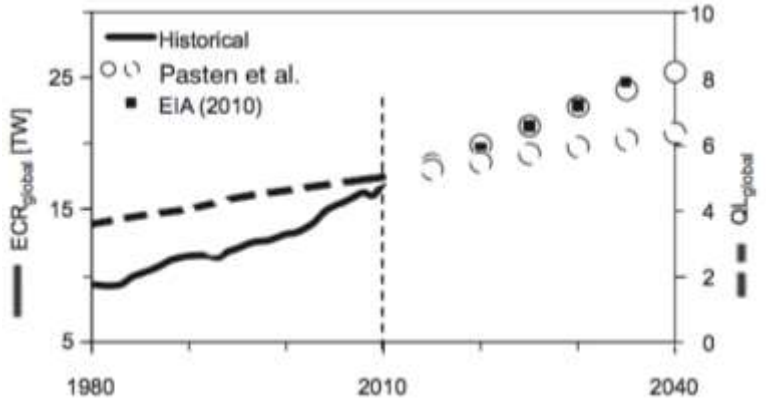

Figure 1.1 Historical evolution and predictions of the global energy consumption rate (ECR_{global}) and global quality of life (QLglobal) (redrawn with data from [1,2]).

The increase in energy consumption observed in figure 1.1 is also related to the world population growth. In this frame, the necessity to increase the energy production in order to fulfill the new required needs becomes one of the most challenging problems that our civilization has to face. The figure 1.2a,b shows the evolution and estimation of global population and primary energy consumption growth up to the year 2035. From the year 1975 to 2015, the population has been grown approximately from 4 to 7 billion people. By 2035, the world's population is expected to reach a staggering 8.3-8.7 billion [4,5], representing an approximately 1.6 billion additional people with energy needs (figure 1.2a). As population is in constant growth, the primary energy consumption also increases by 37% in the interval of 2013-2035 (figure 1.2b), mainly driven by Asian countries (e.g. China and India) [5]. In order to satisfy this increase in consumption, the production of energy using different sources (e.g. oil, coal and gas) has to be increased, which consequently increases the harmful collateral effects.

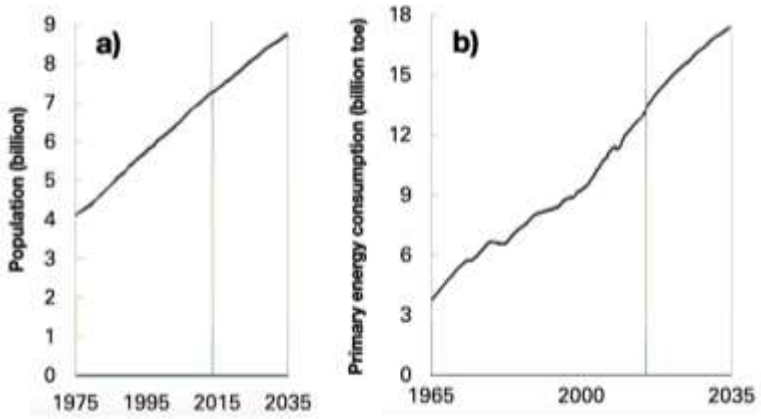

Figure 1.2 Global population (a) and primary energy consumption (b) growth from the year 1975 to 2015 and predictions to 2035 (redrawn with data from [5]). Note: 1 billion ton of oil equivalent (toe)= 11.630 x10^3 TWh.

A fair distribution of energy is another aspect that must be taken into consideration given a large number of people that still do not have access to it in this modern age. In 2012, 15% of world's population consumed 5 kW/person representing 49% of the world's total power consumption. This consumption represents the energy required to reach the highest quality of life index [1]. In comparison, 6% of the world's population consumed less than 100 W/person, living in unhealthy conditions without basic services and poor educational systems, relying their energy production on wood as fuel source [1]. Figure 1.3a,b shows the life expectancy and mean years of schooling (both related with quality of life index) with respect to the electric power consumption [6-8]. It is inevitable to observe a close relation between low electric power consumptions and low life expectancy/mean years of schooling. African countries exhibit the lowest indicators in the world, which are related, but not only, to the fact that the African has one of the lowest national electrification rates (43%) with a stunning 622 million people without access to electricity [9]. In contrast, developed countries (e.g. Germany, France, Japan, United States), which have high power consumption rates, show the best life expectancy and years of schooling. One way to achieve higher global indicators is the reduction in social inequality through the improved distribution of energetics by the implementation of available technology focused on the use of non-expensive energy sources available worldwide. In

this manner, the quality of life of each country will be less dependent on poverty and geopolitical situations, compared to what happens at this moment.

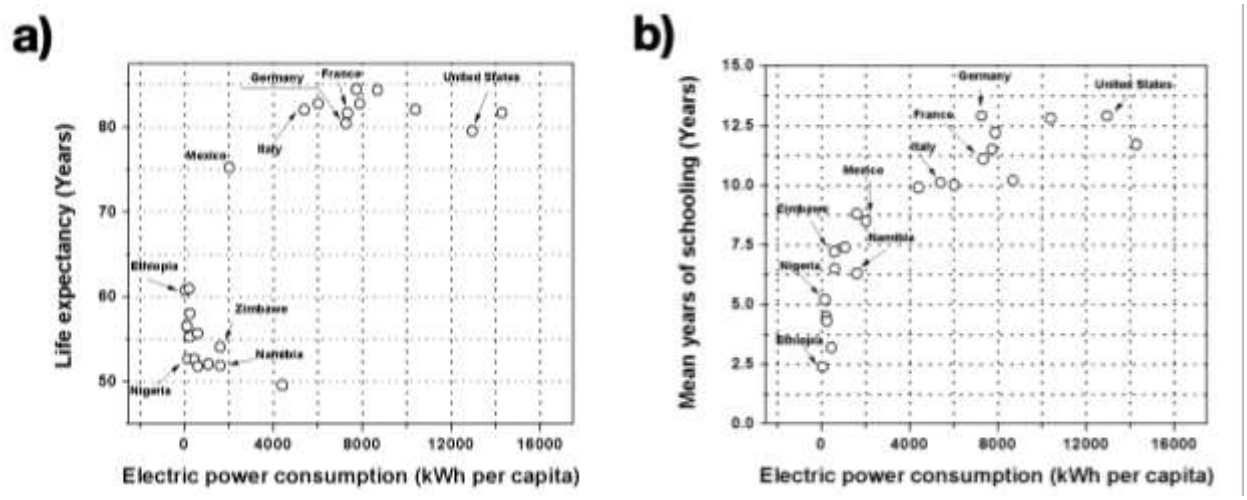

Figure 1.3 Evolution of the life expectancy (a), mean years of schooling (b) with respect to the electric power consumption per capita.

At this moment we have observed the importance of the relation between energy consumption, quality of life, population growth and fair distribution of energy. The production of energy is another important factor that involves all the aforementioned. The way we obtain the primary energy nowadays is mainly through non-renewable fossil fuels namely oil, coal and natural gas. Although the limited data availability and poor data consistency on energy use limit the capacity to exactly describe the situation, the available information (e.g. International Energy Agency, British Petroleum) is useful to establish trends in order to understand energy consumption. Table 1.1 shows the energy consumption by type of fuel of the top energy consumer countries in the year 2014 [10]. As observed, the oil remained the world's leading fuel with 32.6% global energy consumption (mainly driven by US, China, Japan and India), corresponding to nearly 100 million barrels per day [10]. Meanwhile, coal comprised the 30% (dominated by China) and natural gas 23.7% (dominated by US, China and Iran) of primary energy consumption [10]. Furthermore, it has been shown that if we continue in a similar trend of energy consumption, in 2035 the fossil fuels will contribute with a 26-28% share each source (i.e. oil, coal and gas) to the world's energy needs [5]. Nevertheless, it is necessary to

remember that, at a certain moment, these resources will start to run out (non-renewable), leaving behind not only a hole in energy production but also a high increase of prices. These will directly affect the quality of life of the entire population.

The utilization of the non-renewable fossil fuels through combustion is well known to produce greenhouse gas emissions. Organizations such as the Intergovernmental Panel on Climate Change (IPCC) [11] have shown evidence of climate change across the planet (atmosphere, soil and oceans) driven by greenhouse gases such as carbon dioxide (CO_2), methane (CH_4) and nitrous oxide (N_2O). In the period 1750-2011, cumulative CO_2 emissions (promoted by human activity) were approximately 2040 Gigaton of CO_2 (1Gt= 1 billion tons) mainly remaining in atmosphere (40%), ocean (30%) and soils (30%) [11]. This accumulation of emissions promoted increase of surface temperature from 0.65 to 1.06 ºC (land and ocean), an increase of global mean sea level by 0.19 m (larger than in previous two millennia) and acidification of the ocean (26% increase in acidity) [11]. Considering these unprecedented changes in our climate, important policy commitments at the 1992 Rio Conference, 1997 Kyoto Protocol and 2015 Paris Conference of Parties have been adopted in order to reduce greenhouse gases emissions through the reform of our energy consumption and production habitudes based on energy savings and the development of new energy sources. Hydroelectric, nuclear, and renewables are today's most important alternative sources.

Table 1.1 Top energy consumer countries in relation to the consumption and type of fuels.

	Oil		Coal		Natural gas	
Country	Million tonnes	Share of total (%)	Million tonnes oil equivalent	Share of total (%)	Million tonnes oil equivalent	Share of total
US	836.1	19.9	453.4	11.7	695.3	22.7
Canada	103	2.4	21.2	0.5	93.8	3.1
Mexico	85.2	2	14.4	0.4	77.2	2.5
Total North America	1024.4	24.3	488.9	12.6	866.3	28.3
Brazil	142.5	3.4	15.3	0.4	35.7	1.2
Total S&C America	326.5	7.8	31.6	0.8	153.1	5
France	76.9	1.8	9	0.2	32.3	1.1
Germany	111.5	2.6	77.4	2	63.8	2.1
Italy	56.6	1.3	13.5	0.3	51.1	1.7
Russian Federation	148.1	3.5	85.2	2.2	368.3	12
United Kingdom	69.3	1.6	29.5	0.8	60	2
Total Europe&Eurasia	858.9	20.4	476.5	12.3	908.7	29.6
Iran	93.2	2.2	1.1	0.05	153.2	5
Saudi Arabia	142	3.4	0.1	0.05	97.4	3.2
Total Middle East	393	9.3	9.7	0.3	418.6	13.7
Australia	998	1.1	43.8	1.1	26.3	0.9
China	520.3	12.4	1962.4	50.6	166.9	5.4
India	180.7	4.3	360.2	9.3	45.6	1.5
Japan	196.8	4.7	126.5	3.3	101.2	3.3
Total Asia Pacific	1428.9	33.9	2776.6	71.5	610.7	19.9
Total World	4211.1	100	3881.8	100	3065.5	100

In order to have a scenario of constant growth in population with an equilibrium between high life quality, energy production needs, fair distribution of energetics and a non-threatened climate, the use of clean renewable energy sources is necessary as a forward step that humanity has to take in the energy production evolution. The most important renewable sources are wind, solar photovoltaic, hydropower, bioenergy and solar thermal electricity. The International Energy Agency (IEA) Tracking Clean Energy Progress 2015

[12] report addresses a renewable electricity generation corresponding to 22% share of global generation. Renewable electricity generation is expected to increase 45% in the period 2013-2020, reaching 7310 TWh [12]. Among the different renewable energies, solar photovoltaic (PV) is one of the fastest growing market (growth of installed capacity 49%/yr) [13] given that it takes advantage of highly energetic/highly available solar energy and directly converts it into electricity. From 2009 to 2013, the solar PV market grew from 23 GW to an historical global cumulative installed capacity of 138.9 GW capable to produce around 160 TWh per year [14]. This is equivalent to the electricity produced by 32 coal power plants. In the same period of time, the countries with more than 100 MW photovoltaic installed capacity increased from 9 to 23 countries. This was achieved with an increase of annual investment from USD 48 billion to USD 96 billion [13]. Europe, Asia and America are the most important regions in accumulative installed capacity. Table 2 shows the global photovoltaic cumulative installed capacity share in 2013 [14]. Europe region dominated the market, while China was the non-European leading country followed by Japan and US. Projections of Greenpeace and the International Energy Agency with different scenarios (low-carbon energy) show a cumulative solar electrical capacity from 663-4674 GW in the year 2035, turning photovoltaic as the most used renewable energy source [14]. These projections show an incomparable opportunity for photovoltaics, which in contrast to fossil fuels, offers a reduction rather than increase in cost. Already in 2013 PV power plants in Australia, Germany, Italy and Netherlands reached a levelized cost of electricity (LCOE involving cell efficiency, module cost, installation materials, location, etc) of 0.078 € (0.11 USD) – 0.142€ (0.19 USD)/kWh, achieving grid parity to their respective variable portion of tariffs (~0.25-0.32 USD/kWh) [13].

Table 1.2 Global photovoltaic cumulative installed capacity share in 2013.

Country	Global share (%)	Global cumulative capacity (MW)
Germany	26	36.09
China	13	18.04
Italy	13	18.04
Japan	10	13.88
US	9	12.49
Spain	4	5.55
France	3	4.16
Australia	2	2.77
Belgium	2	2.77
Czech Republic	2	2.77
Greece	2	2.77
India	2	2.77
United Kingdom	2	2.77
Rest of the world	10	13.88

1.2 Role of Europe and Sunbelt countries (Latin America) in PV

The development of photovoltaic is concentrated in 13 PV markets, in which 8 are located in Europe. In 2013, Europe represented the ~59% of world's cumulative installed capacity (81.5 GW); share in which Germany, Italy, Spain, France, United Kingdom, Belgium, Greece and Czech Republic were the most important markets (figure 1.4) [14]. Germany widely dominated the European market, even though the country showed a decrease of 56% in new installed PV systems [15,16]. PV power plants have reached a levelized cost of electricity in the range of 0.08-0.107 € /kWh, comparable to cost of energy obtained by hard coal (0.08-0.065 €/kWh), thus getting closer to "grid parity" [17]. Moreover, scenarios considering higher solar irradiation (2000 kWh/m^{2}a) indicate that PV system could produce electricity for 0.06 €/kWh, comparable to power generated from oil or gas [17]. By the end of 2013 Italy increased its accumulative PV installed capacity to 18 GW, providing 8.5% of the total electricity generated in the first months of 2014 [15]. Spain had

a big a boom of total cumulative installed PV systems in 2008 with a capacity of 5.3 GW. In 2013, PV systems generated 3.2% (8.3 TWh) of the Spanish electricity demand. In France, key country for PV development in Europe, PV systems with 640 MW capacity were installed in 2013 [18], increasing the total cumulative installed capacity to 4.7 GW. Electricity production from PV systems was 1.24 % (4.45 TWh) of the total French national demand. Despite these improvements, a greater role of France is expected given its huge potential.

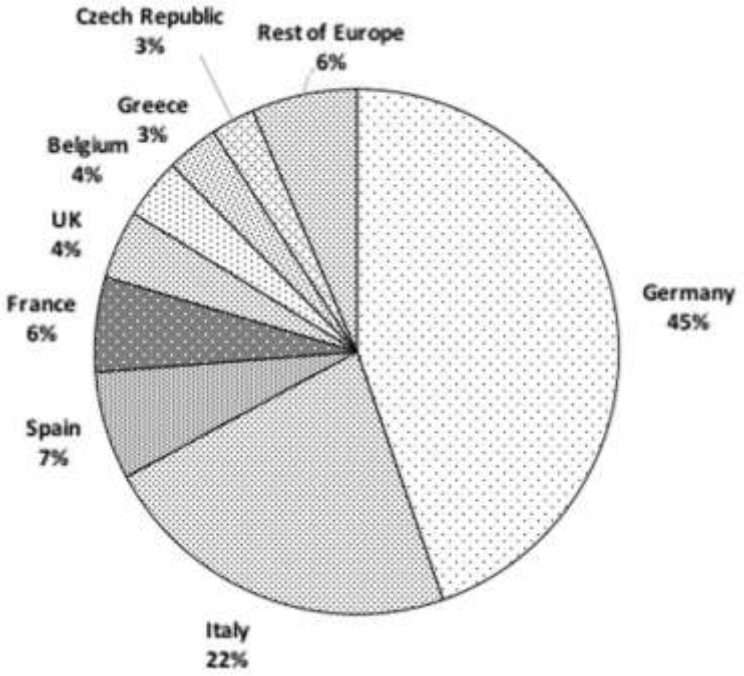

Figure 1.4 Global PV cumulative installed capacity in Europe (2013).

As mentioned above, Europe leads the market with 81.5 GW, followed by Asia Pacific countries (40.6 GW) and American countries (13.7 GW). Nevertheless, Europe leadership decreased from ~75% in 2011 to ~59% in 2013 [14]. This sharp decrease of installations in Europe is leading to a gradual transition of change in world leadership responsible for the future photovoltaic growth. Asian (e.g. China, India) and other developing countries (e.g. Mexico, Brazil) have a great opportunity to inquire deeply into the photovoltaic market considering that these countries have a tremendous potential due to geographical

location in the “Sunbelt zone” where the solar radiation is the highest in the world (1900-2700 kWh/m^2) [19].

The Sunbelt countries such as Mexico, Brazil, India and China (figure 1.5) represent 75% of the world population representing 80% of the expected global energy demand growth. In the year 2010, however, they represented only ~9% (2 GW) of the cumulative installed PV capacity, mainly driven by China [16]. This is in contradiction with the tremendous PV potential related to the high available solar radiation in the region. According to some scenarios [16], the PV potential generation ranges from 257 to 1,130 GWp by 2030. Some barriers for this development are the lack of research support, policy support, finance and infrastructure. China, India, Australia and Mexico are considered the most promising Sunbelt countries, given its investment and PV attractiveness [16]. In 2010, Latin America (LA) represented only 4% (56MW) of the Sunbelt PV installed capacity and 95% is located in Brazil, Argentina and Mexico [16]. In 2013, Mexico had a total cumulative PV capacity of 112 MW, projected to 2 GW by 2020. By the end of 2013, Brazil and Argentina had a cumulative installed capacity of 170 MW and 20 MW, respectively [15]. Despite these efforts, Latin American PV installed capacity is still far from the projected schemes predicting of 29 GW by 2030 [16]. To achieve all these goals mentioned afore, further research on PV technology has to be done in order to increase the efficiencies, decrease the production cost ($/kWh) and reduce environmental impact of solar cells fabrication.

Considering the roles that Europe and Latin American countries play in the actual global situation, it is possible to observe that the next step in the development of global photovoltaics sector is to take advantage of (i) the knowledge and experience of PV laboratories/industries from Europe and (ii) the perfect geographical location (in terms of solar radiation) of “Sunbelt” countries. In this manner, the PV power generation could reach historical minimums LCOE compared to the corresponding cost of oil, gas or coal, through high efficiency photovoltaic power plants located in high solar radiation environments.

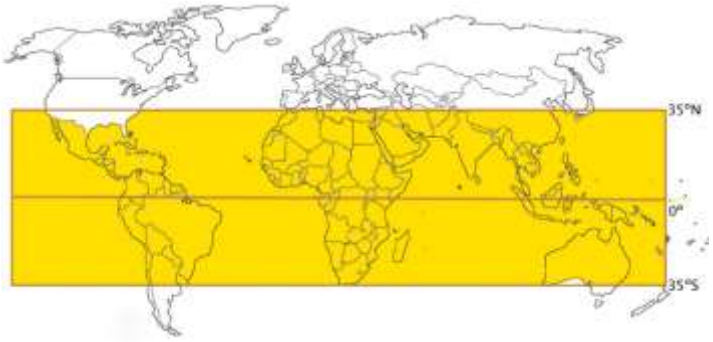

Figure 1.5 Countries in the Sunbelt region. China, Singapore, Mexico India, Australia, Malaysia, Brazil, Argentina, Chile ere the most attractive countries for PV development.

1.3 Photovoltaic technologies

Generally, the PV market is divided into different technologies depending mainly on the type of absorber semiconductor material used in the solar cell fabrication. Table 1.3 shows the best cell and module efficiencies of different PV technologies reported in the literature [20]. It is possible to observe that the cells could be classified into three generations. The first generation involves the bulk crystalline silicon-based solar cells (mono and multicrystaline), which is the most mature technology with conversion efficiencies of around 25.6% (cell), 22.9% (module) [20] and a share of 85-90% in the global annual PV production [21]. The second generation consists of thin film solar cell technology, which reduces the production cost of final modules through the development of new growth and deposition methods of materials with thickness in the few μm range. The photovoltaic thin-film technology is mainly divided into (i) amorphous Si (a-Si), (ii) Cadmium telluride (CdTe) and (iii) $Cu(In,Ga)Se_2$ (CIGSe). The characteristic of these three materials is their high optical absorption coefficient, which is a critical issue in solar cells fabrication. The third generation includes all the new approaches, which attend to reduce manufacturing costs by offering high efficiency (e.g. multijunction cells, hot carriers use) and/or very low cost devices (e.g. organic solar cells, dye sensitized cells). The relatively new concepts applied to this technology cause a long-term adaptation to the industry sector.

Table 1.3 Cells and modules efficiencies of different solar cells technologies, measured under global AM1.5 spectra (1000W/m^2) at 25 ºC [20].

Type of cell	Efficiency (%)	Area (cm2)	Voc(V)	Jsc(mA/cm2)	Fill factor (%)	Manufacturer
Silicon						
Si (crystalline)	25.6± 0.5	143.7	0.74	41.8	82.7	Panasonic
Si (crystalline module)	22.9±0.6	778	5.6	3.97	80.3	UNSW
Si (multicrystalline)	**20.8± 0.6**	**243.9**	**0.662**	**39.03**	**80.3**	**Trina Solar**
Si (multicrystalline-module)	18.5±0.4	14661	38.97	9.149	76.2	Q-Cells
Thin film						
Si (thin film minimodule)	10.5±0.3	94	0.492	29.7	72.1	CSG Solar
a-Si/nc-Si (thin film)	12.7±0.4	1.000	1.342	13.45	70.2	AIST
a-Si/nc-Si (module)	12.2±0.3	14322	202.1	1.261	68.8	TEL Solar
GaAs (multicrystalline)	18.4±0.5	4.011	0.994	23.2	79.7	RTI
GaAs (thin film)	28.8±0.9	0.992	1.122	29.68	86.5	Alta Devices
GaAs (thin film- module)	24.1±1.0	858.5	10.89	2.255	84.2	Alta Devices
InP (crystalline)	22.1±0.7	4.02	0.878	29.5	85.4	Spire
CIGSe (cell)	20.5±0.6	0.988	0.752	35.3	77.2	Solibro
CIGSe (cell)	**21.7±0.7**	**0.497**	**0.796**	**36.59**	**79.3**	**ZSW**
CIGSe (module)	15.7±0.5	9703	28.24	7.254	72.5	Miasolé
CIGSe (Cd free-submodule)	**17.5±0.5**	**808**	**47.6**	**0.408**	**72.8**	**Solar Frontier**
CdTe (cell)	21.0±0.4	1.062	0.8759	30.25	79.4	First Solar
CdTe(thin film-module)	17.5±0.7	7021	103.1	1.553	76.6	First Solar
Dye sensitized						
Dye	11.9±0.4	1.005	0.744	22.47	71.2	Sharp
Multijunction						
InGaP/GaAs/InGaAs	37.9±1.2	1.047	3.065	14.27	86.7	Sharp

Considering the cost of electricity presented previously, it is clear that PV electricity needs to turn into cheaper costs in order to gain an important share in the energy mix production for fulfilling the population's needs in the future. PV Modules based on silicon wafers have limitations in relation to cost reductions. Silicon is an indirect band gap semiconductor, which is produced in form of crystal ingots. Because of these characteristics and considering solar cell applications, a thick absorber of around 200 μm thickness is

needed. Besides, sawed wafer from ingots always represents material waste. Moreover, the modules need to be connected by wiring the front and back of the solar cells. Thus the module needs to be encapsulated from both sides. Thin film technology could eliminate several of these deficiencies. In contrast to Si, CIGSe and CdTe are direct band gap materials with high absorption coefficient (figure 1.6) allowing to completely absorb the sunlight in ~2 μm thickness with the advantage of being grown directly on the substrates (rigid or flexible) which are used as mechanical support in final modules. In addition, the thin films solar cells require 2 or 3 times less production energy than crystal silicon, which directly impacts the payback time [22]. Monolithic integration of thin film technology allows to connect devices from the front of one cell to the back of next one in the same front plane. This integration allows the encapsulation of only one half of the module considering the substrate (where solar cell is deposited) as other half of encapsulation. These characteristics of thin film technology represent an important potential for reduction of fabrication cost compared to Si-based technology.

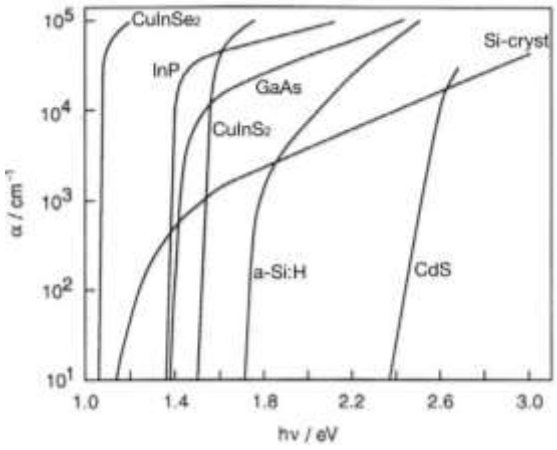

Figure 1.6 Dependence of absorption coefficient on the photon energy for different semiconductors [23].

Among of the thin film technologies, CIGSe is one of the most promising technology to keep up with todays PV energy production challenge given that devices exhibit the best thin film conversion efficiency of 22.3% (lab scale cells on glass, press information) [24] and 17.5% (Cd-free module) [20]. The CIGSe technology shows important characteristics such as (i) low-cost manufacturing process (non-vacuum/vacuum deposition, monolithic integration), (ii) high efficiencies on glass and flexible (20.4%) substrates [25], (iii) use of

less or any amount of toxic cadmium compare to CdTe solar cells, (iv) very high stability reflected in an energy output module degradation (%/yr) of 0.02, the lowest compare to a-Si, µm-Si (both 0.95), CdTe (0.3), c-Si (0.23) and multi-Si (0.59) [26]. Figure 1.7 shows the annual global PV module production of the different thin film technologies [21]. It is possible to observe that production of CIGSe modules importantly increase from 2009 to 2014, year where CIGSe (1.7GWp) is reaching parity with CdTe (1.9 GWp) modules. Despite of all mentioned above, CIGSe market share in the photovoltaic field is around 3-4% of the total PV share. However, recent industrial development of this technology by Solar Frontier (major manufacturer), Manz, Solibro, MiaSolé, Avancis, among other companies (Table 1.4) suggests a significant growth in the near future. Moreover, in 2015 Manz Company reported a levelized cost of energy of 4.76 €ct/kWh for thin films CIGSe-based solar cells, the lowest compared to c-Si Passivated Emitter Rear Cell (5.32 €ct/kWh), standard (5.13 €ct/kWh) and bifacial (4.78 €ct/kWh) [27].

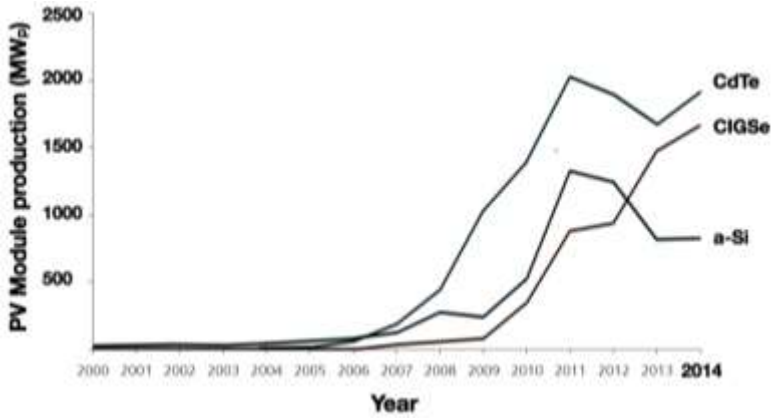

Figure 1.7 Evolution of annual global PV module production of thin film technologies.

Table 1.4 Most important companies producing CIGSe modules, along with the corresponding deposition method and conversion efficiencies.

Manufacturer	Deposition method	Champion product efficiency (%)
Solar Frontier/TSMC	Sputtering + H_2Se/S	13.8 [28] 15.2 [29]
Manz (Würth) Solibro	Co-evaporation 1-stage	16 [30] 13.3 [31]
MiaSolé	Reactive sputtering	15.7 [32]
Avancis	Sputtering+Selenization+Rapid Termal Process	16.6 [33]
Global Solar (Flexible substrate)	---	12.7 [34]
STION	Sputtering	14 [35]
Dow Solar (NuvoSun) (flexible substrate)	---	14 [36]

The development of $Cu(In,Ga)Se_2$ technology is based on two main research paths. The first is focused on understanding the fundamental aspects of the material itself and its behavior in the solar cell. The second is to address all this “fundamental” research to the development of technology for industrial application. Indeed, the progress in industrial technology is closely related to the economic factor. Thus, to develop CIGSe technology, it is compulsory to reduce the production cost [14]. Table1.5 shows the approximate production cost (%) of a high efficiency CIGSe-based solar cell on glass substrate [37,38].

Table 1.5 Production cost of a high efficiency CIGSe-based solar cell

Component	Cost (%)
Equipment	26
Glass substrate and encapsulation	14
Contacts(including TCO’s)	14
Copper, indium, gallium, selenium	11.5
Other materials	9
Other costs (labor, depreciation, electric power)	25.6

As observed in table 1.5, the most expensive components of a CIGS-based solar cell are the equipment (~26%) and materials (~34.5%, 11.5% absorber). Considering the

materials for the absorber deposition, different studies (e.g South American Silver Corp., European commission) [39,40] reported the scarcity of raw indium and gallium for electronic applications (ITO, LED, PV, among others). Moreover, in 2011 American Silver Corp. [39] estimated an indium market annual growth of 15-20% with an annual producing growth of only 1-2%. This difference in demand and supply have a direct impact on the cost of indium in the coming years [39], thus increasing CIGSe-based solar cells production cost.

One strategy to reduce costs is the development of cheaper manufacturing processes without compromising conversion efficiencies [38, 41]. This could be done with the implementation of the following (but not only) approaches [38,42-48]:

1) Development of alternative deposition methods to co-evaporation by the use of low-cost non-vacuum techniques.
2) Limit the utilization of indium through the development of (i) CuGaSe2-based solar cells (wide-bandgap absorber), (ii) an alternative Cu(Zn,Sn)Se absorber or (ii) CIGSe thickness reduction to less than 1 μm.
3) Increase conversion efficiency through a better understanding the physio-chemical process that occur within the CIGSe structure and during its growth by co-evaporation or any other method.
4) Utilization of less pure precursor materials.
5) Increase material-utilization efficiency during deposition.

This research work focuses on the growth and properties of $CuInSe_2$ and $Cu(In,Ga)Se_2$ absorber thin films prepared by vacuum co-evaporation technique. The work also explores a first approach to the design of a novel hybrid deposition process based on the idea of a possible increase of material utilization efficiency of the, more and more scarce, indium and gallium raw materials. The proposed hybrid process attempts to take the advantages of high conversion efficiency vacuum and low-cost/high material utilization non-vacuum deposition techniques. The effects induced by oxygen and sodium in the CISe and CIGSe absorbers and corresponding solar cells are investigated with a

discussion related to the possible involved mechanisms. These issues are important for the understanding of CIGSe growth by co-evaporation, spray pyrolysis and our proposed method. In this work, recommendations for the CISe and CIGSe growth on the use of hybrid deposition processes are developed, mainly related to the achievement of solar cells with higher performance.

This dissertation is divided into three main parts. The first part (chapter 2 and 3) is an introductory framework dedicated to an overview of the operation principles of solar cells and the CIGSe solar cells technology, describing the material properties (structural, optical and electronic), thin film properties, and solar cell performances. The impact of structural defects (e.g. vacancies and antisites) on the electrical properties of absorbers and the role of extrinsic impurities such as sodium and oxygen on CIGSe-based devices are addressed. Furthermore, a particular attention is given to the different methods and growth conditions of CIGSe thin films and its relevance to the performance of the corresponding solar cell are also presented. Based on the information mentioned above, a hybrid deposition of CIGSe thin films based on chemical spray pyrolysis and co-evaporation deposition methods is proposed. The second part (chapter 4) is meant to describe the experimental conditions of the CIGSe layers growth and solar cells. The growth conditions of baseline co-evaporation and hybrid growth processes are given, especially the related to chemical spray pyrolysis and co-evaporation deposition methods. The third part (chapter 5) describes the achieved results on the CIGSe thin films and solar cells obtained by co-evaporation and hybrid deposition method, focusing on the effects that the use of both growth methods has on the absorber properties. Finally, the summary and general conclusions are given.

References

[1] C. Pasten, J.C. Santamarina, Energy and quality of life, Energy Policy 49 (2012) 468-476.
[2] Energy Information Administration, International Energy Outlook 2010, 2010.
[3] Energy Information Administration, International Energy Statistics 2011, 2011.
[4] United Nations, World Population to 2300, 2004.
[5] British Petroleum p.l.c., Energy Outlook 2035, 2015.
[6] The World Bank Group, 2012, http://date.worldbank.org/indicator/EG.USE.ELEC.KH.PC.
[7] Central Intelligence Agency, 2012, http://www.cia.gov/library/publication/the-world-factbook/rankorder/2102rank.html.
[8] United Nations Development Programme, 2012, htt://hdr.undp.org/en/content/mean-years-schooling-adults-years.
[9] International Energy Agency, World Energy Outlook 2014-Electricity database, 2014, http://www.worldenergyoutlook.org/resources/energydevelopment/energyaccessdatabase/
[10] British Petroleum, BP Statistical Review of World Energy, 2015.
[11] Intergovernmental Panel on Climate Change, Climate Change 2014: Synthesis Report. Contribution of Working Groups I, II and III, 2014.
[12] International Energy Agency, Tracking Clean Energy Progress 2015, 2015.
[13] Intenational Energy Agency, Technology Roadmap Solar Photovoltaic Energy, 2014.
[14] European Photovoltaic Industry Association, Global Market Outlook for Photovoltaics 2014-2018, 2014.
[15] European Commission, PV Status Report 2014, 2014.
[16] European Photovoltaic Industrial Association, Unlocking the sun belt potential of photovoltaics, 2010.
[17] Fraunhofer Institute for Solar Energy Systems, Levelized cost of electricity renewable energy technologies, 2013.
[18] International Energy Agency, Trends 2014 in Photovoltaic Applications, 2014.
[19] SolarGIS, Geo Model Solar, 2015, http://solargis.info/doc/free-solar-radiation-maps-GHI.
[20] M.A. Green, K. Emery, Y. Hishikawa, W. Warta, E.D. Dunlop, Solar cell efficiency tables (Version 45), Prog. in Photovolt.: Res. And Appl. 23 (2015) 1-9.
[21] Fraunhofer Institute for Solar Energy Systems, Photovoltaics report, 2015.
[22] B. Dimmler, CIGS and CdTe based thin film PV modules, an industrial r/evolution, in: 38th IEEE Photovoltaic Specialist Conference, 2012: pp. 2494-2499.
[23] H.J. Lewerenz, H. Jungblut, Photovoltaik. Grundlagen und Anwendungen. Heidelberg: Springer-Verlag, 1995.
[24] Solar Frontier, Solar Frontier achieves world record thin-film solar cell efficiency: 22.3%, 2015, http://www.solar-frontier.com/eng/news/2015/C051171.html.
[25] A. Chirila, P. Reinhard, F. Pianezzi, P. Bloesch, A. R. Uhl, C. Fella, L. Kranz, D. Keller, C. Gretener, H. Hagendorfer, D. Jaeger, R. Erni, S. Nishiwaki, S. Buecheler, A.N. Tiwari, Potassium-induced surface modification of Cu(In,Ga)Se2 thin films for high-efficiency solar cells, Nat. Mater. 12 (2013) 1107-1111.
[26] M.J. de Wild-Scholten, Energy payback time and carbon footprint of commercial photovoltaic systems, Sol. Energy Mater. Sol. Cells 119 (2013) 296-305.
[27] Manz, 2015, http://www.manz.com/markets/solar/cigs-fab/business-model/levelized-cost-of-energy/.
[28] Solar frontier, 2015, http://www.solar-frontier.com/eng/solutions/modules/S002210.html.
[29] TSMC, 2015, http://www.tsmc-solar.com/siteutilities/downloads.

[30] Manz, 2015, http://www.manz.com/markets/solar/cigs-fab/.
[31] Solibro, 2015, http://solibro-solar.com/en/product/modules/.
[32] Miasolé, 2015, http://miasole.com/en/product/flex-02n/.
[33] Avancis, 2015, http://www.avancis.de/en/cis-technology/cis-world-records/.
[34] Global Solar, 2015, http://www.globalsolar.com/products/flexible-modules/.
[35] STION, 2015, http://www.stion.com/products/.
[36] Dow Solar (NuvoSun), 2015, http://www.dowsolar.com/en/nuvosun/nuvosun-flex-pv-cells.
[37] H. Zervos, Highlights of photovoltaic beyond conventional silicon Europe 2009, Printed Electronics World, 2009.
[38] B. Dimmler, CIGS and CdTe based thin film PV modules, an industrial r/evolution, in: 38th IEE Photovoltaic Specialists Conference, 2012: pp. 2494-2499.
[39] South American Silver Corp., Growing and advancing one of the world's largest undeveloped silver and indium resources, Corporated presentation, 2011.
[40] European commission, Report on critical raw materials for the EU, 2014.
[41] S. Hegedus, Thin film solar modules: The low cost, high throughput and versatile alternative to Si wafers, Prog. Photovolt: Res. Appl. 14 (2006) 393-411.
[42] D.Lincot, JF. Guillemoles, S. Taunier, D. Guimard, J. Sicx-Kurdi, A. Chaumont, O. Roussel, O. Ramdani, C. Hubert, J.P. Fauvarque, N. Bodereau, L. Parissi, P. Panheleux, P. Fanouillere, N. Naghavi, P.P. Grand, M. Benfarah, P. Mogensen, O. Kerrec. Chalcopyrite thin film solar cells by electrodeposition. Sol. Energy 77 (2004) 725-737.
[43] S.J. Sung, D.H. K.W. Wang, S.Y. Han et C.H. Chang. 8.01 % Cu(In, Ga)Se_2 solar cells fabricated by air-stable low-cost inks. Phys. Chem. Chem. Phys., 14 (2012) 11154–11159.
[44] B.J. Babu, S. Velumani, R. Asomoza, An (ITO or AZO)/ZnO/Cu($In_{1-x}Ga_x$)Se_2 superstrate thin film solar cell structure prepared by spray pyrolysis, in: 37th IEEE Photovoltaic Specialist Conference, 2011: pp. 1238-1243.
[45] D.L. Young, J. Keane, A. Duda, J.A. M. AbuShama, C.L. Perkins, M. Romero, R. Noufi. Improved performance in ZnO/CdS/$CuGaSe_2$ thin-film solar cells. Prog. Photovolt: Res. Appl. 11 (2003) 535–541.
[46] Q. Guo, G. M. Ford, W.C. Yang, B. Walker, E. Stach, Hugh W. Hillhouse, R. Agrawal, Fabrication of 7.2 % efficient CZTSe solar cells using CZTSe nanocrystals. J. Am. Chem. Soc. 132 (2012) 17384-17386.
[47] A. Han, Y. Zhang, W. Song, B. Li, W. Liu, Y. Sun, Structure, morphology and properties of thinned Cu(In, Ga)Se_2 films and solar cells, Semicond. Sci. Technol. 27 (2012) 35022(8pp).
[48] P. Reinhard, F. Pianezzi, L. Kranz, S. Nishiwaki, A. Chirila, S. Buecheler, A.N. Tiwari, Flexible Cu(In,Ga,)Se2 solar cells with reduced absorber thickness, Prog. Photovolt.; Res. Appl. 23 (2015) 281-289.

Chapter 2 $Cu(In,Ga)Se_2$ solar cells

This chapter presents an overview of the $Cu(In,Ga)Se_2$-based solar cells technology. The first part describes general information related to the basic operational aspects of solar cells. This information includes the radiation spectrum of the sun, basic structure and operation of a single junction solar cell (homojunction and heterojunction) and basic parameters of solar cells (open circuit voltage, short circuit current and fill factor). The second part comprises an overview of the structure of a CIGSe-based solar cell (constituent layers) giving particular attention to the CIGSe absorber material. This chapter also reviews the structural, optical and electrical properties of CIGSe semiconductor that allow the achievement of high-efficient solar cells. Particular importance is given to the phase diagrams of compounds systems involved in the synthesis of CIGSe, the impact of structural defects (e.g. vacancies and antisites) on the electrical properties of absorbers, energy band diagram of complete solar cell structure and the different recombination processes involved in the device operation. Additionally, the role of extrinsic impurities such as sodium and oxygen on CIGSe-based devices is addressed. All this information will help to understand the relation between the properties of the CIGSe absorber layer and how its modification impacts on the resulting device performance.

2.1 Operation principle of solar cells

The Sunlight is composed of photons, each one carrying a specific quantity of energy and behaving with a wavelike character. The photon energy ($E\lambda$) is related to its wavelength (λ) as:

$$E_\lambda = \frac{hc}{\lambda} \approx \frac{1240eV \cdot nm}{\lambda(nm)} \qquad \text{(eq. 2.1)}$$

Where *h* is the Plank's constant (6.626×10^{-34} Joule-s) and *c* is the speed of light (2.998×10^{8}m/s). Given that the sunlight is the driven energy of the solar cells, its spectral nature has to be considered in choosing the absorber material of a solar cell. Figure 2.1

shows the radiation spectrum of the sun, approximated by a black-body radiation at a 5762 K. The spectral distribution air mass zero (AM0) is the space radiation intensity in the near earth's space (1.353 kW/m^2) [1]. This intensity decreases due to the reflection and absorption in the atmosphere. The AM1.5G (global) spectrum integrates the direct and diffused light that reach the earth crust. The normalized radiation intensity of AM1.5G spectrum (1000 W/m^2) is commonly employed to characterize the solar cells. Figure 2.1 shows the maximum Sunlight radiation in the range of 250-1000 nm (i.e. 1.0-4.96 eV). The design of high-efficiency solar cell exploits at its maximum expression this portion of the solar spectrum.

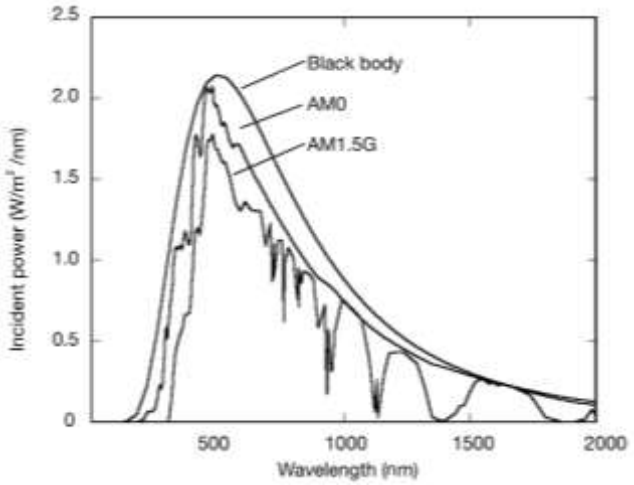

Figure 2.1 Radiation spectrum of a black body at 5762 K, AM0 and AM1.5G spectrum.

The solar cell is a photovoltaic device that converts solar energy into electricity based on the photogeneration of charge carriers (electron: e^- and hole: h^+) in an absorbing semiconductor. Figure 2.2 shows a typical single junction solar cell structure. There are three main steps involved in the operation of a solar cell, namely (i) generation of charge carriers by absorption of photons, (ii) separation and (iii) collection of those charges. A semiconductor material will absorb photons with an energy ($E\lambda$) greater than its band-gap (E_g). The absorbed photons excite electrons from the valence band to the conduction band of the absorber material (i.e. creation of electron-hole pairs). The generated charge carrier pairs can either recombine (representing losses in device performance) or be separated and then collected (contributing to photogenerated power). The number of

absorbed photons (i.e. photogenerated electron-hole pair) depend on the thickness and absorption coefficient of the absorber material. The most important part of a solar cell is the p-n junction, which consist of two semiconductor materials in contact, one n-doped (excess of electrons) and another p-doped (excess of holes). In a silicon solar cell, the p-n junction is formed with a boron (p side) and phosphorus (n side) doped Si material. In this case, both sides of the junction are of the same material; thus the structure is called an homojunction. In a CIGSe-based solar cell, various semiconductor materials are used for the p-n junction formation; hence the structure is called heterojunction. The operational principle is the same for both types of junctions, although with some differences worthy of mention.

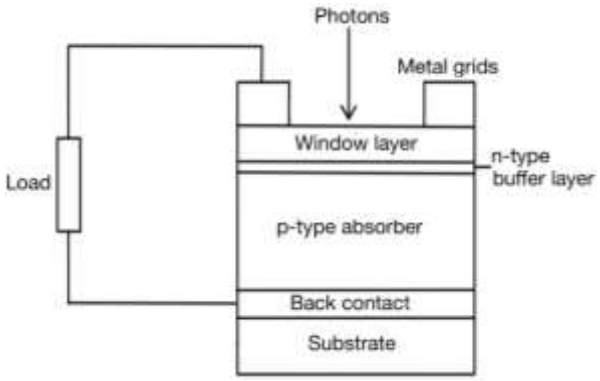

Figure 2.2 Solar cell simplified structure.

2.1.1 Homojunction

As mentioned above, an n-p homojunction is formed with a different type of doping in the same semiconductor material. This doping could be extrinsic (e.g. introducing different elements than the base material) or intrinsic (e.g. induced by defects). Figure 2.3 shows the ideal situation in an homojunction structure. Electrons and holes act as mobile charges carriers in the n- and p-type material, respectively. Upon the formation of the p-n junction, electrons will diffuse from n-type to the p-type semiconductor, leaving behind positively ionized dopants atoms in the n-side. The holes travel from p-type to n-type material, resulting in negatively charged ionized atoms in the p-side (see figure 2.3). Thus, the diffusion creates a depletion region of mobile charge carriers in both sides of the

junction where only the ionized atoms will remain. The positively and negatively charged ionized atoms promote the formation of an electric field. In this stage, an electrostatic potential is formed between n- and p-type quasi-neutral parts. The built-in electric field will separate the mobile negative and positive charges (i.e. photogenerated electron-hole pairs), leaving a region depleted of these mobile electrical charges. The depleted zone is called the space charge region (SCR). When charge carrier pairs are created inside the SCR, the electron and hole will drift in the electric field and driven to opposite sides with a low recombination probability. The charges generated outside the SCR need to diffuse in the direction of the depletion zone in order to be separated by the electric field. This diffusion represents a higher recombination probability. Hence, the diffusion length and lifetime of charge carriers are important factors in a high-efficiency device.

In the solar cell showed in figure 2.2, the photons travel through the window layer (n-side, wide band-gap) and absorbed in the p-side, where the creation of electron-hole pairs takes place. The more photons are absorbed, the more charge carriers are generated, and the more electric current will be produced. To collect the charge carriers, the p- and n-side (both) must be contacted by ohmic contacts. At the back side, an opaque metallic contact is often used, while the front side is contacted with optically transparent conductive layers (i.e. window layer). Finally, the solar cell is connected to a load in order to have a current flow across the formed circuit [1,2].

The maximum absorption of light and thus the maximum generation of charge carriers in a solar cell occur close to the surface of the material. In a solar cell illuminated through a thick n-side material, most of the charge carriers will be generated in the neutral zone of the n-side far from the SCR, increasing the probability to be recombined in the surface. An approach to solve this issue is the formation of a p-n heterojunction structure with a wide band-gap n-type material (i.e. window layer). In this case, the light passes through the window layer to have a maximum absorption in the adjacent p-n interface zone, thus reducing the surface recombination.

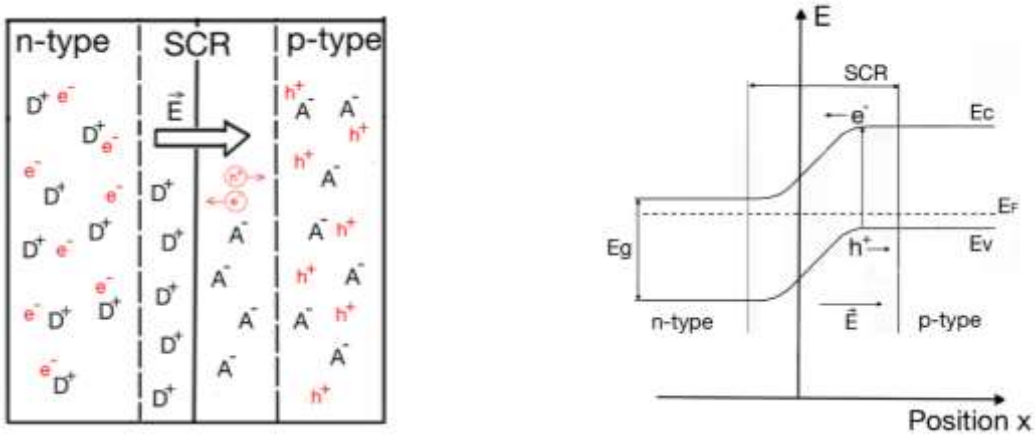

(a) (b)

Figure 2.3 a) Simplified schematic of a p-n junction with the respective space charge region (SCR) generated in both sides of the interface. D+ and A- are the ionized dopants atoms corresponding to donors and acceptors, respectively. The photogenerated electron-hole pairs are separated by the electric field E. b) Band structure of p-n homojunction.

2.1.2 Heterojunction

As mentioned above, the utilization of heterojunction-based solar cell permits the use of a wide band-gap window layer and hence reduce the surface recombination. Figure 2.4 shows the band structure of a p-n heterojunction. The use of different materials in the junction formation has two main effects on the device operation. In the first place, the valence and conduction band have discontinuities along the device structure, being the most important in the p-n junction. This junction represents the possible formation of energetic barriers for the charge carriers transport. In the second place, the presence of interface states due to the contacting of materials with different crystalline lattice, could act as recombination centers and thus reduce device performance. Two main approaches could be adopted to reduce the effects mentioned above, namely: (i) Decoupling of the physical and electronic junction by the formation of a buried junction (i.e. n-type layer creation into the former p-type material). (ii) The inversion of the interface by the formation of a n^+p interface in the absorber layer, where the conduction band of the p-type material is close the Fermi level. In this way, the minority carriers (electrons) in the p-type absorber

layer become majority carriers at the adjacent interface zone, hence decreasing the recombination probability discussed above. The implementation of these two approaches allows the development of high-efficiency solar cells, even with the presence of interface states.

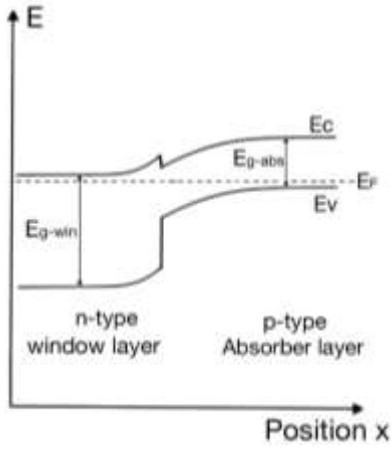

Figure 2.4 Electronic band diagram of a pn heterojunction.

2.1.3 Basic properties of solar cells

Figure 2.5 shows a solar cell represented by an equivalent circuit. Considering a simple single-diode model, where one charge carrier flows through the external circuit per each absorbed photon, two different currents are considered: (i) A photocurrent I_{photo} in the reverse direction and (ii) a forward current I_{dark} corresponding to the diode [2,3]. The current flow could be affected by series resistance (R_s) and parallel (or shunt) resistance (R_{sh}) of the solar cell. If the R_s and R_{sh} are considered to be zero and infinity (respectively), an ideal diode is considered with a total current I given by

$$I(V) = I_{dark} + I_{photo} = I_0 \left[exp\left(\frac{qV}{Ak_BT}\right) - 1 \right] - I_{photo} \qquad \text{(eq. 2.2)}$$

where I_0 is the reverse saturation current of the diode, A the diode ideality factor (A=1 for an ideal diode), K_BT the Boltzmann constant multiplied by the absolute temperature, q the elementary charge and V is the voltage applied to the diode.

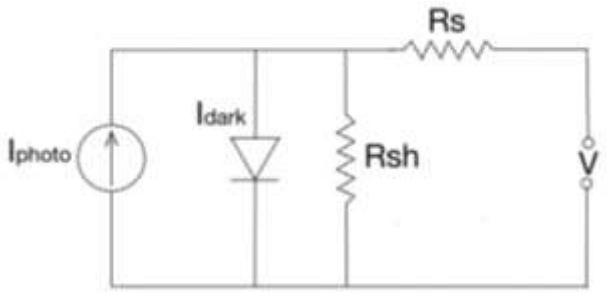

Figure 2.5 Equivalent circuit of a solar cell.

In the study of solar cells, the concept of current density (*J*) is commonly used. This notion is the relation between current (*I(V)*) and the surface of the solar cell (*S*):

$$J(V) = \frac{I(V)}{S} \qquad \text{(eq. 2.3)}$$

Figure 2.6 shows the typical variation of total current with applied voltage under illuminated conditions. If conditions of short-circuiting are applied (*V*=0), then

$$J = -J_{photo} = J_{sc} \qquad \text{(eq. 2.4)}$$

where J_{sc} is the short-circuit current, which is controlled by the current generation and recombination processes [2]. If the flowing current is zero (*J*=0), then

$$V_{oc} = \frac{Ak_BT}{q} ln\left[\left(\frac{J_{photo}}{J_0}\right) + 1\right] \qquad \text{(eq. 2.5)}$$

where V_{oc} is the open-circuit voltage, controlled by the diode current (dependence on *A* and J_0) [2]. Thus, a relationship between J_{sc} and V_{oc} can be found by:

$$J_{sc} = J_0\left[exp\left(\frac{qV_{oc}}{Ak_BT}\right) - 1\right] \qquad \text{(eq. 2.6)}$$

It is possible to observe that J_{sc} has the same form as the current-voltage in dark conditions observed as in Eq. 2.2, which means that A and J_0 values should be the same in both, dark and illuminated conditions [2]. It is important to mention that the current-voltage characteristic is the most used tool to study solar cells.

Given that the solar cell is a power conversion device, it is desirable that it works at maximum efficiency. Considering the diode curve (figure 2.6), the point where maximum power (MPP) occurs is related to the voltage and current at that maximum power point (V_{MP} and J_{MP}). The efficiency of a solar cell (η) is determined by the maximum output power divided by the irradiation power of sunlight:

$$\eta = \frac{J_{MP}V_{MP}}{P_{light}} \qquad \text{(eq. 2.7)}$$

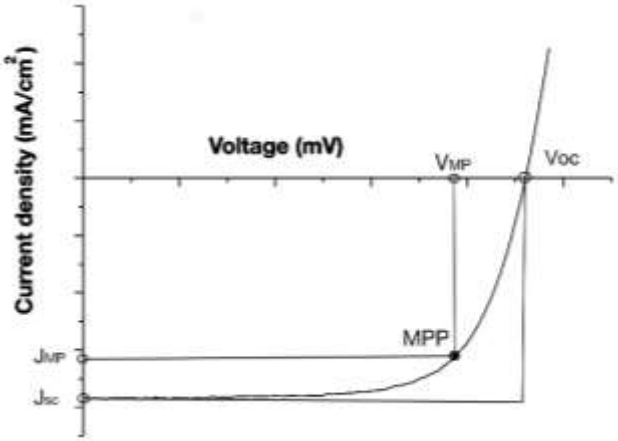

Figure 2.6 Diode curve of a solar cell highlighting basic parameters.

Another way to describe the quality of a solar cell is by using the fill factor (*FF*), which is a measure of the ideal shape or “squareness” of current-voltage curve and defined as

$$FF = \frac{J_{MP}V_{MP}}{J_{sc}V_{oc}} \qquad \text{(eq. 2.8)}$$

then the efficiency can be rewritten as

$$\eta = \frac{J_{sc}V_{oc}FF}{P_{light}} \qquad \text{(eq. 2.9)}$$

Low series resistance (R_s) and high shunt resistance (R_{sh}) allows the achievement of high fill factor values. The thickness of the layers and grids affect the series resistance, thus also affect the FF. The ideality factor also influences fill factor value [4].

The current density of the diode (Eq. 2.2) could also be rewritten considering the non-ideal resistance values ($R_s \neq 0$ and $R_{sh} \neq \infty$) and expressed as [5]:

$$J(V) = J_0 \left[exp\left(\frac{q(V-R_sJ)}{Ak_BT}\right) - 1 \right] + \frac{V-R_sJ}{R_{sh}} - J_{photo} \qquad \text{(eq. 2.10)}$$

Figure 2.7 shows the changes in the diode characteristic considering the effect of parasitic resistances. In the figure, it is possible to observe that the diode curve changes from an almost perfect rectangle to a more rounded shape.

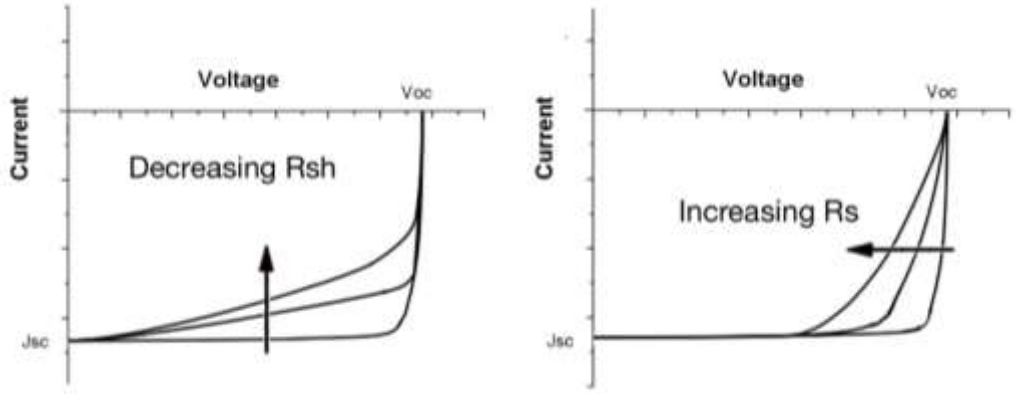

Figure 2.7 Changes in shape of diode curve including series (R_s) and shunt (R_{sh}) resistance.

2.2 $Cu(In,Ga)Se_2$ solar cell structure

The typical structure of a Cu(In,Ga)Se2-based solar cells (see figure 2.8) is a stack of thin films of different materials. As observed in the figure, the constituents are the soda lime glass (substrate), molybdenum (back contact), $Cu(In,Ga)Se_2$ (absorber layer), cadmium sulfide (CdS-buffer layer), zinc oxide (ZnO-window layer) and nickel/aluminum (contacts). The structure showed in figure 2.8 is the most successful concerning conversion efficiency, with reports showing 21.7%-22.6% [6,7]. In the following subsections, a brief description of each component is discussed.

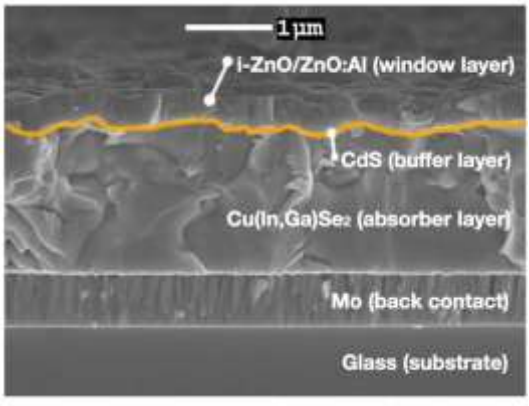

Figure 2.8 Schematic of CIGSe-based solar cell fabricated in this work.

2.2.1 Glass substrate

The most used substrate in CIGSe-based solar cells is a slide of soda lime glass (SLG) with a thickness of 1 or 3 mm. The use of SLG substrates allows record efficiencies in lab scale solar cells (21.7%). Some of the advantages offered by this type of substrate are the high availability, low cost, low roughness and a thermal expansion coefficient ($9x10^{-6}$/K) matching with CIGSe films [8]. Moreover, its good mechanical and chemical properties offered during the synthesis process at specific temperatures are essential characteristics. The soda lime glass consists of three main components: (i) glass forming materials (e.g. SiO_2), (ii) alkali metal oxides (e.g. Na_2O, K_2O, MgO) and (iii) stabilizers (e.g. CaO, ZnO). The alkaline components offer a source of alkali impurities that diffuse through the Mo layer up to CIGSe absorber. Indeed, it has been observed that sodium

diffusion into the CIGSe layer has a strong impact on its electrical and structural properties [9–12]. To nullify the effects caused by the diffusion of sodium, a diffusion barrier layer (e.g. Al_2O_3) is deposited between the glass substrate and the Mo back contact [13,14]. More on the role of sodium in CIGSe will be discussed further in this chapter. The use of SLG substrates for the deposition of high device quality CIGSe films (e.g. those obtained by evaporation processes) limits the synthesis temperatures to a maximum of 600°C, which is the softening point of the glass substrate. Furthermore, considering an industrial scale deposition with large area substrates (e.g. area of ~1m^2), the substrate temperature is restricted to ~520°C.

2.2.2 Molybdenum back contact

The back contact of a CIGSe-based solar cell should fulfill four main requirements. Firstly, the contact should not degrade in a selenium atmosphere at substrate temperatures of 600°C. Secondly, the selected material must form a low resistive contact to easily extract charge carriers (holes), thus minimizing recombination in CIGSe/Mo interface. Thirdly, the contact should possess a good reflectivity to minimize optical losses for long wavelengths (>700nm). Finally, the material should have a good adhesion to both, the glass substrate and CIGSe layer. Among many materials (e.g. Au, Ni, W) [15–17], molybdenum thin film offers a good comprise with all the characteristics mentioned above [1]. A Mo layer in the range of 0.5-1 μm thickness is deposited on the SLG using magnetron DC sputtering [18]. For a 1 μm Mo thin film thickness, the sheet resistance is in the range of 0.1 to 0.2 Ω/square [1].

The importance of use molybdenum as back contact lies in the unique behavior of the interface that forms with the CIGSe. Russell et al. [19] reported the formation of a Schottky barrier for a CISe/Mo interface. Nevertheless, several reports [20–23] reported the formation of ohmic contact between Mo and CISe through the formation of $MoSe_2$ at the interface of both materials. Thus, the formation of a CIGSe/$MoSe_2$/Mo interface became an important aspect of high efficiency CIGSe-based solar cells, considering that this leads to a better energy band alignment [23]. Another important characteristic of Mo back

contact is its permeability to the alkali metal oxides, allowing the diffusion of sodium oxide (Na_2O) into the CIGSe absorber film [1]. This permeability depends on the degree of tension and compression of the Mo layer (i.e. its porosity).

2.2.3 $Cu(In,Ga)Se_2$ thin film absorber

The polycrystalline $Cu(In,Ga)Se_2$ is a direct band-gap p-type semiconductor used as the absorber layer in a solar cell. Most of the photogeneration of electron-hole pairs occurs within this layer. An important characteristic of this material is the variable band-gap energy (1.04 to 1.68 eV) with increased gallium content. The increase of band-gap has a direct impact on the device performance [24]. The CIGSe film is grown by vacuum and non-vacuum techniques (further discussion in Chapter 3). The properties of this layer will be further discussed in the following sections.

2.2.4 Cadmium Sulfide buffer layer

The deposition of an n-type semiconductor window layer (i.e. wide band-gap material) on the p-type absorber film forms the p-n junction of a solar cell. The window buffer material must have a larger band-gap compared to the absorber in order to allow the incident photons to reach the absorber layer. Also, the buffer layer has a higher carrier density (around 10^{17} cm^{-3}) compared to the absorber film. In this way, the extension of SCR is wider into the absorber material, thus maximizing collection of photogenerated carriers [25]. In high efficiency CIGSe-based solar cells, the buffer layer is a cadmium sulfide (CdS) film deposited by chemical bath deposition (CBD) [6,7]. The CdS is an II–VI n-type semiconductor with a direct band-gap of 2.38-2.58 eV (higher than CIGSe 1.04-1.68 eV) and a wurtzite (stable, Eg=2.58 eV) or cubic (metastable, Eg=2.38) structure [26–28]. The CdS film deposited by chemical bath deposition has a mixed hexagonal/cubic or only hexagonal structure depending on the growth conditions [28]. For high-efficiency CIGS-based solar cells, a buffer layer with hexagonal structure is preferred over the cubic one, because its higher optical band-gap.

Another important parameter for a buffer film is the lattice mismatch in relation to the absorber layer, which impacts on the number of interface states. Wada et al. [28] reported a space between planes (d-spacing) of 3.36 Å corresponding to the (111)-plane of cubic-CdS or (002)-plane of hexagonal-CdS. The d-spacing of CdS corresponded to the ones related to the (112)-plane of CIGSe (d=3.34 Å). It was also observed that those planes of CdS were parallel to the (112)-plane of CIGSe. It is important to highlight that the mismatch increases with increasing Ga content [28].

The CdS buffer layer (50-80 nm thick) couples the CIGSe absorber and ZnO window layer in three main aspects: (i) electronically (i.e. band alignment), (ii) structurally (i.e. lattice match) and (iii) chemically (i.e. interdiffusion) [29,30]. The CdS film grown by CBD participates not only in the formation of the p-n junction but also in the passivation of surface states of CIGSe layer, elimination of surface oxides and protection of the absorber surface from potential damage during the deposition of ZnO window layer [31]. Although many attempts have been carried out to use another CdS growth technique (e.g. evaporation), lower performance has been obtained as compared to CBD [32].

Even though the CdS prepared by chemical bath deposition is the best buffer layer for high-efficiency solar cells, it has two main disadvantages: (i) there are concerns about environmental issues and waste disposal because its toxic nature and (ii) CBD process is not compatible with the in-line vacuum deposition of CIGSe modules. For these reasons, the CIGSe community is trying to replace the CdS buffer layer by different alternative materials such as In_2S_3 [33], Zn(OH,S) [34], among others.

2.2.5 ZnO based transparent conducting oxides (TCO)

The CdS buffer layer is followed by the RF sputtering deposition of a double layer ZnO structure [35]. The first layer is a highly resistive undoped zinc oxide film (i-ZnO) with a thickness of ~50 nm and a band-gap of 3.3 eV. The second layer is a degenerated n+ type Al-doped zinc oxide film (ZnO: Al) with a doping rate of 10^{20} cm^{-3}, ~300 nm thickness, and a band-gap of 3.6 eV [36]. The role of i-ZnO film is to provide protection against shunt

paths and also reduce Al diffusion into CdS. The purpose of the ZnO:Al layer is to provide a highly conductive top contact [37]. Both ZnO layers must have maximum transparency while ensuring a minimum resistivity in order to allow the transmission of all incident light to the absorber film. The p-n junction built with different materials is called a heterojunction. The transition of the Cu(In,Ga)Se2/CdS/i-ZnO structure from p-type to n-type is debated [38].

2.2.6 Ni/Al/Ni metallic contacts

Metal contacts are deposited on the ZnO:Al window layer by thermal evaporation in order to extract the photogenerated charge carriers. These grids consist of a stack layer structure made of nickel, aluminum, and nickel with a total thickness of ~2100 nm. Each part of this structure has a specific purpose. Firstly, the direct contact of nickel to the ZnO:Al prevents the oxidation of aluminum present in this window layer. Secondly, the aluminum layer represents the front ohmic contact of the solar cell. Finally, the second Ni layer avoids oxidation of the Al ohmic contact and allows contacting top of the grids.

2.3 Properties of the $Cu(In,Ga)Se_2$ absorber layer

2.3.1 Structural properties

The $Cu(In,Ga)Se_2$ is an I-III-VI_2 semiconductor material that crystallizes in a tetragonal chalcopyrite structure (figure 2.9). The Cu-In-Ga-Se quaternary system is based on the Cu-In-Se and Cu-Ga-Se ternary systems. The chalcopyrite lattice of $CuInSe_2$ (space group-I2d, lattice space a=5.782 Å, c=11.619 Å) [39] is obtained from the zinc blende structure with the introduction of an additional ordering of the cation sublattice, requiring a doubled primitive cell (tetragonal structure). This structure is visualized as two interpenetrating face-centered cubic (fcc) lattices, the first anion lattice consisting of group VI atoms (Se^{2-}) and the other being an ordered array of group I (Cu^{+}) and III (In^{3+}) cations. The group-I and group-III atoms are coordinated to 4 atoms of the group-VI in a tetrahedral manner. Each group-VI atom is coordinated to two group-I atoms and two

group-III atoms also in a tetrahedral way. The transition from CuInSe2 to Cu(In,Ga)Se_2 is achieved by the partial aleatory substitution of indium for gallium atoms. One of the most noticeable effects on the CISe structure with the addition of gallium is the decrease of the lattice parameters. This decrease represents a distortion of the crystal structure and is directly related to size difference of indium and gallium atoms (atomic radii ratio $r_{Ga}/r_{In} \approx 3/4$) [40]. The magnitude of the tetragonal distortion is given by $u=2-c/a$ ($c/a=2$ for undistorted structure) and linearly depends on Ga content [41]. In addition to this, other repercussions could be found such as the change of energies formation of crystalline defects and change of electrical properties [42].

To indicate the ratio of group-III elements (indium and gallium) in the CIGSe material the notation $CuIn_{1-x}Ga_xSe_2$ is commonly used, where

$$x = \frac{[Ga]}{[In+Ga]} \qquad \text{(Eq. 2.11)}$$

represents the gallium content in the material. Considering the tetragonal distortion, c/a value is higher (smaller) than 2 for x<0.23 (x>0.23) [41]. Another important ratio is related with the content of copper, defined as

$$y = \frac{[Cu]}{[In+Ga]} \qquad \text{(Eq. 2.12)}$$

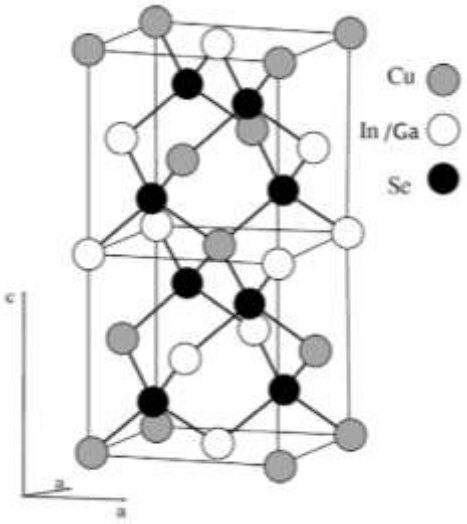

Figure 2.9 Unit cell of CIGSe crystalline structure.

2.3.1.1 Cu-In-Se system

Figure 2.10a shows the phase diagram of the Cu-In-Se ternary system, displaying the most probably formed phases [35]. The CuInSe2 (JCPDS 40-1487, space group $I\bar{4}2d$, lattice parameters a=5.782 Å, c=11.619 Å) is synthesized from the Cu_2Se and In_2Se_3 binary compounds. The tie-line between these two binary compounds represents the range of composition existing in the Cu-In-Se system. Figure 2.10b shows the Cu_2Se-In_2Se_3 binary phase diagram under thermodynamic equilibrium. It is important to point out that CIS and CIGS thin films used for photovoltaic applications are deposited under non-equilibrium conditions, thus, there is the possibility that the systems will not follow the same phase transitions showed in the following diagrams. These diagrams, nevertheless, offer valuable information in order to understand the growth mechanisms of CIGSe and CISe. The CISe-based high-efficiency solar cells are constituted by a p-type alpha-phase absorber (α-CISe), which is slightly Cu-poor as compared to its stoichiometric (Cu:25 at%, In:25 at%, Se:50 at%). In fact, the deposition conditions for standard α-CISe films used for photovoltaic applications lie at Cu concentrations in the range of 22 to 24.5 at% at temperatures of 500 °C.

Herberholz et al. [43] observed the extension of the formation region of CISe in a 2 at% of copper towards the In_2Se_3 binary compound with the incorporation of 0.1-0.2 at% of sodium. At high temperatures, the δ-CISe (sphalerite) phase is formed. The structure of this phase (unstable at room temperature) is a zinc blende unit cell in which the metallic cations (Cu^+ and $In^{3+}$are randomly distributed [35]. In the figure 2.10b, it is also possible to observe the presence of a mixture of α-CISe and Cu_2Se phases for Cu concentrations corresponding or above the stoichiometry of $CuInSe_2$.

Concerning the Cu-poor composition range, many phases can be formed. Copper concentrations of 16-23 at% promote the formation of α-$CuInSe_2$ along with the Cu-poor $CuIn_3Se_5$ phase (β-CISe), which similarly crystallize as $CuInSe_2$. In this In-rich $CuIn_3Se_5$ phase, the crystal structure is also composed of antisite defects (e.g. In_{Cu}) and Cu

vacancies (V_{Cu}) [35]. The β-CISe is also referred as Ordered Defect Compound (ODC) or Ordered Vacancy Compound (OVC), attributed to the regular arrangement of the vacancies sites. At lower Cu content (<16 at%), a $CuIn_5Se_8$ phase (γ-CISe) along with an In_2Se_3 phase is observed. Further crystalline phases could be formed such as a CuAu metastable phase with an energy formation slightly higher than the one needed for α-CISe. $CuInSe_2$ compound with Cu- and In-rich compositions could show this CuAu phase [44].

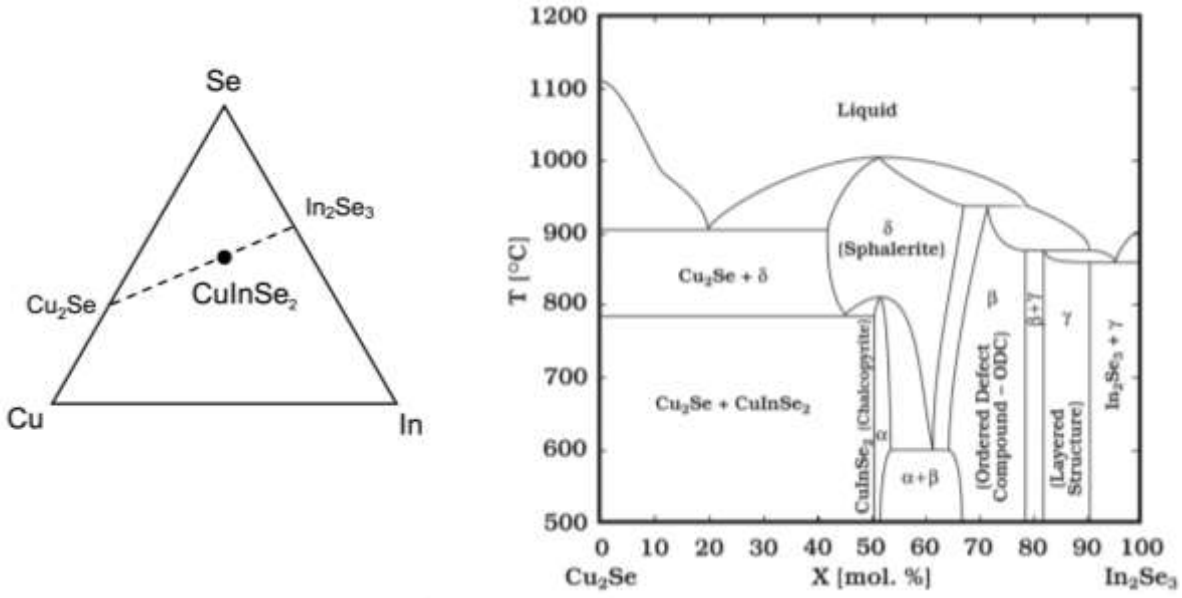

(a) (b)

Figure 2.10 Phase diagram of (a) Cu-In-Se ternary system and (b) pseudo binary Cu_2Se-In_2Se_3 system.

Folmer et al. [45] reported that the lattice of selenium atoms is the base of all compounds belonging to the Cu_2Se–In_2Se_3 tie-line (see figure 2.10b). The {100} planes of γ-In_2Se_3 have a structure consisted of distorted Se^{2-} hexagons. Further, the {111} plane of β-Cu_2Se contains hexagons formed by Se anions. The hexagons in {100} planes of γ-In_2Se_3 are centered into the ones of {111} planes of Cu_2Se. In this case, the Se^{2-} anions sublattice attain the epitaxial relation with the anion sub-lattice of β-Cu_2Se [46]. Thus, a transition from In_2Se_3 to α-$CuInSe_2$ by the addition of Cu and Se could indeed occur. The transition occurs by the in-diffusion of Cu atoms and out-diffusion of In atoms, where the basic

structure of the lattice needs to be modified only in the beginning when the CIS films are still very Cu-poor.

The conductivity type and carrier density of α-$CuInSe_2$ depends not only on its composition but also in the defects formed within its structure. During the formation of $CuInSe_2$, various point defects are certainly created. For $CuInSe_2$, copper vacancies (V_{Cu}) and selenium vacancies (V_{Se}) are of particular importance given its significance in the determination of conductivity type. A p-type CISe semiconductor is formed under Cu-poor and high Se vapor pressure conditions. The n-type CISe material is obtained with Cu-rich and Se deficiency conditions. In theses cases, the V_{Se} acts as a compensating donor and V_{Cu} as the dominant acceptor. These defects are formed in the bulk and surface (including grain boundaries) of the semiconductor material. Defects at grain boundaries (e.g. V_{Se}) are of special attention given its effects on high-efficiency CIGSe devices. Table 2.1 shows the most significant defects in device-quality CISe semiconductor.

Table 2.1 Most important intrinsic defects in CuInSe2 and its electronic character [35,47].

	Defect	**Type**
Vacancies	V_{Cu}	Acceptor
	V_{Se}	Donor
	V_{In}	Acceptor
Antisite	Cu_{In}	Acceptor
	In_{Cu}	Donor
	Cu_{Se}	Acceptor
	Se_{Cu}	Donor
	In_{Se}	Acceptor
	Se_{In}	Donor
Interstitial	Cu_i	Donor
	In_i	Donor
	Se_i	Acceptor

One important aspect to emphasize is that a deviation from the $CuInSe_2$ stoichiometric of

0.1 at% in composition induces defect concentrations on the order of ~10^{20}cm^3. However, the effective carrier concentration in CISe films is on the order of ~$10^{16\text{-}17}$cm^3 [35,48]. Considering the role of defects in the CISe films (i.e. acting as donors or acceptors) and the difference between the defects and carrier concentration, it is apparent the existence of a carrier compensation and/or that not all the defects are electrically active. Concerning this situation, a relevant observation is the formation of defect complexes (e.g. $2V_{Cu}+In_{Cu}$). The $(2V_{Cu}+In_{Cu})^0$ defect, likely formed in In-rich material, has no net effect on the electrical properties of CISe (i.e. is a neutral defect complex) [35,49]. Thus, the material has tolerance to a great off-stoichiometric range of compositions, accommodating a substantial amount of excess indium (or copper deficiency) and maintaining the electrical performance of the CISe [47]. Some of the defects mentioned before can be passivated, particularly those formed on the surface or grain boundaries of the film. The most important type of passivation is the one related to oxygen as proposed by Cahen et al. [50]. This model suggested the substitution of selenium vacancies by oxygen atoms forming In-O bonds, thus neutralizing the V_{Se} donor. More on this will be discussed in next subsections.

Herberholz et al. [43] observed the extension of the formation region of CISe in a 2 at% of copper towards the In_2Se_3 binary compound with the incorporation of 0.1-0.2 at% of sodium. Moreover, the substitution of indium by gallium atoms also allows the extension of the synthesis region of α-CISe. As mentioned above, the inclusion of Ga into the CISe crystal lattice will distort the structure due to a smaller atomic radii ($r_{Ga}/r_{In}\approx0.75$) and also modify the optical-electrical properties [41].

2.3.1.2 In-Se system

Okamoto et al. [51] reported the In-Se phase diagram. There are six compounds, namely In_4Se_3, InSe, In_6Se_7, In_9Se_{11}, In_5Se_7, and In_2Se_3. Regarding the CISe synthesis, the most important compound is the In_2Se_3, which exists in four different phases depending on synthesis temperature and composition (figure 2.11). The two most commonly used phases for CISe synthesis are the β- and γ-In_2Se_3, which coincides at temperatures

between 200 and 745 °C. The γ-In_2Se_3 is stoichiometric (60 at% of Se) whereas the β-phase is comparatively selenium deficient (59 at%) [46,52]. The γ-In_2Se_3 has a hexagonal crystal structure (space group P61) with lattice parameters a=7.128 Å, c=19.382 Å (JCPDS 40-1407). As mentioned in the previous subsection, the (100) plane contains distorted corrugated hexagons formed by Se^{2-} anions, allowing to fulfill the epitaxial relation with β-Cu_2Se. The β-In_2Se_3 has a rhombohedral layered structure (space group R-$\bar{3}$m) with lattice parameters a=4.05 Å and c= 29.41 Å [51,53].

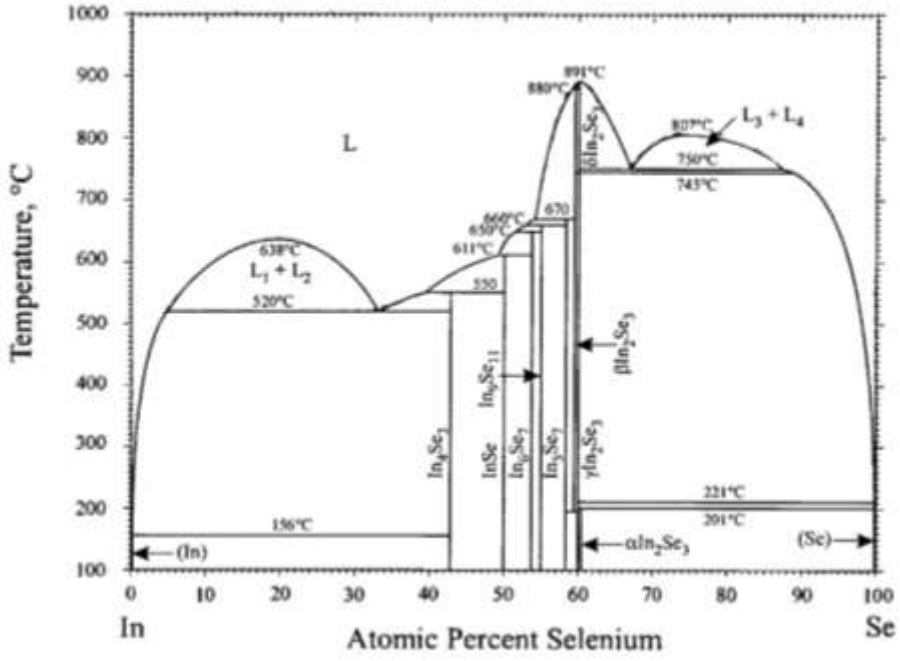

Figure 2.11 The indium-selenium phase diagram from [51].

2.3.1.3 Cu-Se system

The most important Cu-Se compound participating during the CISe growth is the $Cu_{2-x}Se$ (figure 2.12). There are two different $Cu_{2-x}Se$ phases: (i) the α-phase stable at low temperature (< 123°C) and (ii) high temperature β-phase [54]. The β-Cu_2Se (x=0) at high temperature crystallized in a cubic zincblende structure (space group F-43m, lattice parameter a=5.84 Å), having the same Se sublattice structure and similar lattice constant "a" as $CuInSe_2$ compound [55]. This structure has an ambipolar ion character with both

mobile cations (Cu^+) and electrons [56]. As mentioned above, the β-Cu_2Se and γ-In_2Se_3 combination results in a high diffusivity of In into the Cu_2Se compound, forming the final CISe semiconductor.

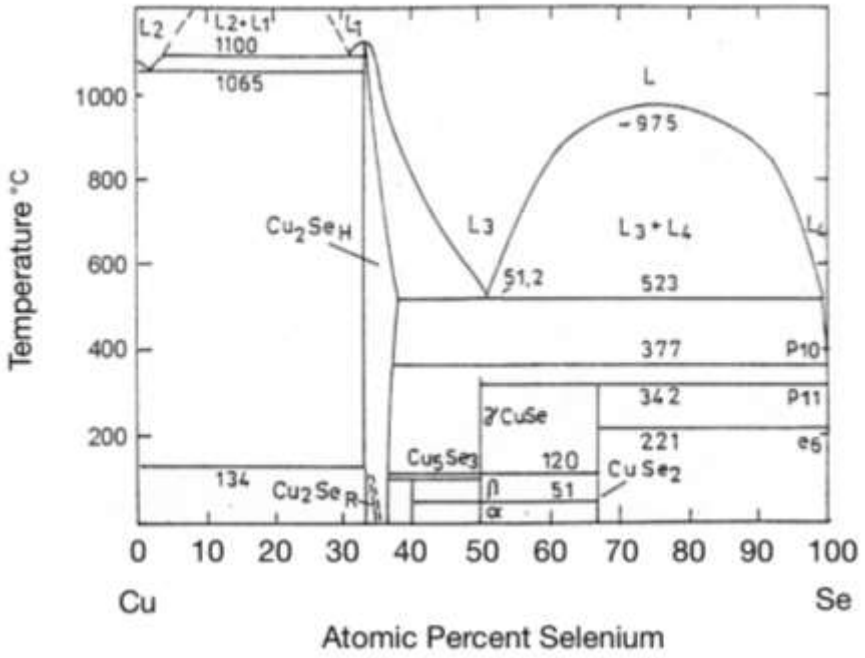

Figure 2.12 The Cu-Se phase diagram from [54] showing the transition:

221°C: Se(solid)→Se(liquid)

342°C: $CuSe_2$→γ-CuSe + Se

377°C: 2γ-CuSe→β-Cu_2Se

An important aspect related to the growth of CISe at Cu-rich condition is the presence of a liquid (or pseudo-liquid) Cu-Se phase at temperatures above 523°C (see figure 2.12). This phase is reported to promote the CISe grain growth through a vapor-liquid-solid growth mechanism, which enhance the diffusion of constituent atoms (more detailed discussion in Chapter 3). The Cu-Se pseudo-liquid phase form at high Se contents. This particular condition makes very plausible the formation of Cu-rich phases in the CISe material given that high-quality p-type absorber formation requires Se-rich conditions. Although there is a controversy whether the Cu-Se phases are in the liquid or solid state given that the growth takes place at non-thermodynamic equilibrium conditions with the

presence of impurities (e.g. In, Ga, Na), its beneficial effects during the growth of CISe are widely recognized [57,58]. In Chapter 3, a more detailed examination associated to the relation between Cu-Se phases and grain growth will be discussed.

2.3.1.4 In-Ga-Se system

The In-Ga-Se system is relevant for the synthesis of $Cu(In,Ga)Se_2$ material. Figure 2.13 shows the In_2Se_3-Ga_2Se_3 phase diagram with the presence of an $(In,Ga)_2Se_3$ compound. The $(In_{1-x}Ga_x)_2Se_3$ compounds with $x<0.5$ are reported to have hexagonal structure whereas compounds with reportedly $x>0.6$ values hold a zincblende structure [59,60]. Effectively, high-quality CIGSe could be synthesized through the utilization of a γ-$(In_{1-x}Ga_x)_2Se_3$ precursor material with a layered defect wurtzite structure (hexagonal, space group P61), similar as in the case of γ-In_2Se_3 used to obtain CISe [61].

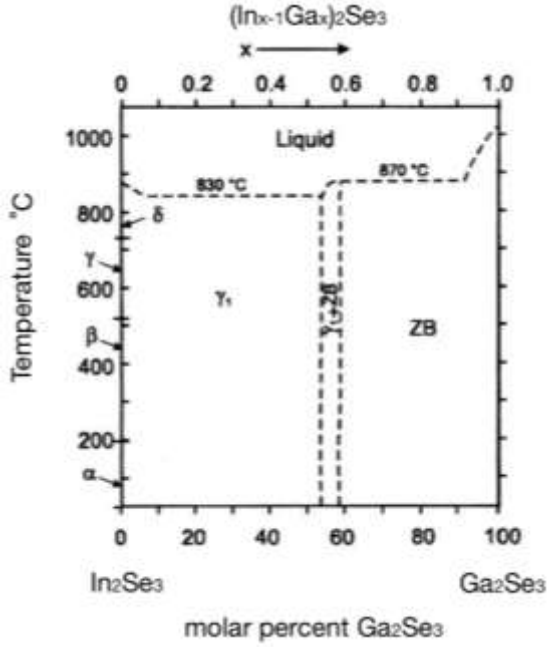

Figure 2.13 In-Ga-Se system phase diagram from [59,60].

2.3.2 Optical properties

The CuInSe2 material has a direct band-gap of 1.04eV and, therefore, absorbs light more efficiently compared to silicon (indirect band-gap). The high absorption coefficient $\alpha(h\nu)$ of CISe (~$2x10^5$ cm^{-1}) allows the absorption of almost all the portion of the solar spectrum in a ~2 μm thickness thin film. Moreover, the modulation of the band-gap is achieved by the substitution of indium by gallium atoms such that band-gap could change from 1.04 eV (CISe) to 1.65 eV (CGSe) [35] following the equation [24]:

$$E_g(x) = 1.04 + 0.65x + bx(1-x) \qquad \text{(eq. 2.13)}$$

where x = [Ga]/[In+Ga] represents the Ga content in CIGSe, and b = 0.15-0.24 eV is the bowing parameter [42].

The use of band-gaps between 1.1 and 1.5 eV allows to obtain the maximum theoretical efficiencies for single-junction solar cells (AM1.5 global radiation) [62]. Nevertheless, the best performance of CIGSe-based solar cells is achieved with Eg=1.2 eV, which corresponds to 30 at% gallium [6]. Furthermore, the band-gap of CIGSe is also influenced by copper content, in such manner that the Eg value of a $CuIn_3Se_5$ is 0.2 - 0.3 eV greater than the band-gap of $CuInSe_2$ [63].

2.3.3 Electrical properties

The electrical properties of the CIGSe depend on the chemistry and concentration of the doping either by intrinsic defects or extrinsic dopants (Table 2.1). The copper vacancies (V_{Cu}^-) give the p-type character to the CIGSe semiconductor. The creation of copper vacancies is due to the sub-stoichiometry in copper along with its low formation energy (the lowest in CIGSe) [64]. Other crystal defects affect the electrical properties of CIGSe. The selenium vacancies (V_{Se}^{2+}) and the antisites In_{Cu}^{2+} and Ga_{Cu}^{2+} act as compensating donor defects and thus contribute to the n-doping of the material. The copper atoms on indium sites (Cu_{In}^-), copper on gallium sites (Cu_{Ga}^{2-}) and indium vacancies (V_{In}^-) perform

as acceptors [64,65]. The p-type behavior could be counterbalanced by the formation of low-energy defect complex ($2V_{Cu}^{-} + In_{Cu}^{2+}$). The vacancy and antisite defects have mutually opposite charges, thus, it is said that the complex defect is electrically compensated.

Considering the mentioned above, is possible to observe that the electrical properties of CIGSe have a strong dependency on the growing methods and material composition. For example, Cu-rich CIGSe films ([Cu]/([In]+[Ga])=y>1) present the formation of Cu_{In}^{-} and V_{In}^{-} defects (i.e. acceptors) [64]. In Cu-poor CIGSe layers (0.85<y<0.95), In_{Cu}^{2+} donor and V_{Cu}^{-} acceptor defects are created [66]. CIGSe layers formed at high temperatures and under Se-deficient conditions are more likely to have selenium vacancies [67]. Additionally, Wei et al. [42] reported the increase of holes concentration in CIGSe thin films with the rise of gallium content. Moreover, the addition of sodium (diffused from glass) also allows to increase the hole carrier concentration in one order of magnitude, representing a decrease in resistivity in half or two orders of magnitude [68,69]. Thus, the growth conditions of a p-type CIGS absorber of device-quality are a lightly Cu-deficient composition, selenium in excess and a Ga content of 28-30 at% as well as the addition of sodium as an extrinsic impurity. These conditions allow to achieve films with a resistivity lower than 0.1 Ωcm, carrier densities of about 10^{16} cm^{-3} and charge carriers lifetime of ~200 ns [36,47].

2.3.3.1 Role of sodium

The role of sodium in CIGSe thin films is an important subject worth to mention. As indicated before in this chapter, very low concentrations of sodium (~0.1 at%) diffuse from SLG substrate through the Mo back contact into the absorbing CIGSe layer [70]. Different studies have shown that the presence of sodium in the absorber film improves solar cell efficiency by increasing the concentration of holes. This improvement in efficiency is observed mainly due to the enhancement of open circuit voltage and fill factor [13,68,71,72]. There are different theories on how the Na interacts with the CIGSe material. Nelson et al. [71] reported the increase of doping level by sodium acting as an

acceptor level by substituting indium (Na_{In}) or gallium (Na_{Ga}). Contreras and Rudmann [13,68] showed the beneficial effect of Na doping through the reduction of In_{Cu}^{2+} donor defects substituted by weak donor Na_{Cu} defects.

The sodium, along with oxygen, is mostly found at grain surfaces with a considerable lower concentration in grains interiors [73]. Furthermore, almost all the diffused Na, as well as the O, are concentrated at the grain boundaries, which represents the existence of a correlation between grain boundary density and the concentration of sodium and oxygen [73–75]. The sodium also has a significant influence on the growth of CIGSe films. The Na has a high sticking coefficient with Se; thus, sodium could form Na_2Se_x binary complexes on the growing surfaces [72]. These binary complexes act as Se reservoir during the growth of the CIGSe layer and thus reduces the formation of undesirable donor selenium vacancies. Although several results have been reported regarding the effect of sodium, the exact consequences in CIGSe are still controversial. The achievement of high-efficiency solar cells is also based on the energy bands engineering considering aspects such as surface inversion (p-type to n-type), gallium composition gradients, among others.

2.3.4 Energy band diagram of CIGSe-based solar cell

In CIGSe-based solar cells, the heterojunction is formed by contacting the CIGSe p-type absorber (χ_{CIGSe}=4.1 eV, E_g=1.15 eV-30 % Ga) and the n-type CdS ((χ_{CdS}=3.8 eV, E_g=2.4 eV)/ZnO ((χ_{ZnO}=4 eV, E_g=3.3 eV) window layers. The figure 2.14 shows the band diagram of the mentioned above heterojunction. The discontinuity observed in the conduction band at the interface is of particular importance because this will modify the flow of minority charge carriers (i.e. photogenerated electrons) from the CIGS absorber toward the buffer layer. Hence, this modifies the collection of charge carriers in the device. The energy discontinuities depend on the electronic affinities, band-gaps and doping of both materials. For high-efficiency CIGSe devices with a x=[Ga]/([Ga]+[In]) $\approx$0.3, the positive discontinuity ($\Delta Ec=\chi_{CIGSe}-\chi_{CdS}$) observed in figure 2.14 represents a energetic barrier of around 0.3 eV [76,77]. Although there are plenty of studies on this topic, the

absorber/window interface is still not well understood and is a controversial subject in literature.

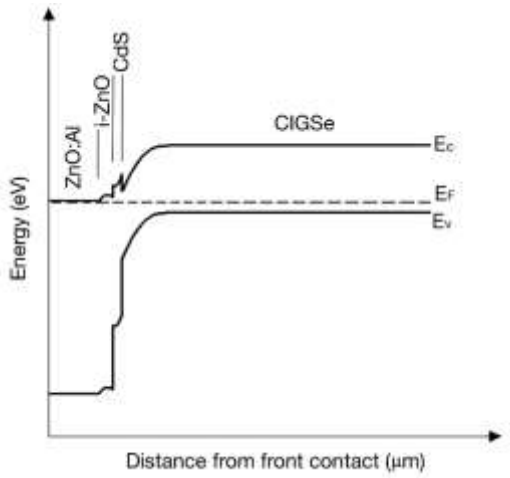

Figure 2.14 Electronic bands of the Al:ZnO /i-ZnO/CdS/ CIGSe solar cell structure simulated by AFORS-HET software [78].

The surface of CISe and its role on the heterojunction is also an important issue to point out. The importance lies in the inversion of the surface (from p-type to n-type), thus decreasing the recombination at the interface by promoting the separation of the physical junction from the electronic junction. Three models trying to explain this effect are worthy to mention. The first model is based on the formation of ordered vacancy compounds (OVC) on the surface [79]. In high-efficiency CISe-based solar cells, the absorber is grown with a copper content slightly lower than its stoichiometric, i.e. y~0.9. This copper deficiency promotes the creation of a copper-depleted region, with a composition close to $CuIn_3Se_5$ compound (OVC phase), located at the surface of the film [63]. Different studies [63,80] showed that the $CuIn_3Se_5$ compound is an n-type semiconductor with a band-gap of ~1.2-1.3 eV, clearly greater than 1.04 eV corresponding to CISe material. Considering the presence of $CuIn_3Cu_5$ on the surface of a $CuInSe_2$ layer, the Fermi level in (and near) the surface will be located farther from the maximum of the valence band in comparison with its location in the bulk material (figure 2.15a). Therefore, it is said that the OVC allows the p-type inversion of the absorber surface, separating the physical junction (with a large density of defects) from the electronic junction, hence minimizing

the recombination at the interface. For $Cu(In,Ga)Se_2$ the same phenomenon occurs at low gallium contents [80].

The second model proposed by Cahen et al. [50] is based on the surface inversion promoted by the formation of surface defects, giving particular attention to selenium vacancies (V_{Se}^{2+}). The CIGSe surface has dangling bonds that can be considered as positively charged Se vacancies. As a consequence of these positively charged surface, the type inversion of the absorbed surface is produced (figure 2.15b). As mentioned in subsection 2.3.1.2 (Cu-In-Se system), the selenium vacancies could be passivated by being replaced with oxygen atoms. This passivation results in the formation of In-O compounds, which in turn reduce the positive charges. In this case, the inversion (i.e. the band bending of the conduction band towards the Fermi level) is diminished [11].

The third model [81] explains of the surface inversion through the electro-migration of copper caused by an electric field promoted in turn by positively charged donor states at the absorber surface. The Cu^+ cations migrate towards the bulk of the material, leaving the surface with a high concentration of negatively charged defects (i.e. V_{Cu}^-). The combination of this effect with the one promoted by selenium vacancies at the surface results in the surface inversion observed in figure 2.15c. Furthermore, during the formation of CdS (CBD)/CIGSe heterojunction it is observed that the Cd occupies Cu sites (Cd_{Cu}), acting as a donor defect and thus causing further inversion of the surface [82,83].

2.3.4.1 Role of oxygen

High-efficiency CIGSe thin film solar cells critically depend on minimizing current and voltage losses across the grain surface. One approach to accomplish this is by oxidation-related passivation of surfaces. Previous experiments have shown the beneficial effect of air annealing treatments on the performance of CISe based solar cells [84]. This effect is explained by an oxygen passivation of surface dangling bonds related to Se vacancies (donor defects) [50]. This passivation (i.e. O_{Se}) takes place on interface states at the

CdS/CISe interface and grain boundaries (GB's) in the bulk of the film. The passivation of GB's states reduces the number of recombination centers along with the positive surface charge, which in turn reduces the band bending and space charge region within the grain (decreasing the portion depleted of free holes) [47]. Thus, the passivation of GB's surface states results in the increase of net acceptor doping concentration. Indeed, Cahen and Noufi [50] observed the increase of net acceptor concentration from ~10^{14} to ~10^{16} cm^{-3} on air annealed samples. Hence, passivation of GB's in the bulk of the film is beneficial to solar cell performance. The CdS/CISe interface passivation has two effects on the electronic properties. The first effect is the removal of interface recombination centers which facilitates the collection of photogenerated carriers. The second effect is the reduction of positive interface charge that is detrimental to solar cells due to a decrease of band bending in the absorber, enhancing interface recombination. In this case, the detrimental effect could surpass the beneficial one.

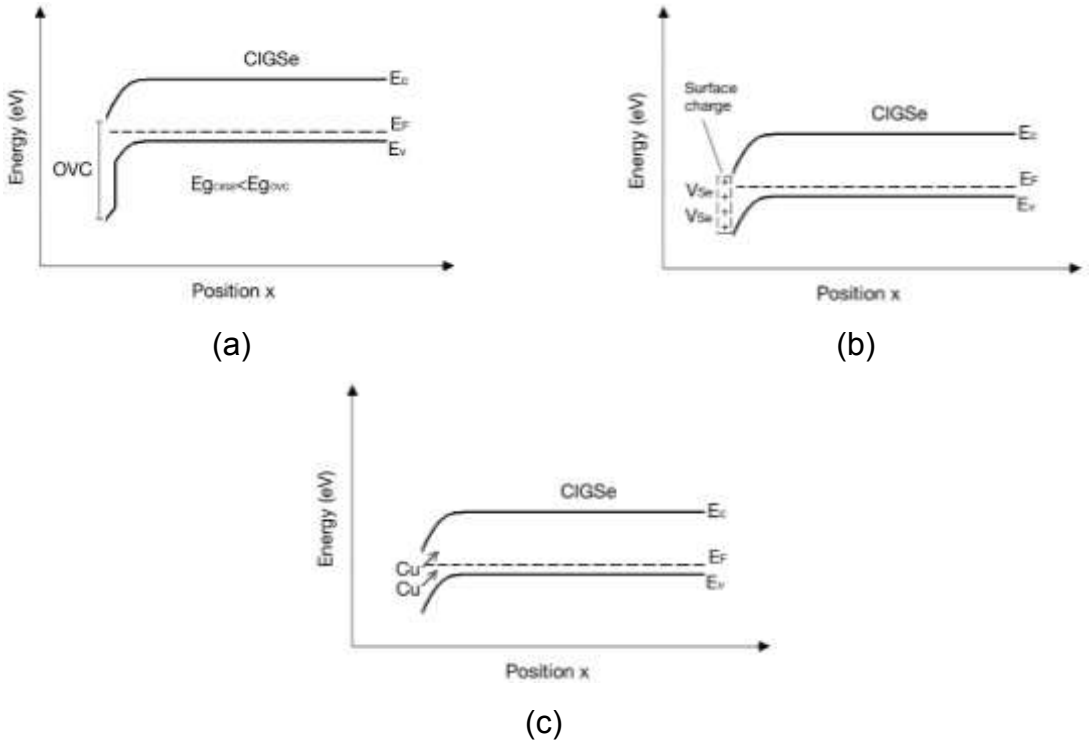

Figure 2.15 Inversion of the CIGSe surface by different models: (a) ordered vacancy compounds, (b) selenium vacancies and (c) copper migration.

An important aspect of the presence of oxygen in the CIGSe is its close relation to sodium. As mentioned before in subsections 2.2.2 and 2.3.3 (Molybdenum back contact and Electronic Properties), the sodium diffused from the SLG substrate to the CIGSe grain boundaries improves solar cell performance, especially by increasing open circuit voltage. Kronik et al. [11] attributed this enhancement to the increase of net p-type doping developed by Na-promoted oxidation and passivation of grain boundaries. Certainly, Na and O contents were found to be correlated using X-ray photoelectron spectroscopy (XPS) and secondary ion mass spectroscopy (SIMS) [85,86]. The Na Alkali metal has a catalytic effect on surface oxidation of semiconductors. These metals polarize the physisorbed O_2 molecule and increase the formation of O^{-2}, which in turn is easily chemisorbed. In CIGSe layers, the neutralization of selenium vacancies (located at grain boundary) could be achieved by the formation of Na-catalyzed In-O bonds (figure 2.16). An additional effect of oxidation is the copper migration from CIGSe surfaces. Rau et al. [87] suggested an oxygen-induced Cu release caused by the indirect weakening of Cu-Se bonds by the strong polar In-O bonds.

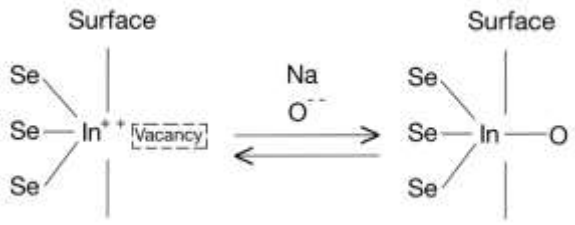

Figure 2.16 Passivation of surface selenium vacancies considering the Na catalytic effect.

2.3.5 Recombination paths in Cu(In,Ga)Se_2 solar cells

As mentioned previously in this chapter, there is the possibility that a photogenerated electron-hole pair recombines before its collection and participation in power generation. For a solar cell, this recombination represents charge losses. The main recombination in a semiconductor material are the radiative, Auger and Shockley-Read-Hall (both non-radiative). The radiative recombination occurs when an electron at the conduction-band

minima “returns” to the valence-band maxima with an emission of a photon with an energy equivalent to the band-gap of the semiconductor material. In the Auger recombination [88], the electron-hole recombines in a band-to-band transition but in this case, the resulting energy is given to another charge carrier, e.g. an electron in the conduction band. Next, the new excited electron eventually thermalizes and returns to the minimum of the conduction band. The importance of Auger recombination increases with increasing carrier concentrations (i.e. heavy doping). The Shockley-Read-Hall (SRH) recombination suggests the presence of defects (e.g. point defect, dislocation, impurity, grain boundaries) at the surface or bulk of the material. These defects generate energy levels inside the semiconductor band-gap that could trap the photogenerated electron (or hole). If a hole “jumps” into the same energy level where the electron is still captured (i.e. before re-emission to conduction band), then it is said that the electron recombines [89,90]. The most efficient recombination centers are the ones located near the middle of the band-gap.

In a defected polycrystalline material such as CIGSe, the SRH recombination is considered as the dominant effect in comparison with the radiative and Auger [91]. Moreover, the creation of defects in specific regions in CIGSe-based solar cells (e.g. CdS/CIGSe and CIGSe/Mo interfaces) also contribute to the dominance of SRH recombination. Another important issue related to defects is observed at the grain boundaries (GB's), where many defects accumulate and thus a high concentration of recombination centers is expected (i.e. lost in device performances). Nevertheless, efficiency reduction is not observed in polycrystalline CIGSe-based solar cells, thus exhibiting a certain level of tolerance to defects at the grain boundaries. In a research work to study the high efficiencies obtained in photovoltaic devices that use co-evaporated CIGSe absorbers, Persson and Zunger [92] attributed a beneficial contribution of GB's defects through the formation of ($2V_{Cu}$+In_{Cu}) complex defects, which reduces recombination at GB's by the decrease of hole concentration (i.e. valence band lowered with respect Fermi level). There are many other theories on the role of defects at grain boundaries; however, a consensus has not been reached.

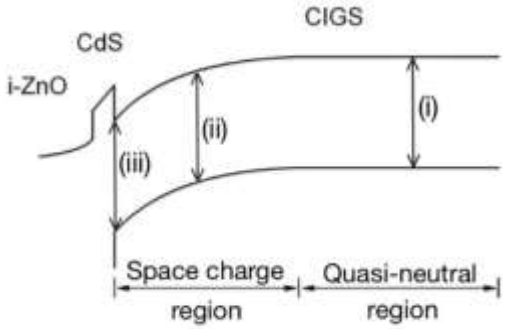

Figure 2.17 Schematic of band diagram of a ZnO/CdS/CIGSe structure and recombination paths. Paths A and B represent recombination in the quasi-neutral and space-charge regions of the absorber, respectively, path C represents interface recombination.

Figure 2.17 shows the band structure of a CIGSe/CdS heterointerface illustrating the recombination paths as presented by Rau and Schock [47]. The three main recombination mechanisms in CIGSe-based solar cells are (i) the recombination in the quasi-neutral region of the absorber, (ii) recombination in the space charge region (SCR) of the absorber and (iii) recombination at the CdS/CIGSe interface. Walters and Rau [91,93] observed that, in a high-quality CIGSe-based solar cell, the recombination of charge carriers mostly takes place in the volume of the CIGSe and particularly in the SCR. The recombination at the buffer and window layers is neglected given that they have a large band-gap values (i.e. lower concentration of photogenerated carriers compared to CIGSe). At the Mo back contact, the recombination is reduced owing to the formation of p-type $MoSe_2$, which decrease the concentration of electrons at the contact [23].

In a non-ideal junction, like those in CIGSe photovoltaic devices, the V_{oc} is determined by the dominant recombination path [47]. In CIGSe-based solar cells, the open circuit voltage is below the limit specified by radiative recombination. Thus, non-radiative recombination also has to be considered. If recombination in the quasi-neutral region is dominant (figure 2.17, path i), V_{oc} is given by

$$V_{oc} = \frac{E_g}{q} - \frac{k_B T}{q} ln\left(\frac{q D_n N_C N_V}{J_{sc} L_d N_A}\right) \quad \text{(eq. 2.14)}$$

where D_n is the electron diffusion constant, $N_{c/v}$ is the effective density of states in the conduction and valence bands (respectively), N_A is the acceptor density of the absorber, and L_d the diffusion length of the electrons in the absorber layer. Considering recombination at grain boundaries and recombination at back contact, then, L_d must be replaced by an effective diffusion length (L_{eff}) taking into consideration the grain size (g) and the grain boundary recombination velocity (S_{gb}):

$$L_{eff} = \frac{1}{\sqrt{\frac{1}{L_n^2} + \frac{2S_{gb}}{D_n g}}} \quad \text{(eq. 2.15)}$$

When recombination in the SCR dominates (path ii) and considering a $L_d = \sqrt{D_n \tau_n}$ (τ_n the electron lifetime), the following expression can be found for V_{oc}

$$V_{oc} = \frac{E_g}{q} - \frac{2k_B T}{q} ln\left(\frac{k_B T D_n \pi \sqrt{N_c N_v}}{J_{sc} L_d^2 F_m}\right) \quad \text{(eq. 2.16)}$$

where $F_m = \sqrt{2qN_A V_{bm}/\varepsilon_s}$ is the electrical field at the point of maximum recombination, ε_s is the dielectric constant of the absorber and V_{bm} is the band bending. Considering recombination in both quasi-neutral (eq. 2.14) and space charge region (eq. 2.16), the absorber band-gap is the common feature for the open circuit voltage. Moreover, in equations 2.14 and 2.16 is possible to observe that the V_{oc} depends on the concentration of acceptors in CIGSe (N_A) and the effective diffusion length (L_{eff}). An increase in N_A (e.g. Na incorporation) or L_{eff} (e.g. passivating grain boundaries) will result in an increment of open circuit voltage. Indeed, Rau et al. [47] reported a V_{oc} increased by ~60 mV with an increase of N_A in one order of magnitude. Nonetheless, a rise in acceptor concentration will reduce the SCR width in the CIGSe side, which directly impacts in the collection of photogenerated charge carriers and also in the upturn of recombination (Auger or tunneling related).

Considering the CdS/CIGSe interface recombination (path iii), the V_{oc} could be expressed as

$$V_{oc} = \frac{\phi_b^p}{q} - \frac{k_B T}{q} ln\left(\frac{q S_p N_V}{J_{sc}}\right) \quad \text{(eq. 2.17)}$$

where S_p is the interface recombination velocity for holes and Φ_b^p is the barrier height for holes, the latter corresponding to the energy difference between Fermi level and valence-band edge at the junction. In this case, the V_{oc} is strongly influenced by Φ_b^p and S_p. Rau and Schock [47] reported a V_{oc} of ~650 mV with a S_p of ~10^4 cm^{-3} and Φ_b^p of ~1 eV.

References

[1] A. Luque, S. Hegedus, Handbook of Photovoltaic Science and Engineering, John Wiley and Sons, 2011.

[2] R. Bube, Photoelectronic Properties of Semiconductors, Cambridge University Press, 1992.

[3] H. Mathieu, Physique des semiconducteurs et des composants électroniques, Dunod, 2004.

[4] A. Fahrenbruch, R. Bube, Fundamentals of solar cells: Photovoltaic Solar Energy Conversion, Academic Press, 1983.

[5] M.D. Archer, R. Hill, Clean electricity from photovoltaics, in: Imperial College Press, 2001. doi:10.1142/9781848161504_fmatter.

[6] P. Jackson, D. Hariskos, R. Wuerz, O. Kiowski, A. Bauer, T.M. Friedlmeier, M. Powalla, Properties of Cu(In,Ga)Se $_2$ solar cells with new record efficiencies up to 21.7%, Phys. Status Solidi - Rapid Res. Lett. 9 (2015) 28–31. doi:10.1002/pssr.201409520.

[7] P. Jackson, R. Wuerz, D. Hariskos, E. Lotter, W. Witte, M. Powalla, Effects of heavy alkali elements in Cu(In,Ga)Se $_2$ solar cells with efficiencies up to 22.6%, Phys. Status Solidi - Rapid Res. Lett. 4 (2016) 1–4. doi:10.1002/pssr.201600199.

[8] D. Boyd, D. Thompson, Kirk-Othmer Encyclopedia of Chemical Technology, John Wiley & Sons, Inc., Hoboken, NJ, USA, 1980. doi:10.1002/0471238961.

[9] J. Hedstrom, H. Ohlsen, M. Bodegard, A. Kylner, L. Stolt, D. Hariskos, M. Ruchh, H.-W. Schock, ZnO/CdS/Cu(In,Ga)Se2 thin film solar cells with improved performance, in: 23rd IEEE Photovolatic Spec. Conf., 1993: pp. 364–371. doi:10.1109/PVSC.1993.347154.

[10] U. Rau, M. Schmitt, F. Engelhardt, O. Seifert, J. Parisi, W. Riedl, J. Rimmasch, F. Karg, Impact of Na and S incorporation on the electronic transport mechanisms of Cu(In, Ga)Se_2 solar cells, Solid State Commun. 107 (1998) 59–63. doi:10.1016/S0038-1098(98)00154-9.

[11] B.L. Kronik, D. Cahen, H.W. Schock, Effects of Sodium on Polycrystalline Cu(In,Ga)Se_2 and Its Solar Cell Performance, Adv. Mater. 10 (1998) 31–36. doi:10.1002/(SICI)1521-4095(199801)10:1<31::AID-ADMA31>3.0.CO;2-3.

[12] S.-H. Wei, S.B. Zhang, A. Zunger, Effects of Na on the electrical and structural properties of $CuInSe_2$, J. Appl. Phys. 85 (1999) 7214–7218. doi:doi:10.1063/1.370534.

[13] D. Rudmann, G. Bilger, M. Kaelin, F.J. Haug, H. Zogg, A.N. Tiwari, Effects of NaF coevaporation on structural properties of Cu(In,Ga)Se_2 thin films, Thin Solid Films. 431 (2003) 37–40. doi:10.1016/s0040-6090(03)00246-3.

[14] A. Chirilă, P. Reinhard, F. Pianezzi, P. Bloesch, A.R. Uhl, C. Fella, L. Kranz, D. Keller, C. Gretener, H. Hagendorfer, D. Jaeger, R. Erni, S. Nishiwaki, S. Buecheler, A.N. Tiwari, Potassium-induced surface modification of Cu(In,Ga)Se_2 thin films for high-efficiency solar cells., Nat. Mater. 12 (2013) 1107–11. doi:10.1038/nmat3789.

[15] R.J. Matson, O. Jamjoum, A.D. Buonaquisti, P.E. Russell, L.L. Kazmerski, P. Sheldon, R.K. Ahrenkiel, Metal contacts to $CuInSe_2$, Sol. Cells. 11 (1984) 301–305. doi:10.1016/0379-6787(84)90019-X.

[16] E. Moons, T. Engelhard, D. Cahen, Ohmic contacts to p-$CuInSe_2$ crystals, J. Electron. Mater. 22 (1993) 275–280. doi:10.1007/BF02661377.

[17] K. Orgassa, H.W. Schock, J.H. Werner, Alternative back contact materials for thin film Cu(In,Ga)Se_2 solar cells, Thin Solid Films. 431-432 (2003) 387–391. doi:10.1016/S0040-6090(03)00257-8.

[18] J.H. Scofield, A. Duda, D. Albin, B.L. Ballard, P.K. Predecki, Sputtered molybdenum bilayer back contact for copper indium diselenide-based polycrystalline thin-film solar cells, Thin Solid Films. 260 (1995) 26–31. doi:10.1016/0040-6090(94)06462-8.

[19] P.E. Russell, O. Jamjoum, R.K. Ahrenkiel, L.L. Kazmerski, R.A. Mickelsen, W.S. Chen, Properties of the Mo-$CuInSe_2$ interface, Appl. Phys. Lett. 40 (1982) 995–997. doi:10.1063/1.92955.
[20] W.N. Shafarman, J.E. Phillips, Direct current-voltage measurements of the Mo/$CuInSe_2$ contact on operating solar cells, in: 25th IEEE Photovolt. Spec. Conf., 1996: pp. 917–919. doi:10.1109/PVSC.1996.564278.
[21] S. Nishiwaki, N. Kohara, $MoSe_2$ layer formation at Cu (In, Ga) Se_2/Mo Interfaces in High Efficiency Cu $(In_{1-x}Ga_x)Se_2$ Solar Cells, Jpn. J. Appl. Phys. 37 (1998) 71–73. http://iopscience.iop.org/1347-4065/37/1A/L71.
[22] L. Assmann, J.C. Bernède, A. Drici, C. Amory, E. Halgand, M. Morsli, Study of the Mo thin films and Mo/CIGS interface properties, Appl. Surf. Sci. 246 (2005) 159–166. doi:10.1016/j.apsusc.2004.11.020.
[23] T. Wada, N. Kohara, S. Nishiwaki, T. Negami, Characterization of the Cu(In,Ga)Se_2/Mo interface in CIGS solar cells, Thin Solid Films. 387 (2001) 118–122. doi:10.1016/s0040-6090(00)01846-0.
[24] M.I. Alonso, M. Garriga, C.A. Durante Rincón, E. Hernández, M. León, Optical functions of chalcopyrite $CuGa_xIn_{1-x}Se_2$ alloys, Appl. Phys. A Mater. Sci. Process. 74 (2002) 659–664. doi:10.1007/s003390100931.
[25] M.E. Ozsan, D.R. Johnson, M. Sadeghi, D. Sivapathasundaram, L.M. Peter, M.J. Furlong, G. Goodlet, A. Shingleton, D. Lincot, B. Mokili, J. Vedel, Optical and electrical characterization of chemically deposited cadmium sulfide thin films, in: 1st IEEE World Conf. Photovolt. Energy Convers., 1994: pp. 327–330. doi:10.1109/WCPEC.1994.519874.
[26] P. Reyes, S. Velumani, Structural and optical characterization of mechanochemically synthesized copper doped CdS nanopowders, Mater. Sci. Eng. B. 177 (2012) 1452–1459. doi:10.1016/j.mseb.2012.03.002.
[27] M. Cardona, M. Weinstein, G.A. Wolff, Ultraviolet reflection spectrum of cubic CdS, Phys. Rev. 140 (1965) A633–A637. doi:10.1103/PhysRev.140.A633.
[28] T. Wada, Microstructural characterization of high-efficiency Cu(In,Ga)Se_2 solar cells, Sol. Energy Mater. Sol. Cells. 49 (1997) 249–260. doi:10.1016/s0927-0248(97)00201-8.
[29] R. Hunger, M. V. Lebedev, K. Sakurai, T. Schulmeyer, T. Mayer, a. Klein, S. Niki, W. Jaegermann, Junction formation of $CuInSe_2$ with CdS: A comparative study of “dry” and “wet” interfaces, Thin Solid Films. 515 (2007) 6112–6118. doi:10.1016/j.tsf.2006.12.120.
[30] C. Heske, D. Eich, R. Fink, E. Umbach, T. van Buuren, C. Bostedt, L.J. Terminello, S. Kakar, M.M. Grush, T.A. Callcott, F.J. Himpsel, D.L. Ederer, R.C.C. Perera, W. Riedl, F. Karg, Observation of intermixing at the buried CdS/Cu(In, Ga)Se_2 thin film solar cell heterojunction, Appl. Phys. Lett. 74 (1999) 1451–1453. doi:10.1063/1.123578.
[31] J. Kessler, M. Velthaus, M. Ruckh, R. Laichinger, H.W. Schock, D. Lincot, R. Ortega, J. Vedel, Chemical bath deposition of cds on $CuInSe_2$, etching effects and growth kinetics, in: 6th Int. Photovolt. Sci. Eng. Conf., 1992: pp. 1005–1010.
[32] M. Rusu, T. Glatzel, C.A. Kaufmann, A. Neisser, S. Siebentritt, S. Sadewasser, T. Schedel-Niedrig, M.C. Lux-Steiner, High-Efficient ZnO/PVD-CdS/Cu(In,Ga)Se_2 Thin Film Solar Cells: Formation of the Buffer-Absorber Interface and Transport Properties, MRS Proc. 865 (2005) F14.25. doi:10.1557/PROC-865-F14.25.
[33] J. Sterner, J. Malmstrom, L. Stolt, J. Malmström, L. Stolt, Study on ALD In_2S_3/Cu(In,Ga)Se_2 interface formation, Prog. Photovoltaics Res. Appl. 13 (2005) 179–193. doi:10.1002/pip.595.
[34] C. Platzer-Bjorkman, J. Kessler, L. Stolt, Atomic layer deposition of Zn(O,S) buffer layers for high efficiency Cu(In,Ga)Se_2 solar cells, in: 3rd World Conf. Photovolt. Energy Convers., 2003: pp. 461–464. http://ieeexplore.ieee.org/stamp/stamp.jsp?arnumber=01305320.

[35] B.J. Stanbery, Copper Indium Selenides and Related Materials for Photovoltaic Devices, Crit. Rev. Solid State Mater. Sci. 27 (2002) 73–117. doi:10.1080/20014091104215.
[36] I. Repins, S. Glynn, J. Duenow, T.J. Coutts, W.K. Metzger, M.A. Contreras, Required material properties for high-efficiency CIGS modules, in: Proc. SPIE 7409, 2009: p. 74090M–14. doi:10.1117/12.828365.
[37] J. Kessler, M. Ruckh, D. Hariskos, U. Ruhle, R. Menner, H.W. Schock, Interface engineering between CuInSe2 and ZnO, in: 23rd IEEE Photovolt. Spec. Conf., 1993: pp. 447–452. doi:10.1109/PVSC.1993.347140.
[38] A. Nelson, A. Gabor, M. Contreras, A. Mason, P. Asokakumar, K. Lynn, Relation of polycrystalline Cu(In,Ga)Se_2 device efficiency with junction depth and interfacial structure, Sol. Energy Mater. Sol. Cells. 41-42 (1996) 315–323. doi:10.1016/0927-0248(95)00104-2.
[39] D.K. Suri, K.C. Nagpal, G.K. Chadha, X-ray study of $CuGa_xIn_{1-x}Se_2$ solid solutions, J. Appl. Crystallogr. 22 (1989) 578–583. doi:10.1107/S0021889889008289.
[40] S.C. Abrahams, J. Bernstein, Piezoelectric nonlinear optic $CuGaSe_2$ and CdGeAs2:Crystal structure, chalcopyrite microhardness, and sublattice distortion, J. Chem. Phys. 61 (1974) 1140–1146. doi:10.1063/1.1681987.
[41] D. Abou-Ras, R. Caballero, C.A. Kaufmann, M. Nichterwitz, K. Sakurai, S. Schorr, T. Unold, H.W. Schock, Impact of the Ga concentration on the microstructure of $CuIn_{1-x}Ga_xSe_2$, Phys. Status Solidi – Rapid Res. Lett. 2 (2008) 135–137. doi:10.1002/pssr.200802059.
[42] S.H. Wei, S.B. Zhang, A. Zunger, Effects of Ga addition to $CuInSe_2$ on its electronic, structural, and defect properties, Appl. Phys. Lett. 72 (1998) 3199–3201. doi:10.1063/1.121548.
[43] R. Herberhotz, H.W. Schock, U. Rau, J.H. Werner, T. Haalboom, T. Godecke, F. Ernst, C. Beilharz, K.W. Benz, D. Cahen, New aspects of phase segregation and junction formation in $CuInSe_2$, in: 26th IEEE Photovolt. Spec. Conf., 1997: pp. 323–326. doi:10.1109/PVSC.1997.654093.
[44] Y. Horikoshi, M. Kawashima, H. Yamaguchi, Low-Temperature Growth of GaAs and AlAs-GaAs Quantum Well Layers by Modified Beam Epitaxy, Jpn. J. Appl. Phys. 25 (1986) L868–L870.
[45] D. Cohen, J.C.W. Folmer, J.A. Turner, R. Noufi, Structural and Solar Conversion Characteristics of the $(Cu_2Se)_x(In_2Se_3)_{1-x}$ System, J. Electrochem. Soc. 132 (1985) 1319–1327. doi:10.1149/1.2114110.
[46] F. Hergert, S. Jost, R. Hock, M. Purwins, A crystallographic description of experimentally identified formation reactions of Cu(In,Ga)Se_2, J. Solid State Chem. 179 (2006) 2394–2415. doi:10.1016/j.jssc.2006.04.033.
[47] U. Rau, H.W. Schock, Electronic properties of Cu(In,Ga)Se_2 heterojunction solar cells-recent achievements, current understanding, and future challenges, Appl. Phys. A Mater. Sci. Process. 69 (1999) 131–147. doi:10.1007/s003390050984.
[48] D.J. Schroeder, J.L. Hernandez, G.D. Berry, A. a Rockett, Hole transport and doping states in epitaxial $CuIn_{1-x}$ Ga_xSe_2, J. Appl. Phys. 83 (1998) 1519–1526.
[49] C. Domain, S. Laribi, S. Taunier, J.F. Guillemoles, Ab initio calculation of intrinsic point defects in $CuInSe_2$, J. Phys. Chem. Solids. 64 (2003) 1657–1663. doi:10.1016/S0022-3697(03)00208-7.
[50] D. Cahen, R. Noufi, Defect chemical explanation for the effect of air anneal on CdS/$CuInSe_2$ solar cell performance, Appl. Phys. Lett. 54 (1989) 558–560. doi:10.1063/1.100930.
[51] H. Okamoto, In-Se (indium-selenium), J. Phase Equilibria Diffus. 25 (2004) 201. doi:10.1361/15477030418604.
[52] J.-B. Li, M.-C. Record, J.-C. Tedenac, A Thermodynamic Assessment of the In–Se

System, Zeitschrift Für Met. 94 (2003) 381–389. doi:10.3139/146.030381.
[53] K. Osamura, Y. Murakami, Y. Tomiie, Crystal Structures of α-and β-Indium Selenide, In_2Se_3, J. Phys. Soc. Japan. 21 (1966) 1848–1848. doi:10.1143/JPSJ.21.1848.
[54] T.B. Massalski, Binary Alloy Phase Diagrams, 1990.
[55] T. Wada, N. Kohara, T. Negami, M. Nishitani, Growth of $CuInSe_2$ crystals in Cu-rich Cu–In–Se thin films, J. Mater. Res. 12 (1997) 1456–1462. doi:10.1557/JMR.1997.0200.
[56] Z. Vucic, J. Gladic, Shape relaxation during equilibrium-like growth of spherical cuprous selinide single crystals, Fiz. A. 9 (2000) 9–26.
[57] W.N. Shafarman, J. Zhu, Effect Of Grain Size, Morphology and Deposition Temperature on $Cu(InGa)Se_2$ Solar Cells, MRS Proc. 668 (2001) H2.3.1–H2.3.6. doi:10.1557/PROC-668-H2.3.
[58] D. Rudmann, F.-J. Haug, M. Kaelin, H. Zogg, A.N. Tiwari, G. Bilger, Low Temperature Growth of CIGS Thin Films for Flexible Solar Cells, MRS Proc. 668 (2001) H3.8.1–H3.8.6. doi:10.1557/PROC-668-H3.8.
[59] A. Tonejc, S. Popović, B. Gržeta-Plenković, Phases, lattice parameters and thermal expansion of $(Ga_xIn_{1-x})_2Se_3$, $1 \geq x \geq 0$, between room temperature and melting point, J. Appl. Crystallogr. 13 (1980) 24–30. doi:10.1107/S0021889880011454.
[60] I.A. Ivashchenko, V.V. Halyan, I.V. Danylyuk, V.Z. Pankevuch, G.Y. Davydyuk, I.D. Olekseyuk, Crystal growth of the $(Ga_{1-x}In_x)_2Se_3$, $0.32<x<0.42$ phase and investigation of physical properties of obtained single crystals, in: IEEE Int. Conf. Oxide Mater. Electron. Eng., 2012: pp. 33–34. doi:10.1109/OMEE.2012.6464856.
[61] T. Mise, T. Nakada, Microstructural properties of $(In,Ga)_2Se_3$ precursor layers for efficient CIGS thin-film solar cells, Sol. Energy Mater. Sol. Cells. 93 (2009) 1000–1003. doi:10.1016/j.solmat.2008.11.028.
[62] W. Shockley, H.J. Queisser, Detailed balance limit of efficiency of p-n junction solar cells, J. Appl. Phys. 32 (1961) 510–519. doi:10.1063/1.1736034.
[63] M.A. Contreras, R. Noufi, Chalcopyrite $Cu(In,Ga)Se_2$ and defect-chalcopyrite Cu(In,Ga)3Se5 materials in photovoltaic P-N junctions, J. Cryst. Growth. 174 (1997) 283–288. doi:10.1016/s0022-0248(96)01160-8.
[64] S.B. Zhang, S.-H. Wei, A. Zunger, H. Katayama-Yoshida, Defect physics of the $CuInSe_2$ chalcopyrite semiconductor, Phys. Rev. B. 57 (1998) 9642–9656. doi:10.1103/PhysRevB.57.9642.
[65] H. Neumann, R.D. Tomlinson, Relation between electrical properties and composition in $CuInSe_2$ single crystals, Sol. Cells. 28 (1990) 301–313. doi:10.1016/0379-6787(90)90065-D.
[66] A. Rockett, R.W. Birkmire, $CuInSe_2$ for photovoltaic applications, J. Appl. Phys. 70 (1991) R81–R97. doi:10.1063/1.349175.
[67] R. Noufi, R. Axton, C. Herrington, S.K. Deb, Electronic properties versus composition of thin films of $CuInSe_2$, Appl. Phys. Lett. 45 (1984) 668–670. doi:10.1063/1.95350.
[68] M.A. Contreras, B. Egaas, P. Dippo, J. Webb, J. Granata, K. Ramanathan, S. Asher, A. Swartzlander, R. Noufi, On the role of Na and modifications to $Cu(In,Ga)Se_2$ absorber materials using thin-MF (M=Na, K, Cs) precursor layers, in: 26th IEEE Photovolt. Spec. Conf., 1997: pp. 359–362. doi:10.1109/PVSC.1997.654102.
[69] H. Ruckh, D. Schmid, M. Kaiser, R. Schaffler, T. Walter, H.W. Schock, Influence of substrates on the electrical properties of $Cu(In,Ga)Se_2$ thin films, in: 1st World Conf. Photovolt. Energy Convers., 1994: pp. 156–159. doi:10.1109/WCPEC.1994.519831.
[70] J.E. Granata, J.R. Sites, S. Asher, R.J. Matson, Quantitative incorporation of sodium in CuInSe2 and $Cu(In,Ga)Se_2$ photovoltaic devices, in: 26th IEEE Photovolt. Spec. Conf., 1997: pp. 387–390. doi:10.1109/PVSC.1997.654109.
[71] A.J. Nelson, D.W. Niles, D. Rioux, R. Patel, H. Höchst, H. Höchst, Soft x-ray photoemission investigation on the effect of In doping in $CdS/CuInSe_2$ heterojunction

formation, J. Appl. Phys. 72 (1992) 5888–5891. doi:10.1063/1.351895.
[72] D. Braunger, D. Hariskos, G. Bilger, U. Rau, H.W. Schock, Influence of sodium on the growth of polycrystalline Cu(In,Ga)Se_2 thin films, Thin Solid Films. 361 (2000) 161–166. doi:10.1016/S0040-6090(99)00777-4.
[73] D. Abou-Ras, S.S. Schmidt, R. Caballero, T. Unold, H.W. Schock, C.T. Koch, B. Schaffer, M. Schaffer, P.P. Choi, O. Cojocaru-Miredin, Confined and chemically flexible grain boundaries in polycrystalline compound semiconductors, Adv. Energy Mater. 2 (2012) 992–998. doi:10.1002/aenm.201100764.
[74] F. Couzinié-Devy, E. Cadel, N. Barreau, P. Pareige, J. Kessler, Atom probe contribution to the caracterisation of CIGSe grain boundaries, in: 37th IEEE Photovolt. Spec. Conf., 2011: pp. 001966–001971. doi:10.1109/PVSC.2011.6186339.
[75] A. Rockett, J.S. Britt, T. Gillespie, C. Marshall, M.M. Al Jassim, F. Hasoon, R. Matson, B. Basol, Na in selenized Cu(In,Ga)Se_2 on Na-containing and Na-free glasses: Distribution, grain structure, and device performances, Thin Solid Films. 372 (2000) 212–217. doi:10.1016/S0040-6090(00)01028-2.
[76] T. Minemoto, T. Matsui, H. Takakura, Y. Hamakawa, T. Negami, Y. Hashimoto, T. Uenoyama, M. Kitagawa, Theoretical analysis of the effect of conduction band offset of window/CIS layers on performance of CIS solar cells using device simulation, Sol. Energy Mater. Sol. Cells. 67 (2001) 83–88. doi:10.1016/S0927-0248(00)00266-X.
[77] M. Gloeckler, J.R. Sites, Efficiency limitations for wide-band-gap chalcopyrite solar cells, Thin Solid Films. 480-481 (2005) 241–245. doi:10.1016/j.tsf.2004.11.018.
[78] R. Varache, C. Leendertz, M.E. Gueunier-Farret, J. Haschke, D. Muñoz, L. Korte, Investigation of selective junctions using a newly developed tunnel current model for solar cell applications, Sol. Energy Mater. Sol. Cells. 141 (2015) 14–23. doi:10.1016/j.solmat.2015.05.014.
[79] D. Schmid, M. Ruckh, F. Grunwald, H.W. Schock, Chalcopyrite/defect chalcopyrite heterojunctions on the basis of CuInSe2, J. Appl. Phys. 73 (1993) 2902–2909. doi:10.1063/1.353020.
[80] M.A. Contreras, H. Wiesner, D. Niles, K. Ramanathan, R. Matson, J. Tuttle, J. Keane, R. Noufi, Defect chalcopyrite $Cu(In_{1-x}Ga_x)_3Se^5$ materials and high Ga-content Cu(In,Ga)Se_2-based solar cells, in: 25th IEEE Photovolt. Spec. Conf., 1996: pp. 809–812. doi:10.1109/PVSC.1996.564251.
[81] R. Herberholz, U. Rau, H.W. Schock, T. Haalboom, F. Ernst, C. Beilharz, K.W. Benz, D. Cahen, Phase segregation, Cu migration and junction formation in Cu(In,Ga)Se_2, Eur. Phys. J. Appl. Phys. 6 (1999) 131–139. doi:10.1051/epjap:1999162.
[82] P. Migliorato, J.L. Shay, H.M. Kasper, S. Wagner, Analysis of the electrical and luminescent properties of CuInSe2, J. Appl. Phys. 46 (1975) 1777–1782. doi:10.1063/1.321782.
[83] T. Nakada, A. Kunioka, Direct evidence of Cd diffusion into Cu(In,Ga)Se_2 thin films during chemical-bath deposition process of CdS films, Appl. Phys. Lett. 74 (1999) 2444–2446. doi:10.1063/1.123875.
[84] R.J. Matson, R. Noufi, R.K. Ahrenkiel, R.C. Powell, D. Cahen, EBIC investigations of junction activity and the role of oxygen in CdS/$CuInSe_2$ devices, Sol. Cells. 16 (1986) 495–519. doi:10.1016/0379-6787(86)90106-7.
[85] D.W. Niles, Na impurity chemistry in photovoltaic CIGS thin films: Investigation with x-ray photoelectron spectroscopy, J. Vac. Sci. Technol. A Vacuum, Surfaces, Film. 15 (1997) 3044. doi:10.1116/1.580902.
[86] N. Kohara, T. Negami, M. Nishitani, Y. Hashimoto, T. Wada, Electrical properties of Na-incorporated $Cu(In_{1-x}Ga_x)_3Se_5$ thin films, Appl. Phys. Lett. 71 (1997) 835. doi:10.1063/1.119661.
[87] U. Rau, D. Braunger, R. Herberholz, H.W. Schock, J.-F.F. Guillemoles, L. Kronik, D.

Cahen, Oxygenation and air-annealing effects on the electronic properties of $Cu(In,Ga)Se_2$ films and devices, J. Appl. Phys. 86 (1999) 497–505. doi:10.1063/1.370758.
[88] P. Auger, Sur les rayons beta secondaries produits dans gaz par des rayons X, C.R.A.S. 177 (1923) 169–171.
[89] W. Shockley, W.T. Read, Statistics of the Recombination of Holes and Electrons, Phys. Rev. 87 (1952) 835–842. doi:dx.doi.org/10.1103/PhysRev.87.835.
[90] R.N. Hall, Electron-Hole Recombination in Germanium, Phys. Rev. 87 (1952) 387–387. doi:10.1103/PhysRev.87.387.
[91] U. Rau, A. Jasenek, H.W. Schock, F. Engelhardt, T. Meyer, Electronic loss mechanisms in chalcopyrite based heterojunction solar cells, Thin Solid Films. 361 (2000) 298–302. doi:10.1016/S0040-6090(99)00762-2.
[92] C. Persson, A. Zunger, Anomalous grain boundary physics in polycrystalline $CuInSe_2$: the existence of a hole barrier., Phys. Rev. Lett. 91 (2003) 266401. doi:10.1103/PhysRevLett.91.266401.
[93] T. Walter, R. Herberholz, C. Müller, H.W. Schock, Determination of defect distributions from admittance measurements and application to $Cu(In,Ga)Se_2$ based heterojunctions, J. Appl. Phys. 80 (1996) 4411–4420. doi:10.1063/1.363401.

Chapter 3 $Cu(In,Ga)Se_2$ growth processes

As mentioned in chapter 2, the CIGSe thin film is the most important layer in the solar cell structure. On one hand, growth conditions of the absorber layer have a crucial role on the structural, optical and electrical properties of the CIGSe absorber. Thus the choice of the growth method, as well as the growth process, is a key factor for the achievement of high-performance devices. On the other hand, and as mentioned in the first chapter, one of the most important difficulties for a thin film photovoltaic technology to become globally adopted is closely related to the cost of energy produced by this (cost per Watt). The reduction of this cost could be achieved by either improving conversion efficiencies of solar cells or by the optimization of fabrication processes (e.g. material utilization) or development of new fabrication/deposition methods (e.g. implying the use of low-cost techniques, less pure precursors, inclusion of sulfur). Nowadays, the thin film deposition methods are mainly divided into two groups, namely, non-vacuum and vacuum. Electrochemical- [1,2], nanoparticle- (doctor blade, spin coating) [3,4] and spray-based deposition [5–8] are among the non-vacuum techniques. Amidst the existing vacuum techniques, the co-evaporation [9,10], sputtering [11] and selenization [12] are the most important ones.

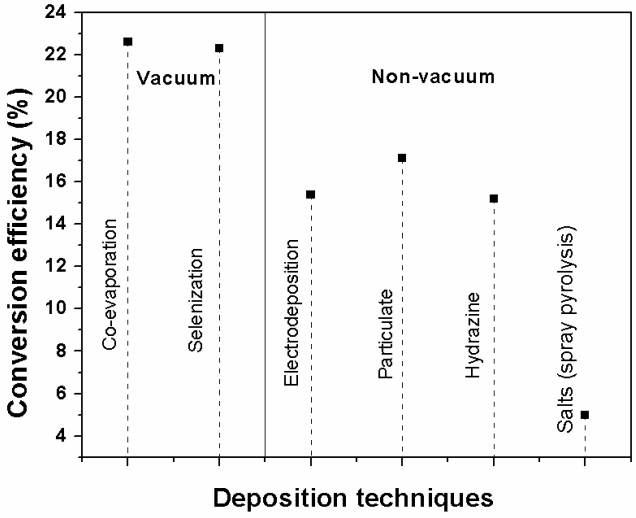

Figure 3.1 Conversion efficiencies of CIGSe-based solar cell grown by different vacuum and non-vacuum techniques from [8,9,13].

Figure 3.1 shows the conversion efficiencies of CIGSe-based solar cells (lab-scale and module) prepared with absorber layers deposited by different non-vacuum and vacuum techniques. As observed in figure 3.1, high-efficiency devices are achieved mostly by those techniques performed under vacuum conditions. Co-evaporation of elemental precursors [9,14] and reactive annealing of precursor films under selenium atmosphere (elemental Se or H_2Se_3 vapor) [15] are the techniques allowing the achievement of highest efficiencies. Although these techniques offer the best performances, also involve high capital investments in specialized equipment that have issues with the material-utilization efficiency (depending on the vacuum deposition technique). In comparison, non-vacuum deposition techniques represent a low production cost through the utilization of low-cost equipment, high material-utilization efficiency, and easy scale-up. Nevertheless, solar cells prepared by non-vacuum methods exhibit lower conversion efficiencies in comparison of those achieved with vacuum processes. Considering large scale productions of CIGSe, a simple example to elucidate one difference between the deposition cost of films with vacuum and non-vacuum methods, rather than the deposition itself, is the storage of the precursor chemicals. In one hand, the storage of Ga trace metals basis (Ga source used in vacuum co-evaporation) has to be done at 2-8°C in low humidity atmosphere to prevent melting and harmful oxidation of the material. In other hand, the gallium (III) chloride (Ga source used in non-vacuum chemical spray pyrolysis) could be storage as an aqueous precursor solution at room temperature. Stockpiling of precursors in less controlled environments could represent a reduction in cost.

This chapter gives a brief review of the different thin-film deposition techniques, giving special attention to co-evaporation (vacuum) and chemical spray pyrolysis (non-vacuum), which are the deposition techniques used in this work. Concerning co-evaporation deposition, the different processes (e.g. Boeing, CURO, CUPRO, 3-stage), as well as the importance of the presence of a copper rich phase during the formation of CIGSe, will be discussed. Further, the description of thin-film growth by chemical spray pyrolysis is reviewed. Finally, this chapter gives a description of the proposal to develop a hybrid deposition process, which exploit the advantages of both chemical spray pyrolysis and co-evaporation techniques.

3.1 $Cu(In,Ga)Se_2$ deposition by vacuum processes

As mentioned in Chapter 1 and 2, vacuum processes offer the best solar cell conversion efficiencies, in particular with the co-evaporation and sputtering technique that allow the achievement of the highest CIGSe-based solar cell efficiency in lab- and large-scale [9,16]. The vacuum deposition processes are classified by (i) the number of steps or stages required (i.e. 1, 2, 3-stages) and (ii) the presence (or not) of a crystallization or recrystallization phase (i.e. the existence of excess copper in determined conditions during certain stages of deposition). The next subsections give a brief description of the different vacuum processes, focusing primarily on the selenization of metallic precursor films and the co-evaporation of elemental precursors.

3.1.1 Selenization of metallic precursor layers

The CIGSe growth by selenization is a two-step process, which allows conversion efficiencies of 22.3% and 16.6% in small- and large-scale, respectively [16,17]. The most common process is the selenization of stacked metal or alloy layers. Different techniques are used to deposit these metals or alloys films, being sputtering [18,19] and evaporation [20,21] which allows the best efficiencies. The metal precursors are deposited at room temperature in single (e.g. Cu-In alloy) [22], bilayer (e.g. Cu/In, Cu-Ga/In) [23,24] or multilayer (e.g. Cu/In/Cu/In) configuration [25]. Then, a high-temperature annealing process (450-550°C) of the metallic precursor under selenium atmosphere (selenization step) is performed. The selenium source could be either H_2Se (best results but highly toxic) [26] or elemental Se [20,27]. The effect of selenization treatment depends on the duration (normally 30-60 min), thickness, composition of precursor film, temperature (heating curve), selenium source and stacked layer structure [28]. Another approach to deposit CISe films by this selenization process is the rapid thermal processing (RTP) of Cu-In-Se elementary layers [29]. Considering the formation of $Cu(In,Ga)Se_2$ layers, the reaction is slower and more energetic demanding in comparison to CISe films [30]. The inclusion of gallium in $CuInSe_2$ results in a non-uniform film where the Ga accumulates

close to the back contact promoting the formation of a $CuInSe_2$/$CuGaSe_2$ structure. This limits the performance of CIGSe-based devices, especially the open-circuit voltage, in comparison with co-evaporated-based solar cells [29,31]. Besides the precursors mentioned above, encouraging results on $CuInSe_2$ films were also obtained by the selenization of Cu-In-O precursor layers [32].

3.1.2 Co-evaporation processes

The co-evaporation is the most used technique for the deposition of high-quality $Cu(In,Ga)Se_2$ thin films, resulting in the best solar cell efficiencies. In this technique, vapors of different elemental materials are generated simultaneously from evaporation sources. These vapors condense together to form the absorber layer on a heated substrate at a certain distance from sources. The co-evaporation process consists in multiple steps (or stages) sequentially linked, each one characterized by fixed evaporation rates of individual elements and a set time. The total flux (i.e. atoms per time unit) of each element depends on its vapor pressure in the source and the temperature of the melt. The temperature of the melted material controls the evaporation rate (R) of the sources as observed in the approximation:

$$ln(R) \approx B + \frac{A}{T_s} \qquad \text{(eq. 3.1)}$$

where T_s is the surface temperature, *A* and *B* are constants. This equation works in the small interval of evaporation rates used for CIGSe growth [33]. Each evaporation source has an *A* and *B* constant determined by the measurement of the evaporation rate (quartz crystal monitor) or the thickness of the evaporated film. The arrival rate of the atoms to the substrate mainly depends on the distance from evaporation source and the shape of the flux beam (Φ). When an evaporated atom reaches the substrate, this could be adsorbed (stick to the substrate) or re-evaporated. The sticking coefficient (S_c) [34] is the ratio between the atoms used in the formation of the CIGSe layer (absorbed) and all the atoms that reach the substrate.

$$S_c = \frac{N_{adsorbed}}{N_{impinging}} \quad \text{(eq. 3.2)}$$

In the co-evaporation process of CIGSe, sources containing elemental copper, indium, gallium and selenium are used. The sticking coefficients of copper, gallium and indium are close to one. In this case, the deposition rate of each material could be considered to be equal the arrival rate. Furthermore, the sticking coefficient of selenium is lower than that of the other metals (i.e. Cu, In, Ga). For this reason, selenium is evaporated in excess (compared to the necessary to form an stoichiometric CIGSe film) with the objective to form an absorber without deficiency of selenium.

As indicated in Chapter 2, the structural, optical and electrical properties of CIGSe are closely related to the y=[Cu]/([In]+[Ga]) and x=[Ga]/([In]+[Ga]) ratios. Slightly sub-stoichiometric “y” values (i.e. $0.88 \leq y \leq 0.92$) and “x” values of around $0.3 \leq x \leq 0.33$ allow the achievement of the highest solar cells efficiencies [9]. Nevertheless, the "y" and "x" values are not necessarily constants during the growth process, especially the one related to copper whose evolution has a great impact on the structural and electrical properties of the final absorber film.

As mentioned in Chapter 2, the CIGSe-based solar cells prepared with co-evaporated absorbers reached more than 22% conversion efficiency [9,17]. This high efficiency is the result of almost 30 years of research focused on the development of growth processes [35]. The figure 3.2 shows the CIGSe laboratory-scale solar cell efficiency evolution with respect to time. In this figure, it is possible to observe a clear differentiation between solar cells efficiencies using CIGSe absorbers grown by two-step processes (1980-1993) [36] and the ones deposited by three-step processes (starting from 1993-1994 to date) [37]. The description of the most important processes and the difference in device conversion efficiencies, are explained further in this chapter (Sections 3.1.2.2-3.1.2.4). For the moment it will be suffice to mention that the most important two-step processes are the so-named Boeing and CURO (Cu-Rich then Off) [36]. The 3-step processes, allowing the highest efficiencies until now, are the so-called CUPRO (Cu-Poor then Cu-Rich then Off)

[38] and the 3-stage [37]. In these growth processes, the role of Cu-Se phases are fundamental for the achievement of high efficiency devices. In the next subsection, more on this will be discussed.

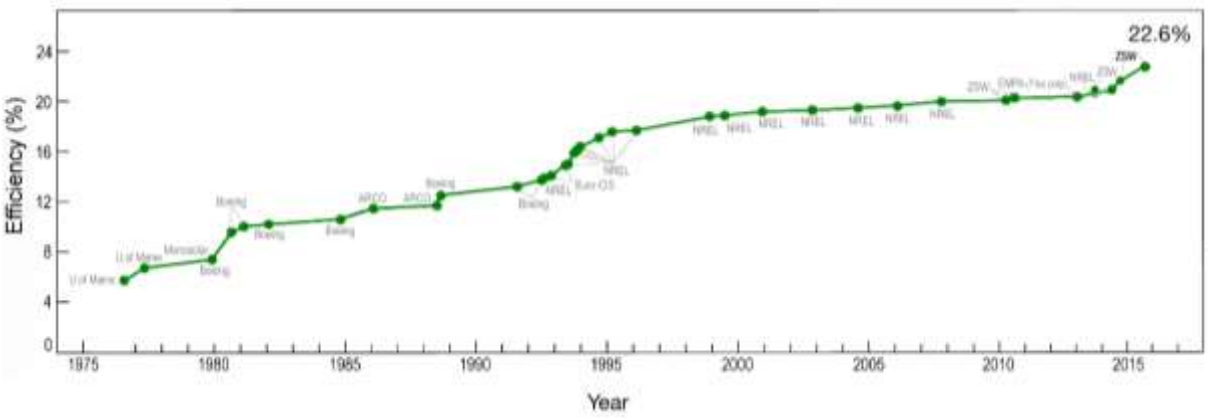

Figure 3.2 Laboratory-scale solar cell efficiency evolution with respect of time of CIGSe technology [9,35].

3.1.2.1 Role of the Cu-Se phase on the co-evaporation of $Cu(In,Ga)Se_2$

In relation to the co-evaporation growth processes mentioned in the above paragraph, an important point to highlight is that the processes giving the highest efficiencies (e.g. 3-stage, CUPRO, CURO) include the presence of a cooper-rich composition ([Cu]/[In+Ga]>1) at a certain instant during the growth of the absorber layer. As mentioned in Chapter 1 (section 2.3.1.4), growth of CIGSe at Cu-rich conditions promotes the presence of a Cu-Se phase at the surface of the grains. Shafarman et al. [39] observed that the Cu-rich composition condition favors the achievement of CIGSe with large grains and hence improves conversion efficiencies through the reduction of possible loss of photogenerated electron-hole pair in a high density of grain boundaries (i.e. reduction of recombination centers). The achievement of large grains is explained through the enhancing diffusion of group III elements within the liquid (or pseudo-liquid) Cu-Se phase segregated on the grain surfaces of Cu-rich films [40,41]. Even though the grain growth mechanism could be different for each deposition process, the Cu-rich condition (i.e. presence of Cu-Se phase) is similar for the case of growing CIGSe with large grains. Considering all the above mentioned, it could be suggested that the grain growth, along

with device efficiency, is enhanced by the appearance of Cu-Se phase at the surface of CIGSe grains.

In the following subsections, a brief description and particularities of different co-evaporation processes are given. The processes are classified into the number of steps that comprise the growth procedure and the offered details mainly include the substrate temperature, the flux of the elements ($\Phi_{Cu,In,Ga}$) and the evolution of "y" ([Cu]/[In+Ga]) ratio.

3.1.2.2 One step process

This process consists in the simultaneous evaporation of all elements at fixed evaporation rates at a constant substrate temperature [39]. The morphology of the growth layers is distinguished by relatively small (<1 μm) columnar grains [38]. The conversion efficiencies of CIGSe devices using the absorbers obtained by this process, are around the 16% [39].

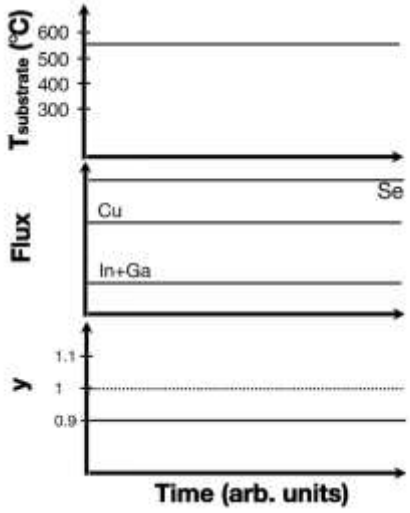

Figure 3.3 Schematic of the CIGSe deposition by one step process.

3.1.2.3 Two-step processes

3.1.2.3.1 Bilayer or Boeing process

First proposed by Mickelsen et al. [36], this process is based on two steps:
(i) The first step is the deposition of a copper rich CIGSe layer (y>1) at low substrate temperature (350 °C-450 °C);
(ii) The second step consist in the decrease of Cu flux along with the increase of indium and gallium fluxes at a high substrate temperature (550 °C -600 °C). This variation in fluxes will decrease the final composition to a sub-stoichiometric in copper (y<1) [42].

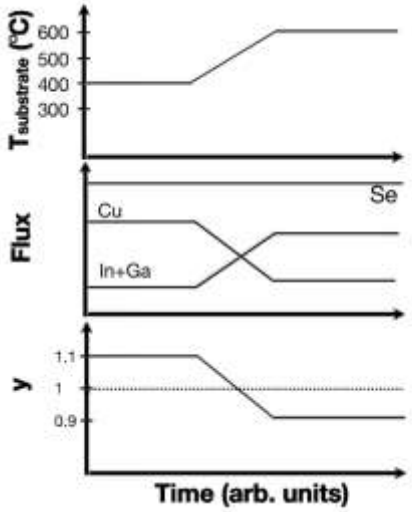

Figure 3.4 Schematic of the CIGSe deposition by boeing process.

Tuttle et al. [43] proposed a growth model of the two-step bilayer process. During the first step (y>1), a separation of CuSe (liquid)-$CuInSe_2$(solid) phases occurred in the form of islands. When the CISe islands coalesce, a thin layer of liquid Cu_xSe ($1 \leq x \leq 2$) is formed on the CISe surface. In the second step, the transformation of the "residual" Cu_xSe layer into $CuInSe_2$ is performed with an indium excess (copper flux off) consuming the Cu_xSe phase. The liquid Cu_xSe phase promotes the film growth through a vapor-liquid-solid mechanism, which improves the diffusion, transport and reaction kinetic. With this improvement, an epitaxial-like $CuInSe_2$ growth is achieved at the liquid-solid interface

[43]. The presence of the Cu_xSe phase has an important impact on the observed enhanced grain size (≈1 μm), in comparison to the one-step process (<1 μm) [36,43]. Wada et al. [44] proposed another growth model with the formation of a CuSe(liquid)/Cu_2Se(solid) interface. A chemical solid-state reaction takes place from Cu_2Se to $CuInSe_2$ through the replacement of copper atoms (in Cu_2Se) by indium atoms diffused through the liquid CuSe. Regarding the conversion efficiency of devices, this deposition process allows to obtain around 13% [43].

3.1.2.3.2 CURO (Cu-rich/Off) process

Based on the Boeing process, this consists in fixing the substrate temperature along with the indium and gallium fluxes during the whole process. At certain deposition time, the copper flux is stopped in order to obtain a final CIGSe composition slightly Cu-poor (y<1) [45]. The morphology of the growth layers is formed by columnar grains with sizes of more than 1 μm [39].The conversion efficiency of devices using absorbers deposited by this process are around 15-16% [39,45].

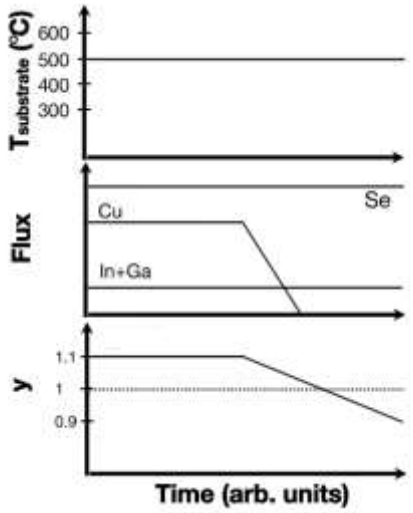

Figure 3.5 Schematic of the CIGSe deposition by CURO process.

3.1.2.3.3 Inverted process

The growth of absorber layers is based on an inverse Boeing process in which a deposition of a Cu-free $(In,Ga)_2Se_3$ (at low substrate temperature) is followed by the deposition of Cu and Se (at same substrate temperature). Immediately afterwards, a heat treatment of the film is performed under selenium flux at high substrate temperature (>500 °C). During this process, the "y" ratio does not exceed the value of 1 [46,47]. The observed grain sizes of the films grown by this growth process are in the range of 1-2 μm [48]. The efficiency of devices obtained with absorber films grown by this process are in the range of 13-17% [46–48].

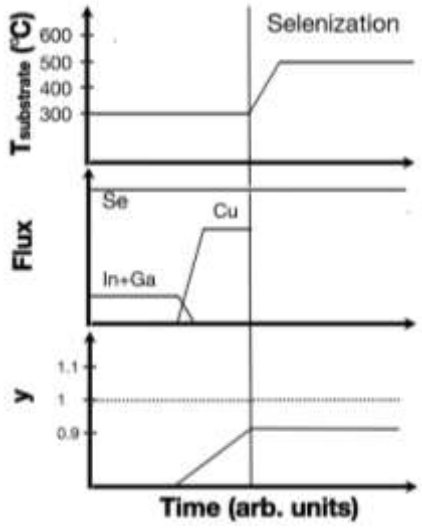

Figure 3.6 Schematic of the CIGSe deposition by inverted process.

3.1.2.4 Three-step processes

3.1.2.4.1 The 3-stage process

The CIGSe-based solar cells achieve the best conversion efficiencies [14,49] by using the so-called 3-stage process. The baseline 3-stage process consists of:

- Stage-1. The growth of a 1 μm thick $(In,Ga)_2Se_3$ thin film at rather low substrate temperatures (250 °C - 400 °C).

- Stage-2. The $(In,Ga)_2Se_3$ layers are used as precursor during the co-evaporation of copper and selenium at high substrate temperatures (550 °C - 600 °C), where a Cu-rich film is yielded (y=[Cu]/([In]+[Ga])>1).
- Stage-3. The indium, gallium and selenium are co-evaporated, and the film evolves gradually to Cu-poor (y<1) until the final composition is reached (y~0.9) [37,50].

The $(In,Ga)_2Se_3$ is transformed via γ-$Cu(In,Ga)_5Se_8$ followed by β-$Cu(In,Ga)_3Se_5$ (both Cu-poor phases) to a final α-$Cu(In,Ga)Se_2$. During this transformation process, the Cu_2Se and $(In,Ga)_2Se_3$ materials are brought together to form $Cu(In,Ga)Se_2$. To achieve this, a solid state interdiffusion of In, Ga, and Cu atoms is necessary. This diffusion could be carried out via (i) atom replacing another atom, (ii) interstitial migration or (iii) vacant lattice sites, being this last the most probable [51,52]. The diffusion rate of copper (diffusion coefficient at 400 °C $\sim 10^{-9}$ cm^2/s) is higher than those of indium and gallium ($\sim 10^{-13}$-10^{-12} cm^2/s) [51,53]. Thus, the most probable mechanism for CIGSe formation is the diffusion of Cu atoms into the $(In,Ga)_2Se_3$ along to the correspondent counter diffusion of vacancies into Cu_2Se, which is a characteristic of atomic transport via vacancies [54]. These diffused vacancies accumulate beyond the solid solubility threshold and promotes the formation of voids in the solid [54].

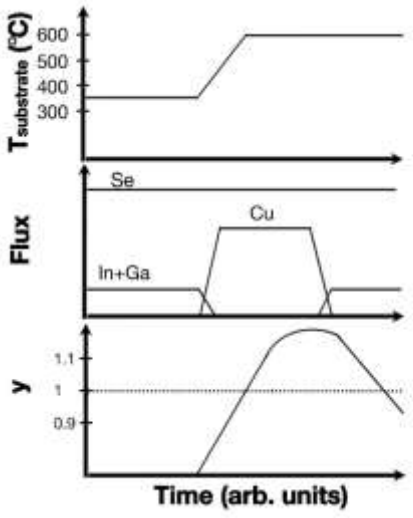

Figure 3.7 Schematic of the CIGSe deposition by 3-stage process.

The selenium flux (not shown in figure 3.7) is constant through all the 3-stage growth process. Even though each laboratory uses different selenium fluxes, the general aim is the use of an In, Ga, and Se general flux containing an excess of Se. Gabor et al. has reported the growth of $(In,Ga)_2Se_3$ films using a [Se]/([In]+[Ga]) flux ratio of approximately 3 [37]. His group also has reported the deposition of CIGSe with the use of a [Se]/[Cu] flux ratio of ~3 [37]. Mise at al. has reported the growth of $(In,Ga)_2Se_3$ with [Se]/([In]+[Ga]) flux ratio of 10 [55]. Although the Se flux is fixed, it has an important role in the deposition process. Indeed, the Se flux used during the growth of both $(In,Ga)_2Se_3$ and $Cu(In,Ga)Se_2$ thin films has been reported to affect their morphological, structural and electrical properties [56–58]. Ishizuka et al. [56] have reported the change in surface morphology of $(In,Ga)_2Se_3$ films from triangular to granular grains with the increase in Se flux. One effect of Se flux in CIGSe films is the increase in film porosity with the increase in [Se]/[Cu] flux ratio, probably related to a modification of the Cu-Se phase and the growth kinetics during the third stage of the deposition process [38,59]. Another effect in CIGSe films is the decrease of hole density with the decrease of Se flux, probably related to the formation of donor-like point defects (e.g. Se vacancies, see Chapter 2 section 2.3.1.1) [56]. As a consequence of all the changes in morphology, structure and electrical properties of CIGSe films, an impact on the solar cell parameters is also observed, with a substantial change in V_{oc} and *FF* [57,58].

3.1.2.4.2 The recrystallization phenomenon

As mentioned in subsection 3.1.2.1, high efficient CIGSe-based solar cells are close related to (but not only) an absorber film composed of large grains. During the growth process of CIGSe, a Cu-rich composition condition assists the attainment of CIGSe with large grains. Considering the growth processes presented in this chapter, both, two-step and three-step-based processes have a temporary Cu-rich composition of the film. Nevertheless, significant differences in the morphology of the grains of final CIGSe layers are obtained from the two distinct growth approach. In the two-step-based processes, the morphology of the grains of final absorbers is delineated within the first monolayers of CIGSe material deposited on the substrate. Considering the three-step-based processes,

the grains grown in the first stage (Cu-poor layer) are significantly smaller than the ones in the final film.

The grain size expansion is achieved by a mechanism known as the recrystallization phenomenon, which occurs when the film evolves from Cu-poor (y<1) to Cu-rich (y>1) composition at the end of the second stage of the 3-stage growth [60,61]. The recrystallization enables a reconstruction of the initial layer by a grain boundary migration mechanism [62], which change its structure from small to large grains while minimizing crystalline defects in the grains. As a consequence, the crystalline and electronic properties of the CIGSe layers are drastically changed during the recrystallization. Although not fully understood, the sudden mean grains size expansion (higher than any other growth process) is essential to achieve high-efficiency devices and is a key step in the 3-stage process. Considering the above mentioned, the transition from a poor to a high crystalline quality material occurring during the recrystallization, additionally suggests the existence of a wide window of the structural and electrical properties of the $(In_{1-x}Ga_x)_2Se_3$ precursors films that result on high-quality final $Cu(In,Ga)Se_2$ absorbers.

Considering all the afore mentioned growth processes, it is possible to notice that an important parameter during the growth of CIGSe films is the y=[Cu]/[[In]+[Ga]] ratio, which is a flag to determine the copper composition of the layer. As mentioned before, In the case of the 3-stage process the recrystallization step is identified by the Cu composition of the layer. Thus, the tracking of the Cu content during the deposition process is crucial for the achievement of high efficiency CIGSe solar cells. In the next subsection, the in-situ copper monitoring method used in this work is briefly explained.

3.1.2.5 In-situ monitoring of copper rate

To obtain high-quality CIGSe films, the composition of the material (during its growth) has to surpass a stage excess of copper (y>1). As discussed in Chapter 2 (section 2.3.1.2 and 2.3.1.4), when the composition of the growing layer is in copper excess, two phases are formed, namely, chalcopyrite CIGSe phase and Cu-Se phase. The emergence of the

Cu-rich phase at the surface of the CIGSe introduce a change in the optical, morphological and thermic properties of the growing film. One specific change is the increase of thermic emissivity of the layer due to the superficial segregation of the Cu-rich phase. Considering the substrate heating system during the deposition process, the change in emissivity of the film could result in a modification of the substrate heating power at a constant temperature. Thus, it is possible to detect the transition from a layer sub-stoichiometric to an over-stoichiometric in copper (or vice versa), depending on the power required to maintain the substrate at a constant temperature. The presence of a segregated Cu-rich phase will cause an increase in emissivity and a decrease of the substrate surface temperature. Hence, the heating power has to be increased in order to maintain a constant substrate temperature. The technique which monitors this emissivity/heating-power variation is called “End Point Detection” (EPD) [63]. The close relation between the heating power variation and the change in copper ratio in the film has been reported by Kessler et al. [45].

The figure 3.8a shows the EPD signal of the so-called 3-stage process. It is possible to observe that the end of the second stage is defined by the increase of the heater power signal consequence of the Cu-rich phase segregation on the surface of the CIGSe. At this point, the film is over-stoichiometric ($y>1$). Next, in the third stage, the signal decreases consequence of obtaining a layer slightly sub-stoichiometric in copper ($y<1$). In this work, the substrate temperature has been kept constant while monitoring the electrical power feed to the substrate heater. A thermocouple at the back of the substrate reads the temperature, which is feedbacked to a temperature controller, that controls the electric power supply of the heater lamps (see figure 3.8b).

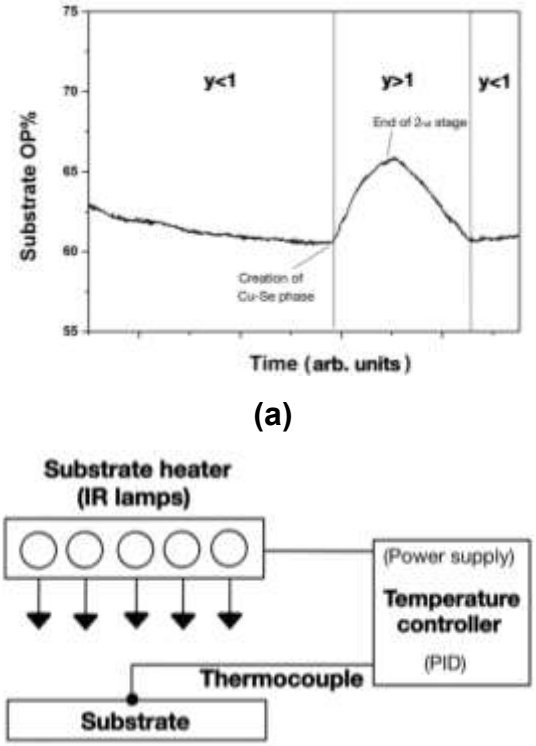

Figure 3.8 (a) Substrate output power during the recrystallization step in a 3-stage process, (b) Schematic of the feedback system of the substrate heater.

3.2 Non-vacuum processes

The non-vacuum processes are mainly based on a two-step procedure, which consists of (i) the deposition of a precursor film at rather a low temperature (room temperature to 400 °C) in atmospheric conditions followed by (ii) post-deposition annealing treatment in selenium atmosphere at a high temperature (450 °C to 600 °C). This sort of procedure offers several advantages, such as:

(i) The simplicity of necessary equipment reduces the cost of production. This is vital in the implementation of large-scale processes.

(ii) High material-utilization efficiency close to 100%.

(iii) Non-vacuum methods are potentially less energetic intensive compared to vacuum- based process (high substrate temperatures, vacuum machines, among others).

(iv) Easy deposition on flexible substrates (roll-to-roll process).

The CIGSe non-vacuum deposition processes are mainly divided into three categories depending on the deposition method and the mixing of the precursor materials: (i) electrochemical, (i) particulate (e.g. coating inks) and (iii) solution based processes (e.g. spray pyrolysis, spin coating). A brief description of some of this methods is given in the following subsections, with a particular emphasis in chemical spray pyrolysis given that is the technique used in this work.

3.2.1 Electrochemical process

Electrochemical techniques for the preparation of CISe-based films include one-step deposition, sequential deposition of binary compounds, and deposition of elemental layers followed by annealing under either an inert or a Se/H_2Se reactive atmosphere [64]. The One-step electrodeposition of CIS is usually carried out at room temperature from aqueous solutions that contain simple compounds of Cu^{2+} or Cu^{+} and In^{3+} [65,66]. The reactions involve metal chalcogenides such as Cu_2Se and In_2Se_3 and are comparable to the reactions taking place at the substrate surface during co-evaporation of CISe. The incorporation of gallium by electrodeposition is yet more challenging than that of indium.

3.2.2 Particulate process

Coating a substrate with a particulate ink offers a highly material-efficient method of deposition. The best device conversion efficiencies are obtained by two types of precursors, namely, oxides or metal-selenides [67,68]. In the oxides precursors developed by International Solar Electric Technology (ISET), the particles are first reduced in an atmosphere containing an H_2/N_2 gas mixture to form a metal layer (Cu, In and Ga). Then, this layer is selenized in an atmosphere containing H_2Se/N_2. The metal-selenides approach developed by Nanosolar uses a mixture of Cu-Se, In-Se and Ga-Se nanoparticles followed by an annealing treatment. In both methods, Ga segregation near the back contact was observed, which could be attributed to the presence of sodium in

the film. This last is also seen in layers deposited by co-evaporation.

3.2.3 Solution process

In this process, the precursors can be completely dissolved in the solvent, forming a solution with the required elements mixed on a molecular level. The precursors can be classified as: (i) metal salts (e.g. chlorides and nitrites), (ii) organometallic and (iii) hydrazine-based. In this work, some of the studied thin films are deposited by a metal salt-based deposition. Thus, a deeper discussion on the metal salt-based deposition process is given in the following.

3.2.3.1 Metal salt based process: Chemical spray pyrolysis

The deposition of CIGSe through the use of metal salts precursor solution is considered one of the easiest approaches, given that the salts have a good solubility in water and alcohol. This precursor solution could be used in a spray pyrolysis deposition system (e.g. pneumatic, ultrasonic) to deposit thin films. The chemical spray pyrolysis (CSP) deposition has the advantages of low-cost equipment, low energy needs, easy scale-up, simple atomization process and operation at moderate temperature (e.g. 100-500°C). This deposition is based on the pyrolytic decomposition of small droplets of precursor solution onto a heated substrate under atmospheric conditions [69]. Typical CSP equipment consists of an atomizer (nozzle), a substrate heater, carrier gas, temperature controller and a solution container (figure 3.9).

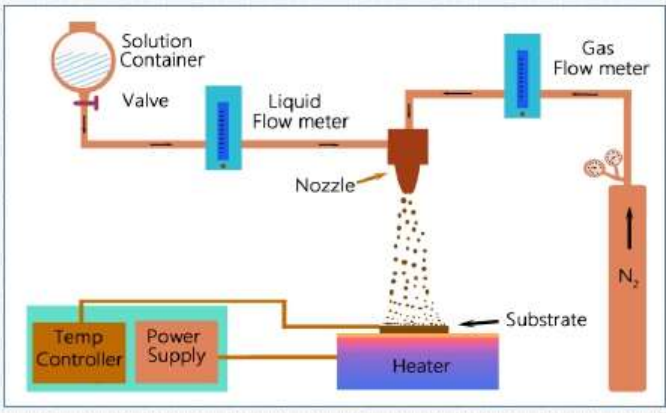

Figure 3.9 Schematic diagram of chemical spray pyrolysis equipment.

The deposition process of CSP has three main steps: the atomization of precursor solutions, transportation of the resultant aerosol and decomposition of the precursor on the substrate. The aerosol droplets experience evaporation during the transport from the nozzle to the substrate, leading to a size reduction and concentration gradient within the droplet [70].

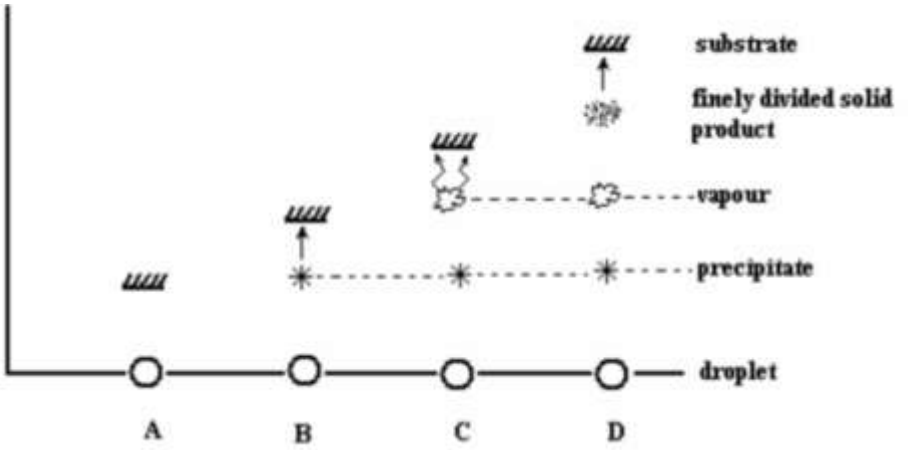

Figure 3.10 Spray processes taking place with an increased temperature.

Different processes occur when a droplet approaches the heated substrate surface (i.e. increasing temperature): evaporation of the solvent, spreading of droplet and salt decomposition. The figure 3.10 describes the four possible processes occurring with increasing temperature [71]. In process A (lowest temperature), the thermal energy absorbed by a droplet is not enough to vaporize the solvent before its arrival to the heated substrate. As a consequence, the droplet splashes on the substrate and the residual solvent is then evaporated from the substrate leaving a dry precipitate in which decomposition occurs, resulting in localized cool spots and a correspondingly poor quality film. In process B, the droplet vaporizes just before reaching the substrate, leaving precipitated particles of the reactants. These are deposited on the substrate, where they melt/sublime, again causing localized cooling and consequently films of inferior quality. In process C, the solvent evaporates completely, long before reaching the substrate. Then, the precipitated particles melt, sublimes and diffuse to the substrate surface. Here

the reactant molecules undergo processes of adsorption, surface diffusion, and reaction, leading to nucleation and layer growth while by-products evaporate and diffuse away from the surface [72]. This process represents a chemical vapor deposition (CVD) [73,74]. In process D (highest temperature), the metallic compound vaporizes before it reaches the substrate and chemical reaction takes place in vapor phase [71]. In this case, the product molecules may condense as micro-crystallites which form a powdery deposit giving poor crystalline quality.

Considering the afore mentioned, it is possible to notice that some important chemical spray pyrolysis deposition parameters are: i) Substrate temperature, ii) properties of the precursor solutions, iii) spray rate, iv) nozzle to substrate distance, v) pressure, vi) carrier flow rate and type of carrier gas. The CIGSe deposition by chemical spray pyrolysis manly consists on the use of a chloride-based solutions (80% water, 20% ethanol) which includes $CuCl_2$, $InCl_3$, $GaCl_3$ and N-N-dimethyl-selenourea (DMSeU), as the Cu, In, Ga and Se sources, respectively [75,76]. The proportion of these in the final precursor solution is such that Se precursor will be always in excess (Cu:DMSeU ratio of at least 1:3). The deposition temperatures are in the range of 250-400°C [77,78]. Brown and Bates [77] [BROWN1990] proposed a model for the formation of $CuInSe_2$ material by chemical spray pyrolysis considering the $CuCl_2$, $InCl_3$, $GaCl_3$ and N-N-dimethyl-selenourea (DMSeU) as precursors. In this model, the formation of CISe requires the creation of complexes that relates the metal and the chalcogen precursor material, which under high temperature conditions (pyrolysis) forms the I-III-VI_2 compound. The formation of these complexes takes place in the precursor solution (before spraying) and are described by the equation 3.3 and 3.4. The DMSeU plays an important role in the formation of the complexes by reducing the cupric ions (Cu^{2+}) to cuprous ions (Cu^{+}). One part of the DMSeU helps in the reduction of the Cu^{+2} through its oxidation, producing N,N-dimethyl formamidine diselenide (equation 3.3). Another part of the DMSeU stabilizes the Cu^{+}, resulting in a soluble complex (equation 3.4). When precursor solutions of $CuCl_2$, $InCl_3$ and DMSeU are mixed in water at room temperature, a CuCl·2[DMSeU] precipitated is formed. In an aqueous solution composed of 80% water and 20% ethanol, the ethanol displaces the chloride ion as a ligand in the CuCl·2[DMSeU] segregate (equation 3.4). It

is important to notice that the formation of the complex requires three molecules of DMSeU (Cu:DMSeU ratio of 1:3).

$$Cu^{2+}(aq) + NH_2(CH_3)_2NC{=}Se(aq) \rightarrow Cu^{+}(aq) + 1/2\ (NH(CH_3)_2NC\text{-}Se)_2(aq) + H^{+}\ (aq)$$

(eq. 3.3)

$$Cu^{+}(aq) + 2NH_2(CH_3)_2NCSe(aq) + CH_3CH_2OH(aq) \rightarrow Cu{\cdot}2NH_2(CH_3)_2NCSe{\cdot}\ CH_3CH_2OH^{+}\ (aq)$$

(eq. 3.4)

Once the precursor solution is prepared and the different complexes are formed, this is sprayed onto the heated substrate. At this stage, the solvents evaporates and the $Cu{\cdot}2[DMSeU]{\cdot}[\ CH_3CH_2OH]^{+}$ complex reacts with the indium ions to form solid $CuInSe_2$ and other by-products (equation 3.5):

$$Cu{\cdot}2NH_2(CH_3)_2NCSe{\cdot}CH_3CH_2OH^{+}\ (aq) + In^{3+}\ (aq) + 4Cl^{-}\ (aq) + 4H_2O \rightarrow$$
$$CuInSe_2\ (s) + 2CO_2\ (g) + 2(CH_3)_2NH\ (g) + 2NH_3\ (g) + 4HCl\ (g) + CH_3CH_2OH\ (g)$$

(eq. 3.5)

The remaining N,N-dimethyl formamidine diselenide produced in reaction 3.3 is probably reduced by the oxidation of chloride ions to chlorine gas (equation 3.4).

$$1/2\ (NH(CH_3)_2NCSe)_2\ (aq) + HCl\ (aq) + 2H_2O \rightarrow$$
$$H_2Se\ (g) + (CH_3)_2NH\ (g) + NH_3(g) + CO_2\ (g) + 1/2\ Cl_2\ (g)$$

(eq. 3.6)

In this manner, it is possible to have an overall reaction for the formation of $CuInSe_2$ by chemical spray pyrolysis from equations (eq. 3.5) and (eq. 3.6) [77]:

$$CuCl_2\ (aq) + InCl_3\ (aq) + 3NH_2\ (CH_3)_2NCSe\ (aq) + 6H_2O \rightarrow$$
$$CuInSe_2\ (s) + 3(CH_3)_2NH\ (g) + 3NH_3\ (g) + 3CO_2\ (g) + H_2Se(g) + 4HCl\ (g) + 1/2\ Cl_2\ (g)$$

(eq. 3.7)

In the case of the $Cu(In,Ga)Se_2$ thin film deposition, the proposed reaction occurring during the deposition process is:

$$CuCl_2\,(aq)+InCl_3\,(aq)+GaCl_3\,(aq)+3.5NH_2(CH_3)_2NCSe(aq) + 6H_2O \rightarrow Cu(InGa)Se_{2.5}\,(s)+3(CH_3)_2NH\,(g)+3NH_3\,(g)+3CO_2\,(g)+H_2Se\,(g)+4HCl\,(g) + 2Cl_2\,(g) \quad \text{(eq. 3.8)}$$

As seen in the previous reactions, undesirable by-products in the film are expected (i.e. oxygen, hydrogen, carbon, among others). These could have an impact in the electrical properties of the final films, which could decrease solar cell performance [79]. Thermodynamics calculations of the formation of the single-phase chalcopyrite compounds $CuInSe_2$ has been undertaken by Mooney et al. [80] with the aim of optimizing the thin film deposition parameters. In their calculations, the values of heat of formation and entropy for the different compounds of interest (e.g. Cu_2Se, In_2Se_3) were employed to estimate the concentration of solid in thermodynamic equilibrium. They concluded that the $CuInSe_2$ would be the dominant solid product. However, deficiency in selenium or an excess in either copper or in oxygen, result in a significant amount of second phases in the thin films. The selenium deficiency favors the formation of Cu_2Se and In_2O_3 [80]. The excess of copper and oxygen give rise to the formation of CuSe and $CuSeO_4/In_2(SeO)_3$ phases, respectively [80]. Even though the chemical spray pyrolysis deposition undergoes under non-equilibrium conditions, these equilibrium thermodynamic data are useful to stablish initial experimental conditions for the growth of chalcopyrite films. As a matter of fact, it is highly difficult to predict all the thermodynamic equilibrium affecting the film growth process, mainly because of the numerous possible complexes in the solution and in the deposition.

3.3 Hybrid process (non-vacuum/vacuum)

It has already been shown previously in this chapter that a 3-stage growth process implies a sudden mean grains size expansion (recrystallization) of the growing film during Cu-poor to Cu-rich transition at the end of the 2nd stage [60,61]. The recrystallization phenomenon is essential for the achievement of high efficiency. Further investigations of this phenomenon suggest that the most stable grains grow at the expense of least stable ones, which are consumed through grain boundary motion [62]. As a consequence, the crystalline and electrical properties of the CIGSe layers are drastically changed during Cu-poor to Cu-rich transition. This suggests that the characteristics of the initial film (precursor) could be highly improved at the end of the growth process, which highlight the existence of a wide window of structural and electrical properties of the $(In_{1-x}Ga_x)_2Se_3$ precursor films that could result on high-quality CIGSe absorbers.

During the 3-stage process, the Cu-poor to Cu-rich transition occurs when at least 50 % of the total thickness of the absorber is already deposited. Taking into consideration the integration of the 3-stage process to a low-cost and high-yield concept, the last signifies that 50 % of the layer could be deposited very fast, as already proposed by Painchaud et al. [81], or by using another technique than co-evaporation such as non-vacuum deposition. Moreover, if the effect of the recrystallization phenomenon on the improvement of structural and electrical properties of precursor layers is considered, a range of opportunities for new deposition processes development is created.

The hybrid approach proposed in this work, combining chemical spray pyrolysis (non-vacuum) and co-evaporation (vacuum) deposition techniques, offers opportunities to increase production throughputs, save source materials and possibly minimize lateral non-homogeneities in comparison with the conventional co-evaporation technique. The chemical spray pyrolysis deposition represents a good option for this hybrid process since it possesses the advantages of low-cost equipment, high material-utilization efficiency, and easy scale-up. The co-evaporation deposition also denotes a great choice

considering the recrystallization phenomenon occurred during the growth of films and the resulting high efficiencies of the resulting solar cells.

The hybrid deposition process (see figure 3.11) consists of a 3-step process, which includes the next steps:

- The growth of a 1st-stage-equivalent In_2Se_3 layer on Mo-coated soda-lime glass (SLG/Mo) substrates by non-vacuum chemical spray pyrolysis (CSP)
- The absorbers are completed by the co-evaporation of Cu+Se and In+Se, being these the 2nd and 3rd steps of the process, respectively.

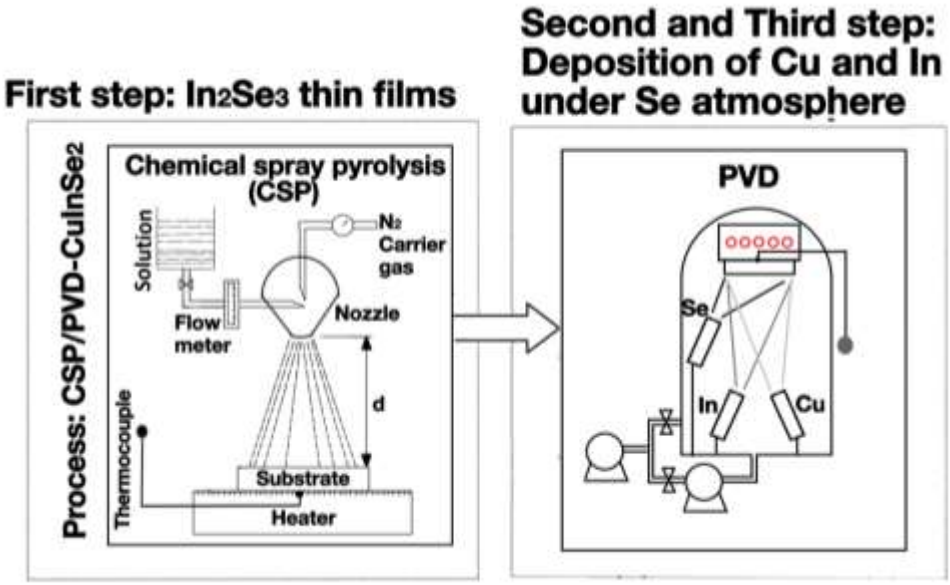

Figure 3.11 Hybrid deposition process.

References

[1] D. Lincot, J.F. Guillemoles, S. Taunier, D. Guimard, J. Sicx-Kurdi, A. Chaumont, O. Roussel, O. Ramdani, C. Hubert, J.P. Fauvarque, N. Bodereau, L. Parissi, P. Panheleux, P. Fanouillere, N. Naghavi, P.P. Grand, M. Benfarah, P. Mogensen, O. Kerrec, Chalcopyrite thin film solar cells by electrodeposition, Sol. Energy. 77 (2004) 725–737. doi:10.1016/j.solener.2004.05.024.

[2] D. Lincot, Electrodeposition of semiconductors, Thin Solid Films. 487 (2005) 40–48. doi:10.1016/j.tsf.2005.01.032.

[3] M. Kaelin, D. Rudmann, F. Kurdesau, H. Zogg, T. Meyer, A.N. Tiwari, Low-cost CIGS solar cells by paste coating and selenization, Thin Solid Films. 480-481 (2005) 486–490. doi:10.1016/j.tsf.2004.11.007.

[4] W. Wang, S.-Y. Han, S.-J. Sung, D.-H. Kim, C.-H. Chang, 8.01% CuInGaSe2 solar cells fabricated by air-stable low-cost inks, Phys. Chem. Chem. Phys. 14 (2012) 11154. doi:10.1039/c2cp41969f.

[5] B. Pamplin, R.S. Feigelson, Spray pyrolysis of $CuInSe_2$ and related ternary semiconducting compounds, Thin Solid Films. 60 (1979) 141–146. doi:10.1016/0040-6090(79)90184-6.

[6] M.S. Tomar, F.J. Garcia, A ZnO/p-$CuInSe_2$ thin film solar cell prepared entirely by spray pyrolysis, Thin Solid Films. 90 (1982) 419–423. doi:10.1016/0040-6090(82)90551-X.

[7] C.R. Abernathy, C.W. Bates, A. a. Anani, B. Haba, G. Smestad, Production of single phase chalcopyrite $CuInSe_2$ by spray pyrolysis, Appl. Phys. Lett. 45 (1984) 890–892. doi:10.1063/1.95403.

[8] S. Duchemin, J. Bougnot, A. El Ghzizal, K. Belghit, Studies on the improvement of sprayed CdS-$CuInSe_3$ solar cells, in: 9th Eur. Photovolt. Sol. Energy Conf., 1989: pp. 476–479.

[9] P. Jackson, R. Wuerz, D. Hariskos, E. Lotter, W. Witte, M. Powalla, Effects of heavy alkali elements in Cu(In,Ga)Se_2 solar cells with efficiencies up to 22.6%, Phys. Status Solidi - Rapid Res. Lett. 4 (2016) 1–4. doi:10.1002/pssr.201600199.

[10] B. Dimmler, R. Wächter, Manufacturing and application of CIS solar modules, Thin Solid Films. 515 (2007) 5973–5978. doi:10.1016/j.tsf.2006.12.150.

[11] J.H. Shi, Z.Q. Li, D.W. Zhang, Q.Q. Liu, Z.Z. Sun, S.M. Huang, Fabrication of Cu(In, Ga)Se2 thin films by sputtering from a single quaternary chalcogenide target, Prog. Photovoltaics Res. Appl. 19 (2011) 160–164. doi:10.1002/pip.1001.

[12] Y. Tanaka, N. Akema, T. Morishita, D. Okumura, K. Kushiya, Improvement of Voc upward of 600 mV/Cell with CIGS-based Absorber Prepared by Selenization/Sulfurization, in: Conf. Proceedings, in: 17th EC Photovolt. Sol. Energy Conf. München, 2001: pp. 989–994.

[13] P. Reinhard, S. Buecheler, A.N. Tiwari, Technological status of Cu(In,Ga)(Se,S)$_2$-based photovoltaics, Sol. Energy Mater. Sol. Cells. 119 (2013) 287–290. doi:10.1016/j.solmat.2013.08.030.
[14] P. Jackson, D. Hariskos, R. Wuerz, O. Kiowski, A. Bauer, T.M. Friedlmeier, M. Powalla, Properties of Cu(In,Ga)Se $_2$ solar cells with new record efficiencies up to 21.7%, Phys. Status Solidi - Rapid Res. Lett. 9 (2015) 28–31. doi:10.1002/pssr.201409520.
[15] S. Aksu, S. Pethe, A. Kleiman-Shwarsctein, S. Kundu, M. Pinarbasi, Recent advances in electroplating based CIGS solar cell fabrication, in: Conf. Rec. IEEE Photovolt. Spec. Conf., 2012: pp. 3092–3097. doi:10.1109/PVSC.2012.6318235.
[16] Avancis, CIS technology, (2015). http://www.avancis.de/en/cis-technology/cis-world-records/, 2015.
[17] Solar-Frontier, Solar Frontier achieves world record thin-film solar cell efficiency: 22.3%, (2015). http://www.solar-frontier.com/eng/news/2015/C051171.html.
[18] T. Nakada, A. Kunioka, Sequential Sputtering / Selenization Technique for the Growth of $CuInSe_2$ Thin Films, Jpn. J. Appl. Phys. 37 (1998) 1065–1067.
[19] G.S. Chen, J.C. Yang, Y.C. Chan, L.C. Yang, W. Huang, Another route to fabricate single-phase chalcogenides by post-selenization of Cu-In-Ga precursors sputter deposited from a single ternary target, Sol. Energy Mater. Sol. Cells. 93 (2009) 1351–1355. doi:10.1016/j.solmat.2009.02.014.
[20] R. Cabellero, C. Guillen, Comparative studies between Cu-Ga-Se and Cu-In-Se thin film systems, Thin Solid Films. 403-404 (2002) 107–111. doi:10.1016/S0040-6090(01)01537-1.
[21] F.B. Dejene, Material and device properties of Cu(In,Ga)Se_2 absorber films prepared by thermal reaction of InSe/Cu/GaSe alloys to elemental Se vapor, Curr. Appl. Phys. 10 (2010) 36–40. doi:10.1016/j.cap.2009.04.008.
[22] J. Bekker, V. Alberts, A.W.R. Leitch, J.R. Botha, Properties of $CuIn(Se,S)_2$ thin films prepared by two-step growth processes, Thin Solid Films. 431-432 (2003) 116–121. doi:10.1016/S0040-6090(03)00218-9.
[23] P. Berwian, A. Weimar, G. Müller, In situ resistivity measurements of precursor reactions in the Cu-In-Ga system, Thin Solid Films. 431-432 (2003) 41–45. doi:10.1016/S0040-6090(03)00250-5.
[24] K. Kushiya, M. Tachiyuki, Y. Nagoya, A. Fujimaki, B. Sang, D. Okumura, M. Satoh, O. Yamase, Progress in large-area Cu(In,Ga)Se -based thin- film modules with a Zn (O , S , OH) bu ffer layer, 67 (2001) 11–20.
[25] K T Ramakrishna Reddy, P.K. Datta, M.J. Carter, Detection of Crystalline Phases in CuInSe 2 Films Grown by Selenisation Process, Phys. Status Solidi. 182 (2000) 679–686.
[26] K. Kim, G.M. Hanket, T. Huynh, W.N. Shafarman, Three-step H 2Se/Ar/H 2S reaction of

Cu-In-Ga precursors for controlled composition and adhesion of $Cu(In,Ga)(Se,S)_2$ thin films, J. Appl. Phys. 111 (2012). doi:10.1063/1.4704390.
[27] J. Bekker, V. Alberts, M.J. Witcomb, Influence of selenization techniques on the reaction kinetics of chalcopyrite thin films, Thin Solid Films. 387 (2001) 40–43. doi:10.1016/S0040-6090(01)00797-0.
[28] J. Liu, A.X. Wei, Y. Zhao, Z.Q. Yan, Effect of stacking type in precursors on composition, morphology and electrical properties of the CIGS films, J. Mater. Sci. Mater. Electron. 24 (2013) 2553–2557. doi:10.1007/s10854-013-1132-3.
[29] V. Probst, W. Stetter, W. Riedl, H. Vogt, M. Wendl, H. Calwer, S. Zweigart, K.D. Ufert, B. Freienstein, H. Cerva, F.H. Karg, Rapid CIS-process for high efficiency PV-modules: Development towards large area processing, Thin Solid Films. 387 (2001) 262–267. doi:10.1016/S0040-6090(00)01800-9.
[30] M. Klenk, O. Schenker, V. Alberts, E. Bucher, Preparation of device quality chalcopyrite thin films by thermal evaporation of compound materials, Semicond. Sci. Technol. 17 (2002) 435–439. doi:10.1088/0268-1242/17/5/305.
[31] M. Marudachalam, R.W. Birkmire, H. Hichri, J.M. Schultz, a. Swartzlander, M.M. Al-Jassim, Phases, morphology, and diffusion in $CuIn_xGa_{1-x}Se_2$ thin films, J. Appl. Phys. 82 (1997) 2896. doi:10.1063/1.366122.
[32] T. Yamamoto, M. Nakamura, J. Ishizuki, T. Deguchi, S. Ando, H. Nakanishi, S. Chichibu, Use of diethylselenide as a less-hazardous source for preparation of CuInSe2 thin films by selenization of metal precursors, J. Phys. Chem. Solids. 64 (2003) 1855–1858. doi:10.1016/S0022-3697(03)00146-X.
[33] Wiley-VCH, ed., Ullmann's Chemical Engineering and Plant Design, (2004) 1399.
[34] T. King-Ning, J.W. Mayer, L.C. Feldman, Electronic Thin Film Science: For Electrical Engineering and Materials Scientist, 1996.
[35] NREL, Research cells efficiencies records, (2015). http://www.nrel.gov/ncpv/.
[36] R.A. Mickelsen, W.S. Chen, High photocurrent polycrystalline thin-film $CdS/CuInSe_2$ solar cella, Appl. Phys. Lett. 36 (1980) 371–373. doi:10.1063/1.91491.
[37] A.M. Gabor, J.R. Tuttle, D.S. Albin, M.A. Contreras, R. Noufi, A.M. Hermann, High-efficiency CuInxGa1-xSe2 solar cells made from $(In_x,Ga_{1-x})_2Se_3$ precursor films, Appl. Phys. Lett. 65 (1994) 198–200. doi:10.1063/1.112670.
[38] J. Kessler, C. Chityuttakan, J. Lu, J. Schöldström, L. Stolt, $Cu(In,Ga)Se_2$ thin films grown with a Cu-poor/rich/poor sequence: Growth model and structural considerations, Prog. Photovoltaics Res. Appl. 11 (2003) 319–331. doi:10.1002/pip.495.
[39] W.N. Shafarman, J. Zhu, Effect of substrate temperature and depostion profile on evaporated $Cu(InGa)Se_2$ films and devices, Thin Solid Films. 362 (2000) 473–477. doi:Gabor A

et al., Appl. Phys. Lett. 65, 198–200 (1994).
[40] J.R. Tuttle, D.S. Albin, R. Noufi, Thoughts on the microstructure of polycrystalline thin film $CuInSe_2$ and its impact on material and device performance, Sol. Cells. 30 (1991) 21–38. doi:10.1016/0379-6787(91)90034-M.
[41] R. Klenk, T. Walter, H.-W. Schock, D. Cahen, A model for the successful growth of polycrystalline films of $CuInSe_2$ by multisource physical vacuum evaporation, Adv. Mater. 5 (1993) 114–119. doi:10.1002/adma.19930050209.
[42] W.S. Chen, J.M. Stewart, B.J. Stanbery, W.E. Devaney, R.A. Mickelsen, Development of thin film polycrystalline $CuIn_{1-x}Ga_xSe_2$ solar cells, in: 19th Photovolt. Spec. Conf., 1987: pp. 1445–1447.
[43] J.R. Tuttle, M. Contreras, A. Tennant, D. Albin, R. Noufi, High efficiency thin-film $Cu(In,Ga)Se_2$-based photovoltaic devices: progress towards a universal approach to absorber fabrication, NREL (1993).
[44] T. Wada, N. Kohara, T. Negami, M. Nishitani, Growth of CuInSe crystals in Cu-rich Cu-In-Se thin films, J. Mater. Res. (1997) 1433–1436. doi:10.1557/JMR.1997.0058.
[45] J. Kessler, J. Schöldström, L. Stolt, Rapid $Cu(In,Ga)Se_2$ growth using “end point detection,” Conf. Rec. IEEE Photovolt. Spec. (2000) 509–512. doi:10.1109/PVSC.2000.915883.
[46] A.M. Gabor, J.R. Tuttle, D.S. Albin, A.L. Tennant, M.A. Contreras, R. Noufi, A.M. Hermann, High efficiency polycrystalline $Cu(In,Ga)Se_2$-based solar cells, AIP Conf. Proc. 306 (1994) 59–66. doi:10.1063/1.45732.
[47] J. Kessler, D. Schmid, S. Zweigart, H. Dittrich, H.W. Schock, $CuInSe_2$ film formation from sequential depositions of In(Se):Cu:Se, 12th Eur. PV Sol. Enerfy Conf. (1994) 648–652.
[48] S. Nishiwaki, T. Satoh, S. Hayashi, Y. Hashimoto, S. Shimakawa, T. Negami, T. Wada, Preparation of Cu (In , Ga) Se thin Films from Cu-Se /In - Ga - Se precursors for high-efficiency solar cells, Sol. Energy Mater. Sol. Cells. 67 (2001) 217–223.
[49] P. Jackson, D. Hariskos, R. Wuerz, W. Wischmann, M. Powalla, Compositional investigation of potassium doped $Cu(In,Ga)Se_2$ solar cells with efficiencies up to 20.8%, Phys. Status Solidi - Rapid Res. Lett. 8 (2014) 219–222. doi:10.1002/pssr.201409040.
[50] S. Nishiwaki, T. Satoh, S. Hayashi, Preparation of $Cu(In,Ga)Se_2$ thin films from In-Ga-Se precursors for high-efficiency solar cells, J. Mater. Res. 14 (1999) 4514–4520. doi:10.1557/JMR.1999.0613.
[51] D.J. Schroeder, G.D. Berry, A. a. Rockett, Gallium diffusion and diffusivity in $CuInSe_2$ epitaxial layers, Appl. Phys. Lett. 69 (1996) 4068. doi:10.1063/1.117820.
[52] O. Lundberg, J. Lu, a. Rockett, M. Edoff, L. Stolt, Diffusion of indium and gallium in $Cu(In,Ga)Se_2$ thin film solar cells, J. Phys. Chem. Solids. 64 (2003) 1499–1504. doi:10.1016/S0022-3697(03)00127-6.

[53] K. Gartsman, L. Chernyak, V. Lyahovitskaya, D. Cahen, V. Didik, V. Kozlovsky, R. Malkovich, E. Skoryatina, V. Usacheva, Direct evidence for diffusion and electromigration of Cu in $CuInSe_2$, J. Appl. Phys. 82 (1997) 4282. doi:10.1063/1.366252.
[54] C. Lei, a. Rockett, I.M. Robertson, W.N. Shafarman, M. Beck, Void formation and surface energies in $Cu(InGa)Se_2$, J. Appl. Phys. 100 (2006) 073518. doi:10.1063/1.2357422.
[55] T. Mise, T. Nakada, Microstructural properties of $(In,Ga)_2Se_3$ precursor layers for efficient CIGS thin-film solar cells, Sol. Energy Mater. Sol. Cells. 93 (2009) 1000–1003. doi:10.1016/j.solmat.2008.11.028.
[56] S. Ishizuka, A. Yamada, P. Fons, S. Niki, Texture and morphology variations in $(In,Ga)_2Se_3$ and $Cu(In,Ga)Se_2$ thin films grown with various Se source conditions, Prog. Photovoltaics Res. Appl. 21 (2013) 544–553. doi:10.1002/pip.1227.
[57] K.H. Kim, K.H. Yoon, J.H. Yun, B.T. Ahn, Effects of Se Flux on the Microstructure of $Cu(In,Ga)Se_2$ Thin Film Deposited by a Three-Stage Co-evaporation Process, Electrochem. Solid-State Lett. 9 (2006) A382. doi:10.1149/1.2208011.
[58] S. Chaisitsak, A. Yamada, M. Konagai, Preferred Orientation Control of $Cu(In_{1-x}Ga_x)Se_2$ ($x \approx 0.28$) Thin Films and Its Influence on Solar Cell Characteristics, Jpn. J. Appl. Phys. 41 (2002) 507–513. doi:10.1143/JJAP.41.507.
[59] H. Rau, A. Rabenau, Vapour pressure measurements in the copper-selenium system, J. Solid State Chem. 1 (1970) 515–518. doi:10.1016/0022-4596(70)90135-0.
[60] H. Rodriguez-Alvarez, N. Barreau, C.A. Kaufmann, A. Weber, M. Klaus, T. Painchaud, H.W. Schock, R. Mainz, Recrystallization of $Cu(In,Ga)Se_2$ thin films studied by X-ray diffraction, Acta Mater. 61 (2013) 4347–4353. doi:10.1016/j.actamat.2013.04.006.
[61] H. Rodriguez-Alvarez, A. Weber, J. Lauche, C.A. Kaufmann, T. Rissom, D. Greiner, M. Klaus, T. Unold, C. Genzel, H.W. Schock, R. Mainz, Formation of $CuInSe_2$ and $CuGaSe_2$ thin-films deposited by three-stage thermal co-evaporation: A real-time X-ray diffraction and fluorescence study, Adv. Energy Mater. 3 (2013) 1381–1387. doi:10.1002/aenm.201300339.
[62] N. Barreau, T. Painchaud, F. Couzinié-Devy, L. Arzel, J. Kessler, Recrystallization of CIGSe layers grown by three-step processes: A model based on grain boundary migration, Acta Mater. 58 (2010) 5572–5577. doi:10.1016/j.actamat.2010.06.025.
[63] T. Negami, T. Wada, M. Nishitani, Composition monitoring method in CuInSe , thin film preparation, 258 (1995) 313–316.
[64] R.N. Bhattacharya, K. Rajeshwar, Electrodeposition of $CuIn_X$ (X=Se,Te) thin films, Sol. Cells. 16 (1986) 237–243. doi:10.1016/0379-6787(86)90087-6.
[65] M. GANCHEV, K. KOCHEV, Investigation of the electrodeposition process in the Cu-In-Se system, Sol. Energy Mater. Sol. Cells. 31 (1993) 163–170. doi:10.1016/0927-0248(93)90048-8.

[66] A.G. Chowles, J.H. Neethling, H. Van Niekerk, J.A.A. Engelbrecht, V.J. Watters, Deposition and characterization of $CuInSe_2$, Renew. Energy. 6 (1995) 613–618. doi:10.1016/0960-1481(95)00068-U.

[67] V.K. Kapur, A. Bansal, P. Le, O.I. Asensio, Non-vacuum processing of $CuIn_{1-x}Ga_xSe_2$ solar cells on rigid and flexible substrates using nanoparticle precursor inks, Thin Solid Films. 431-432 (2003) 53–57. doi:10.1016/S0040-6090(03)00253-0.

[68] J. Van Duren, D. Jackrel, F. Jacob, C. Leidholm, A. Pudov, M. Robinson, Y. Roussillon, The next generation in thin film photovoltaic process technology, in: 17th Int. Photovolt. Sol. Energy Conf., 2007.

[69] J.B. Mooney, S.B. Radding, Spray Pyrolysis Processing, Annu. Rev. Mater. Sci. 12 (1982) 81–101. doi:10.1146/annurev.ms.12.080182.000501.

[70] H.-F. Yu, W.-H. Liao, Evaporation of solution droplets in spray pyrolysis, Int. J. Heat Mass Transf. 41 (1998) 993–1001. doi:10.1016/S0017-9310(97)00226-3.

[71] J.C. Vigui, J. Spitz, Chemical Vapor Deposition at Low Temperature, J. Electrochem. Soc.Solid-State Sci. Technol. 122 (1975) 585–588.

[72] W.A. Bryant, The fundamentals of chemical vapour deposition, J. Mater. Sci. 12 (1977) 1285–1306. doi:10.1007/BF00540843.

[73] K. Okuyama, I. Wuled Lenggoro, Preparation of nanoparticles via spray route, Chem. Eng. Sci. 58 (2003) 537–547. doi:10.1016/S0009-2509(02)00578-X.

[74] W. Siefert, Properties of thin In_2O_3 and SnO_2 films prepared by corona spray pyrolysis, and a discussion of the spray pyrolysis process, Thin Solid Films. 120 (1984) 275–282. doi:10.1016/0040-6090(84)90242-6.

[75] B.J. Babu, S. Velumani, R. Asomoza, An (ITO or AZO)/ZnO/$Cu(In_{1-x}Ga_x)Se_2$ superstrate thin film solar cell structure prepared by spray pyrolysis, in: 37th IEEE Photovolt. Spec. Conf., IEEE, 2011: pp. 001238–001243. doi:10.1109/PVSC.2011.6186181.

[76] T. Terasako, S. Inoue, T. Kariya, S. Shirakata, Three-stage growth of Cu-In-Se polycrystalline thin films by chemical spray pyrolysis, Sol. Energy Mater. Sol. Cells. 91 (2007) 1152–1159. doi:10.1016/j.solmat.2006.06.063.

[77] B.J. Brown, C.W. Bates, Similarities in the chemical mechanisms of $CuInSe_2$ and CdS thin film formation by chemical spray pyrolysis, Thin Solid Films. 188 (1990) 301–305. doi:10.1016/0040-6090(90)90292-L.

[78] S. Shirakata, Y. Kannaka, H. Hasegawa, T. Kariya, S. Isomura, Properties of $Cu(In,Ga)Se_2$ Thin Films Prepared by Chemical Spray Pyrolysis, Jpn. J. Appl. Phys. 39 (1999) 4997. doi:doi:10.1143/JJAP.38.4997.

[79] B.L. Kronik, D. Cahen, H.W. Schock, Effects of Sodium on Polycrystalline $Cu(In,Ga)Se_2$ and Its Solar Cell Performance, Adv. Mater. 10 (1998) 31–36. doi:10.1002/(SICI)1521-

4095(199801)10:1<31::AID-ADMA31>3.0.CO;2-3.
[80] J.B. Mooney, R.H. Lamoreaux, Spray pyrolysis of $CuInSe_2$, Sol. Cells. 16 (1986) 211–220. doi:10.1016/0379-6787(86)90085-2.
[81] T. Painchaud, N. Barreau, L. Arzel, J. Kessler, Fast $Cu(In,Ga)Se_2$ precursor growth: Impact on solar cell, Thin Solid Films. 519 (2011) 7221–7223. doi:10.1016/j.tsf.2011.01.098.

Chapter 4 Fabrication techniques of $Cu(In,Ga)Se_2$ solar cells and characterization

This chapter presents the fabrication and methods of characterization of the $Cu(In,Ga)Se_2$-based solar cells studied in this research work. The first part of the chapter describes the deposition conditions (e.g. substrate temperature, chamber pressure) of each layer composing the solar cell as well as a brief description of the equipment employed for this propose (e.g. spray pyrolysis, co-evaporation, sputtering). Particular attention is given to the description of the hybrid deposition process and the growth conditions. The second part of the chapter comprises an overview of the working principles of the characterization methods and the specific conditions used to characterize the CIGSe-based solar cell.

4.1 Fabrication of $Cu(In,Ga)Se_2$ solar cells

Figure 4.1 shows the cross-section scanning electron microscope (SEM) image of the CIGSe-baseline solar cell fabricated during this thesis. As mentioned in chapter 2, the solar cell is based on a stack of thin films with a Mo/CIGSe/CdS/i-ZnO/ZnO:Al structure, growth on a soda-lime glass (SLG) substrate. The following sections describe the growth conditions of the thin films constituting the CIGS-based solar cell, along with the characterization techniques used in this work.

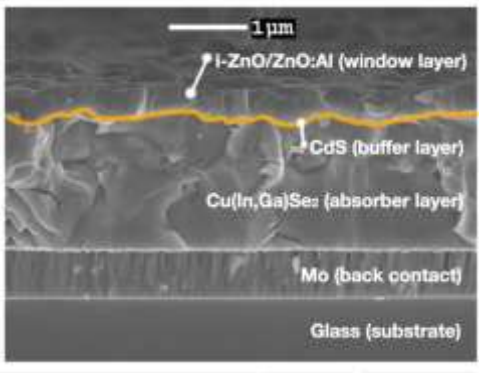

Figure 4.1 Cross-section scanning electron microscope (SEM) image of a complete CIGSe-based solar cell.

4.1.1 Deposition of molybdenum back contacts

Soda-lime glasses (SLG) slides of 1x3 and 1x1 inch^2 were used as substrates in all the experiments performed in this work. The glass slides were cleaned through several washes in water with soap solutions and high purity deionized H_2O in an ultrasonic bath. After these washes, the glasses were dried in nitrogen flux and were directly introduced into the chamber where the Mo back contact layer was deposited. The Mo back contact was deposited by DC sputtering. The sputtering is a vacuum technique based on the deposition of ejected particles from the surface of a solid target by bombardment with energetic ions in an argon atmosphere. The Mo contact is a bilayer structure composed of: (i) a first layer of ~120 nm deposited at high Ar pressure (~15 mTorr) ensuring a proper attachment to the glass substrate and (ii) a second layer of ~460 nm deposited at low Ar pressure (~3 mTorr) assuring a good electrical conductivity and diffusion of sodium. Both layers were deposited at ~280 W in a dynamic mode (moving substrate under static target). The final Mo back contact was a layer of around 580 nm with a sheet resistance of approximately 0.5Ω/• . In the frame of this thesis, samples with sodium (diffusing from SLG substrate) and without sodium were investigated. Samples without sodium diffusion from the SLG were needed in order to study the effects of this dopand on the properties of the films. To block the diffusion of Na, a Si_xN thin film barrier was deposited on the glass substrate before Mo film growth.

4.1.2 Cu(In,Ga)Se_2 absorber deposition

The $CuInSe_2$ and Cu(In,Ga)Se_2 absorbers were grown by two processes: (i) the so-called 3-stage co-evaporation process and (ii) chemical spray pyrolysis/co-evaporation hybrid process.

4.1.2.1 Co-evaporation growth process

Equipment

The deposition of CIGSe was performed in a 55 x 70 x 60 cm^3 chamber (see figure 4.2a) with a vacuum system consisted in a diffusion pump backed up by a rotary pump (see figure 4.2b). The substrates were radiatively heated from the backside by infrared lamps. The substrate temperature was followed by a thermocouple located on the back side and middle of the substrate. To evaporate the high purity raw materials at high temperatures (i.e. 990-1300°C), three Luxel Radak II sources were used. These sources use alumina crucibles and pyrolytic boron nitride (PBN) liners. Some advantages of Radak furnaces are the low consumed power (<10 A) and good evaporation flux stability. The evaporation temperatures were followed by thermocouples located between the source liner and bottom of the crucible. Since the selenium was evaporated at lower temperature in comparison to the other metals, a simpler evaporation source was used. The control of evaporated material deposition was achieved by a manually controlled shutter placed between the substrate and evaporation sources.

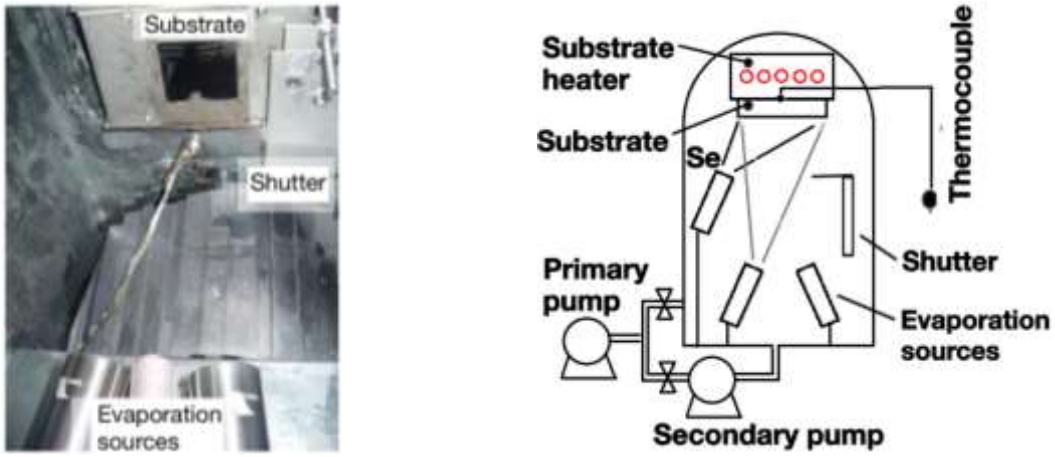

(a) **(b)**

Figure 4.2 The co-evaporation chamber (a) and the schematic (b) of the co-evaporation system.

Deposition by 3-stage process

The deposition of CIGSe was performed under high vacuum conditions (10^{-6}-10^{-7} mbar). The used raw materials were copper (99.998% purity), indium (99.9999% purity) and gallium (99.9999% purity) evaporated at high temperatures (i.e. 990-1300°C). Selenium (99.999% purity) was evaporated at lower temperature (285°C). The baseline 3-stage process followed in this work is represented in the schematic diagram of the metal fluxes showed in figure 4.3. In the first stage, a 1 µm thick $(In_{1-x}Ga_x)_2Se_3$ precursor layer was deposited at a substrate temperature of 380-400 °C. In the second stage, the substrate temperature was increased up to 550-600°C, and only Cu and Se was evaporated onto the $(In_{1-x}Ga_x)_2Se_3$ film. During this stage, the growing film reaches the stoichiometry (y=[Cu]/[[In]+[Ga]]=Cu/III=1) and then off-stoichiometry Cu-rich (y>1) where the Cu-Se phase is formed on the CIGSe surface. After enough deposition time, Cu evaporation was suspended. As mentioned before in Chapter 3, this Cu-rich phase is required for the recrystallization of the CIGSe layer and the subsequent quality improvement. Finally, in the third stage, Ga and In were evaporated together along with Se until the nominal composition returns slightly Cu-poor composition. The final result was a CIGSe layer of ~2 µm thickness with eventual Ga/III and Cu/III ratios values in the range of 0.25-0.3 and 0.85-0.95, respectively. The final films will be referred as 3-stage-CISe and 3-stage-CIGSe layers. In the frame of this work, some variations of the baseline growth process were carried out and indicated at the appropriate moment.

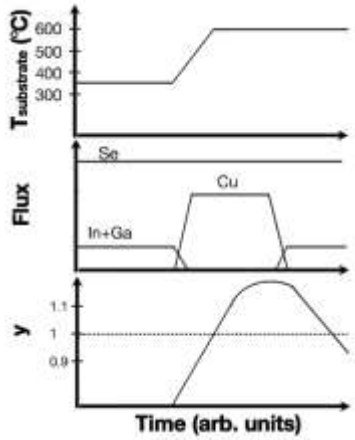

Figure 4.3 Co-evaporation 3-stage baseline growth process.

4.1.2.2 Hybrid process

As mention previously in Chapter 3, our proposed hybrid approach combines non-vacuum chemical spray pyrolysis (CSP) and vacuum co-evaporation (PVD) deposition techniques. In this hybrid process, a 1st-stage-equivalent In_2Se_3 layers were grown on Mo-coated soda-lime glass (SLG/Mo) substrates by chemical spray pyrolysis and the absorbers were completed by performing the 2nd and 3rd stage of the so-called 3-stage co-evaporation process. In the following subsections, the baseline deposition conditions of In_2Se_3 and $(In,Ga)_2Se_3$ precursors layers deposited by CSP along with the condition of subsequent co-evaporation process are mentioned.

4.1.2.2.1 In_2Se_3 and $(In,Ga)_2Se_3$ precursor films deposited by chemical spray pyrolysis technique

Equipment

The deposition of precursor films was performed under atmospheric conditions in a fume hood. The substrates were heated by putting its backside in contact with a hot tin bath. The substrate temperature was followed by a thermocouple immersed in the bath, close to the backside and middle of the substrate. The precursors solutions were disposed in a high position in order to promote the solution flow into the dispersion nozzle. This nozzle consists of two outlets, one for nitrogen gas and another for the precursor solution. The precursor solution was propelled by the N_2 gas, creating the spray jet.

Deposition of precursor layers

The baseline In_2Se_3 and $(In_{0.75},Ga_{0.25})_2Se_3$ layers were deposited by chemical spray pyrolysis (CSP) on molybdenum coated soda lime glass (SLG) substrates. The CSP films were grown on a molten tin bath at 380 °C. The starting solutions contain concentrations of 0.0015 M for gallium trichloride ($GaCl_3$), indium trichloride ($InCl_3$) and 0.0055 M for N-N- dimethyl-selenourea ($C_3H_8N_2Se$, DMSeU), each in a 20% volume ethanol aqueous solution. The $GaCl_3$ and $InCl_3$ solutions were hand stirred and solution containing the

DMSeU were stirred at 550 rpm until clear solutions were obtained. The (In,Ga):Se atomic ratio in the solution was 2:4. The DMSeU was provided in excess in comparison with the stoichiometry (2:3) due to the volatile nature of Se at the deposition temperature. The desired pH (4–5) of the (In,Ga)-Se solution was achieved by the addition of hydrochloric acid (HCl). The total volume of the solution sprayed was 800 ml with a spray rate of 6.5 ml/min with nitrogen as a carrier gas whose flow rate was 1.5 l/min. These parameters yield precursor films of about 1 µm thickness ready to be used in the next step of the hybrid deposition. These films will be referred as CSP-In_2Se_3 or CSP-$(In,Ga)_2Se_3$ in the following work.

4.1.2.2.2 Co-evaporation deposition on precursor films

The equipment used for this process was the same as the one mentioned in Section 4.1.2.1 of this Chapter. The 1st-stage-equivalent CSP precursor layers were introduced into the co-evaporation chamber to be completed by the 2nd (i.e. Cu + Se flux) and 3rd (i.e. In + Ga +Se flux) stages. In the case of CISe deposition, no gallium was evaporated during the last stage. Evaporation conditions, i.e. vacuum and evaporation temperatures of pure elements, were in the range of 10^{-6}-10^{-7} mbar and 990-1300°C, respectively. The substrate temperature during the 2nd and 3rd stage was in the range of 550-600 °C. The final result was an absorber layer of ~2 µm thickness with eventual Ga/III and Cu/III ratios values in the range of 0.25-0.3 and 0.85-0.95. The resulting $CuInSe_2$ and $Cu(In,Ga)Se_2$ layers will be referred as CSP/PVD-CISe and CSP/PVD–CIGSe films. During this research work, variations of the baseline process were carried out and indicated at the appropriate moment.

4.1.1 CdS buffer layer deposition

A CdS layer of 50-60 nm thickness was deposited on the “SLG/Mo/CIGSe” substrate under atmosphere conditions in a home-made chemical bath deposition (CBD) system. The substrate was immersed in an aqueous solution containing cadmium acetate dihydrate ($Cd(CH_3CO_2)_22H_2O$), thiourea ($SC(NH_2)_2$), ammonia (NH_3) and high purity

water. The mixed solution was prepared previously to the introduction to the hot water bath. The soak of the CIGSe substrate in the mixture of these precursors at 60 °C for about 7 minutes allows to obtain the desired CdS layer. The occurred reaction can be described as:

$$Cd(NH3)_4^{2+} + SC(NH_2)_2 + 2OH^- \rightarrow CdS + CN_2H_2 + 4NH_3 + 2H_2O$$

4.1.2 ZnO bilayer window and Ni/Al contacts

The intrinsic ZnO (i-ZnO) and aluminium doped ZnO (ZnO:Al) layers were deposited at room temperature by rf magnetron sputtering from a ZnO target and ZnO target with 2 wt% Al_2O_3, respectively. The substrate-to-target distance was 5.5 cm and the base pressure in the chamber was ~$2x10^{-7}$ Torr. Argon gas was used as sputtering gas for both types of ZnO. The i-ZnO was deposited using a power density of 1.2 W/cm^2 for 1.5 min. Aluminium doped ZnO was deposited with a power density of 1.7 W/cm^2 for 5 min. The thickness of i-ZnO and ZnO:Al was around 50 nm and 200 nm, respectively. These films exhibit high transmittance (~90%, 300-1000 nm) and the sheet resistance of the bilayer was approximately 10-40 Ω/• .

The Ni/Al contacts were deposited by e-beam evaporation of elemental nickel and aluminum through a specially designed mask. The thickness of Ni and Al was around 50 nm and 4 μm, respectively. The surface coverage of the contacts was estimated to be 2% of the cell. Finally, the 0.5 cm^2 solar cells were mechanically scribed.

4.2 Samples characterization

4.2.1 X-ray diffraction

The X-ray diffractometer consists of a basic diffraction unit, a counter, goniometer, and an electronic circuit panel with an automatic recorder. The diffraction angles and intensity of lines can be measured with great accuracy (i.e. scan step size of 0.05º). The schematic diagram of XRD measurements is illustrated in figure 4.4.

The basis of XRD is the Bragg´s law which describes the conditions for constructive interference of X-rays diffracted from atomic planes of a crystal. The condition for constructive interference is

$$2d\sin\theta = n\lambda \qquad \text{(eq. 4.1)}$$

where λ is wavelength of X-rays (CuKα λ=1.5406 Å), d is lattice spacing, n is order of diffraction and θ is the glancing angle of X-rays. The factor d is related to the Miller indices (hkl) of the planes and dimension of unit cells. It is therefore seen that the diffraction direction is determined by the structure and size of the unit cell.

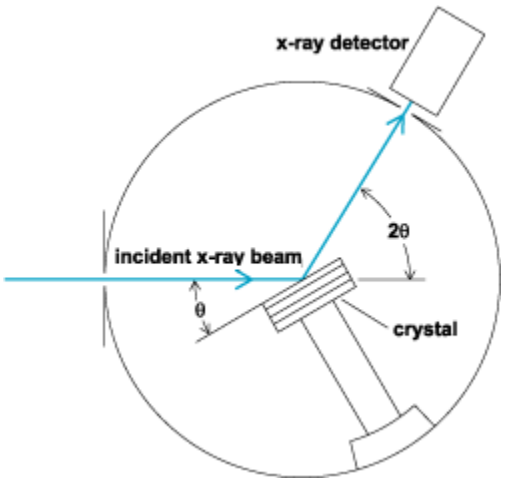

Figure 4.4 Schematic of XRD system.

The crystallite sizes are calculated using the Scherrer's formula.

$$D = \frac{0.94\lambda}{\beta \cos\theta} \qquad \text{(eq. 4.2)}$$

where β is the full width at half maximum (FWHM) of reflected peak at the Bragg angle θ in radians and λ is wavelength of X-rays.

In the present investigation the crystalline quality and orientation of the thin films were characterized by X-ray diffraction (XRD) using a Brucker D8 in Bragg-Brentano configuration with Cu-Kα radiation (λ=1.5406 Å) and stepsize of 0.01°.

4.2.2 Scanning Electron Microscope

In the scanning electron microscopy (SEM) a focused electron beam is employed to gather a variety of information from a sample of interest. The electron beam is created by a field emission gun and accelerated towards the sample by an electric field. Typical electron energies are in the range of several keV, depending on the particular application. A series of electromagnetic lenses are employed to focus the electron beam to probe-diameters of < 1nm. A scanning coil accounts for the lateral motion of the electron beam across the sample and thereby enables SEM imaging. The types of signals produced when electron beam impinges on specimen surface include secondary electrons, Auger electrons, characteristic X-rays and photons of various energies. In general, there are two fundamental methods of data acquisition in SEM. These signals are obtained from specific emission volumes within the samples, which ultimately determines surface topography, crystallography, composition, among others.

In this work, the morphology of the films was observed by scanning electron microscope SEM-model JEOL 6400 F, using an acceleration voltage of 5-2 kV.

4.2.3 Energy dispersive X-ray spectroscopy

The energy dispersive X-ray spectroscopy (EDS) helps to determine the elemental composition of the sample. In this technique, an energetic beam of electrons is allowed to be incident on the film. These incident electrons interact inelastically with both the inner shell electrons and outer shell electrons of the atoms in the sample and thus generating X-rays. Outer shell electrons generate soft X-rays due to this interaction whereas innermost shells generate characteristic X-rays which depend on energies of these shells and hence are the characteristic of atoms radiating these rays. The energy of a particular x-ray is equal to the energy difference between the two inner-core electron states corresponding to the transition. By analyzing the energy of these characteristic X-rays (e.g. Kα, Kβ, Lα, Lβ) (figure 4.5), information about the type of atoms present in the sample and their concentration can be determined.

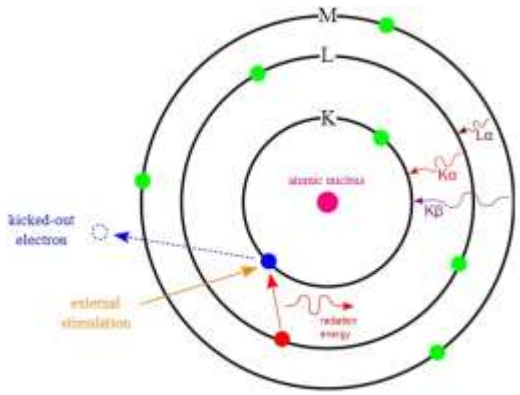

Figure 4.5 Physical principle of EDS.

In the present study, the average composition of the films was measured by a JEOL 6400 F SEM equipped with a germanium X-ray detector using an acceleration voltage of 20 kV (penetration depth of ≤1 μm). For the compositional estimation, the Cu-K, In-L, Ga-K and Se-L signals were employed.

4.2.4 Raman spectroscopy

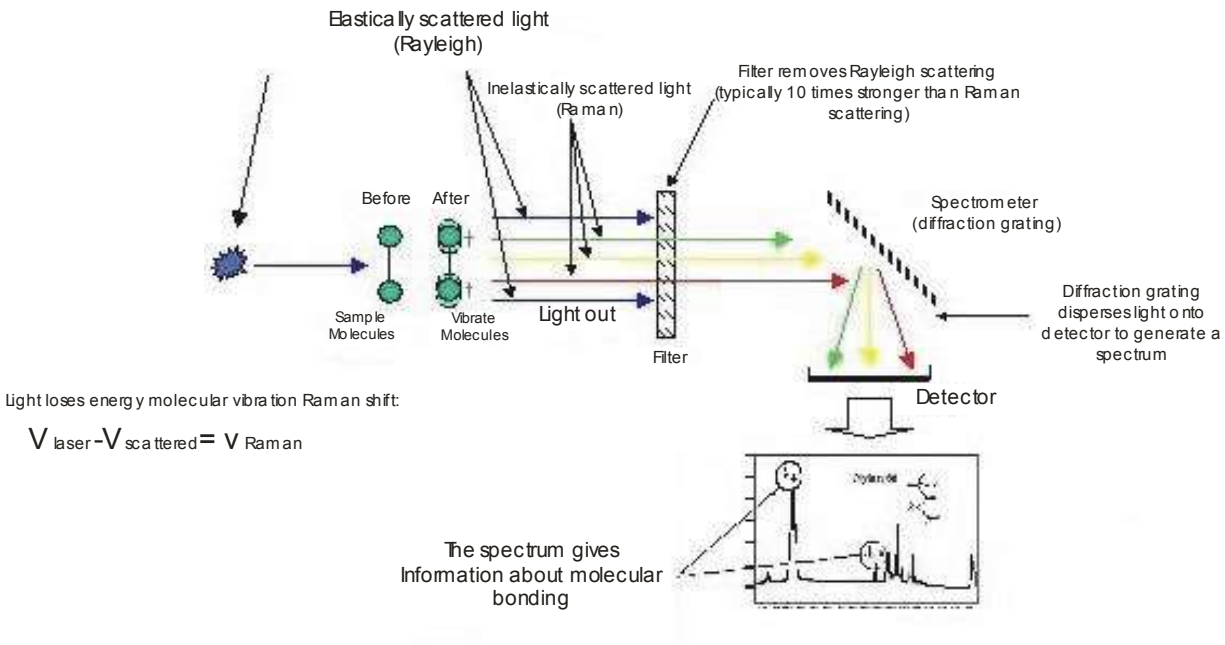

Figure 4.6 Physical principles of Raman spectroscopy. Source from University of Exeter (https://newton.ex.ac.uk/research/biomedical-old/optics/sers.html, Physics and Astronomy, surface enhanced Raman spectroscopy).

Raman spectroscopy is a technique used to study vibrational, rotational, and other low-frequency modes in a system (figure 4.5) and determine single or poly-type structures and secondary phases of the sample. Raman spectroscopy analysis is based on impacting a beam of monochromatic light with frequency v_o to a sample whose molecular characteristics are desired to identify. Most of the scattered light has the same frequency as the incident light; only a small fraction has a frequency change resulting from the interaction of light with matter. The light that keeps the same frequency as the incident one is known as Rayleigh scattering or elastically scattered light and provides no information on the composition of the sample. The scattered light that presents different frequencies from the incident radiation, provides information on the molecular composition of the sample and is known as Raman scattering (inelastically scattered light). The new frequencies are called Raman frequencies and represent characteristics of the chemical nature and physical state of the sample. For the light coming from the sample, a filter is used in order to remove Rayleigh scattering and then a spectrometer

disperses light onto the detector to generate the spectrum. Raman dispersion studies were carried out in a Jobin-Yvon T64000 using an argon laser (λ=514.5nm) with a probe area around 1μm^2 for an acquisition time of 5 min.

4.2.5 Current–voltage characteristics

The performance of the solar cells was determined from the measurement under illumination, of the current density (*J*) versus the voltage (*V*) applied to its contacts. The J-V characteristics of devices were recorded at 25ºC. The conditions of measurement are standardized to a light output of 1000W/m^2 and a close spectral distribution of AM 1.5G spectrum.

The figure 4.7 shows a J(V) curve of a CIGSe-based solar cell. From this measurement, it is possible to determine the characteristic parameters of the solar cell, namely, the open circuit voltage (Voc), short-circuit current density (Jsc) and the fill factor (FF). From these parameters, the efficiency could be calculated as:

$$\eta = \frac{P_{delivered}}{P_{incident}} = \frac{J_{MP}V_{MP}}{P_{incident}} = \frac{J_{sc}V_{oc}FF}{P_{incident}} \qquad \text{(eq. 4.2)}$$

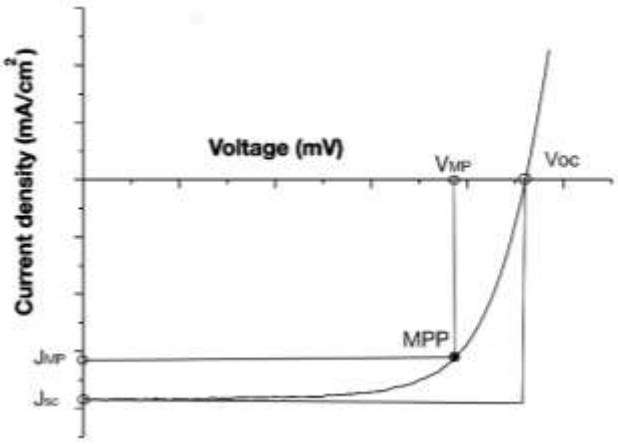

Figure 4.7 Diode curve of a solar cell highlighting basic parameters.

For a more detailed explanation, see Chapter 2 section 2.1.1 and the enclosed references.

4.2.6 External quantum efficiency measurements

The quantum efficiency (QE) is a dimensionless parameter which is useful to characterize the collected current in solar cells. The QE is the ratio between the number of charge carriers collected by the solar cell and the number of incident photons at a specific wavelength (λ).

$$QE_{external} = \frac{Quantity\ of\ electron - hole\ pairs\ collected}{Quantity\ of\ incident\ photons} = \frac{I(\lambda)/q}{\Phi_p(\lambda)}$$

where Φ_p is the incident photon flux at each λ, I(λ) is the photocurrent and q is the elementary charge.

The QE opto-electronic parameter allows to elucidate the losses in J_{sc} present in the devices. These losses are represented in Figure 4.8.

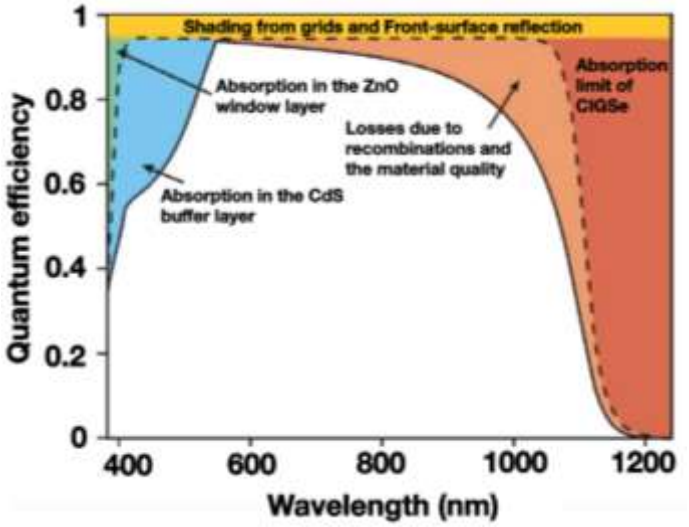

Figure 4.8 External Quantum Efficiency of a CIGSe-based solar cell and loss mechanisms.

In this work, the external quantum efficiency (EQE) measurements have been achieved at room temperature using a grating monochromator-based dual-beam setup under chopped light from a xenon lamp. With the knowledge of external quantum efficiency (as a function of wavelength) for a given cell, the current per unit area of the device (short-circuit current, Jsc) of a solar cell can be calculated by integrating the external quantum efficiency and the photon flux (number of photons per unit area per unit time) over the wavelength in the solar spectrum, and scaling by the electron charge:

$$J_{sc} = q \int_{\lambda} EQE(\lambda)\, \phi \quad (\lambda) d\lambda$$

Chapter 5 Deposition and characterization of $CuInSe_2$ absorbers and solar cells

5.1 Growth of $CuInSe_2$ absorbers by co-evaporation 3-stage process

High-efficient solar cells are closely related to the morphological and crystalline quality of their absorber films, being the size of grains one of the most important characteristic (but not the only one). The grain size is heavily dependent on the growth conditions and the specific deposition process used for the preparation of the films. This study is focused on the deposition parameters (particularly substrate temperature) of a 3-stage growth process which have a strong influence on obtaining high-crystalline quality absorbers films with large grains.

5.1.1 The growth process of $CuInSe_2$ films

5.1.1.1 Details of the study

The objective of this study is the exploration of the $CuInSe_2$ (CISe) absorbers prepared by the so-called 3-stage growth process, giving special attention to the effects of the substrate temperature, at the initial stage of the process, on the morphological and structural properties of the final CISe layers. For the study, the CISe absorbers were grown by a bi-thermal 3-stage process, as previously described in Chapter 3 (Section 3.1.2.3) [1,2]. In the first stage, the In_2Se_3 precursor layers were grown on molybdenum coated soda-lime glass (SLG/Mo) at three different substrates temperatures, namely 250°C, 325°C and 400°C, with similar thickness for all the films (1.1 μm ± 7.5%). From these three samples, the second and third stage were carried out at the same substrate temperature, namely 580°C. The thickness of the final absorbers was similar for all the samples (~1.7 μm). It is worth to mention that the design of deposition processes in this

work is focused on the use of substrate temperatures as low as possible considering a decrease in the fabrication cost of solar cells. Figure 5.1 shows the representation of the 3-stage co-evaporation process utilized for the growth of CISe thin films.

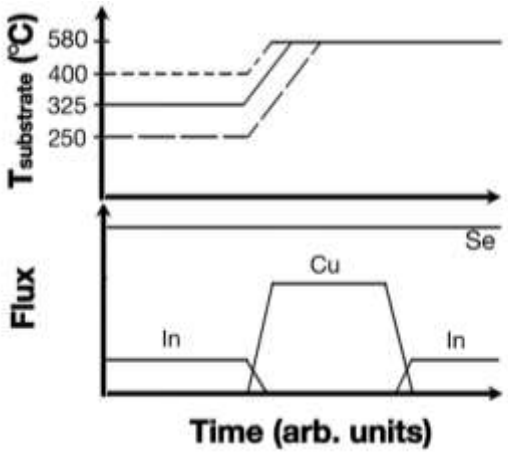

Figure 5.1 Representation of the 3-stage co-evaporation process used for the growth of CISe thin films at different initial substrate temperatures.

As mentioned in Chapter 2 (Section 2.3.1.2), the copper content in the CISe films is an important parameter for the determination of the electrical properties of the final absorbers. It is important to mention that the In_2Se_3 precursors for this study were grown independently and then all processed together through the same growth process to obtain the final CISe films. In this manner, the copper content in the three samples is assured to be as similar as possible. The supply of indium during the third stage of the growth process was such that the copper ratios (y=[Cu]/[In]) were $0.8 < y < 0.85$ for all the absorbers. The flux of selenium was kept constant during all the three growth stages of all the deposition processes. All the materials fluxes (Cu, In and Se) were controlled by the temperature of the evaporation sources. The temperature of each source was the same for all the growth processes. Thus, the speed of deposition was similar for all the experiments. Table 5.1 shows the duration of the three stages used for the CISe layers growth.

The impact of the substrate temperature at the initial growth stage is described at the absorbers level and solar cells through the scanning electron microscopy (SEM), X-ray

diffraction (XRD), voltage-current (J-V) and external quantum efficiency (QE) measurements. The Cu ratios of the films were estimated by the end point detection technique (EPD) and final ratios subsequently measured by energy dispersive spectroscopy (EDS). Figure 5.2 shows the EPD signal (Output Power vs deposition time) of the 2nd and 3rd stage of the deposition process. The thicknesses of final films were obtained with a profilometer equipment.

Table 5.1 Duration of the growth stages of CISe showing the different substrate temperatures used in the 1st-stage. The temperatures were constant at the 2nd- and 3rd-stage.

1st-stage substrate temperature (Sample ID)	1st-stage duration (In flux)	2nd-stage duration (Cu flux)	3rd-stage duration (In flux)
CISe-250°C	40’	22’	12’’
CISe-325°C	40’		
CISe-400°C	40’		

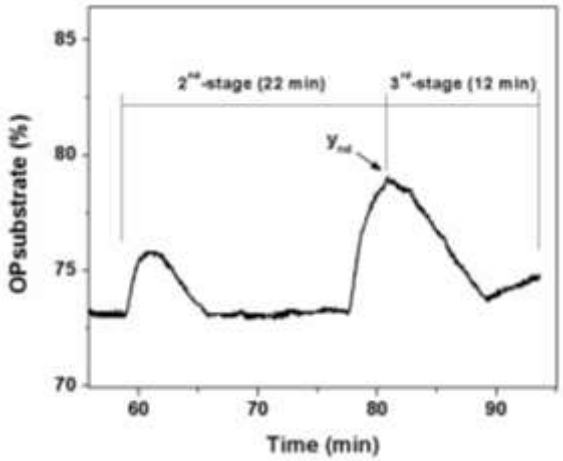

Figure 5.2 End point detection (EPD) signal of the Cu-poor/Cu-rich/Cu-poor transition during the 2nd and 3rd stage of the 3-stage co-evaporation process used for the growth of CISe thin films at different 1st-stage substrate temperatures.

5.1.1.2 Morphological and structural properties of In_2Se_3 precursor films

Morphological properties

A problem in establishing the substrate temperature of the In_2Se_3 film growth in the initial deposition stage is obtaining high-quality CISe films. Figure 5.3 shows the cross-sectional SEM images of the In_2Se_3 precursor layers deposited at substrate temperatures of 250°C, 325°C, and 400°C. At 250°C substrate temperature, it is possible to observe a film with a flat surface and formed of small grains with size ranging from 0.08 μm to 0.4 μm, approximately (Figure 5.3a). The In_2Se_3 film deposited at 325°C (Figure 5.3b) showed a very different morphology compared to layers deposited at lower temperatures. The film exhibited a more defined grain structure showing some grains with a columnar-like structure and sizes ranging from 0.25 μm up to 0.85 μm. The endings of some grains at the surface show a marked triangular-shape morphology probably related to the stronger development of (110) and (300) crystalline planes. This type of morphology is also observed by Mise et al. [3] and Ishizuka et al. [4]. The change in morphology denotes the development of a more textured surface with the increase of substrate temperatures from 250°C to 325°C. The precursor thin film deposited at 400°C (Figure 5.3c) is composed of bigger grains, compared to the previous samples, with sizes of approximately the entire film thickness (0.95-1 μm). The surface of the sample also showed a triangular-shape morphology but significantly less marked than in the sample deposited at 325°C.

As observed in Figure 5.3, the morphology of the In_2Se_3 films clearly changed as the substrate temperature increased. This is in agreement with the structure zone model developed by Movchan-Demchishin [5] in which the substrate temperature plays a significant role. In this model, the films deposited at low temperatures are composed of small grains promoted mostly by the low diffusivity of the impinging adatoms, which results in a high density of nucleation centers. This kind of behavior is observed in the small-grained In_2Se_3 films deposited at 250°C (Figure 5.3a). With increased substrate temperatures, the diffusion of impinging adatoms increases and thus promotes the crystals to grow in such a way that the adatoms are incorporated preferentially in surfaces

with low energies. The aforementioned type of growth is called competitive growth and is characterized by low-surface-energy triangular-shaped columnar grains growing on other grains with higher surfaces energies. Evidence indicating the start of this competitive growth is observed in the In_2Se_3 layers deposited at 325°C (Figure 5.3b), with the development of some columnar triangular-shaped grains. At high substrate temperatures, the morphology of the film is controlled by diffusion processes (e.g. intergrain, intragrain) and is distinguished by grains which size increases with the deposition temperature until the grains show a bulk-like proportion. The In_2Se_3 films deposited at 400°C (Figure 5.3c) showed an apparent grain growth with respect to the layer growth at 325°C, extending the grain size through all the film thickness (~0.95-1 μm). This could suggest that the diffusion-controlled growth is starting to take place, up to some extent, at this high substrate temperature. The observed large grain size agrees with the results of Mise et al. [3] showing an increase of lateral grain size of films with an increment of deposition temperatures. It is important to mention that the morphology of the In_2Se_3 films could affect the morphology properties (e.g. grain size, surface rugosity) of the final CISe absorber layer, which in turn could affect the efficiency of devices.

The relative chemical compositions of the In_2Se_3 films are shown in Table 5.2. The film grown at 250°C shows an In_2Se_3 material close to the desired stoichiometric Se:In (60:40, Se/In=1.5). As the substrate temperature increased, the Se content in the films slight decreased. This reduction is due to the re-evaporation of highly-volatile selenium from the heated substrate. Thus, considering the re-evaporation of Se is possible to assume the formation of Se vacancies (V_{Se}) in the films and a possible increase in the number of vacancies as the substrate temperature increases.

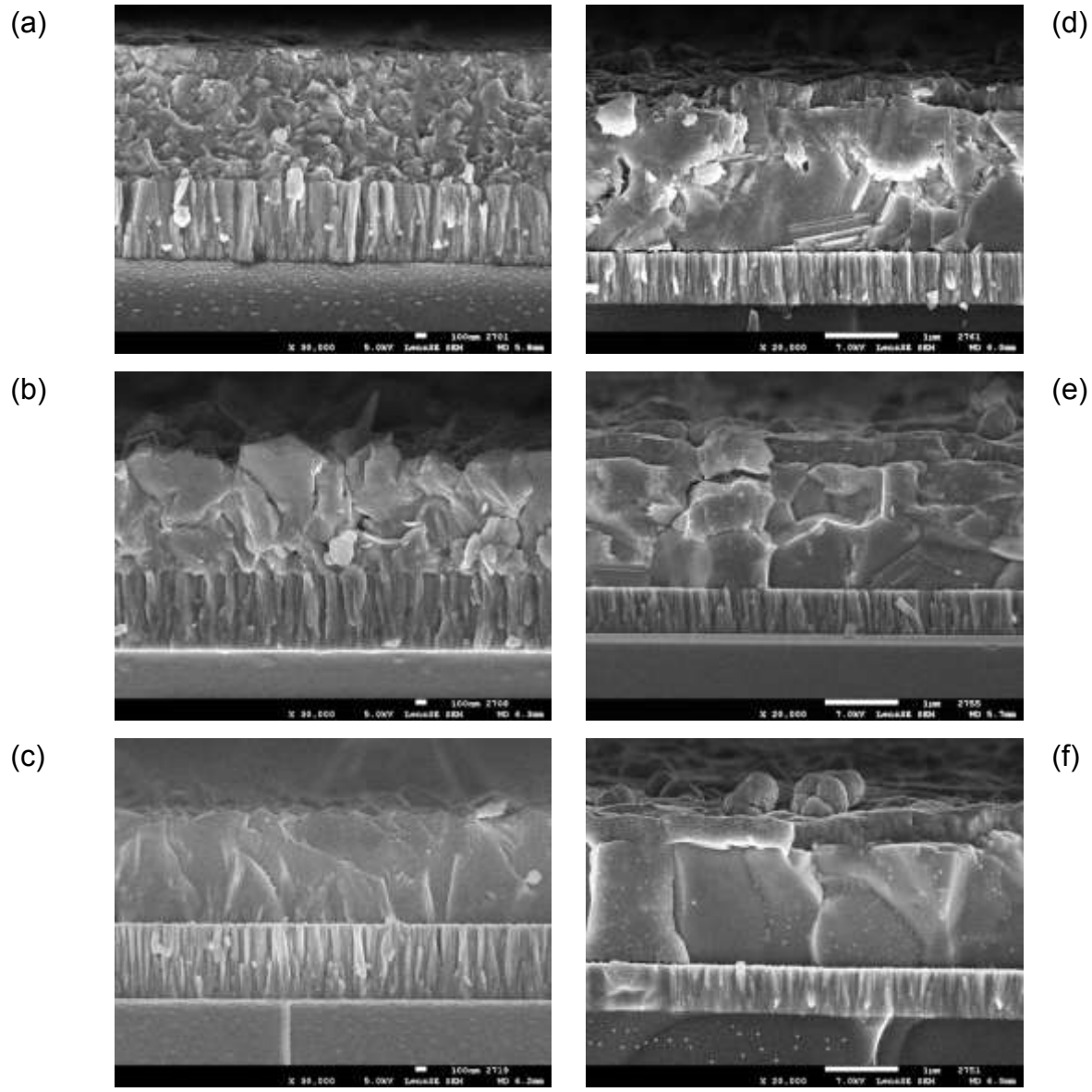

Figure 5.3 SEM cross-section images of In_2Se_3 precursor films deposited at various substrate temperatures: (a) 250°C, (b) 325°C and (c) 400°C and its corresponding CISe absorber layers (d), (e) and (f).

Table 5.2 EDS analysis of relative chemical compositions of the In_2Se_3 films deposited at various deposition temperatures.

Sample ID	In(at%)	Se(at%)	Se/In
In_2Se_3-250°C	39.56(±0.66)	60.43(±1.18)	1.52
In_2Se_3-325°C	41.87 (±0.68)	58.13(±1.26)	1.38
In_2Se_3-400°C	42.03 (±0.65)	57.97 (±1.63)	1.37

Structural properties

The In_2Se_3 films were studied by X-ray diffraction (XRD) in order to determine their crystalline properties. Figure 5.4 presents the XRD patterns of the films deposited on Mo/SLG substrates at different temperatures, namely 250°C, 325°C and 400°C. Table 5.3 shows the textures of the films determined by Lotgering factors. The Lotgering factor, F(hkl), is defined by the following equation 1 [6]:

$$F(hkl) = \frac{P(hkl) - P_0(hkl)}{1 - P_0(hkl)} \qquad \text{(eq. 5.1)}$$

where F(hkl) is the degree of (hkl) orientation, P(hkl) = I(hkl) / ΣI(hkl) and $P_0(hkl) = I_0(hkl) / \Sigma I_0(hkl)$. Here I(hkl) is the (hkl) peak intensity and ΣI(hkl) is the sum of the intensities of all peaks in the film diffraction data. $I_0(hkl)$ is the (hkl) peak intensity and ΣI_0 (hkl) is the sum of the intensities of diffraction peaks in the reference powder data (JCPDS #40-1487). Films for which all the Lotgering factor $F(hkl) \leq |0.2|$ are deemed to have a random texture. In the case that there is one orientation (hkl) for which $F(hkl) > |0.2|$, while the others are less than |0.2|, then it is possible to say that there is a preferential orientation in the corresponding {hkl} direction.

Table 5.3 shows the full width at half maximum (FWHM) and the crystallite size (D) calculated from the Scherrer's formula:

$$D = \frac{0.94\lambda}{\beta cos\theta} \qquad (1)$$

Where β is the FWHM, λ is the wavelength of incident X-rays, θ is the angle of incidence relative to the planes in question.

Table 5.3 Lotgering factors (F(*hkl*)) of the In_2Se_3 films deposited at various temperatures.

Sample ID	In_2Se_3-250°C	In_2Se_3-325°C	In_2Se_3-400°C
F(110)	-0.08	0.36	0.47
F(006)	-0.02	-0.07	-0.11
F(300)	-0.20	0.0	0.10
F(101)	---	0.0	0.024
F(102)	---	-0.02	-0.04
F(105)	0.38	---	-0.01
F(113)	0.03	0.0	-0.02
F(201)	---	-0.01	0.02
F(202)	---	0.0	-0.07
F(116)	-0.05	-0.07	-0.09
F(215)	---	-0.02	-0.03
F(208)	---	-0.04	-0.05
F(306)	-0.13	-0.06	-0.10
F(218)	---	-0.04	-0.04

In Figure 5.4, it is possible to observe that the crystallinity of the In_2Se_3 layers evolved with increased deposition temperature. The film deposited at 250°C showed a material with a low crystalline quality showing the largest full width at half maximum (FWHM) values of the (110), (006) and (300) planes as observed in Table 5.4. At 250°C some crystalline planes started to develop (Figure 5.4a), being the principal planes (110), (006) and (300) and (105) related to γ- In_2Se_3 phase (JCPDS 40-1407) (Figure 5.4b) which has a defected wurtzite (hexagonal) structure [7]. The γ- In_2Se_3 phase is the phase stable at low temperature also observed by other authors [8,9]. The films showed a (105) preferred orientation as observed in Table 5.3. At low growth temperatures, it could be possible to

expect the formation of a β- In_2Se_3 phase as observed in the In-Se phase diagram (see Chapter 2 section 2.3.1.3). Considering this possible formation, the XRD pattern of samples deposited at 250°C was compared to a reference pattern of β-In_2Se_3 (JCPDS 20-0494) noting that no trace of this phase was observed.

In comparison to the film deposited at the lowest temperature, the films grown at 325°C showed crystalline planes all mostly related to a γ- In_2Se_3 phase with an improved crystallinity and the development of a more textured layer (Figure 5.4a). The XRD pattern also showed three extra peaks at 2θ values of approximately 18.87°, 25.95° and 48.23°, which could correspond to In6Se7-(201) (JCPDS 25-0385), InSe-(101) (JCPDS 42-0919) and β- In_2Se_3-(116) (JCPDS 20-0494) phases, respectively. The emergence of this Se-poor phases could be related to the local loss of Se from the film (Table 5.1) due to the increase of substrate temperature. Other studies [10,11] also reports the co-existence of γ- and Se-poor phases at substrate temperatures in the range of 200°C and 745°C. The FWHM values of the (110), (006) and (300) γ- In_2Se_3 planes (Table 5.4) are clearly lower than the sample deposited at 250°C, denoting the enhanced crystalline quality. The film exhibited an (110) preferred orientation with strong (300) line and a weak (006) peak (Figure 5.4b). The noticed texture is in agreement with the observed morphologies in the SEM images (Figure 5.3), where a clear change of morphology starts from 325°C (Figure 5.3b), related to the development of triangular-shaped grains [4].

Table 5.4 Full width at half maximum (FWHM) values of the In_2Se_3 films deposited at different temperatures.

Sample ID	FWHM			Crystallite size (nm)		
	(110)	(006)	(300)	(110)	(006)	(300)
In_2Se_3-250°C	0.17	0.17	0.29	48	47	29
In_2Se_3-325°C	0.09	0.09	0.12	93	88	71
In_2Se_3-400°C	0.07	0.1	0.09	118	78	98

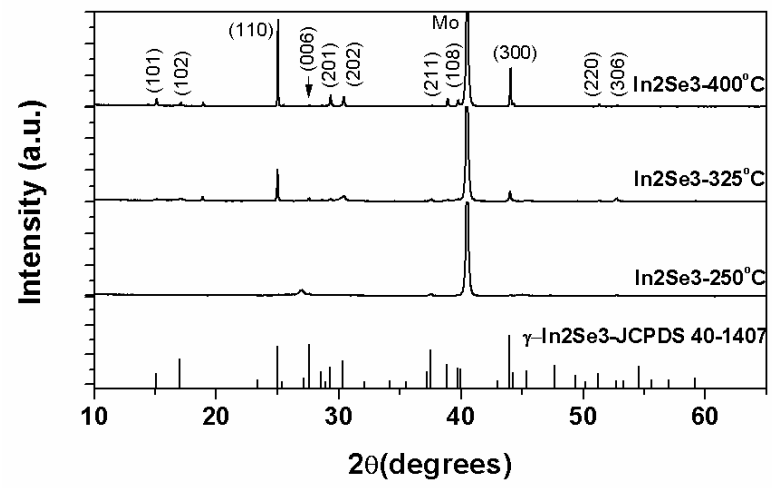

(a)

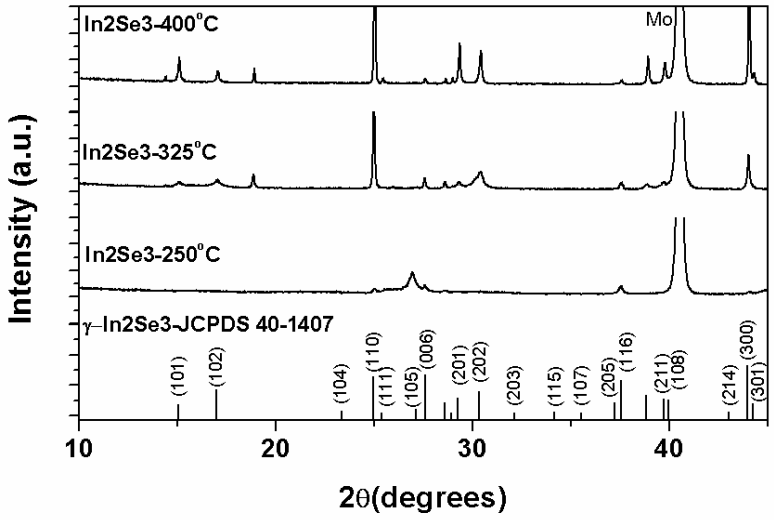

(b)

Figure 5.4 XRD patterns of (a) In_2Se_3 thin films deposited on SLG/Mo substrates at three different temperatures and (b) a zoomed region of the same pattern.

The In_2Se_3 layers deposited at 400°C also displayed crystalline planes belonging to γ-In_2Se_3 phase (Figure 5.4). The two additional peaks at 2θ values of approximately 18.92° and 53.83° could correspond to (-201) and (413) planes of the In_6Se_7 phase (respectively), which could be related to the local loss of Se from the layer. The sample had the best crystalline quality of all samples, showing the lowest FWHM values of the (110) and (300) planes (Table 5.4). In comparison with the previous samples, this film

exhibited a stronger (110) preferred orientation and the same tendency of strong (300) line and a weak (006) peak (Table 5.3). These results show that high substrate temperatures allow obtaining (110)-oriented In_2Se_3 films with high quality not only concerning of morphology but also in terms of crystallinity.

From the last results is possible to observe that γ- In_2Se_3 films can be deposited Mo/SLG at temperatures as low as 250°C. The γ-phase is commonly used in the 3-stage growth process for the fabrication of high-efficiency CISe solar cells [3,12]. On the other hand, the orientation of the films is noted to be dependent on the substrate temperature. As observed by Mise and Nakada [3], the increase of substrate temperatures allows the texture of the films to evolve from a random to an (110) preferred orientation at expenses of the (006) or the (300) orientation. The morphology is also affected by the deposition temperature. The films show an increase of grain size as the substrate temperature increases. The shape of the grains also changes with the rise of temperature from an amorphous to a more columnar-like aspect. The next section describes the effect of the In_2Se_3 films properties (i.e. morphology, crystallinity, composition) on the growth and properties of the CISe layers.

5.1.1.3 Morphological and structural properties of $CuInSe_2$ films

Morphological properties

Three CISe absorber films were grown by completing the 3-stage co-evaporation process using each of the In_2Se_3 precursor films deposited at various substrate temperatures (250°C, 325°C, and 400°C). Figure 5.4d,e,f shows the cross-section SEM images of these final CISe absorbers. The images present not only the absorber layer but all layers that compose the final solar cell structure (i.e. CdS, ZnO, ZnO:Al).

The CISe films deposited at 1st-stage substrate temperature of 250°C (CISe-250°C, Figure 5.4d) showed a layer composed of larger grains in comparison to its corresponding

precursor film observed in Figure 5.4a. The largest grains sizes were around 2 μm. However, the grain size distribution seemed to be mixed, with sizes as low as 0.32 μm. Additionally, the formation of voids inside the layer is observed, which could be related to the consumption of the excess Cu_2Se secondary phase by the indium during the 3rd stage of the deposition process. In the third stage, the Cu inter-diffuses with the In-rich material probably via vacant sites, resulting in the coalescence of vacancies which move opposite to the direction of the diffusion of Cu [13,14]. This kind of voids has been observed in device-quality chalcopyrite films prepared by multistage evaporation deposition processes [15–17].

The CISe layer grown from the precursor deposited at 325°C (CISe-325°C, Figure 5.4d) was also composed by large grains, again bigger than the corresponding In_2Se_3 film. It is possible to observe a film with grain sizes range of 0.6 μm to 2 μm, displaying more uniform sizes in comparison to the CISe-250°C sample. Also, it is noted that the formation of intergrain voids was reduced with the increase of substrate temperature used during the 1st stage. Lei et al. [14] has also observed the reduction of voids with the increase of substrate temperature during the deposition of CIGSe films using a bilayer growth process.

Figure 5.4e shows the SEM image of the CISe absorber deposited with a 1st-stage substrate temperature of 400°C (CISe-400°C). The sample exhibited grains in the size range of 1.3 μm -2 μm, this last size being the entire thickness of the layer. The SEM displays a film with the most uniform grain size in comparison to the CISe samples deposited at lower 1st-stage temperature. The absorbers showed a marked decrease in the formation of voids, which is consistent with the observations of Lei and Rockett [13,14] of absorbers grown at high substrate temperatures.

Concerning the surface flatness of the CISe absorbers, no apparent variation is observed in SEM images despite the different surface morphology seen in the In_2Se_3 precursor films (cross-section). The surface, at most, showed a slight tendency to be flatter as the substrate temperature of 1st-stage increased. This weak dependence in the flatness could

be related to the suppression of the surface roughness of the In_2Se_3 film with the adhesion of Cu and Se atoms on its surface at high temperature (e.g. 580°C) during the second stage of the process. At high deposition temperatures (useable with for glass substrates), the Cu2Se films are known to be in a pseudo-liquid phase (see Chapte2, section 2.3.1.4), resulting in a decreased Cu2Se film surface roughness with increasing deposition temperature [3,18,19]. The nearly independence of CIGSe roughness on the deposition temperatures of (In,Ga)2Se3 precursors films has been also observed by Mise et al. [3].

In a morphological point of view, the growth of the three CISe films shows a significant grain size evolution between the first and third stage of the 3-stage process. The Cu-free layers (i.e. In_2Se_3 films) formed at the first step of the process consist of grains with sizes that depends on the substrate temperature (higher the temperature, larger the grain size). These first-stage grain sizes are smaller than those observed in the final CISe absorbers obtained at the end of the third stage of the deposition process. To have an insight of the grain size evolution is necessary to consider the growth of CISe by a 3-stage growth process, especially the one occurred in the second stage. In the second stage, the Cu content within the growing film is increased in such way that a transition from Cu-poor ($y=[Cu]/([Ga]+[In]) < 1$) to Cu-rich ($y>1$) occurs at the end of the stage after the major part of the final films has been deposited (see Chapter 3, section 3.1.2.3). The institute of Materials Jean Rouxel in Nantes (IMN- MIOPS group) has extensively investigated the three-step based processes, and their different studies have found that the recrystallization phenomenon occurs during the transition from $y\approx0.9$ (Cu-poor) to $y\approx1.1$ (Cu-rich) [20,21]. Such recrystallization involves a reconstruction of the initial layer, which changes its structure from small to large grains while minimizing crystalline defects that may act as recombination centers [22–25]. The reduction of recombination centers in the absorber film through the recrystallization process is one of the principal characteristics that promote the CIS-based solar cells to yield high conversion efficiencies [21,26]. During the growth of the CISe-250°C,-325°C and -400°C absorber, the films were subjected to a Cu-poor/Cu-rich transition, denoted by the abrupt output power (OP) increase in the end point detection (EPD) graph (see Figure 5.2). As indicated in Chapter 3 (section 3.1.3), the increase of OP is related to a rise in emissivity of the film (and a temperature

decrease) due to the formation of a Cu-Se layer on the top of the precursor [27,28]. Hence, the observed changes in morphology of the three final CISe absorbers can be, effectively, attributed to the recrystallization process, which indeed results in an improved film morphology. The observed enhanced morphologies could improve the crystalline quality of the CISe films and thus upgrade its electrical properties by decreasing the number of potential recombination centers of photogenerated electron-hole pairs (e.g. crystalline defects found in grain boundaries) [29].

Another important observation is the degree of changes that each layer suffers in relation to the substrate temperature used in the first stage of deposition. Barreau et al. [21] has reported the small-to-large grain transition as a result of the growth of low energetic grains by the consumption of the higher energetic ones, which gives an epitaxial-like growth. This kind of grain growth occurred during the recrystallization could be attributed to a grain boundary migration process (GBM) which implicates the transfer of atoms from a consumed grain to a growing grain through a grain boundary [21,30]. A detailed description of the model based on the GBM is given in the reference [21,31]. Nevertheless, an important aspect to mention is that the driving force of the grain boundary movement originates from the total system energy decrease, i.e. intragranular defects energy (related to vacancies, dislocations), grain boundary energy (related to grain curvature), chemical energy (related to composition gradients) and stored energy from deformation. Accordingly, and having in mind the growth of CISe films, the grain size before the recrystallization (e.g. that of the precursor layer) is a factor that affects the extent of changes (e.g. structural) during the reconstruction of the film. It is possible to observed that the precursor film composed of the smallest grains (i.e. the one deposited at 250°C) is the layer that suffered the greatest grain size increase in comparison to the CISe films obtained from precursors with larger grains (i.e. those deposited at higher temperatures). Effectively, it is possible to observe that during the deposition process, the grains of the 250°C film grown from ~0.4μm to the ~2μm, while the changes suffered in the 325°C (~0.85μm to ~2μm) and 400°C (~1μm to ~2μm) final films were of lower magnitude. This type behavior is also observed by Couzinié-Devy et al. [20].

The relative chemical compositions of the $CuInSe_2$ films are shown in Table 5.4. As mentioned before, the targeted compositions in this study were 0.8<y<0.85 (y=[Cu]/[In]). These range of compositions have been used for the fabrication of solar cells with good functionality [32]. The observed variations are inherent to the deposition process and associated with the chamber dimensions and the position of the substrates relative to the evaporation sources. The copper composition at the end of the 2nd stage of the deposition process (see Figure 5.2) is estimated as:

$$y_{nd} = \left(\frac{t_1 + t_3}{t_1}\right) y_f$$

Where t_1, t_3 are the duration of the 1st and 3rd stage (respectively), and y_f is the copper ratio of the CISe film at the end of the deposition process. The y_{nd} values greater than one (see Table 5.5) are related to the formation of a Cu-rich phase at the end of the 2nd stage. Taking into account these y values, it is possible to consider that during the deposition process the film composition indeed evolved from Cu-poor (y<1, 1st-stage) to Cu-rich (y>1, 2nd-stage) and again to Cu-poor (y<1, 3rd-stage). Thus, it could be assumed that the recrystallization phenomenon took place in the CISe films. This is further confirmed by the grain growth observed in the SEM cross-section images of Figure 5.3.

Table 5.5 EDS analysis of relative chemical compositions of the $CuInSe_2$ films deposited at various deposition temperatures.

Sample ID	Cu(at%)	In(at%)	Se(at%)	y=Cu/In	y_{nd}
CISe-250°C	21.82 (±0.66)	27.35(±1.79)	50.83 (±3.26)	0.80	1.04
CISe-325°C	22.14 (±0.68)	27.39 (±1.71)	50.47 (±4.43)	0.81	1.05
CISe-400°C	22.41 (±0.54)	27.35 (±1.93)	50.24 (±4.1)	0.82	1.07

Structural properties

The $CuInSe_2$ films were studied by X-ray diffraction in order to determine their crystalline properties. Figure 5.5 presents the XRD patterns of the α-CISe films deposited on Mo/SLG substrates at different 1st-stage temperatures, namely 250°C, 325°C and 400°C. The XRD patterns are the ones obtained after normalization of the (112) peak. The three samples showed the formation of chalcopyrite-like $CuInSe_2$ compounds denoted by the crystallographic planes (101), (112), (103), (211), (105), (213), (204)/(220), (116)/(312) and (305)/(323). The XRD pattern were indexed in accordance with the JCPDS 40-1487 ($CuInSe_2$). The presence of (101), (103) and (211) plane in the XRD shows the development of a CISe material with an ordered cation sublattice [33].

A comparison of the three CISe samples showed the development of the (116)/(312) doublet with the increase in 1st-stage substrate temperature (see Figure 5.5b). The evolution of the (116)/(312) doublet is closely related to the improvement in order of atoms in the chalcopyrite phase [33]. The observed slight shift to lower 2θ angles (e.g. 26.78° to 26.74°, (112) plane) with increased substrate temperature could be related to a change in lattice parameters towards a larger unit cell, probably due to small variations in Cu content to Cu-poor. These match with the variations in Cu compositions observed in the Table 5.5. The presence of the (101), (103) and (211) planes and the evolution of the (116)/(312) doublet shows that all three CISe samples have an ordered chalcopyrite structure which order is improved with the increase of substrate temperature used during the 1st stage of deposition. The full width at half maximum values of the three CISe

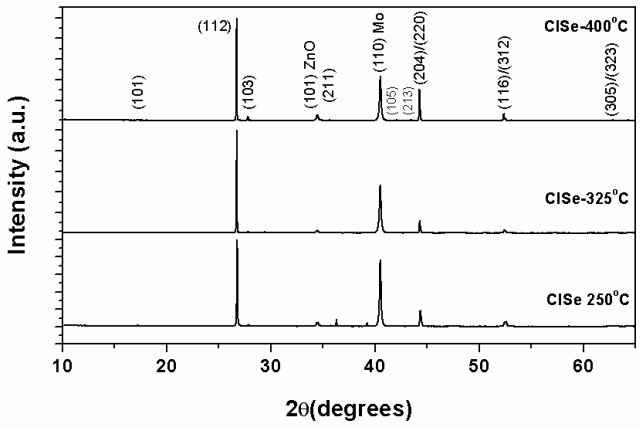

(a)

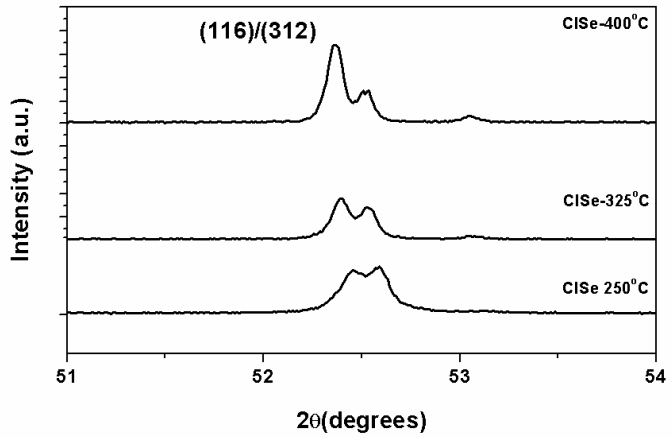

(b)

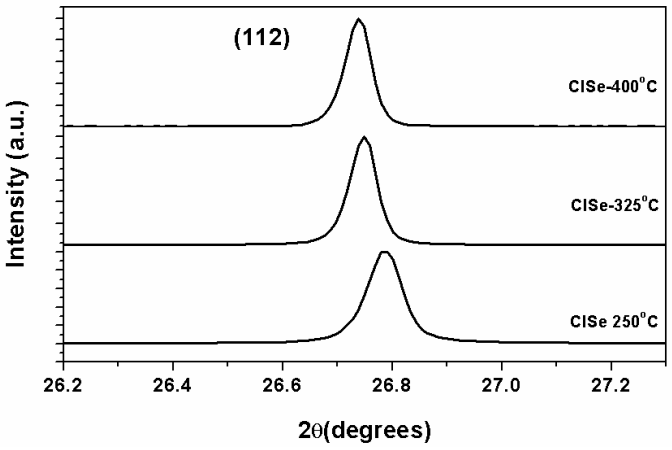

(c)

Figure 5.5 XRD patterns of (a) CISe thin films deposited on SLG/Mo substrates at three different temperatures and zoomed regions of (b) the (116)/(312) and (c) the (112) peaks.

samples (see table 5.6 and Figure 5.5c) are similar. Nevertheless, the values are smaller than the observed in the In_2Se_3 films, in particular for those deposited at low 1-st stage substrate temperature (i.e. 250°C). The decrease of FWHM is an indication of the improvement of the film crystallinity observed after the recrystallization process (i.e. afterward the Cu-poor/Cu-rich/Cu-poor transition).

Table 5.6 Full width at half maximum (FWHM) values of the CISe films deposited at different 1st-stage temperatures.

Sample ID	FWHM (°)	Crystallite size (nm)
	(112)	(112)
CISe-250°C	0.07	109
CISe-325°C	0.06	138
CISe-400°C	0.06	143

Table 5.7 shows the textures of the films determined through Lotgering factors (see equation 5.1). It is possible to observe that all the films exhibited an (112) preferential orientation indistinctly of the orientation of their respective precursor films. A maximum *F*(112) value is attained at a 1st-stage substrate temperature of 325°C. This trend is contrary to the noticed by Mise et al. [3] who reported the development of (220)/(204)-oriented film at substrate temperatures of 300-400°C. However, his group also reported the deposition of (112) oriented films from highly rough precursor films [3]. It seems that a higher apparent roughness of the In_2Se_3 could promote films with a stronger (112) orientation. The (112) preferential orientation of CISe films growing from rough In_2Se_3 precursors (i.e. Tsubstrate=325°C) could be due to the difference in the diffusion rate of Cu atoms and the growth rate of the films [3]. Another important factor to influence the film preferential orientation is the presence of sodium in the absorber, which promotes the development of films with an (112) orientation as the substrate temperature increases (i.e. diffusion of Na to the CISe film increases) [20,34]. It is important to highlight that the precursor layers were exposed to air during the interruption of deposition process (see section 5.1.1), promoting the diffusion of sodium into the film due to Na-O catalytic effect (more discussion on this later on in the chapter). The diffused sodium could have a role

on the preferential orientation observed in Table 5.7. Therefore, the diffused Na into the layer in addition to In_2Se_3 films with faceted planes could promote highly (112)-oriented CISe films.

Table 5.7 Lotgering factors (F(hkl)) of the CuInSe2 films deposited at different 1st-stage temperatures.

Sample ID	CISe-250°C	CISe -325°C	CISe -400°C
F(112)	0.42	0.61	0.36
F(204)	-0.05	-0.08	0.02
F(220)	-0.14	-0.20	-0.18
F(101)	-0.01	-0.01	-0.01
F(103)	0.0	0.0	0.01
F(211)	-0.01	-0.02	-0.02
F(116)	0.0	0.0	0.0
F(312)	-0.07	-0.09	-0.09

Considering all previous results from the SEM images, EDS (composition) and XRD patterns, it is possible to observe a general improvement in the morphological (e.g. grain size increase) and structural (e.g. decrease of FWHM values) properties of the films during the transition from γ-In_2Se_3 to α-$CuInSe_2$ phase. These improvements, which result in high-quality CISe films, are attributed to the recrystallization phenomenon occurred during the Cu-poor/Cu-rich transition in the 2nd-stage. In this stage, the Cu diffuses and accumulates into the layer. Indeed, high-quality films obtained after the recrystallization process are vital for the achievement of high-efficiency solar cells. These results make evident the importance of the recrystallization of films, which can improve the crystalline quality of the layer dramatically even if the starting precursor layer have an inferior quality as compared to final films.

The grain size before the recrystallization (i.e. that of the precursor layer) is a factor that affects the extent of changes during the reconstruction of the film. The major change in morphology is observed from the film deposited at low 1st-stage temperature and composed of small grains. The deposition temperature of the In_2Se_3 precursor is an important parameter which influences the morphology of the final CISe films. A more

uniform grain size (with a trend to 2μm grains) is observed as 1st-stage substrate temperature increases. These last observations could indicate that the morphology of precursor film influences the diffusion of copper and the formation of CISe during the 2nd deposition step.

It is important to mention that the previous results have to be handle with particular precaution. Indeed, the substrate temperature used during the 1st stage of the growth process, although it is a critical parameter, is not the only one affecting the morphology and structure of the CISe (as well as CIGSe) films. In the literature, several growth parameters have been identified to influence the morphological and structural properties of the absorber layers deposited by 3-stage protocol. Some of the most important parameters are the deposition rate, the excess of copper during the 2nd stage, the final thickness of the layer, the selenium evaporation rate and the gallium composition (in the incase of CIGSe absorbers) [35–37]. In the frame of this work, the standard deposition protocol is proposed in the sense of fix the deposition conditions just mentioned before in order to limit the changes in the final deposited layers. In this case, the use of a bithermal 3-stage process with a high 2nd-stage substrate temperature and a relatively slow deposition rate is desirable for high efficient solar cells.

The next section will show the electrical measurements of the solar cells obtained from these CISe absorbers.

5.1.1.4 $CuInSe_2$-based solar cells

The CISe absorbers analyzed in the previous sections were used to prepare solar cells. Eight solar cells of 0.5 cm^2 were prepared for each of the three different absorbers. The solar cells characteristics obtained from current density–voltage measurements (J(V)) are presented in Figure 5.6. The best solar cells achieved 12% (11.7) efficiency with a short circuit current density (J_{sc}) of 37 mA/cm^2, a open circuit voltage (V_{oc}) of 460 (461) mV and a fill factor (FF) of 70% (68.7) using an absorber prepared at a 1st-stage substrate temperature of 400°C. As the temperature decreases, it is possible to observe a similar

V_{oc} for the case of CISe-400°C and -325°C, but an important reduction for the solar cell prepared with the CISe-250°C. Considering the J_{sc}, a general decrease is observed as temperate reduces, with the CISe-325°C sample showing the lowest values. The FF continuously decreases as the 1st-stage substrate temperature diminishes. As a result of theses trends, the performances of the solar cells deteriorate as the substrate temperature reduces.

The general decrease of the solar cell characteristics could be related to an increase in recombination in which the grain boundaries could play a role. The grain boundaries include high density of defects which could acts as recombination centers and modify the diffusion length of the charge carriers. The lower the diffusion length, the lower the V_{oc} [38]. For high-efficiency solar cells the grain-boundary recombination must be low [38]. As observed in the Figure 5.3, the CISe absorbers deposited at low and medium temperature (i.e. 250°C and 325°C, respectively) presented an structure with more grain boundaries compared to samples prepared at high substrate temperatures (i.e. 325°C and 400°C). The higher number of grain boundaries formed at low deposition temperature could impact in a high recombination of charge carriers within the CISe film and thus decrease the V_{oc}.

Another important factor that impacts in the improvement of V_{oc} and FF with increasing deposition temperature is the diffusion of Na into the CISe films. The enhancement of device characteristics with the presence of Na is related to an augmentation of net acceptor concentration in the CISe film probably promoted by the decrease in the number of compensating donors (e.g. V_{Se}) and/or the creation of the acceptor defect (e.g. Na_{In}) [38,39]. It has been observed that the higher the substrate deposition temperature, the higher the quantity of sodium that diffuses inside the absorber film [40] and the greater the improvement of V_{oc} and FF. This situation could be occurring in relation to the In_2Se_3 precursor layers (deposited at different temperatures) and subsequently to the CISe absorbers used in the solar cells presented in Figure 5.6. In next sections of this work, it will be shown that Na is indeed found in the surface of the In_2Se_3 precursor films.

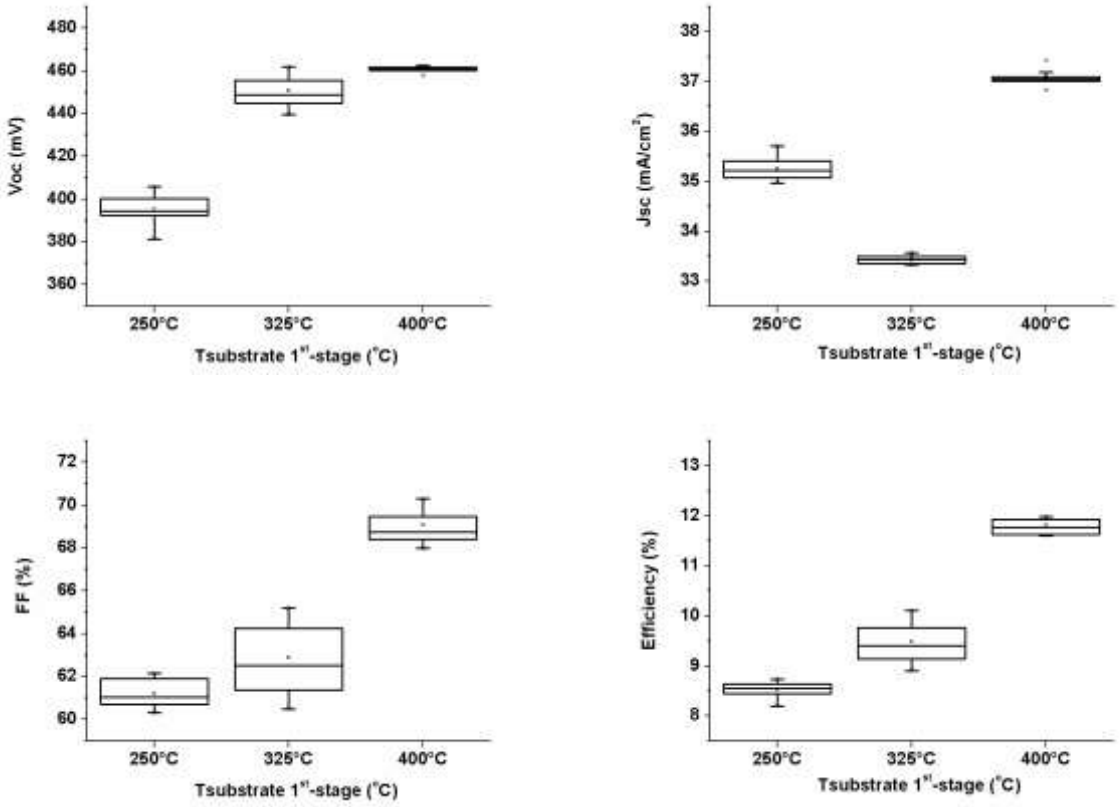

Figure 5.6 Solar cells characteristics for CISe absorbers deposited at different 1st-stage substrate temperature.

Figure 5.7 shows the quantum efficiency (QE) measurements of the solar cells. The CIS-400°C solar cell exhibited the highest quantum efficiency, while the other samples displayed a general decrease in the range of ~500-1200nm. This indicates the increase in losses in the CISe-250°C and -325°C solar cells due to an incomplete collection of photogenerated carriers in the absorber. A higher quantum efficiency of the CISe-250°C sample is observed in the range of ~400-520 nm, which could be related to a thinner CdS layer (i.e. less absorption of photons) [26] as compared to the other two samples. Additionally, in comparison with the CISe-250°C sample, the CISe-325°C cell exhibited a lower QE signal in the range of 650-960 nm. This could indicate a higher recombination in the CISe-325°C solar cell and thus a lower J_{sc} as observed in Figure 5.6.

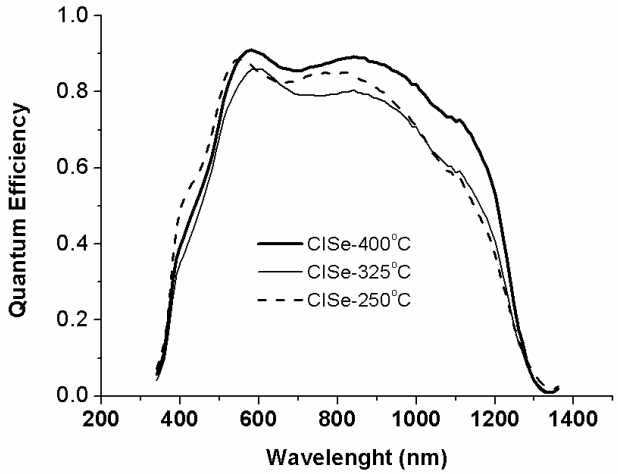

Figure 5.7 Quantum efficiency (QE) measurements of the CISe solar cells prepared with the absorbers deposited at different 1st-stage substrate temperatures.

Considering all the above results, it is apparent that the performances of the prepared devices are affected by the deposition conditions. The performances of solar cells are modified by the change of structural and morphological properties of CISe films promoted by the variation of the 1st-stage substrate deposition temperature during the 3-stage process. In this work, the highest efficiency is achieved with an (110)-oriented γ- In_2Se_3 film precursor with big columnar-like grains ($\sim$1 μm) obtained at a 1st-stage substrate temperature of 400°C. The use of this precursor results in high-quality (112)-oriented α-CISe film with grains sizes of $\sim$2 μm. The high crystalline quality is essential for the fabrication of high-efficient devices and, this is achieved through the recrystallization process occurred during the Cu-poor/Cu-rich transition in the 3-stage growth.

Although the crystalline quality of the films is an important factor, this is not the only characteristic that determines the achievement of high-efficiency solar cells. The performance of a solar cell could also be affected by other factors such as the presence of sodium and oxygen in the absorber layer. The sodium in the CISe film improves the cell efficiency (mainly by increasing Voc and FF), increases the p-type conductivity, affects the grain size and preferred orientation [41,42]. The oxygen in CISe layers enhance the net p doping of the absorber, reduces grain boundary recombination,

improves the intergrain transport [43,44]. Furthermore, the sodium and oxygen interact each other from a catalytic role that sodium has for the surface oxidation of CISe grains [45]. In this work, the role of Na and O_2 are of particular interest given that the deposition of CISe films (either with 3-stage co-evaporation or hybrid vacuum/non-vacuum process) were carried out in an interrupted process in which the precursor layers were exposed to an open air atmosphere. Hence, the Na and O_2 are expected to contribute to the properties of absorber films and the corresponding solar cells fabricated in this contribution. To investigate these factors, the following sections presents studies on the oxidation of In_2Se_3 precursor films, the effect of sodium-oxygen interaction and the consequences on the corresponding solar cells performances.

5.1.2 The effect of oxygen in $CuInSe_2$-based solar cells

As mentioned in Chapter 2 (Section 2.3.4.1), high-efficiency CIGSe thin film solar cells critically depend on minimizing current and voltage losses across the grain surface. An approach to accomplish this is by oxidation-related passivation of grain boundary and surface dangling bonds related to Se vacancies (donor defects) [43]. The passivation of grain boundaries (GB's) in the bulk of the film is beneficial to solar cell performance [38]. The CdS/CISe interface passivation has beneficial as well as detrimental effects on the photovoltaic devices [44]. Nevertheless, the results have been presented only for the oxidation of the entire solar cell structure or for the CISe film prior cell completion. Considering the design of the deposition processes presented in this work, the oxidation of In_2Se_3 precursor films and its consequence in the corresponding solar cell is studied.

5.1.2.1 Oxygenation of In_2Se_3 precursor and $CuInSe_2$ films

5.1.2.1.1 Details of the study

This section explores the effect of the oxygen on the morphological and structural properties of $CuInSe_2$ absorbers prepared by the so-called 3-stage growth process. The

CISe absorbers were grown in a same deposition run by a bi-thermal 3-stage process, as previously described in this chapter (Section 5.1.1.1). To understand the effect of oxygen, it was decided to set the In_2Se_3 precursors films prepared at 400°C as a starting point of the study. Three In_2Se_3 layers were grown on molybdenum coated soda-lime glass (SLG/Mo) with similar thickness for all the films (~1 μm). After this step, the process was interrupted, and two samples were annealed in open air atmosphere at 300°C for 1 and 24 hours in order to expose the precursor film to air. The third sample was used for reference purposes. Using these samples, the second and third stage were carried out at the same substrate temperature, namely 580°C. The thickness of the final absorbers was similar for all the absorber films (~1.7-2 μm). The supply of indium during the third stage of the growth process was such that the copper ratios (y=[Cu]/[In]) were $0.8 < y < 0.85$ for all the absorbers. The remained deposition details are the same as in Section 5.1.1.1. Finally, the CISe films were used to fabricate the corresponding solar cells with an area of ~0.5 cm^2.

The impact of the air annealing on the films is described at the absorbers level and solar cells through the scanning electron microscopy (SEM), X-ray diffraction (XRD), voltage-current (J-V) and external quantum efficiency (QE) measurements.

5.1.2.1.2 Morphological and structural properties of In_2Se_3 and $CuInSe_2$ films

Morphological properties of In_2Se_3 and $CuInSe_2$ films

The Figure 5.8 (top) shows the cross-sectional SEM images of the In_2Se_3 precursor layer reference and annealed in open air atmosphere at 300°C for 1h and 24h. The precursor films are composed of big grains with sizes of approximately the entire film thickness (~1 μm). The films did not show any significant difference between the reference and the air exposed samples.

The cross-section SEM images of all the corresponding CISe films (Figure 5.8 bottom) exhibited very similar morphologies with grains sizes of ~1.7 μm (approximately the whole thickness layer). These grain size is an evidence of a successful recrystallization process occurred during the Cu-poor/Cu-rich transition at the end of the second stage of the deposition process. The CISe absorber films prepared with the air-annealed In_2Se_3 precursors showed the formation of voids located near the middle region of the layer thickness (i.e. ~1 μm). This near 1 μm region matched with the thickness of the In_2Se_3 precursor film. Another important observation is that the number of voids increases as the annealing time rises. These voids are comparable to those observed in CISe films formed at low 1st-stage substrate temperature (see Figure 5.3). The voids result from the interdiffusion (trough vacant sites) of Cu2Se into In_2Se_3, where vacancies move opposite to the direction of the diffusion of Cu-Se into the In-rich material [13,14]. Thus, the voids mostly appear in regions initially rich in Cu2Se material. The species that interacts with the surface of the In_2Se_3 precursor film during the annealing of the samples (e.g. oxygen) could stimulate the appearance of voids by promoting Cu-Se local segregation on the In_2Se_3 film surface at the second step of the 3-stage growth process. It is apparent that the number of places where the segregation takes place increases with the increment of the annealing time, and consequently the number of voids increases.

Structural properties of In_2Se_3 and $CuInSe_2$ films

Figure 5.9a shows the XRD patterns of the reference, 1h, and 24h air-annealed In_2Se_3 films. The XRD patterns were normalized with respect to the (110) peak. The samples displayed a very similar pattern, being the principal planes related to γ- In_2Se_3 phase (JCPDS 40-1407). The films showed an (110) preferential orientation, with the predominant Lotgering factors values of F(110)=0.47, F(110)=0.49 and F(110)=0.48 for the reference, 1h and 24h annealed samples, respectively. The as-prepare precursor showed FWHM values of 0.07, 0.1 and 0.09 for the (110), (006) and (300) peaks, respectively. The FWHM values of the annealed layers did not show any significant change compared to the reference film. Considering these results, it is possible to

observe that there is no significant change in the structural properties of the films after the annealing process (indistinctive of the annealing time).

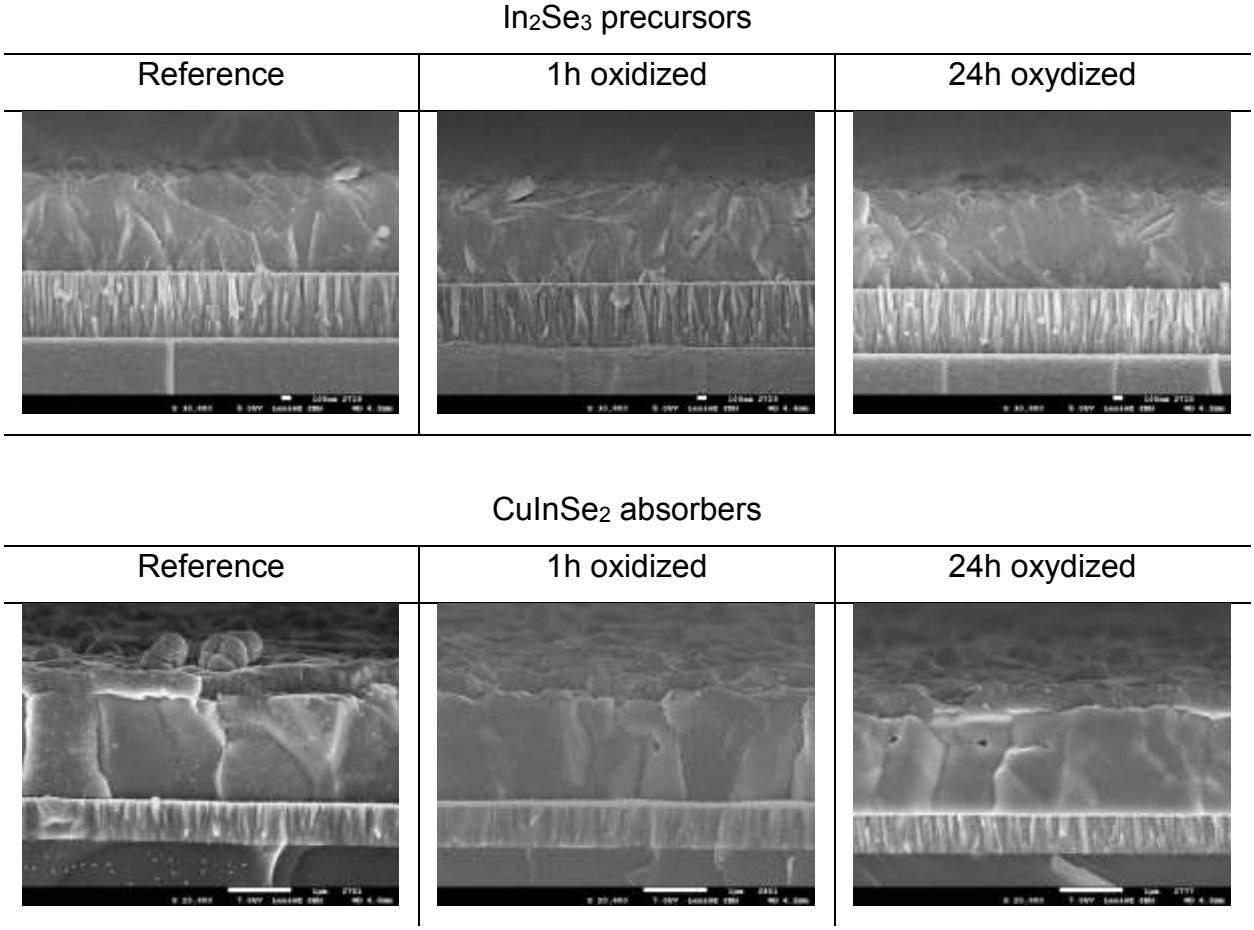

Figure 5.8 SEM cross-section images of In_2Se_3 precursor films deposited at 400°C and the corresponding CISe absorber layers prepared from the precursor films: Reference, 1h and 24h annealed in air at 300°C.

In the case of air-annealed CISe films, it has been reported that the O2 molecule is physisorbed on the surface of the layer [45]. The O2 molecule dissociates into atomic oxygen which most probably reacts with the indium (rather than copper) in order to form an In_2O_3 compound [46]. Figure 5.9b compares the In_2O_3 XRD pattern with the ones of the reference and air-annealed In_2Se_3 samples. The comparison did not show any clear evidence of In_2O_3 compound formation during the annealing.

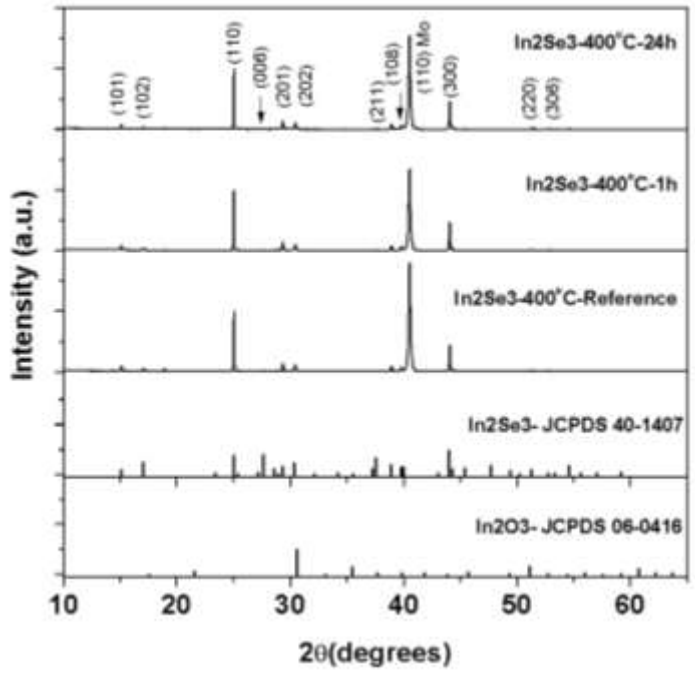

(a)

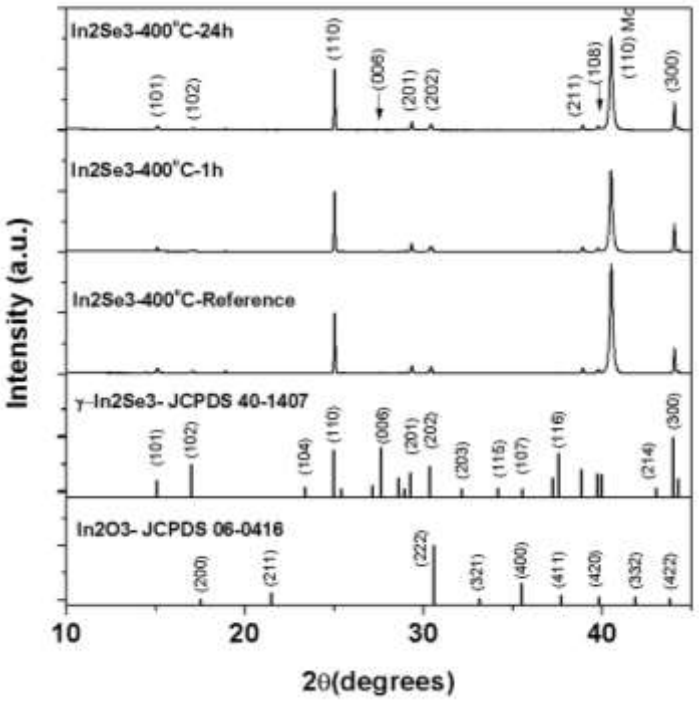

(b)

Figure 5.9 XRD patterns of (a) reference, 1h and 24h air-annealed In_2Se_3 films and (b) a zoomed region of the same pattern..

Figure 5.10 displays the XRD patterns of the CISe absorber films prepared with the reference and 24h annealed In_2Se_3 precursor films. The XRD of the samples were normalized with respect to the (112) peak. The pattern of the 1h annealed films (not shown) exhibited very similar characteristics in comparison with the other two samples. The samples showed the formation of chalcopyrite-like $CuInSe_2$ compounds denoted by the crystallographic planes (101), (112), (103), (211), (105), (213), (204)/(220), (116)/(312) and (305)/(323) (JCPDS 40-1487). There was no evidence of the formation of oxide compounds (e.g. In_2O_3) possibly promoted by the oxygenation of the precursor layers. As described in the previous section, the presence of (101), (103) and (211) plane shows the development of a material with an ordered cation sublattice [33]. The XRD study also showed a well developed (116)/(312) doublet for all the CISe samples which indicated well ordered atoms in the chalcopyrite phase [33].

The full width at half maximum values F(112) of the three CISe samples were similar (~0.06°-0.07°). Although the SEM image of the CISe films (Figure 5.8) suggested a clear grain growth due to the recrystallization process, the same transition is more difficult to observe while comparing FWHM values of In_2Se_3 (~0.7°-0.1°) and CISe films (~0.06°-0.07°). This last could be related to the fact that the changes promoted by the recrystallization are less drastic when the precursor layers are deposited at high substrate temperatures (e.g. 400°C, see Section 5.1.1.3 of this chapter).

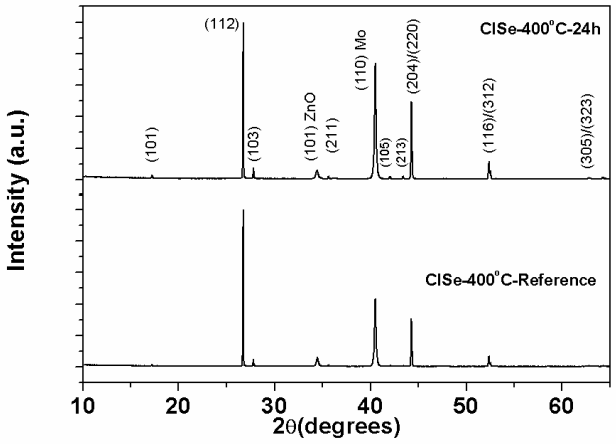

(a)

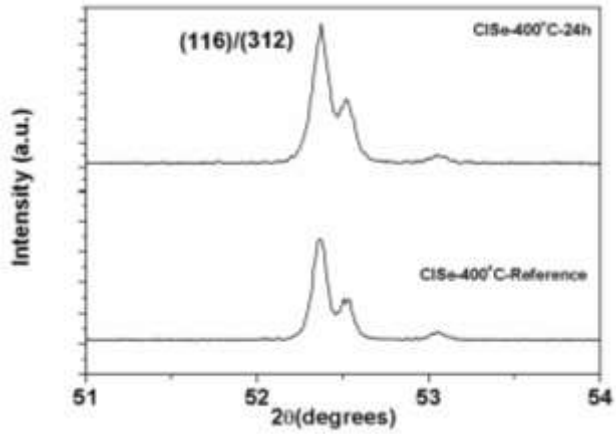

(b)

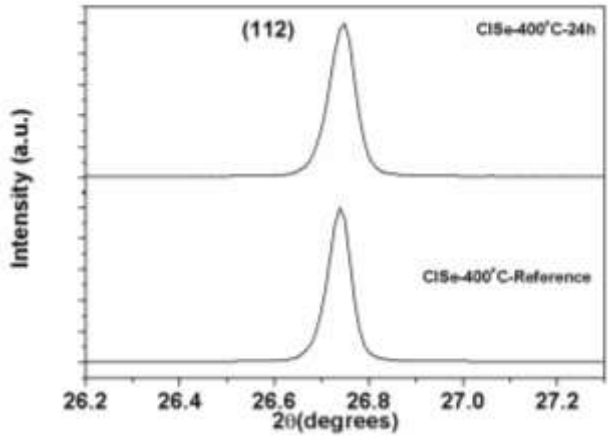

(c)

Figure 5.10 XRD patterns of (a) CISe thin films deposited on SLG/Mo substrates with reference, 1h and 24h air-annealed In_2Se_3 precursor films and zoomed regions of (b) the (116)/(312) and (c) the (112) peaks.

Table 5.8 shows the textures of the films determined through Lotgering factors (see equation 5.1). It is possible to observe the decrease of the (112) preferential orientation with the increase of annealing time. The maximum *F*(112) value is attained with the In_2Se_3 reference sample whereas a randomly CISe oriented film is obtained with In_2Se_3 layers annealed for 24h. Considering these results, it is possible to observe that the preferential orientation could be modified by the air-annealing time, even if the precursor films have the same orientation. This behavior could be related to the interaction of Na, O2, and Se. On one hand, the alkali metals have a catalytic effect on surface oxygenation of semiconductors. The alkali metal induces polarization on the O-O bond of O_2 molecule, resulting in the formation of O_2^- and its dissociation (easier than O_2) [47,48]. Thus, an enhanced oxygenation occurs in the presence of sodium. Certainly, Na and O contents were found to be correlated (the more sodium, the more oxygen and vice versa) using X-ray photoelectron spectroscopy (XPS) and secondary ion mass spectroscopy (SIMS) [49,50]. On the other hand, it has been reported that during the CIS growth, the Na can be found in the form of Na_2Se_x located at the grain boundaries. This sodium compound could influence the availability of selenium on the CISe film and thus change its structural and also its electrical properties [51]. The availability of Se is in the form of Na_2Se_x “reservoir” attached to the CISe surface, delivering the quantity of selenium necessary to growth. Therefore, the more Na is present in the surfaces of the films, the more Se is available for the film to growth. In this regard, Ishizuka et al. have reported the change in preferred orientation with the variation of the available Se during the deposition of CIGSe films by 3-stage process [4]. They reported a decrease of the (112) preferred orientation with the increase of the available Se. The high availability of Se could be one reason of why samples exposed to air for a long period of time and with a high probability of having large quantities of sodium (due to the catalytic effect), have a less (112) preferred orientation. Nevertheless, if the high content of sodium within the CISe film is considered, the observed results are contrary to the ones reported by Couzinie and Kessler et al. [20,34]. In their studies, they reported the development of CIGSe films with an (112) orientation promoted by the presence of sodium within the absorber.

Table 5.8 Lotgering factors (F(hkl)) of the $CuInSe_2$ films deposited with reference, 1h and 24h air-annealed In_2Se_3 precursor films.

Sample ID	CISe-400°C Ref	CISe -400°C 1h	CISe -400°C 24h
F(112)	0.36	0.24	0.15
F(204)	0.02	0.05	0.07
F(220)	-0.18	-0.14	-0.14
F(101)	-0.01	-0.01	-0.01
F(103)	0.0	0.0	0.01
F(211)	-0.01	-0.01	-0.02
F(116)	0.0	0.01	0.02
F(312)	-0.07	-0.07	-0.08

Considering all previous results, it is possible to observe that the air- annealing of In_2Se_3 precursor films has an impact in the morphological (e.g. voids formation) and structural (e.g. change of preferred orientation) properties of the final CISe layers. The FWHM values and the grain size obtained after the recrystallization of the layers seem not to be importantly affected by the annealing process. The interaction of sodium and oxygen could promote different changes in the CISe film. Nevertheless, a confirmation of the relation between these two elements is necessary to further understand the obtained results. In relation to this, the next section is dedicated to confirming the observed results.

5.1.2.1.3 X-ray photoelectron spectroscopy study of the air-annealed In_2Se_3 precursor films

To have a explore and confirmation the interaction of sodium and oxygen in the precursor layer, the surfaces of the In_2Se_3 films were studied by X-ray photoelectron spectroscopy (XPS). With objective of distinguish the change in the signal of the samples, the analyses

were carried out on the In_2Se_3 reference and In_2Se_3 24h air-annealed films. It is important to highlight that the analyzed samples were not kept it in any inert atmosphere (previously to the measurements), thus they were exposed to open-air atmosphere. Hence, the nature of the species observed in XPS will be closer to those actually involved in the phenomena observed in this work. The surface analyses were performed by X-ray photoemission spectroscopy (XPS) in a Kratos Axis Nova with a monochromatic Al K radiation (1486.6 eV) and 20 eV pass energy with an energy step of 0.1 eV. The C1s signal from adventitious carbon with a binding energy E_B = 284.6 eV was used for energy referencing. The peak fit analysis was performed using the CasaXPS software where a linear background was subtracted from the spectra. The spectra were fitted by peaks with a Gauss (60%)–Lorentz (40%) profiles. In this study, Wagner plots were use as a tool for the identification the different compounds formed during the annealing [52]. To further identify the compounds, the Auger Lines In M4N45N45, Se L3M45M45, O KVV and Na KL23L23 are employed. Considering that the CISe samples studied in this work were prepared from In_2Se_3 precursor films partially exposed to air (i.e. interrupted 3-stage growth process), two XPS measurements were carried out. First, the In2Se3 reference and 24h layers without any surface cleaning process were measured. In the following, these samples are referred as “unclean” films. Finally, an etching of the surfaces was carried out for 1 min in order to remove the first 70 nm of the film surface and the measurements were retaken. The last samples are indicated as “clean” films in the subsequent text.

Figure 5.11 shows the In3d core level spectra recorded from the unclean reference and 24h annealed In_2Se_3 films. The reference film (Figure 5.11a) exhibited a In $3d_{5/2}$ peak with a binding energy E_B=444.55 eV corresponding to the In_2Se_3 compound [49]. The Figure 5.11b shows two peaks at E_B=444.17 eV and E_B=444.92 eV which could correspond to In metallic and to a In_2O_3 compound [53,54], respectively.

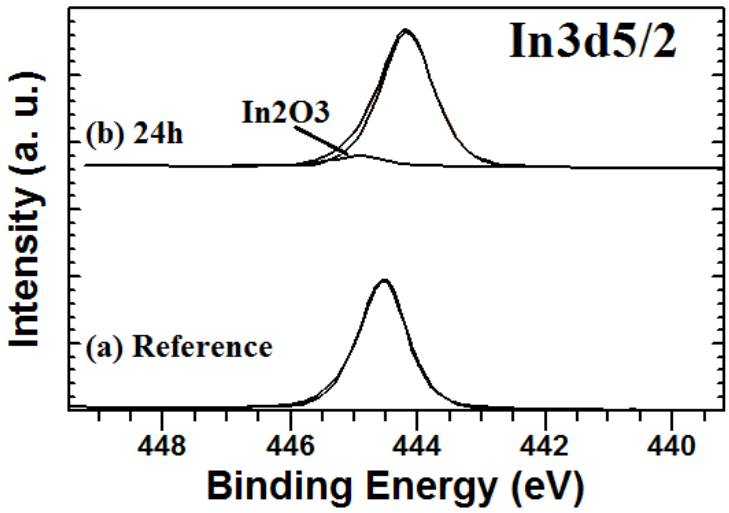

Figure 5.11 In3d spectra of the In_2Se_3 films, (a) reference and (b) 24h air-annealed.

The Figure 5.12 exhibits the spectra of the Se3d from the bare reference and 24h annealed In_2Se_3 films. It is worth to mention that both films showed a broad Se3d peak which contains two set of doublets. The main doublet of the two samples corresponds to the $3d_{5/2}$ (E_B=53.69 eV) and $3d_{3/2}$ peak (E_B=54.49 eV), which could be related to the In_2Se_3 phase. These two peaks arise from the spin-orbit splitting of the 3d electrons. The secondary doublets for both samples, with $E_B(3d_{5/2}/3d_{3/2})$= 54.52/55.32eV, could be related to elemental selenium (Se^0) [55,56]. It is important to mention that the selenium could be oxidized in the form of Se^0, Se^{+4} and Se^{+6} [51]. The presence of Se^0 in both samples signifies that selenium is oxidizing in the two in2Se3 reference and 24h samples. However, difference in the intensities of the Se^0 components relative to the In2Se3 components (dashed lines in Figure 5.12) shows a higher proportion of the Se^0 in the samples annealed for 24 hours. This could indicate a higher oxygenation of the annealed sample. Further confirmation of the last assumption is the development of the peak at around E_B=59.78 eV, which is clearly higher than the one present in the reference sample. The peak can attributed to formation of SeO_2 [46,51,55]. Braunger et al. also reported that this peak could originates from the 3d-emissions of the Se oxidized in the form Se^{+4} and Se^{+6} [51]. Finally, the Se3d spectrum of annealed sample (Figure 5.12b) shows the emergence of a peak at E_B=63.3 eV related to Na2s. This is an important observation given that the appearance of sodium at the surface after air annealing is an

evidence that the sodium is effectively involved in the oxygenation process. The appearance of Na2s peak could confirm, up to some extent, the catalysis effect between sodium and oxygen on the surface of the grains.

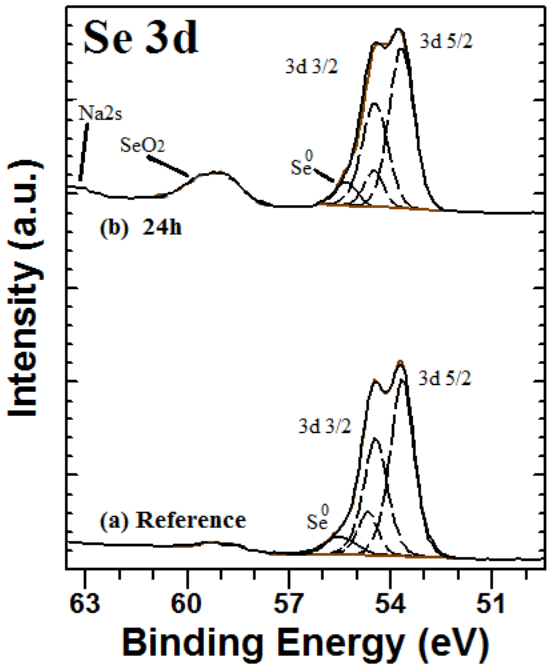

Figure 5.12 Se3d spectra of the In_2Se_3 films, (a) reference and (b) 24h air-annealed.

Figure 5.13 shows the O1s core level spectra recorded from the surface of the unclean In_2Se_3 precursor films. The O1s peak obtained from reference and 24h samples surface could be separated into at least two sub-bands. The peak at higher binding energy is characteristic of surface contaminated by oxygen from air (i.e. physisorbed). The peak at lower E_B corresponds to the oxygen bonded to a metal (i.e. chemisorbed) [54]. For the reference sample (Figure 5.13a), the peaks are located at E_B=531.23 eV and E_B=529.64 eV. Given that in the reference sample there is no trace of In-O bond in the In3d spectrum (Figure 5.11), the peaks could correspond to OH groups and to Na_2O, respectively [57,58]. For the 24h sample (Figure 5.13b), the peaks are located at E_B=530.87 eV and E_B=529.48 eV. In this case, the peaks could correspond to oxygen/OH atoms and to In-O bonding [57,59]. Indeed, the oxygen bonded to indium match with the In_2O_3 related peak observed in the In3d spectrum of the annealed sample (see Figure 5.11b).

Considering the relation between each component (dashed lines in Figure 5.13), it is possible to observe that chemisorbed species (i.e. component at low E_B) are preferable formed in samples subjected to thermal oxidation, rather than in a native oxidation. Comparison between the O1s signals of In2Se3 reference and 24h films shows a higher peak in the surface of the annealed sample, indicating a major content of oxygen.

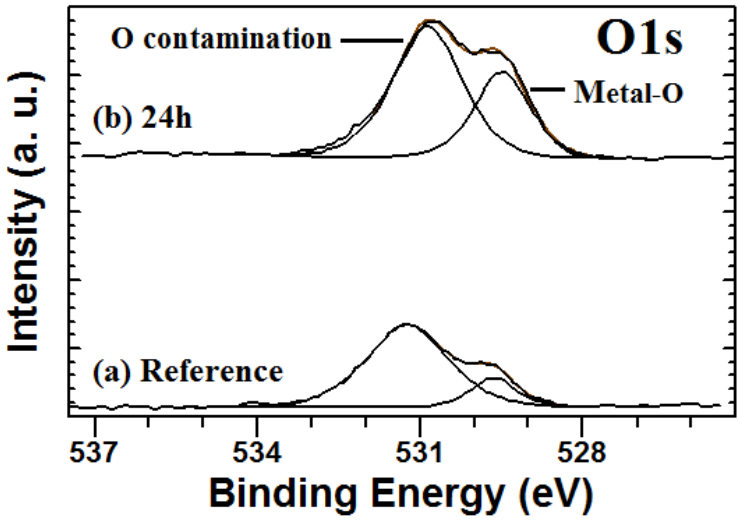

Figure 5.13 O1s spectra of the In_2Se_3 films, (a) reference and (b) 24h air-annealed.

Figure 5.14 shows the Na1s core level spectra on the surface of the In_2Se_3 precursor films. The Na1s peak could be conformed by three components. The position of the components at E_B=1071.23 eV and 1071.78 eV could be related to pure Na and to Na_2CO_3, respectively [51]. Würz et al. have also seen the presence of $NaCO_3$ compound on the surface of native oxidized chalcogen samples [46]. The component at E_B=1072.94 eV is maybe associated with the formation of Na_2O [46]. The Na1s peak of the In2Se3 annealed sample show two components, E_B=1071.0 eV and 1071.69, which also could be related to Na_2SeO_3 and $NaCO_3$, respectively [52]. As mentioned in the Section 5.1.2.2, the formation of Na_2SeO_3 can be linked to the presence of a Na_2Se_x compound working as Se reservoir [51]. Comparison between the Na1s signals of In_2Se_3 reference and 24h films shows a higher content of Na on the surface of the air-annealed sample.

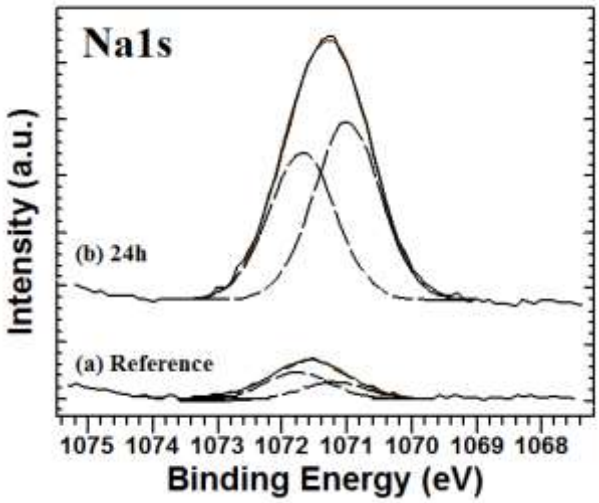

Figure 5.14 Na1s spectra of the In_2Se_3 films, (a) reference and (b) 24h air-annealed.

After having identified some compounds formed on the surface of the In_2Se_3 reference and 24h air-annealed unclean films, the same samples are studied after etching 70nm of the film surface.

Figure 5.15 shows the In3d core level spectra recorded from the clean reference and 24h annealed In_2Se_3 films. The reference and 24h films exhibited a single In $3d_{5/2}$ peak with a binding energy E_B=444.62 eV and 444.54 eV corresponding to the In_2Se_3 compound [49]. After etching the surface of the samples, there is no clear traces of In-O bonds.

The Figure 5.15 exhibits the spectra of the Se3d from the clean reference and 24h annealed In_2Se_3 films. Both films showed a broad Se3d peak which contains two set of doublets. The main doublet of the two samples corresponds to the $3d_{5/2}$ and $3d_{3/2}$ peak, which is related to the In_2Se_3 phase. The secondary doublets for both samples, could be related to elemental selenium (Se^0) [55,56]. The presence of Se^0 in both samples could indicate that the oxidation of Se still occurs at 70 nm from the surface. The difference in the intensities of the Se^0 components relative to the In2Se3 components (dashed lines)

still shows a higher proportion of Se^0 in the samples annealed for 24 hours. Nevertheless, there is no traces of the peak related to SeO_2, Na_2SeO_3 or Na2s, which may imply an important decrease of the oxygenation of the films at a depth of 70 nm.

After surface etching, the O1s peak of the reference sample was almost removed (Figure 5.15). The remaining peak at E_B=529.9 eV could be related to surface oxygen [58]. The O1s peak of the 24h clean sample can be separated into two sub-bands. The peak at low binding energy component could be characteristic of Na_2O bond, whereas the peak for the high binding energy component is may be related to surface oxygen [58].

The Na1s core level spectra on the clean surface of the reference and 24h annealed In_2Se_3 precursor samples were recorded. After etching the reference film, it is noticeable that the sodium was completely wiped out from the top of the film (~70 nm). The Na1s peak of annealed film showed components related to Na_2O and Na_2SeO_3. The presence of this last compound can be associated to the elemental selenium (Se^0) observed in the Se3d peak in 24h clean film (Figure 5.15).

The XPS results of films without surface etching showed the several species formed during the air exposition of the In_2Se_3 precursor layers. The results showed a relation between the O1s and Na1s signals, where the higher the sodium signal, the higher the of oxygen peak. This relation can be an evidence of the catalytic effect between oxygen and sodium reported by Kronik et al. [45]. The highest peak intensities of sodium, oxygen and oxide products are presented by the sample annealed in air. The intensity of a peak is correlated to the amount of oxide products formed during the air exposure. Further more, it is possible to observe a relation between the increased intensities of the sodium and oxygen peaks with those of the oxidized Se (Se^0, Se^{+4}, Se^{+6}). In fact, Brainger et al. proposed the appearance of Se^0 and Se^{4+} due to the reaction of Na_2Se_x with O_2 [51]. The Na_2Se_x on the surface and grain boundaries of the films serve as source of selenium and hence plays an important role on the morphological and structural properties of CISe absorbers layers during its growth. The presence of Na_2Se_x might supports the results observed in Section 5.1.2.2 regarding the decrease of (112) preferred orientation of CISe

films with increasing air-annealing time of In_2Se_3 precursors. Among the most important species formed during oxygenation process, it is possible to find the In_2O_3, elemental selenium, Na_2SeO_3. The presence of In_2O_3 compound may be related to the passivation of Se vacancies (V_{Se}), which might be beneficial or detrimental to solar cell operation depending on its location [44,60]. The elemental selenium in CISe has been identified as a detrimental factor leading to the reduction of open voltages and fill factors [61]. The interaction between the Na and O is an important aspect since this promotes the passivation of grain boundaries and create a reservoir of Se for the film to growth [45,51].

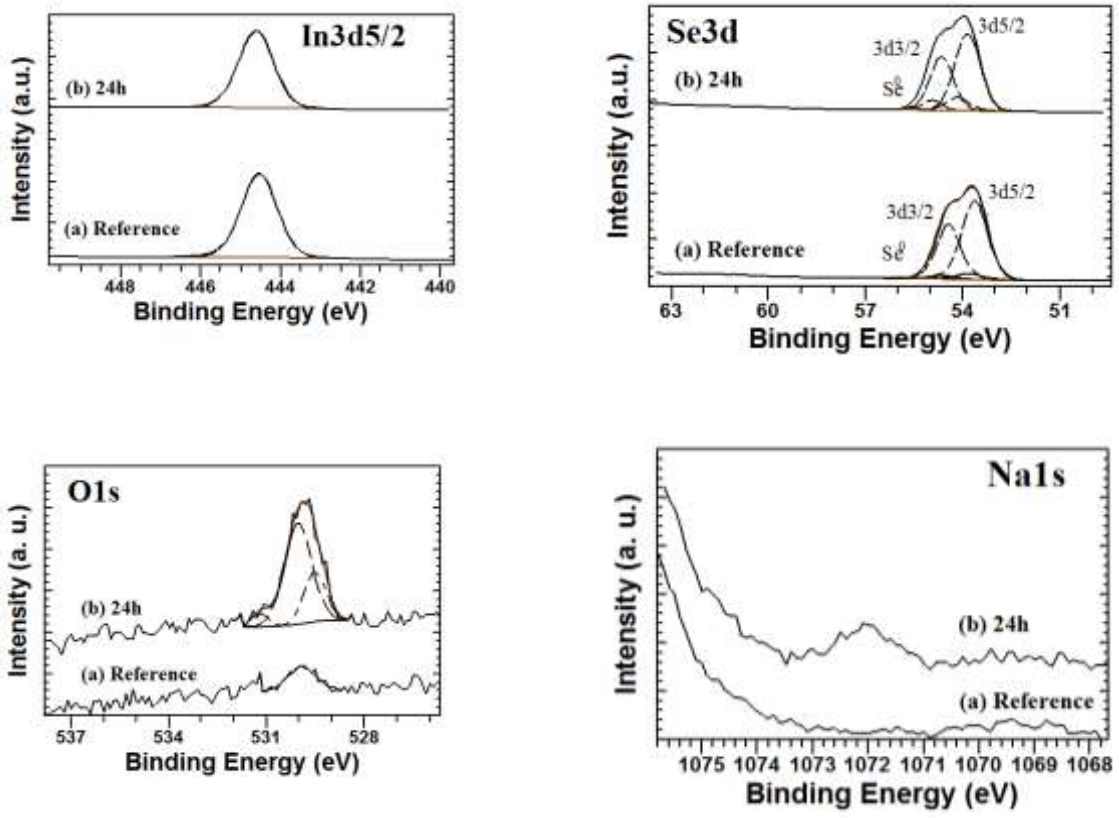

Figure 5.15 XPS measurements of etched In_2Se_3 films, reference and 24h air-annealed.

The XPS measurements of the etched In_2Se_3 films showed that the oxygen, sodium, and the related species, are mostly located on the surface of the layers (within few

nanometers). This means that the air exposed surface can be treated either by a chemical or plasma treatments, and thus remove an important quantity of compounds formed during the oxygenation of the samples (e.g In_2O_3, Na_2O, Se^0) which could affect the the properties of CISe final films and the performance of solar cells. As an illustration of the magnitude of the change suffered by the etching of samples, Figure 5.16 shows the comparison of O1s spectrum of the 24h air-annealed films with and without surface etching. As mentioned before, the important decrease in the intensity of the peak observed after the etching process is related to an important decrease of oxygen content. Similar behavior is observed for the Na1s signal. To further confirm the location of sodium in the film, the figure 5.16c shows the depth analysis of the In2Se3 layer annealed in air for 24h. The analysis was performed each 70nm depth, approximately. The depth analysis confirms the presence of Na preferably on the surface of the film. Even though most of the oxide species are eliminated during the etching, some species such as Na_2O, Na_2SeO_3 and Se^0 are still present. These compounds still could affect the properties of CISe films and the corresponding solar cells.

Having identified the different species (e.g. oxygen, sodium) that probably interact during the growth of the CISe absorber layers, the next aspect to investigate is the manner in which these spices affect the operation of the solar cells. The next section presents the results of the solar cells using the CISe absorber film obtained from the oxidized In_2Se_3 precursor layers.

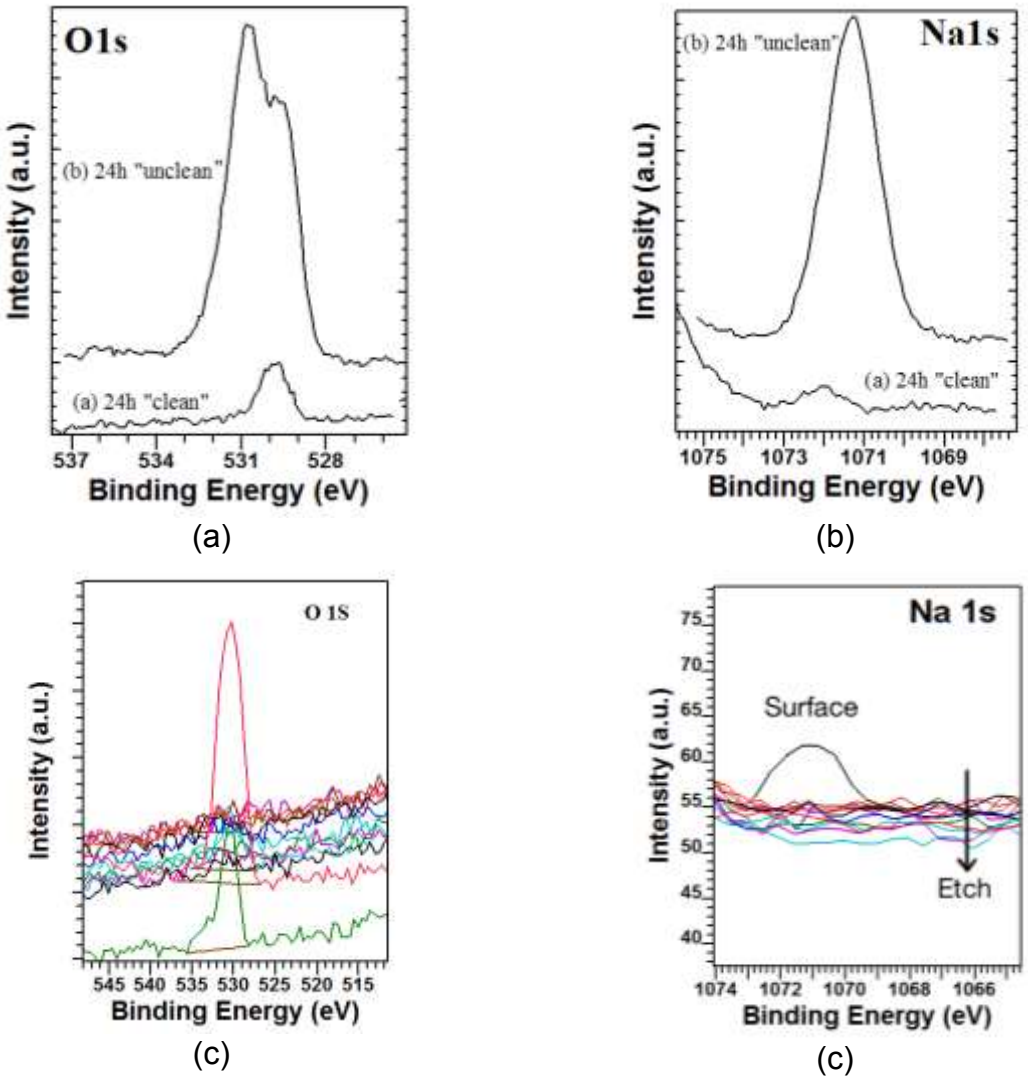

Figure 5.16 The O1s (a) and Na1s (b) spectra of the 24h air-annealed In_2Se_3 films without (unclean) and with (clean) etching. The Na1s depth analysis (c) of annealed film.

5.1.2.1.4 $CuInSe_2$-based solar cells

Figure 5.17 shows current-voltage measurements (J(V)) of the solar cell based on the CISe grown from the 400ºC-In_2Se_3 precursor films Reference (un-annealed), 1h and 24h air-annealed layers (see Section 5.1.2.1). In the next, the results are presented in terms of mean values of typically eight cells per box-and-whisker plot. The open-circuit voltage (V_{oc}) showed a maximum value for the reference solar cells (461 mV). After 1h annealing,

the V_{oc} decreased 33 mV to be finally positioned at 428 mV, whereas the V_{oc} of 24h samples rested almost stable (430 mV) in comparison with 1h annealed sample. The fill factor (FF) showed a similar trend, where the reference sample showed the maximum value (69%) and the 1h and 24h solar cells were stabilized at around 65%. The short-circuit current density (J_{sc}) displayed a different tendency with similar values for the reference and 1h annealed cells (37.1-37.4 mA/cm^2), and a degraded J_{sc} value (34.9 mA/cm^2) for the 24h air-annealed sample. The corresponding efficiencies (η) revealed a continuous degradation with increasing annealing time.

Considering the formation of CISe films starting from the oxidized In_2Se_3 precursor, there is evidence from XPS measurements concerning the emergence of sodium and oxygen on the surface of the oxidized In_2Se_3 precursor film. The XPS results showed the consequent formation of In_2O_3, among other compounds promoted by oxidation of species such as Na_2O, Na_2SeO_3, Se^0. Similar compounds formation have been reported for CISe and CIGSe films [46,49,62]. Given these results, the oxidized surface could be seen as a reservoir of oxygen and sodium, similar to a post-deposition treatment strategy commonly use for Na incorporation [41,42]. Indeed, Wit at al. have shown the availability of oxygen through the decomposition of In2O3 in vacuum conditions at temperatures between 500-800 ºC [63]. When the Cu+Se and In+Se materials are deposited on the In2Se3 film to complete the CISe layer, the available sodium and oxygen could diffuse all along the final absorber (preferentially through the grain boundaries) [39,64] and promote an in-situ oxygenation during the growth process.

As mentioned in Chapter 2 (section 2.3.4.1), the minimization of current and voltage losses across the grain surface of a CISe-based solar cell could be attained by the passivation of surfaces through its oxygenation. The oxygen passivates the surface dangling bonds related to Se vacancies ($V_{Se,}$ donor defects) in order to form In_2O_3 compounds most probably [44,45]. It was also mentioned before that the oxygen passivation (i.e. O_{Se}) takes place in the interface states at the CdS/CISe interface and grain boundaries (GB's) in the bulk of the film. The passivation of GB's states is beneficial for solar cells given that increases the net acceptor doping concentration in the absorber

layer. The CdS/CISe interface passivation has two repercussions: i) a beneficial effect related to the remove of interface recombination centers and ii) a detrimental reaction associated with the enhancing of interface recombination due to the reduce of positive interface charge (i.e. band bending reduction, increase interface recombination).

The results of the solar cells prepared with oxidized absorbers (Figure 5.17) showed a degradation of its characteristics in comparison with CISe un-oxidized based cells. It is possible to infer that the detrimental effect of the CdS/CISe interface passivation surpasses the outcomes of the beneficial GB's passivation. At 1h annealing of the CISe film, the oxygen and sodium could diffuse through the GB's until some portion of it reaches the surface of the CISe absorber. The oxygen in the surface reduce the positive interface charge and (by passivating the V_{Se}^{2+}) and thus decrease the band-bending at the surface (see Chapter 2 section 2.3.4). The reduced band-bending could promote the drop of open-circuit voltage observed in Figure 5.17. Indeed, Kronik and Rau have reported a decrease in open-circuit voltage and an increase of interface recombination with the reduction of band-bending [44,65]. However, these authors have also reported the restoration of band-bending (along with V_{oc} improvement) of the air-exposed CISe film with the deposition of CdS by chemical bath deposition. The recovery of band-bending comes from the oxygen atoms dissolved in ammonia solution or replaced by sulfur atoms. The difference between the reported results and the current-voltage measurements in Figure 5.17 probably indicates that the removed oxygen from the CISe surface by the CdS-CBD treatment is not enough and that the band-bending is not restored. A complementary reason for the detrimental solar cell characteristics can be the Cu migration promoted by the In-O bonds remaining in the near surface zone. The polar bond $In^{\delta^+} - O^{\delta^-}$ indirectly weakens the Cu-Se bond and stimulate the released of Cu^+ ions, which are directed to the bulk of CISe film by the built-in electric field [66,67]. The migrated Cu+ ions occupy the Cu vacancies (acceptor) and hence decrease the effective acceptor density [44,65]. The almost constant Voc and FF with increasing annealing time could be due to a stable oxygen content at the CISe surface while more oxygen is distributed across the grain boundaries.

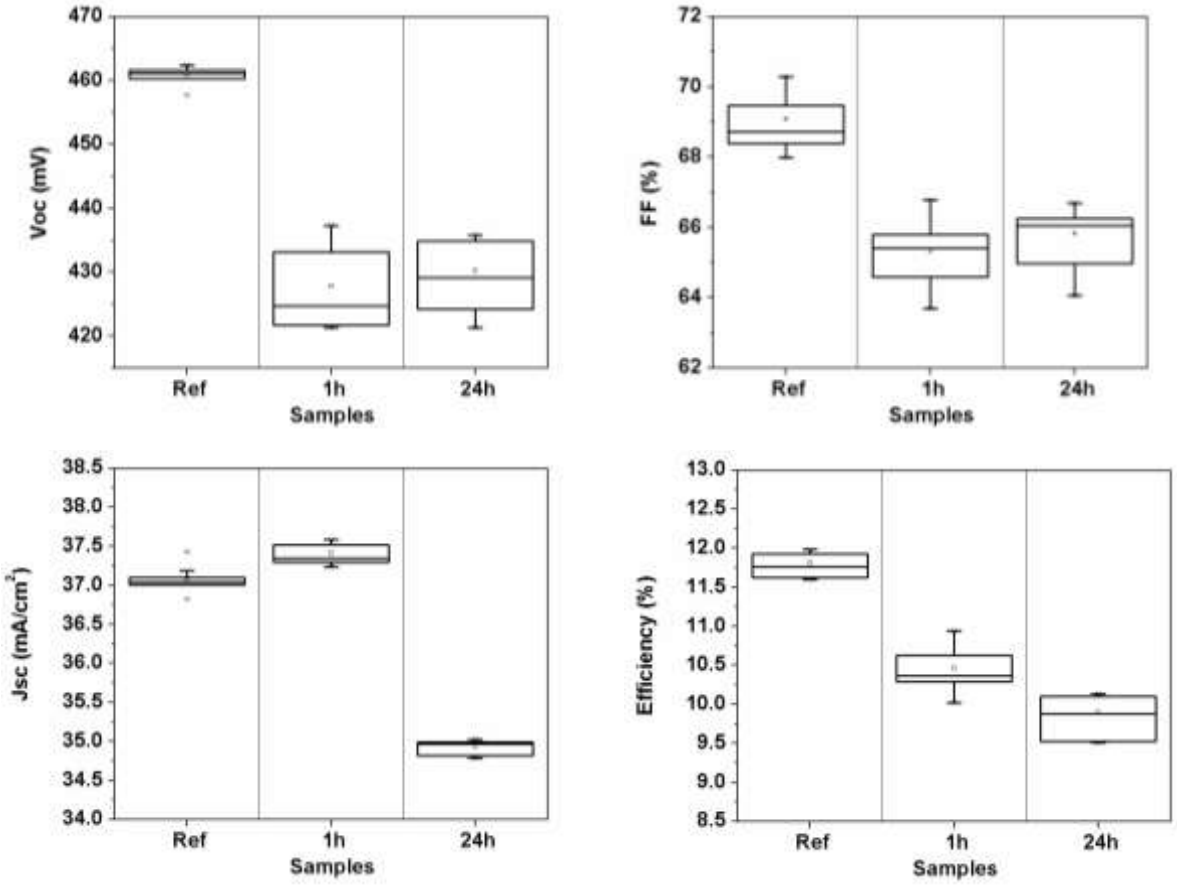

Figure 5.17 Solar cells characteristics for CISe absorbers prepared from the In_2Se_3-400°C precursor films: Reference, 1h and 24h annealed in air at 300°C. The graph shows the minimum, maximum, median and mean values.

Figure 5.18 shows the quantum efficiency (QE) measurements of the solar cells. The CISe reference and 1h air-annealed samples showed similar efficiency, while the 24h annealed cell displayed a decrease in the range of ~700-1200 nm. This last indicates the increase in losses in the 24h annealed CISe solar cell due to an incomplete collection of photogenerated carriers in the absorber. A comparable quantum efficiency of the three samples is observed in the range of ~400-520 nm, which signifies the CdS layer with similar thicknesses. These results match with the observed in Figure 5.17.

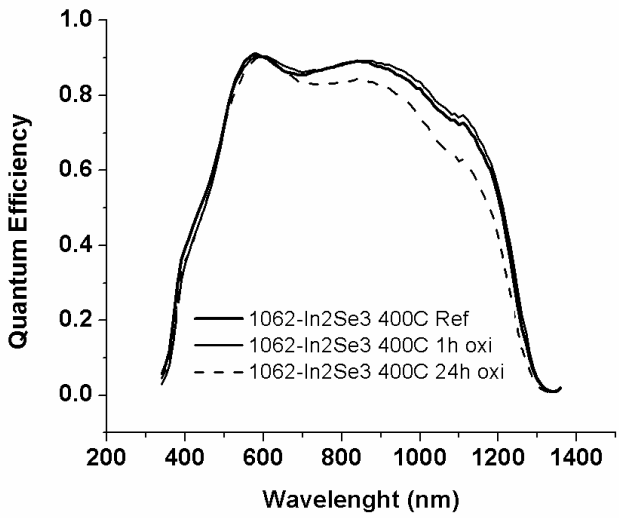

Figure 5.18 Quantum efficiency (QE) measurements of CISe absorbers prepared from the In_2Se_3-400ºC precursor films: Reference, 1h and 24h annealed in air at 300ºC.

From the previous results, it is possible to observe the catalytic effect between sodium and oxygen. These elements could effectively participate in the passivation of defects, especially those related to selenium vacancies (V_{Se}^{++}). In this regard, there are two important aspects to consider. In one hand, is has been reported that sodium and oxygen are preferentially transported through grain boundaries [39]. On the other hand, the capacity of Na and O_2 to passivate defects may depend on how well these elements are distributed along the films. As a matter of fact, a proper distribution of theses elements could decouple the GB's beneficial and CISe/CdS interface detrimental passivation. With this idea in mind, the experiments in the next section intended to show the effect of grain boundaries on the oxygenation of CISe absorber films.

5.1.2.2 Effect of substrate temperature in the oxygenation of In_2Se_3 and $CuInSe_2$ films

5.1.2.2.1 Details of the study

This section explores the effect of grain boundaries density on the oxygenation of $CuInSe_2$ absorbers prepared by the 3-stage growth process. The grain boundary in CISe density

was modified through the variation of substrate temperatures used during the 1st-stage of deposition (see Figure 5.3 and section 5.1.1.2-5.1.1.3). The CISe absorbers were grown in a same deposition run by a bi-thermal 3-stage process, as previously described in this chapter (Section 5.1.2.1.1). Three sets of In_2Se_3 precursors films (~1 μm thickness) were prepared for each substrate temperature, namely, 250°C, 325°C and 400°C. Each precursors were annealed in open air atmosphere at 300°C for 1 and 24 hours. Using these samples, the second and third stage were carried out at the same substrate temperature (i.e. 580°C). The thickness of the final absorbers was similar for all the absorber films (~1.7-2 μm). The supply of indium during the third stage of the growth process was such that the copper ratios (y=[Cu]/[In]) were $0.8 < y < 0.85$ for all the absorbers. The remained deposition details are the same as in Section 5.1.1.1. Finally, the CISe films were used to fabricate the corresponding solar cells with an area of ~0.5 cm^2.

The impact of the air annealing on the films is described at the absorbers level and solar cells through the scanning electron microscopy (SEM), X-ray diffraction (XRD), current-voltage (J-V) and external quantum efficiency (QE) measurements.

5.1.2.2.2 Morphological and structural properties of In_2Se_3 and $CuInSe_2$ films

Figure 5.19 SEM cross-section images of In_2Se_3 reference precursor films deposited at 250°C, 325°C and 400°C and the corresponding CISe absorber layers prepared from the precursor films: Reference, 1h and 24h annealed in air at 300°C. The In_2Se_3 precursor films (Figure 5.19 left) are the ones described previously in this Chapter (section) with grains sizes varying from 0.08 μm to 1 μm with increasing substrate temperature. Consequently, higher number of grain boundaries are observed with the decrease in substrate temperature. The corresponding annealed films (not displayed here) did not show any significant difference in comparison with the reference samples.

As a general overview, the CISe layers (Figure 5.19 right) exhibited an apparent degradation in morphology with increased air-annealing, being the 250°C-CISe sample

the most affected. Furthermore, an improvement in morphology is observed as the 1st-stage substrate temperature increases. The degradation consisted in the formation of voids located near the middle region of the layer thickness (i.e. ~1 μm). In general, a higher number voids are observed with increasing annealing time. As described before, the voids could result from the interdiffusion (trough vacant sites) of Cu_2Se into In_2Se_3 [13,14]. The species that interacts with the surface of the In_2Se_3 precursor film during the annealing of the samples (e.g. oxygen, sodium) may stimulate the appearance of voids by promoting Cu-Se local segregation on the In_2Se_3 film surface at the second step of the growth process. In Figure 5.19, the number of voids in CISe films increases not only with the increment of the annealing time but also with the rise of grain boundaries density (i.e. lower 1st-stage temperature).

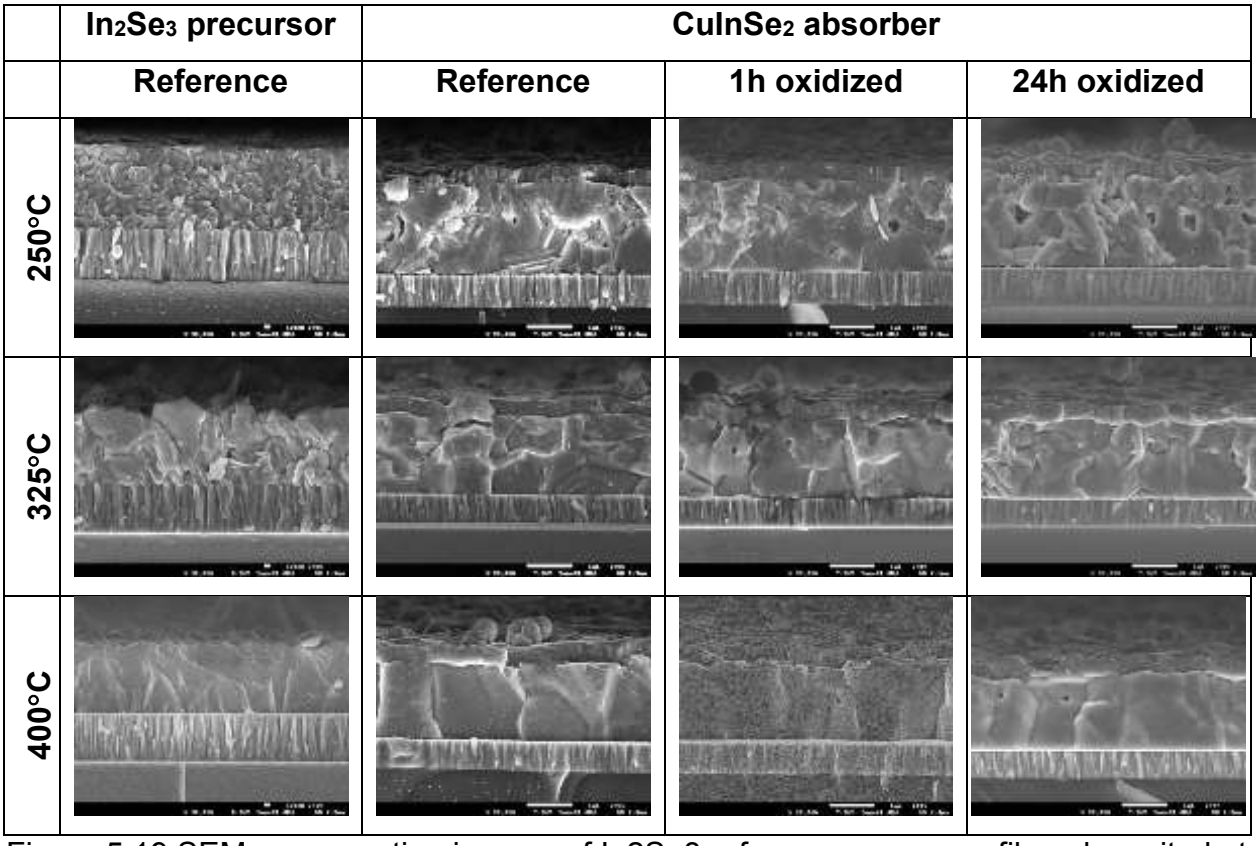

Figure 5.19 SEM cross-section images of In2Se3 reference precursor films deposited at 250°C, 325°C and 400°C and the corresponding CISe absorber layers prepared from the precursor films: Reference, 1h and 24h annealed in air at 300°C.

Figure 5.20, 5.21 and 5.22 shows the XRD patterns of the reference, 1h, and 24h air-annealed In_2Se_3-250ºC, -325 ºC and -400 ºC films, respectively. The XRD patterns were normalized with respect to the (110) peak. The samples did not display a clear difference between the reference and the oxidized samples. The principal planes are related to γ-In_2Se_3 hexagonal phase (JCPDS 40-1407). The In_2Se_3-325 ºC and -400 ºC as-prepared and annealed films showed an (110) preferred orientation, meanwhile the In_2Se_3-325 ºC films displayed a random orientation. The predominant Lotgering factors values for all the samples were quite similar to the observed in Table 5.9. The FWHM values were also very similar to the reported in previous results (Table 5.10), exhibiting a higher crystalline quality with increasing deposition temperature. There is no significant change in the structural properties of the films after the annealing process (indistinctive of the annealing time and deposition temperature).

Table 5.9 Lotgering factors (F(hkl)) examples of the In_2Se_3 films deposited at various temperatures and annealed for 24h. Data from table 5.3.

	In_2Se_3					
Sample ID	250°C	325°C	400°C	250°C-24h	325°C-24h	400°C-24h
F(110)	-0.08	0.36	0.47	-0.09	0.35	0.49
F(006)	-0.02	-0.07	-0.11	-0.03	-0.05	-0.10
F(300)	-0.20	0.0	0.10	-0.18	0.01	0.12
F(101)	---	0.0	0.024	---	0.0	0.01
F(102)	---	-0.02	-0.04	---	-0.01	-0.03
F(105)	0.38	---	-0.01	0.31	---	-0.0
F(113)	0.03	0.0	-0.02	0.03	0.0	-0.01
F(201)	---	-0.01	0.02	---	-0.02	0.02
F(202)	---	0.0	-0.07	---	0.01	-0.05
F(116)	-0.05	-0.07	-0.09	-0.04	-0.05	-0.07
F(215)	---	-0.02	-0.03	---	-0.02	-0.02
F(208)	---	-0.04	-0.05	---	-0.03	-0.05
F(306)	-0.13	-0.06	-0.10	-0.15	-0.07	-0.12
F(218)	---	-0.04	-0.04	---	-0.02	-0.05

Table 5.10 Full width at half maximum (FWHM) and crystallite size values of the In_2Se_3 films deposited at different temperatures and annealed for 24h. Data from table 5.4.

Sample ID	FWHM (°) Reference	FWHM (°) 24h	Crystallite size (nm) Reference	Crystallite size (nm) 24h
	(110)	(110)	(110)	(110)
In_2Se_3-250°C	0.17	0.18	47	45
In_2Se_3-325°C	0.09	0.09	93	90
In_2Se_3-400°C	0.07	0.07	117	116

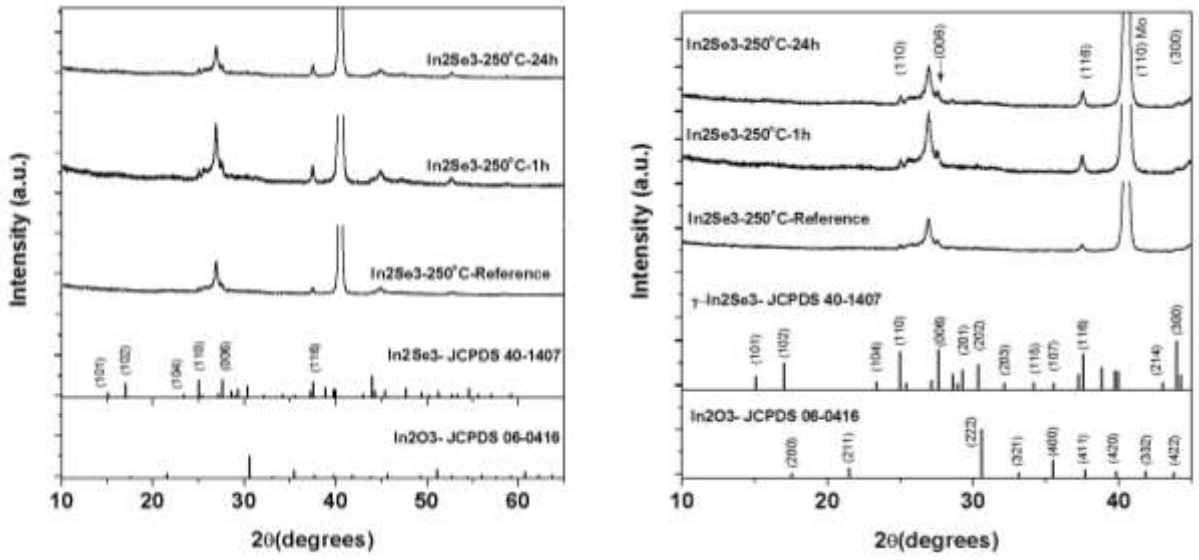

Figure 5.20 XRD patterns of In_2Se^3-250ºC (a) reference, 1h and 24h air-annealed films and (b) a zoomed region of the same pattern.

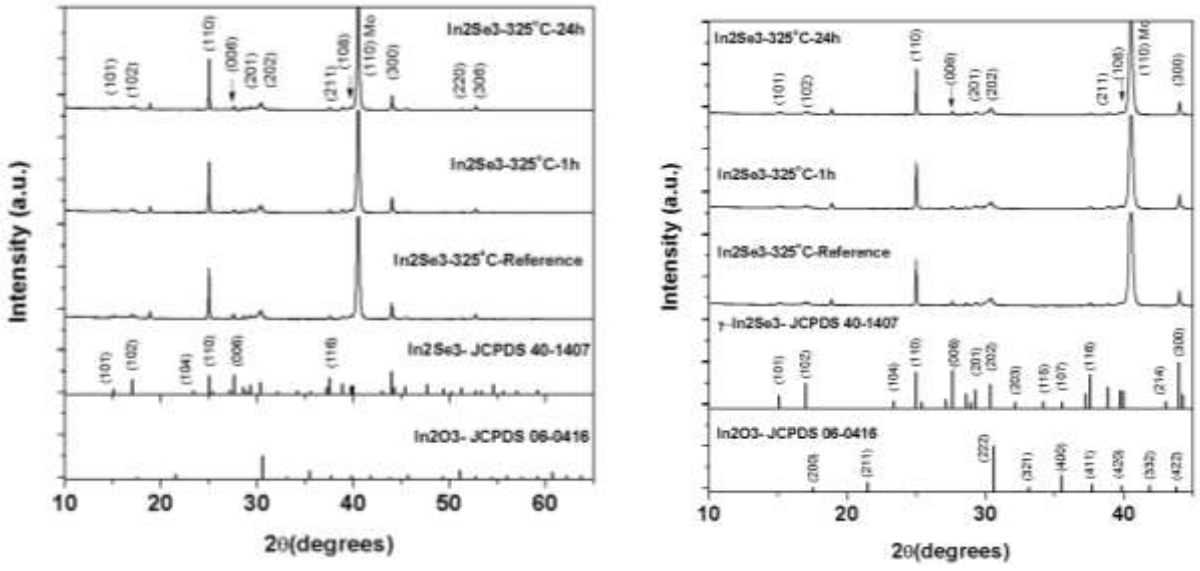

Figure 5.21 XRD patterns of In_2Se_3-325ºC (a) reference, 1h and 24h air-annealed films and (b) a zoomed region of the same pattern.

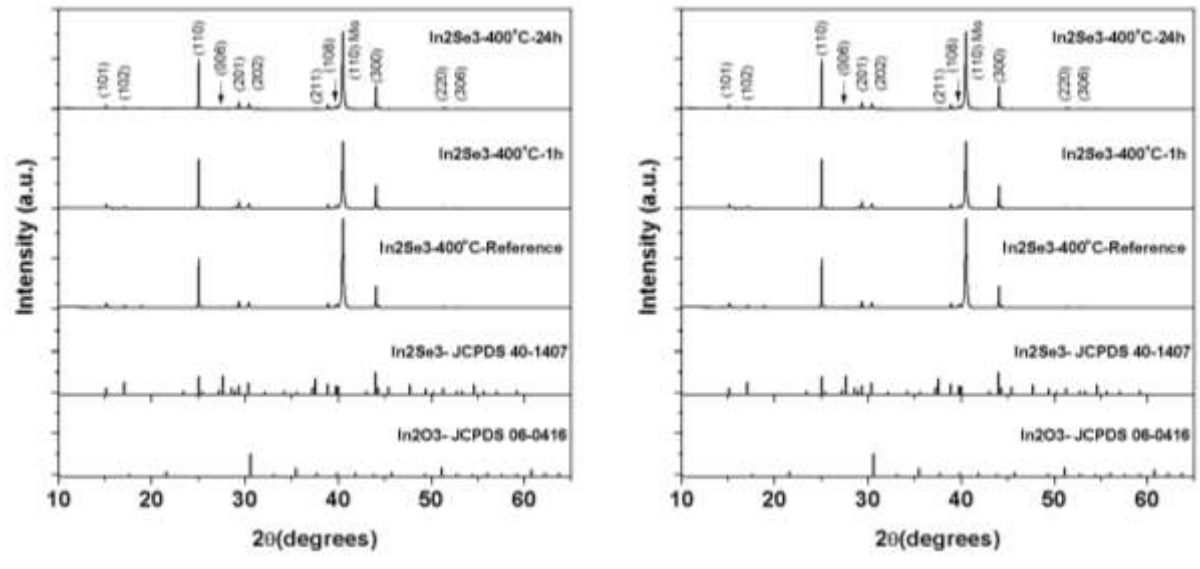

Figure 5.22 XRD patterns of In_2Se_3-400C (a) reference, 1h and 24h air-annealed films and (b) a zoomed region of the same pattern.

Figure 5.23,5.24 and 5.25 displays the XRD patterns of the CISe absorber films prepared with the reference and 24h air-annealed In_2Se_3-250ºC, -325 ºC and -400 ºC layers. The XRD of the samples were normalized with respect to the (112) peak. The pattern of the 1h annealed films (not shown) exhibited very similar characteristics in comparison with the other two samples. All the samples showed the formation of chalcopyrite-like $CuInSe_2$ compounds denoted by the crystallographic planes (101), (112), (103), (211), (105), (213), (204)/(220), (116)/(312) and (305)/(323) (JCPDS 40-1487). There was no evidence of oxide compounds formation (e.g. In_2O_3) possibly promoted by the oxygenation of the precursor layers. The presence of (101), (103) and (211) plane shows the development of a material with an ordered cation sublattice even for oxidized films [33]. The XRD pattern also showed the presence of (116)/(312) doublet for all the CISe samples indicating well-ordered atoms in the chalcopyrite phase [33]. Nevertheless, the doublets are more developed as the 1st-stage substrate temperature increases, which indicates a material with higher quality.

Table 5.11 Full width at half maximum (FWHM) and crystallite sizes values of the CISe films deposited at different 1st-stage temperatures.

Sample ID	FWHM (°) Reference	FWHM (°) 24h	Crystallite size (nm) Reference	Crystallite size (nm) 24h
	(112)	(112)	(112)	(112)
CISe-250°C	0.07	0.08	117	102
CISe-325°C	0.06	0.06	136	136
CISe-400°C	0.06	0.06	136	136

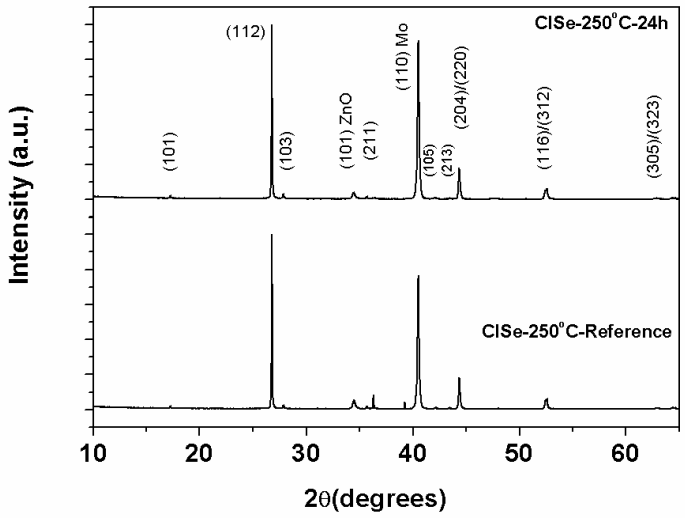

(a)

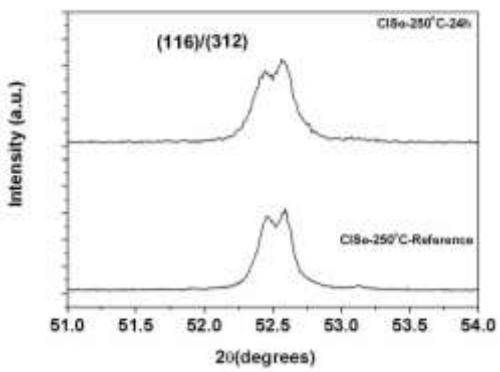

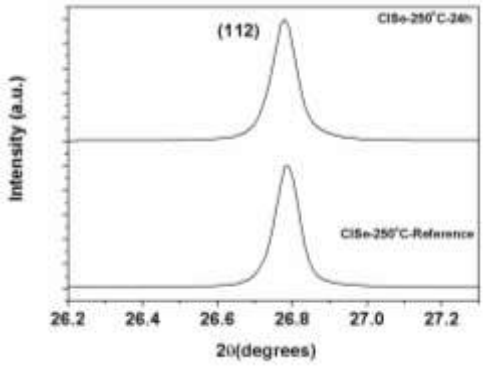

(b) (c)

Figure 5.23 XRD patterns of (a) CISe thin films deposited on SLG/Mo substrates with reference and 24h air-annealed In_2Se_3 -250°C precursor films and zoomed regions of (b) the (116)/(312) and (c) the (112) peaks.

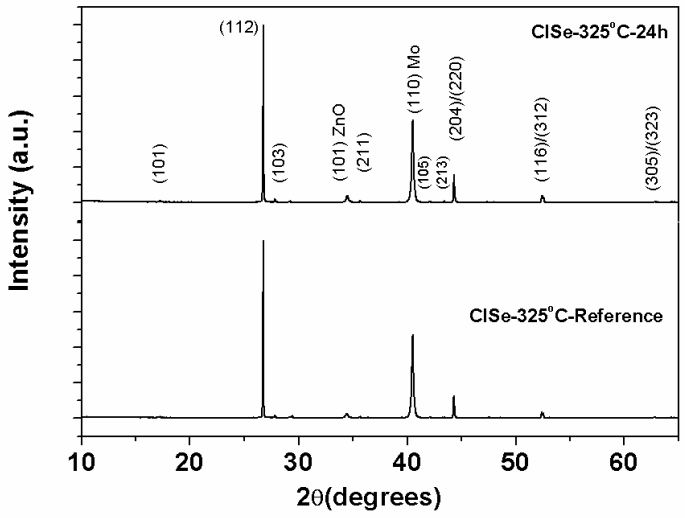

(a)

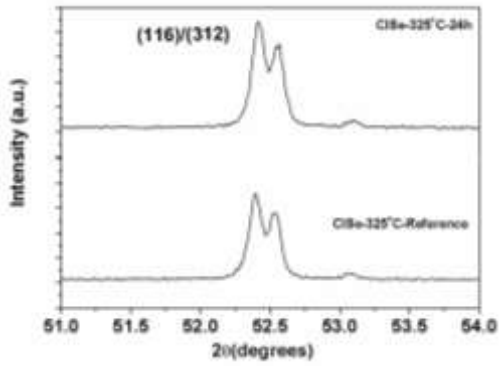

(b)

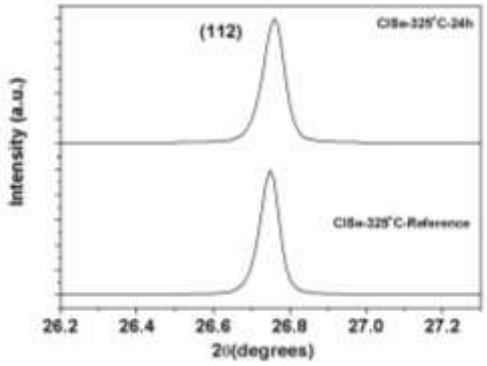

(c)

Figure 5.24 XRD patterns of (a) CISe thin films deposited on SLG/Mo substrates with reference and 24h air-annealed In_2Se_3 -325°C precursor films and zoomed regions of (b) the (116)/(312) and (c) the (112) peaks.

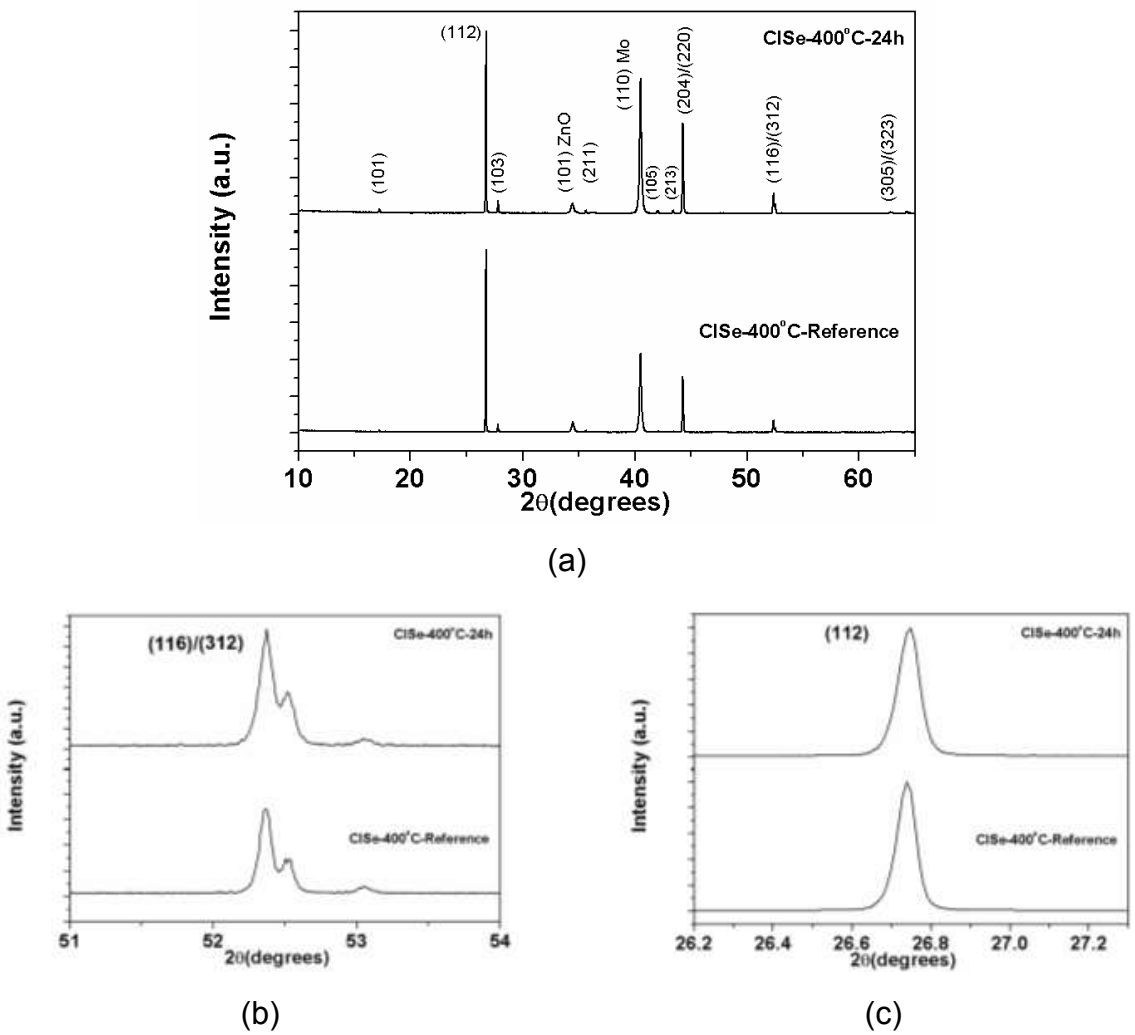

Figure 5.25 XRD patterns of (a) CISe thin films deposited on SLG/Mo substrates with reference, 1h and 24h air-annealed In_2Se_3 -400°C precursor films and zoomed regions of (b) the (116)/(312) and (c) the (112) peaks.

As in the previous results, the full width at half maximum values of oxidized CISe layers was very similar to the reference films (Table 5.11). Although the SEM image of the CISe layers (figure 5.19) suggested a difference in morphology of reference and annealed films, this difference is not observed while comparing FWHM values.

Table 5.12 Lotgering factors (F(*hkl*)) of the $CuInSe_2$ films deposited with reference, 1h and 24h air-annealed In_2Se_3 precursor films.

Sample ID	250°C-Reference	250°C-24h	325°C-Reference	325°C-24h	400°C-Reference	400°C-24h
F(112)	0.42	0.43	0.61	0.58	0.36	0.15
F(204)	-0.05	-0.03	-0.08	-0.07	0.02	0.09
F(220)	-0.14	-0.12	-0.20	-0.18	-0.18	-0.11
F(101)	0.01	0.0	-0.01	-0.01	-0.01	0.0
F(103)	0.0	-0.01	0.0	0.1	0.0	0.01
F(211)	-0.01	-0.02	-0.02	-0.03	-0.01	-0.02
F(116)	0.0	0.01	0.0	0.05	0.0	0.01
F(312)	-0.07	-0.05	-0.09	-0.06	-0.07	0.04

Table 5.12 shows the textures of the films determined through Lotgering factors (see equation 5.1). It is possible to observe a slight decrease of the (112) preferred orientation with the air-annealing of the sample, except for CISe-250ºC film which is almost constant. The maximum *F*(112) value is attained with the In_2Se_3-325ºC reference sample whereas a randomly CISe oriented film is obtained with In_2Se_3-400ºC layers annealed for 24h. As mentioned before in this chapter, the preferential orientation could be slightly modified by the air-annealing time, even if the precursor films have the same orientation. The most affected samples are the ones deposited at high 1^{st}-stage substrate temperature. This behavior could be related to the interaction of Na, O_2, and Se located on the surface of In_2Se_3 films and how easy they get their way to the surface of the precursor layer. Considering all the previous results, the crystallinity of the CISe films do not significantly change after the annealing process (same phase, similar FWHM). Nevertheless, a change in preferred orientation is observed, being the films grown at high 1st-stage substrate temperatures the most affected.

Having identified the morphological and structural properties of the CISe absorber layers, the next step is to investigate how the 1st-stage substrate temperature and the air-annealing of CISe absorber film impact on the corresponding solar cells.

5.1.2.2.3 $CuInSe_2$-based solar cells

Figure 5.26 shows current-voltage measurements (J(V)) of the solar cell based on the CISe absorbers grown from the In_2Se_3-250ºC, -325ºC and -400ºC precursor films un-annealed (Reference), 1h and 24h air-annealed. The next results are presented in terms of mean values of typically 8 cells per box-and-whisker plot. For CISe-250ºC solar cells, the the open-circuit voltage (V_{oc}) graph (Figure 5.26) showed an improvement in V_{oc} for samples annealed in air for 1h. The open-circuit voltage improves from ~395 mV (reference) to 410 mV (1h anneal). Subsequently, the V_{oc} decreases to ~365 mV for longer annealing time. A similar tendency is exhibited by the CISe-325ºC cells, but with a less improvement or even stable V_{oc} (~450 mV) at 1h annealing. At 24h anneal, the voltage is also degraded up to 366 mV. The CISe-400ºC maximum value for the reference solar cells (461 mV). After 1 h annealing, the V_{oc} decreased 33 mV to be finally positioned at 428 mV, whereas the V_{oc} of 24h samples rested almost stable (430 mV) in comparison with 1h annealed sample. The fill factor (FF) showed a comparable trend, with improved values of 62% and 66.5% for 1h annealed CIS-250ºC and CISe-325ºC cells. The CIS-400ºC reference samples displayed the maximum FF value (69%) of all the solar cells, meanwhile the 1h and 24h devices were stabilized at around 65%. The short-circuit current density (Jsc) of CISe-250C cells exhibited a more or less stable value for reference and 1h annealed films (35.2 and 34.7 mA/cm^2, respectively). A degradation is observed (32.7 mA/cm^2) with increasing annealing time. The CISe-325ºC had an enhanced J_{sc} value (35 mA/cm^2) at 1h oxygenation. After 24 hours exposed to air, short-circuit current decrease up to 32 mA/cm^2. The CIS-400ºC showed similar values for the reference and 1h annealed cells (37.1-37.4 mA/cm^2), and a degraded J_{sc} value (34.9 mA/cm^2) for the 24h air-annealed device. The corresponding efficiencies (η) revealed the trend of V_{oc}, FF and J_{sc} of each case. IN general, an increase in V_{oc}, FF and J_{sc} is observed as the 1st-stage substrate temperature increases.

Considering the discussion in Section 5.1.2.1.4 (CISe-400ºC solar cells), the surface and bulk of the CISe absorbers could include oxygen and sodium (most probably in grain boundaries) which promote oxygen passivation (e.g. O_{Se}) [44,65]. The improvements or stabilization of Voc and FF in 1 hour annealed CISe-250ºC and CISe-325ºC cells could be related to a better distribution of oxygen across the grain boundaries (GB's) inside these absorbers (see Figure 5.19). This "enhanced" distribution may promote the passivation of defects (e.g. V_{Se}^{2+}) at the grain boundaries, keeping aside the harmful oxygenation of the CdS/CISe interface. Deterioration of solar cells with 24h annealed absorber may be due to oxygen passivation on the CdS/CISe interface and/or due to an increase in defects concentration (e.g. recombination centers). The SEM image in Figure 5.19 shows the formation of a more defected CISe structure with long air-annealing processes. The degradation of solar cells characteristics of CISe-400ºC sample could be related to a big grains structure with grain boundaries crossing the whole film thickness (from Mo contact to CISe surface), promoting the CdS/CISe interface passivation, and thus surpassing the outcomes of the beneficial GB's passivation.

Figure 5.27 shows the quantum efficiency (QE) measurements of the corresponding solar cells. In general, the CISe reference and 1h air-annealed samples showed similar efficiency, except the CISe-325ºC 1h sample. The 24h annealed cells displayed a decrease in QE in the range of ~700-1200 nm. This last indicates the increase in losses in the 24h annealed CISe solar cell due to an incomplete collection of photogenerated carriers in the absorber. These losses might be involved with the high density of defects created at prolonged air exposure times (e.g. voids, see Figure 5.19). These results well match with the observed in Figure 5.26.

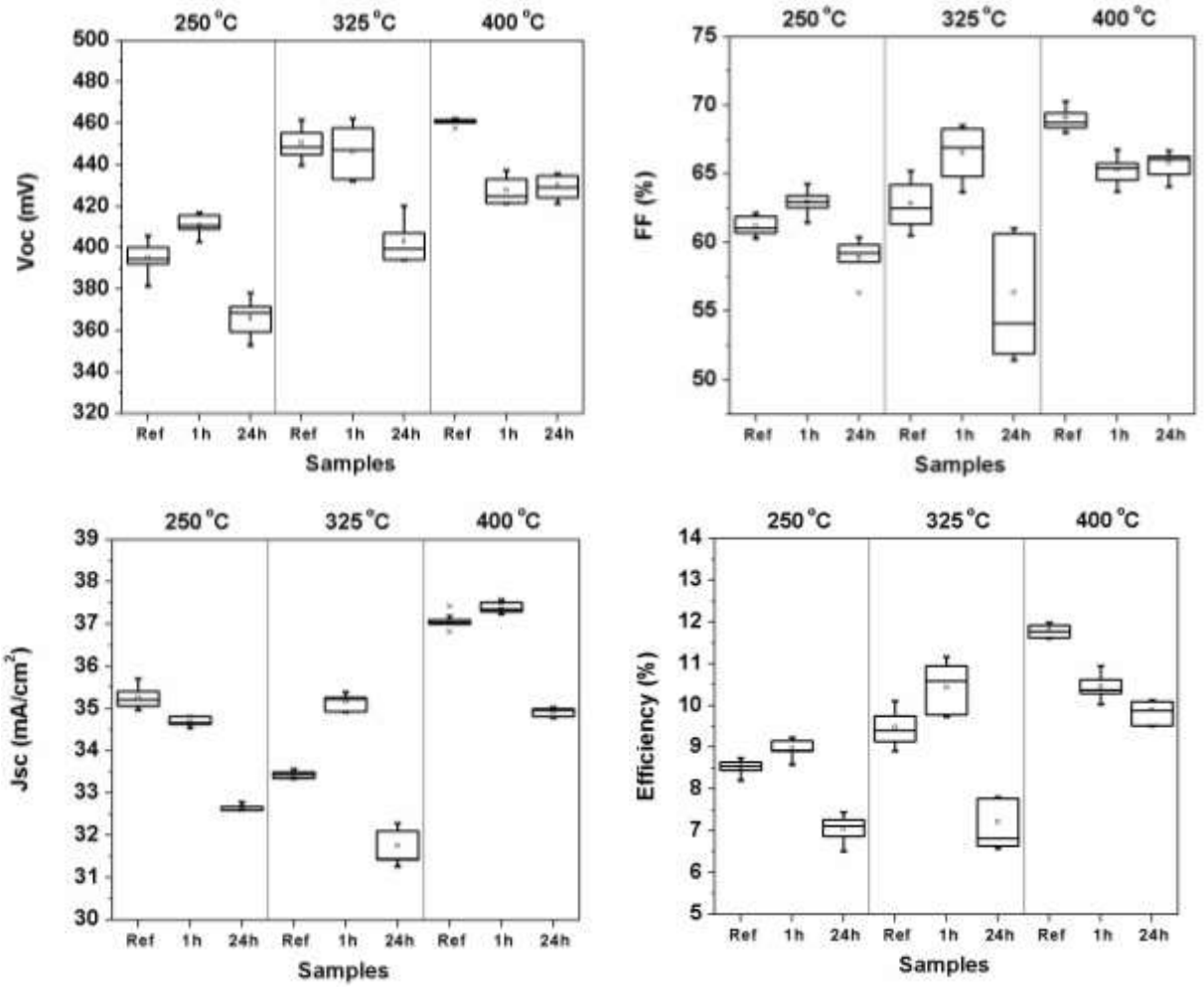

Figure 5.26 Current-voltage measurements of solar cells based on the CISe absorbers grown from the In_2Se_3-250ºC, -325ºC and -400ºC precursor films un-annealed (Reference), 1h and 24h air-annealed. The graph shows the minimum, maximum, median and mean values.

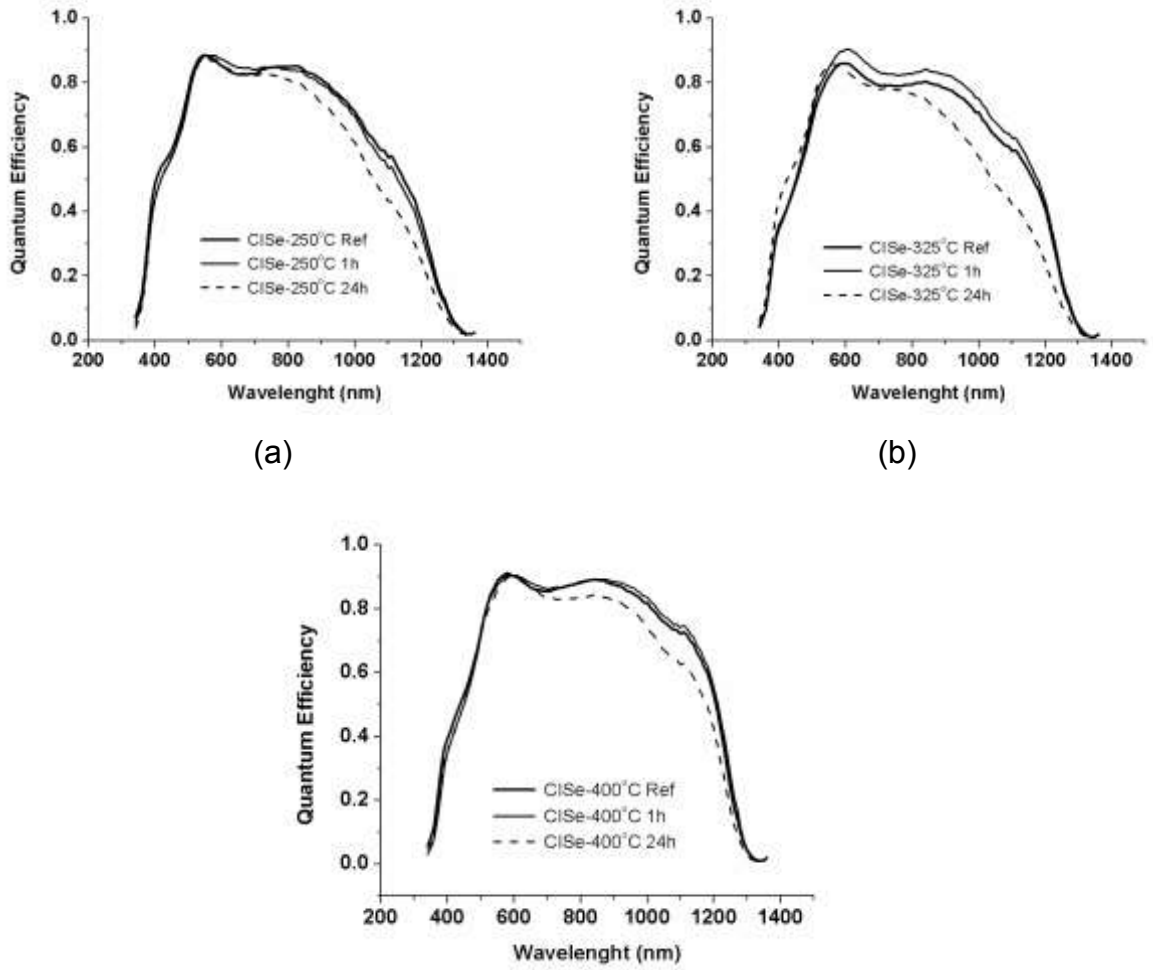

Figure 5.27 Quantum efficiency measurements of solar cells based on the CISe absorbers grown from the In_2Se_3-250ºC (a), -325ºC (b) and -400ºC (c) precursor films un-annealed (Reference), 1h and 24h air-annealed.

Having in mind the above results, it is possible to conclude that the CISe films with a "medium" grain boundary densities, i.e. those observed in samples deposited at 250ºC and 325ºC, are more resilient to moderate exposure to oxygen (i.e. one-hour annealing) in comparison with low GB density absorbers. Hence, concerning oxygenation, a film with a moderate grain size and a certain number of GB`s might be preferable rather than a layer with big grains and a low number of GB's.

The grain boundaries are indeed an important factor participating in the diffusion of oxygen and sodium. Nevertheless, this is not the only factor affecting the distribution of these elements. In fact, the sodium-oxygen catalytic relation itself is a vital aspect during the passivation of defects. With the aim of having a better comprehension of the oxygenation of CISe films, the next experiments focus on the relation between Na and O_2 and its importance.

5.1.2.3 Role of sodium in the oxygenation of $CuInSe_2$ films

5.1.2.3.1 Details of the study

This section examines the effect of sodium on the oxygenation of $CuInSe_2$ absorbers prepared by the 3-stage growth process. The CISe absorbers were grown by a bi-thermal 3-stage process on Mo substrates. To block the diffusion of Na, a Si_xN thin film barrier was deposited on the glass substrate before Mo film growth. Three sets of In_2Se_3 precursors films (namely, reference, 1h and 24h) of ~1 μm thickness were deposited at a substrate temperature of 400°C. Two precursors were annealed in open air atmosphere at 300°C for 1 and 24 hours. Using these samples, the second and third stage were carried out at the same substrate temperature (i.e. 580°C). The thickness of the final absorbers was similar for all the absorber films (~1.7 μm). The supply of indium during the third stage of the growth process was such that the copper ratios (y=[Cu]/[In]) were in the range of $0.79 < y < 0.85$. The remained deposition details are the same as in Section 5.1.1.1. Finally, the CISe films were used to fabricate the corresponding solar cells with an area of ~0.5 cm^2.

The impact of sodium in the air annealing on the films is described at the absorbers level and solar cells through the scanning electron microscopy (SEM), X-ray diffraction (XRD), current-voltage (J-V) and external quantum efficiency (QE) measurements.

5.1.2.3.2 Morphological and structural properties of In_2Se_3 and $CuInSe_2$ films

Morphological properties of In_2Se_3 and $CuInSe_2$ films

The Figure 5.28 displays the cross-sectional SEM images of the reference, 1h and 24h annealed In_2Se_3 precursor layer grown on sodium and sodium-free substrates. The precursor films have similar morphology as the previously mentioned films, consisting of grains with sizes of approximately the entire film thickness (~1 μm). The precursor layers did not show any clear differences between the sodium and sodium-free containing films.

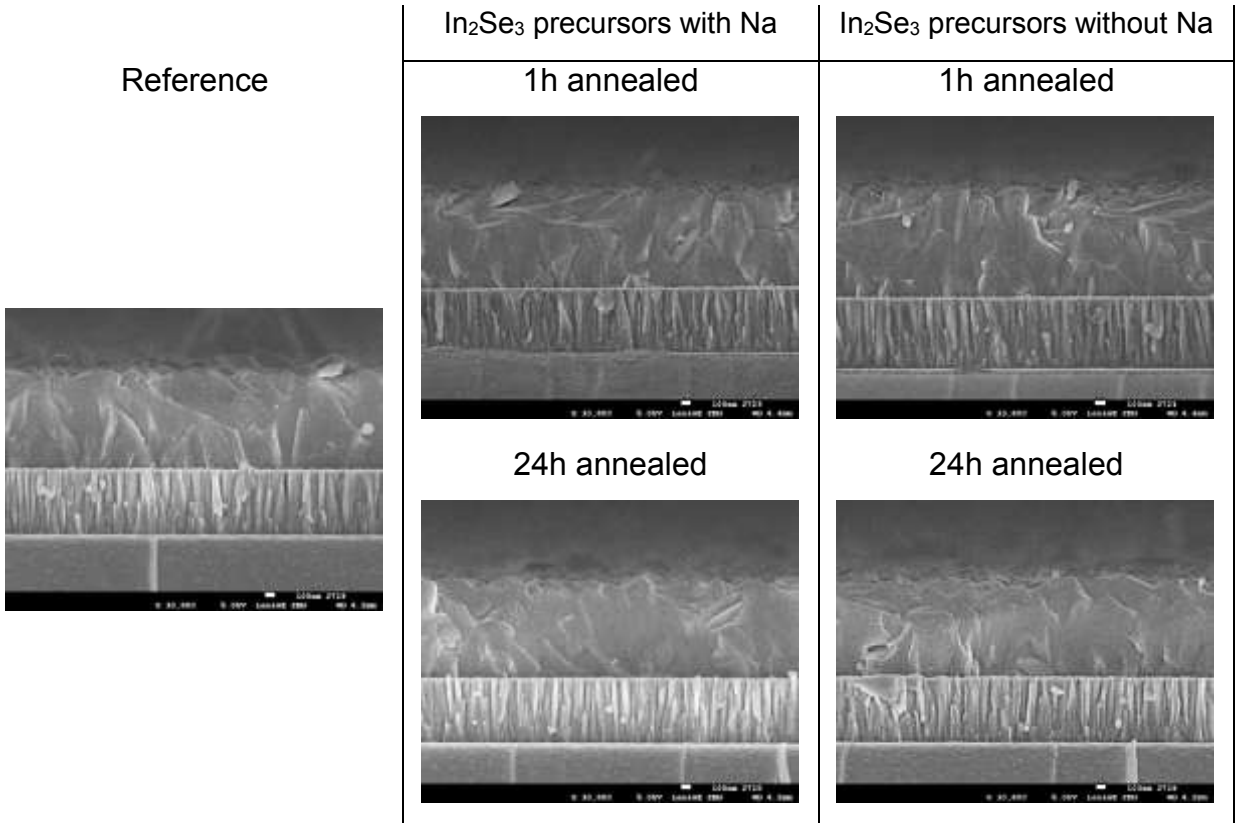

Figure 5.28 SEM cross-section images of In_2Se_3 precursor films deposited at 400°C on sodium and sodium-free substrates: Reference, 1h and 24h annealed in air at 300°C.

The Figure 5.29 shows the cross-sectional SEM images of the corresponding $CuInSe_2$ absorbers. The CISe films deposited on sodium-containing substrates exhibited very similar morphologies with grains sizes of ~1.8 μm. In comparison, the reference CISe Na-

free film is composed of grains with sizes around 1.8 μm, but it s also possible to detect grains with smaller sizes. The 1h and 24h Na-free films showed layers composed of grains with a slight decrease in size. Formation of voids are observed in 24h-annealed sample, approximately at the middle of the film thickness (corresponding to the In2Se3 precursor film thickness). Thus, it is apparent that the oxygen plays a certain role on the morphological properties of the CISe film without sodium. Figure 5.28 and 5.29 show that the impact of Na on grain growth starts during the CISe formation at the second deposition stage, where In_2Se_3 layer reacts with Cu/Se and evolves in composition to $CuInSe_2$ films. During this evolution, the absence of Na could hamper grain growth by influencing the interaction of Cu and Se with the precursor film. In addition to this, the oxygen also has an impact on the morphology of the CISe absorber resulting in the formation of voids generated most probably due to local segregation of Cu_2Se on precursor layers (see section 5.1.2.2.2).

The observed reduction in CISe grain size is contrary to the reported by Rudmann et al. [42], who described an increase in size with the reduction of Na content. However, the impact of sodium on the grain structure of CISe films is still a controversial topic given the contradictory results in the literature [20,41,42] . As mentioned in sections 5.1.2.1.2 and 5.1.2.1.3, the presence of Na could promote the formation of Na_2Se_x, which influence the availability of selenium during the CISe growth [51]. The availability of Se plays a major role in the morphological and structural properties of absorbers films. The absence of Na might change the rate and manner of Se incorporation, and thus modify the growth of CISe layers.

$CuInSe_2$ absorbers with Na

Reference	1h oxidized	24h oxydized
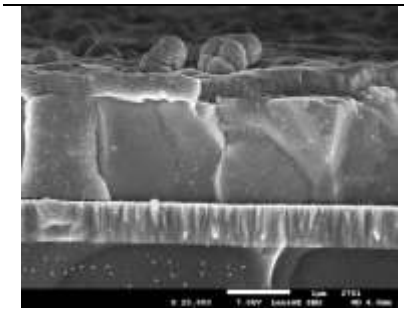	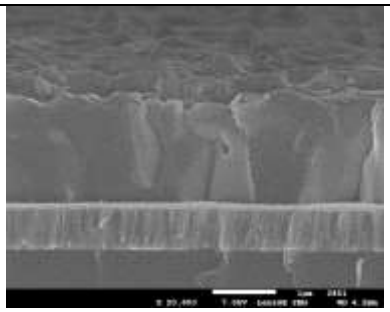	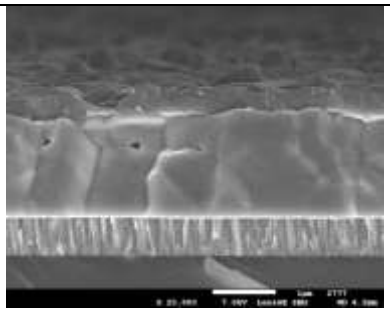

$CuInSe_2$ absorbers without Na

Reference	1h oxidized	24h oxydized
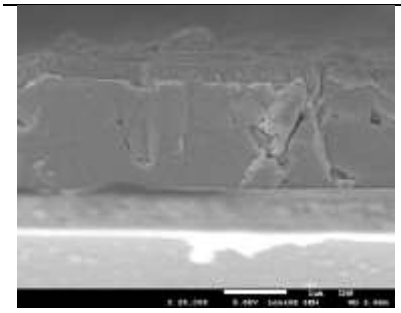	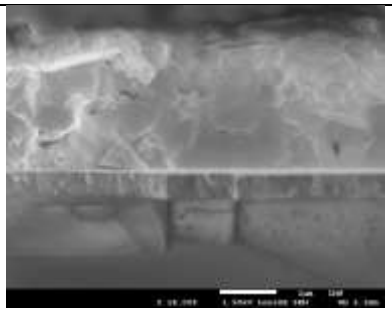	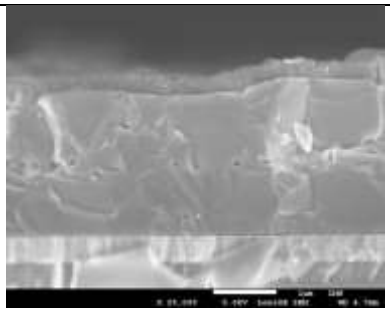

Figure 5.29 SEM cross-section images of In_2Se_3 precursor films deposited at 400°C and the corresponding CISe absorber layers prepared from the precursor films: Reference, 1h and 24h annealed in air at 300°C.

Structural properties of In_2Se_3 and $CuInSe_2$ films

Figure 5.30 shows the XRD patterns of the reference, 1h, and 24h air-annealed In_2Se_3 films deposited on sodium and sodium-free substrates. The XRD patterns were normalized with respect to the (110) peak. The In_2Se_3 films exhibited a very similar pattern, being the principal planes related to defect wurtzite structure of the hexagonal γ-In_2Se_3 phase (JCPDS 40-1407). All the films showed an (110) preferential orientation, with the predominant Lotgering factors values of F(110)=0.50, F(110)=0.46 and F(110)=0.49 for the sodium-free reference, 1h and 24h annealed samples, respectively. The sodium-free reference precursor displayed FWHM values of 0.06º, 0.11 º and 0.09 º

for the (110), (006) and (300) peaks, respectively. The FWHM values of the annealed layers did not show any significant change (±0.01 º) compared to the reference films. It is apparent that there is no significant impact of Na in the structural properties of the In_2Se_3 films before and after the annealing process. Additionally, there is no clear evidence of oxide compounds (e.g. In_2O_3) compound formation during the annealing of Na-free samples.

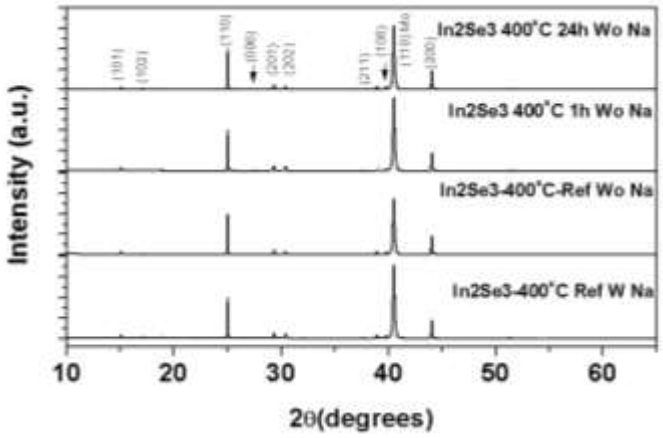

Figure 5.30 XRD patterns of In_2Se_3 films deposited on sodium and sodium-free substrates: Reference, 1h and 24h air-annealed.

Figure 5.31 displays the XRD patterns of the CISe absorber films deposited on sodium and sodium free substrates using reference and 24h air-annealed In_2Se_3 precursor films. The XRD patterns were normalized with respect to the (112) CISe peak. The diffractogram of the 1h annealed film (not shown) exhibited very similar characteristics in comparison with the reference samples. The samples exhibited the formation of chalcopyrite-like $CuInSe_2$ compounds (JCPDS 40-1487) denoted by the crystallographic planes (101), (112), (103), (211), (105), (213), (204)/(220), (116)/(312) and (305)/(323). As mentioned in the previous section, the presence of (101), (103) and (211) plane shows the development of a material with an ordered cation sublattice [33]. Table 13 shows that the (112) peak full width at half maximum values of the CISe samples were similar.

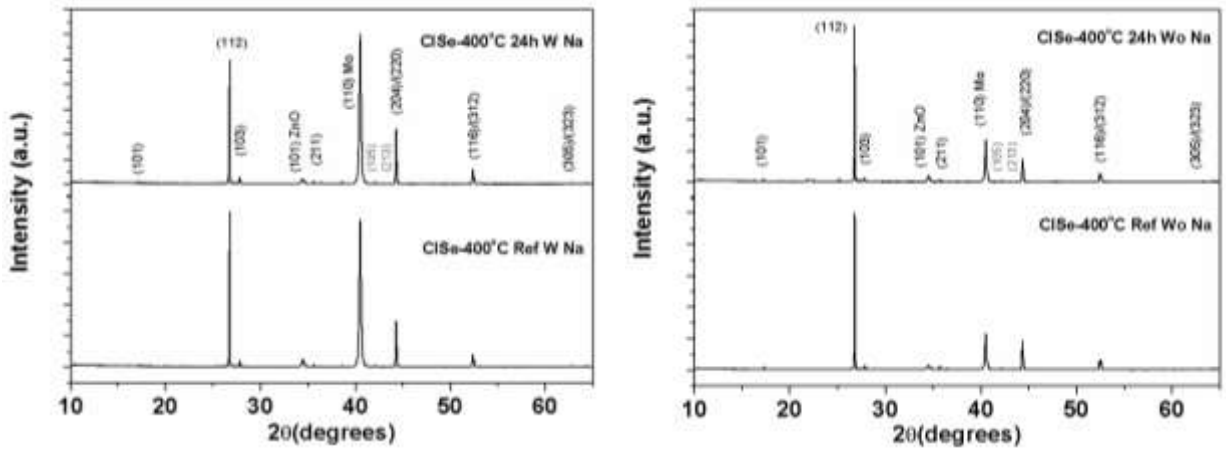

(a) (b)

Figure 5.31 XRD patterns of CISe thin films deposited on (a) sodium and (b) sodium free substrates with reference and 24h air-annealed In_2Se_3 precursor films.

Table 5.13 (112) peak FWHM values of the $CuInSe_2$ films deposited on sodium and sodium free substrates with reference and 24h air-annealed precursor films.

Sample	With Na	Without Na	With Na	Without Na
	FWHM (112) (°)	FWHM (112) (°)	Crystallite size (nm)	Crystallite size (nm)
CISe 400°C Ref	0.06	0.06	136	135
CISe 400°C 1h	0.07	0.07	116	116
CISe 400°C 24h	0.06	0.07	136	116

Table 5.14 lists the textures of the films determined by Lotgering factors (see equation 5.1). The absorbers without sodium exhibited an (112) preferred orientation. This orientation is contrary to the observed by Couzinie and Kessler et al. [20,34]. They reported the development of (204)/(220) preferred orientation for CIGSe films with without Na. Compared to the films with Na, it is possible to observe that the (112) preferred orientation of Na-free samples is not importantly affected by the annealing process. These results could indicate that at least in terms of preferred orientation, the samples without sodium are more resilient to the oxygenation of the film compared to sodium containing

samples. The observed results could be related to the oxygenation of the In_2Se_3 samples and the formed oxide species on its surface (e.g. SeO_2, OH).

Table 5.14 Lotgering factors (F(*hkl*)) of the $CuInSe_2$ films deposited on sodium and sodium free substrates with reference and 24h air-annealed precursor films.

Sample ID	With Na			Without Na		
	F(112)	*F*(204)	*F*(220)	*F*(112)	*F*(204)	*F*(220)
CISe-400°C-Reference	0.33	0.01	-0.16	0.41	-0.05	-0.16
CISe-400°C-1h	0.28	0.00	-0.15	0.50	-0.07	-0.17
CISe-400°C-24h	0.18	0.07	-0.14	0.47	-0.07	-0.15

Figure 5.32 displays the zoomed regions of the CISe films XRD patterns in Figure 5.31. When the patterns of Na and Na-free films are compared, there are no apparent differences in the reference and 1h annealed samples. However, it is possible to observe the presence of additional phases in the 24h annealed film. These extra phases could be mainly related to elemental selenium (JCPDS 51-1389), $CuIn_3Se_5$ (JCPDS 51-1221) and SeO_2 (JCPDS 22-1314). Moreover, the peaks with 2θ values located at approximately 25.15º, 27.25º and 30.56º might correspond to Cu_2Se, In-Se, and In_2O_3 phases, respectively. Würz et al. have reported similar phase formation in the oxidation of $CuGaSe_2$ films.

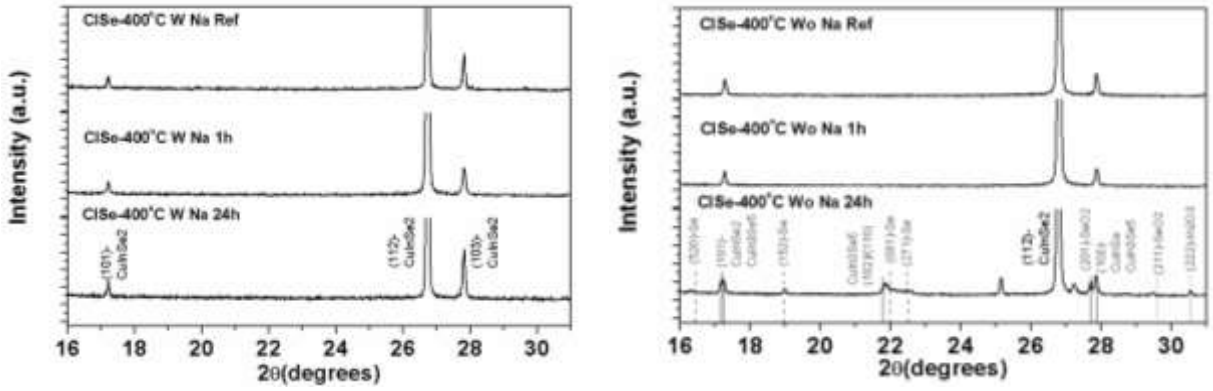

(a) (b)

Figure 5.32 Zoomed XRD patterns of CISe thin films deposited on (a) sodium and (b) sodium-free substrates with reference and 24h air-annealed In_2Se_3 precursor films.

With the previous results, it is possible to observe that the sodium does not have any impact on the morphological neither structural properties of air-annealed In_2Se_3 precursor films. However, the absence of sodium does have an impact on the morphological (e.g. grain size) and structural (e.g. extra phase formation) properties of oxygenized CISe films. The interaction of oxygen with a Na-free precursor surface could promote the different changes noticed in the CISe layers. The next section attempts to elucidate the relation between oxygen and Na-free In_2Se_3 film.

5.1.2.3.3 X-ray photoelectron spectroscopy study of the air-annealed In_2Se_3 precursor films

To have a explore and confirmation the interaction of sodium and oxygen in the precursor layer, the surfaces of the In_2Se_3 films were studied by X-ray photoelectron spectroscopy (XPS). With objective of distinguish the change in the signal of the samples, the analyses were carried out on the In_2Se_3 reference (i.e. as-deposited, not intentionally exposed to air) and In_2Se_3 24h air-annealed films. Contrary to the XPS measurements observed in the section 5.1.2.2.2, the In_2Se_3 precursor films of this study were stored in inert atmosphere immediately after they were grown. In this manner, the unintended oxygenation was avoided into a maximum. The surface analyses were performed by X-ray photoemission spectroscopy (XPS) in a Kratos Axis Nova with a monochromatic Al K radiation (1486.6 eV) and 20 eV pass energy with an energy step of 0.1 eV. The C1s signal from adventitious carbon with a binding energy E_B= 284.6 eV was used for energy referencing. The peak fit analysis was performed using the CasaXPS software where a linear background was subtracted from the spectra. The spectra were fitted by peaks with a Gauss (60%)–Lorentz (40%) profiles. Wagner plots were use as a tool for the identification the different compounds formed during the annealing [52]. To further identify the compounds, the Auger Lines In M4N45N45, Se L3M45M45, O KVV and Na KL23L23 are employed. XPS measurements of two types of samples were carried out: i) Na and Na-free In_2Se_3 reference samples not subjected to intentional oxygenation and ii) 24h air-annealed layers with and without Na.

Figure 5.33 shows the In3d core level spectra recorded from the reference and 24h annealed Na and Na-free In_2Se_3 films. Both reference layers (Figure 5.33a) with and without sodium exhibited an In $3d_{5/2}$ and $3d_{3/2}$ peak with a binding energy E_B=444.50 eV and 452.05 eV (respectively), corresponding to the In_2Se_3 compound [49]. The Figure 5.33b shows the In 3d peaks of 24 h annealed film with and without Na. The 24h film with Na showed main peaks at E_B=444.12 eV and E_B=451.68 eV which could correspond to In_2Se_3 or In metallic [54]. The shoulders at E_B=444.67 eV and E_B=452.25 eV may be related to the formation of In_2O_3 compound [53]. The 24h layer without Na displayed the main peaks at a binding energy of 444.46 eV and 452 eV, probably related to In_2Se_3 compound [49]. The shoulders at E_B= 445.05 eV and 452.63 might correspond to In_2O_3 or $In(OH)_3$ [57,68]. The relation between the areas of the main peaks and the shoulders presented a higher In-O signal in the 24h samples without Na. This match with the trace of In2O3 phase observed in the XRD pattern of Na-free 24h annealed film (see Figure 5.32).

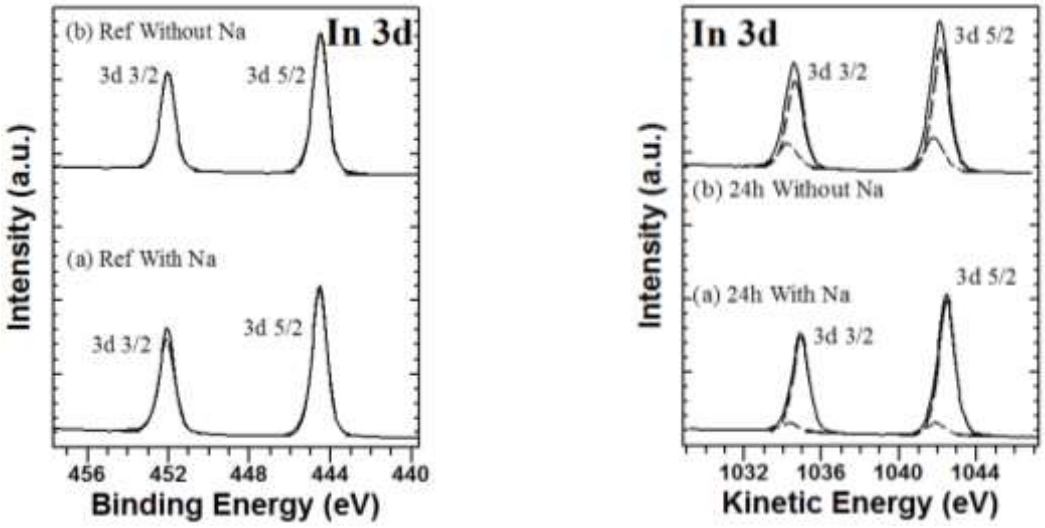

(a) (b)

Figure 5.33 In 3d spectra of Na and Na-free In_2Se_3 films, (a) reference and (b) 24h air-annealed.

The Figure 5.34 exhibits the spectra of the Se3d from Na and Na-free In_2Se_3 films, (a) reference and (b) 24h air-annealed. In contrast to the samples analyzed in section 3.1.2.1.3, these reference layers (both Na and Na-free) showed a narrow Se3d peak

which contains only one set of doublets. The doublet of the Na-free and Na-containing films corresponds to the $3d_{5/2}$ (E_B=53.69 eV) and $3d_{3/2}$ peak (E_B=54.49 eV), related to the In_2Se_3 phase [54]. The difference on the number of doublets between the samples analyzed in this section and those in section 3.1.2.1.3, is the reduction of oxidation through the use of inert gas atmosphere during the sample storage. Thus, there were not evidence of selenium oxidation (e.g. Se^0, Se^{+4}) in the reference films.

The 24h annealed films with and without sodium showed a similar trend in the formation of elemental selenium (Se^0), denoted by the presence of a second set of doublets on the 3d peak. This elemental Se could be related to the oxidation of selenium [51]. A relation of the peak areas of the two doublets showed a higher content of elemental selenium for samples deposited with Na. Nevertheless, more Se^0 formation in the bulk of the film is not ruled out. Indeed, the presence of elemental selenium is also observed in the XRD pattern of CISe 24h annealed Na-free film (see Figure 5.32). Another evidence of the oxidation of Se in both samples is the appearance of a peak related to the formation of SeO_2 species [46,51,55]. This peak could also originate from the 3d-emissions of the Se oxidized in the form Se^{+4} and Se^{+6} [51]. An exclusive feature of Na-containing samples is the emergence of a peak at around E_B=63.1 eV related to Na2s.

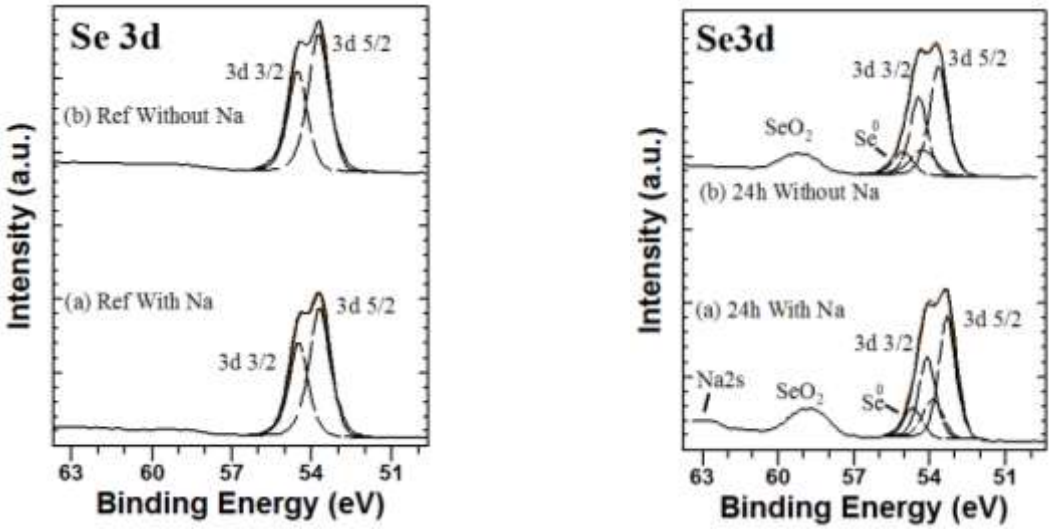

(a) (b)

Figure 5.34 Se3d spectra of Na and Na-free In_2Se_3 films, (a) reference and (b) 24h air-annealed.

Figure 5.35 shows the O1s core level spectra recorded from Na and Na-free In_2Se_3 films, (a) reference and (b) 24h air-annealed. The O1s peak obtained from both reference samples (i.e. Na and Na-free) can be separated into at least four sub-bands. The binding energies of the peaks of both reference samples are at around 531.95, 531.20, 530.58 and 529.59 eV. The components at high binding energy (i.e. 531.95 and 531.2 eV) could be related to OH groups on the surface (e.g. In(OH)3). The components at lower E_B (i.e. 530.58 and 529.59 eV) can correspond to oxygen dissolved in the bulk and oxygen bonded to a metal [54,58]. However, given that the reference samples did not show further evidence of In or Se oxidation, the oxygen signal is expected to be mainly related to physisorbed species. In the case of the reference sample with sodium (Figure 5.35a), some components of O1s the peaks could be attributed to NaOH (E_B=531.95 eV) and Na_xO (E_B=530.58 eV).

The 24h annealed sample with sodium (Figure 5.35b), also showed a peak possibly constituted by of 4 components. These elements are located at a binding energy of 531.95, 530.83, 530.14 and 529.36 eV. The high binding energies (i.e. 531.95 and 530.83 eV) could be related to OH groups on the surface (e.g. $In(OH)_3$, NaOH) or Na_2CO_3 and NaxO [46,68]. The components at lower E_B (i.e. 530.14 and 529.36 eV) can correspond to In_2O_3 and Na_2O [53,57]. The elements of the 24h annealed sample without Na also exhibited a similar trend, but without the formation of Na compounds. The increase in intensity of the component at around 530 eV could indicate that the 24h anneal Na-free film have more chemisorbed species (e.g. In_2O_3) than the Na-containing sample. This match with the results observed in XPS In 3d peaks and the XRD pattern (see Figure 5.32b and 5.33b).

Figure 5.36 shows the Na1s core level spectra of the Na and Na-free In_2Se_3 films, (a) reference and (b) 24h air-annealed. The reference and annealed sample without sodium did not show any trace of Na. The reference sample with Na displayed a very low peak, probably related to Na_2SeO_3 or Na_2CO_3 [46]. The Na1s peak of the In_2Se_3 annealed sample with Na show two components, E_B=1071.51 eV and 1070.90 eV, which can be related to Na_2CO_3 and Na_2SeO_3, respectively [52]. As mentioned in the Section 5.1.2.2, the formation of Na_2SeO_3 can be linked to the presence of a Na_2Se_x compound working

as Se reservoir [51].

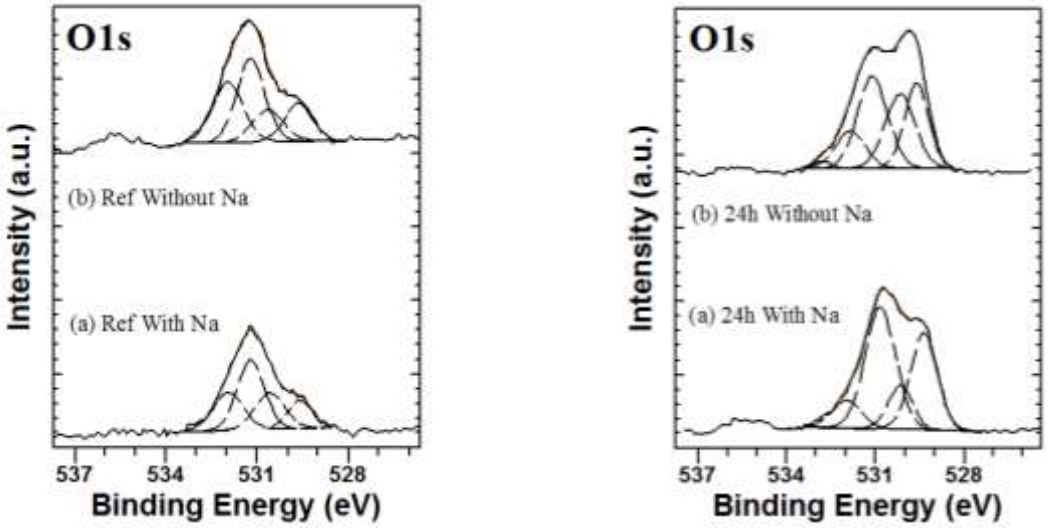

(a) (b)

Figure 5.35 O1s spectra of Na and Na-free In_2Se_3 films, (a) reference and (b) 24h air-annealed.

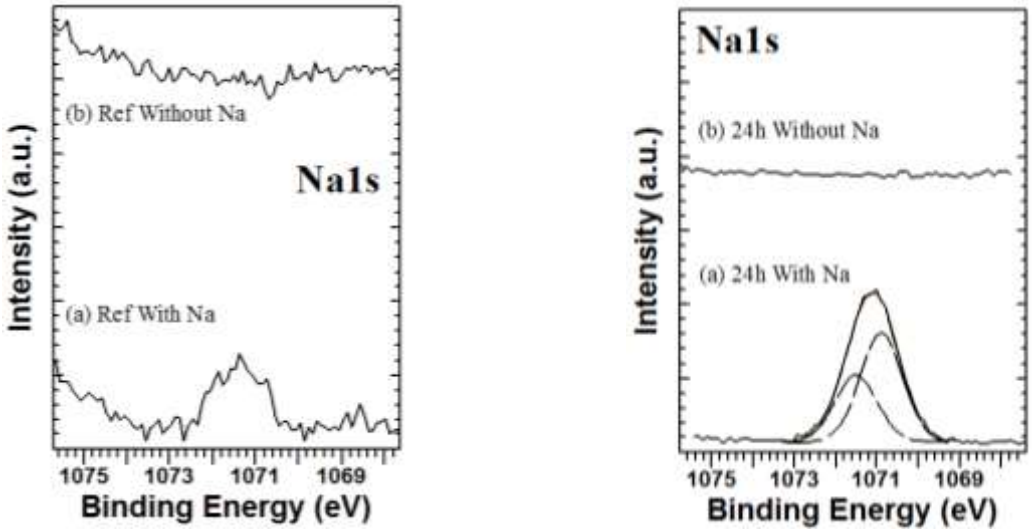

(a) (b)

Figure 5.36 Na1s spectra of Na and Na-free In_2Se_3 films, (a) reference and (b) 24h air-annealed.

The XPS spectrums show that the oxygenation of Na and Na-free In_2Se_3 films results in the formation of similar species. The species formed on films without sodium after 24h annealing are mainly related to In_2O_3, $In(OH)_3$, Se^0 and SeO_2. Additionally, it is apparent that the absence of sodium promotes a higher content of In-O compounds (most probably In_2O_3). These compounds are probably accommodated on the In_2Se_3 film near surface region, rather than in the bulk of the precursor films as also observed in the Na-containing samples (see section 5.1.2.1.3). As mentioned before, the presence of In_2O_3 compound might be related to the passivation of Se vacancies (V_{Se}). The higher presence of In-O bonds could signify a greater number of passivated V_{Se}, which might be beneficial or detrimental to solar cell operation depending whether they are located in the grain boundaries or film surface [44,60]. Additionally, the elemental selenium in CISe has been identified as a detrimental factor leading to the reduction of open voltages and fill factors [61].

Having identified the different species that probably interact during the growth of the CISe absorber layers, the next aspect to investigate is the manner in which these spices affect the operation of the solar cells. The next section shows the results of the solar cells using the CISe absorber film obtained from the oxygenized In_2Se_3 precursor layers.

5.1.2.3.4 $CuInSe_2$-based solar cells

Figure 5.37 shows current density-voltage measurements (J(V)) of the solar cell based on the CISe grown from the 400ºC-In_2Se_3 precursor films reference, 1h and 24h air-annealed layers (with and without sodium). In the next, the results are presented in terms of mean values of typically 8 cells per box-and-whisker plot. The CISe reference cell with and without sodium exhibited a large difference mainly in open circuit voltage (V_{oc}) and fill factor (FF). As mentioned in Chapter 2 (section 2.3.3.1), the sodium diffused from the glass substrate (~0.1 at%) increase the concentration of holes in the CISe film. The increase in carrier concentration mainly improves the V_{oc} and FF of the solar cell [69,70]. The reduction in V_{oc} (~128 mV) and FF (~17.3 %) of CISe reference cell without sodium

is indeed due to the shrinkage of carrier concentration promoted by the lack of Na diffused into the film.

From Figure 5.37 it is also possible to observe a significant and continuous decrease of the Na-free solar cell characteristics (i.e. V_{oc}, FF, J_{sc} and η) with increasing air-annealing time. A comparison between Na-containing and Na-free samples shows a greater decrease in cell parameters in case of sodium-free solar cells. The percentage of losses of each cell parameter were calculated with respect to reference samples in Figure 5.37. In one hand, the V_{oc} of CISe cell with Na decreased 5.4% and remained almost stable after 1h and 24h annealing, respectively. On the contrary, the open-circuit voltage of CISe film without Na decreased 13.5% and 66.6% after the 1h and 24h air-annealing, respectively. A similar trend is observed for the fill factor (- 13.4%), current density (-1.3%) and efficiency (- 29.2%) of CISe Na-free solar cells after 1h annealing. However, the most significant reduction in FF (- 44.5%), J_{sc} (- 15.7%) and η (- 84.6%) is observed at 24h anneal of CISe Na-free sample. In this case, it is apparent that a long oxygenation of In2Se3 Na-free precursors films results in a complete degradation of the CISe-based solar cell, being the V_{oc} and FF the most affected parameters. To have a clearer view on how the solar cells characteristics decremented in comparison with Na-containing films, Figure 5.38 shows the J-V curves of the Na-free CISe reference, 1h and 24h annealed samples. The figure helps to confirm that the oxygenation of Na-free In_2Se_3 precursor layers has a substantial impact on the CISe-based solar cell performance, in particular on the open-circuit voltage and fill factor.

Figure 5.39 shows the quantum efficiency (QE) measurements of the corresponding solar cells. Comparing the Na-free CISe reference and 1h air-annealed samples, the last displayed a decrease in the range of ~600-1300 nm. This indicates an increase in losses due to an incomplete collection of photogenerated carriers in the long-wavelength range. Nevertheless, the Na-free 24h annealed solar cell exhibited a general decrease of the quantum efficiency. This overall decline could involve a reduction of charge carrier diffusion length promoted by recombination at the void defects observed at the middle-thickness of the absorber and/or at grain boundaries in the bulk material.

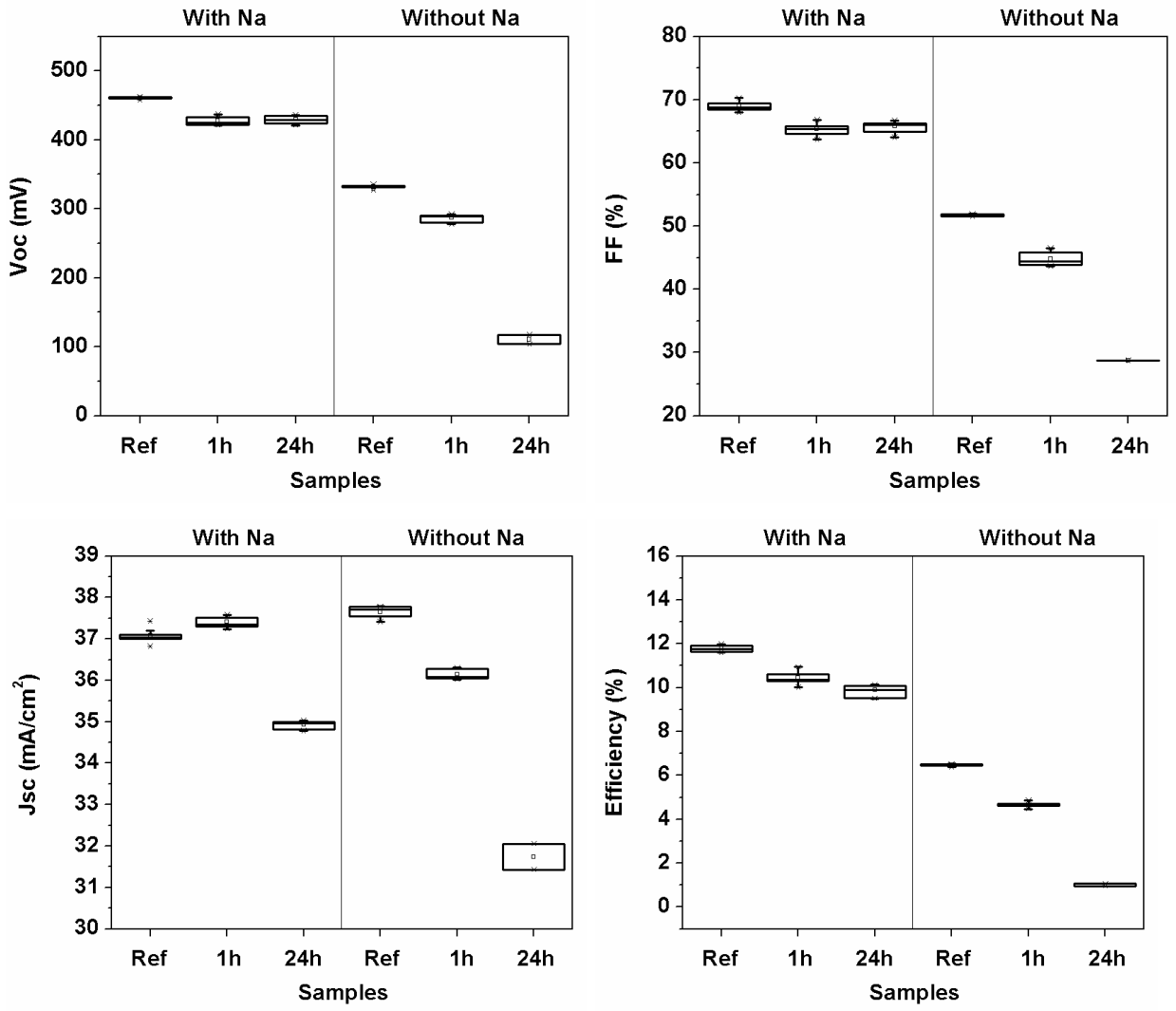

Figure 5.37 Solar cells characteristics for CISe absorbers prepared from Na and Na-free In_2Se_3 films, reference, 1h and 24h annealed in air at 300°C. The graph shows the minimum, maximum, median and mean values.

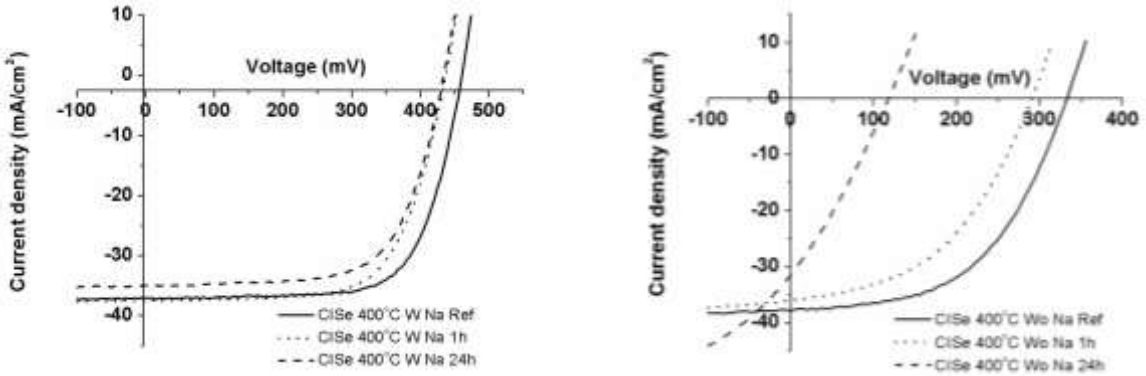

(a) (b)

Figure 5.38 Current density- voltage curves of solar cells based on CISe absorbers prepared from (a) Na and (b) Na-free In_2Se_3 films, reference, 1h and 24h annealed in air at 300°C.

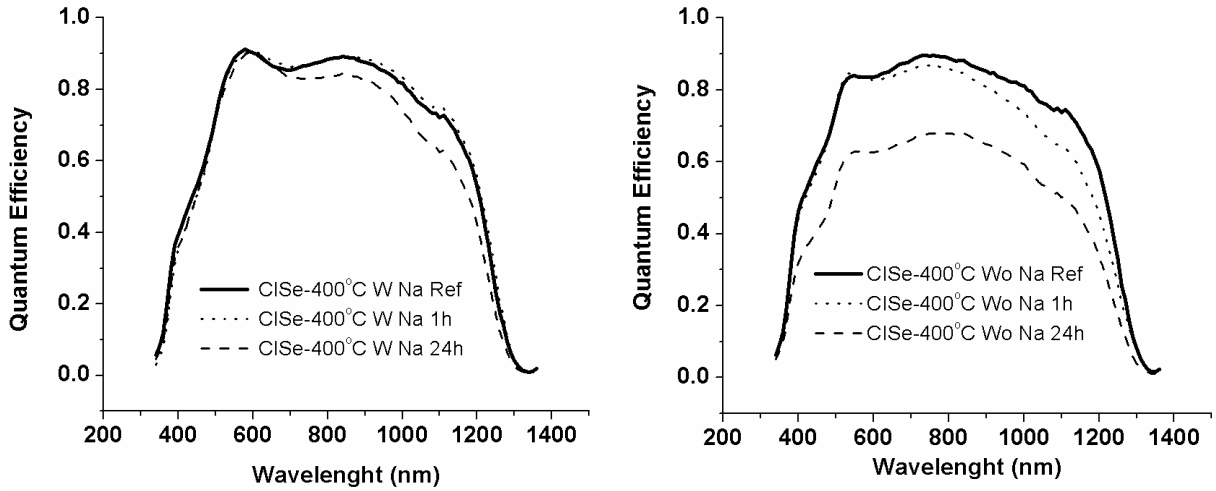

(a) (b)

Figure 5.39 Quantum efficiency (QE) measurements of CISe absorbers prepared from the In_2Se_3-400ºC precursor films: Reference, 1h and 24h annealed in air at 300ºC.

About the morphological and structural properties of the CISe films, the influence of Na on the growth of $CuInSe_2$ is taking place only after the deposition of Cu+Se (i.e. 2nd and 3rd stage of 3-stage process). The absence of sodium is related to the modification of morphology of CISe film (e.g. grain size), texturization (e.g. (112)-oriented), and the development of crystalline phases (e.g. Se^0, SeO_2, $CuIn_3Se_5$, and In_2O_3). Some of the

observed results are contrary to the reported in the literature. The increase in grain size with the inclusion of Na into the absorbers have been detected by different authors [41,51,71]. Nevertheless, other works have been reported an unclear effect of Na on CISe grain size [72,73]. In fact, various influences of Na have been found for the same CIGS growth processes. In the case of oxygenized precursor films, the oxygen indeed plays a role in the determination of morphological and structural properties of absorbers layers. All the aforementioned suggest that multiple parameters influence the morphology and texture of the CISe films. Some parameter influencing the last two characteristics are the quantity of Se present during growth, growth rate, substrate temperature, Cu excess, properties of Mo contact, impurities (i.e. oxygen), among others. Thus, for the same CIGSe growth process, different influences of Na can found from one laboratory to another.

As discussed before, the XPS results of Na-free In_2Se_3 precursors showed the formation of In_2O_3, Se^0, SeO_2, among others. Similar compounds have been reported for CISe and CIGSe films annealed in air [46,49,62]. In the absence of Na, it is apparent that the oxidized surface could contain a higher accumulation of oxygen-related species in comparison with the sodium containing samples. This accumulation of oxides could be seen as a reservoir of oxygen [63]. When the Cu+Se and In+Se materials are deposited on the In_2Se3 film to complete the CISe layer (3-stage process), the absence of Na may accelerate the diffusion of oxygen directly to the surface of the absorber film. With the lack of Na-O catalytic effect, the oxygen might not be well distributed along the grain boundaries and thus be preferentially located on the surface of the CISe layers [39,64]. The oxygen will passivate the dangling bonds related to Se vacancies ($V_{Se,}$ donor defects) and form In_2O_3 compounds on the surface where the CdS/CISe interface will be formed [44,45]. Oxygen passivation at the CdS/CISe interface states can have detrimental or beneficial effects.

The oxygenation of the solar cells prepared with films without sodium (Figure 5.38) showed a greater degradation of its characteristics in comparison with CISe Na-containing cells. It is possible to infer that a probable higher content of oxygen on the surface of the Na-free annealed CISe film could further promote the detrimental effect of

the CdS/CISe interface passivation (surpassing the beneficial GB's passivation). The oxygen in the CdS/CISe interface reduces the positive interface charge (by passivating the V_{Se}^{2+}), decreasing the band-bending at the surface, and thus reducing the V_{oc} and FF (see Chapter 2 section 2.3.4). The possible continuous reduction of band-bending with increasing annealing time could promote the further decrease of open-circuit voltage observed in Figure 5.38. Additionally, the deposition of CdS by chemical bath deposition is probably not enough to restore the band-bending (and thus improve V_{oc}) of Na-free films. Another reason for the detrimental solar cell characteristics can be the related to the junction formation and recombination of charge carriers at the grain boundaries and/or at voids located at half of the CISe film thickness. The SEM images (see Figure 5.29) show more defected grain structures of CISe films without Na. These structures could increase the apparent roughness of the films (which might impact the CdS/CISe interface formation) as well as the number of recombination centers related to grain boundaries. Furthermore, the lack of sodium in the film may hinder an easy diffusion of oxygen through GB's and thus impede the passivation of recombination centers.

From the previous results, it is possible to realize that the presence of sodium in CISe films is vital to minimize the adverse effects of air-annealing treatment (e.g. reduction of positive interface charge, Cu removal) and maximize the beneficial ones (e.g. grain boundary passivation). The sodium and oxygen interaction (i.e. catalytic effect) could indeed promote the passivation of defects, especially those related to selenium vacancies (V_{Se}^{++}) at the grain boundaries in the bulk of the film.

Effect of substrate temperature and sodium availability on the oxygenation of CuInSe2 films

To have a further idea on the effect of the availability of sodium on structural and electrical properties of CISe films, three absorbers were deposited at different 1st-stage deposition temperature (namely 250ºC, 325ºC and 400ºC) on substrate with and without sodium. As observed in previous results (see section 5.1.2.2), lower grain sizes (higher GB's density)

are expected as the substrate temperature decreases. Figure 5.40 exhibits the current-voltage measurements (J(V)) of the solar cell based on Na-containing and Na-free CISe absorbers grown from In_2Se_3-250ºC, -325ºC and -400ºC precursor films (reference, 1h and 24h air-annealed). The results present 8 cells per box-and-whisker plot. The Figure 5.40 shows a general decrease in the electrical measurements for the continuous oxygenation of Na-free CISe solar cells. The CISe-250ºC solar cell (expected to have the highest number of GB's) is the most resilient samples to the oxygenation process, exhibiting near stable parameters after 1h air-annealing (i.e. V_{oc}, FF, Jsc and η) with respect to reference sample. After the exposure to oxygen, the most affected sample is the cell deposited at 400ºC, which exhibited the lowest solar cell parameters after 24h air-annealing. These results show that the CISe films deposited from large-grains/low-GB's-density In2Se3 precursor films are more prone to be affected by the presence of oxygen, probably through the increase of interface recombination (related to reduction of surface band bending) and limitation of minority carrier diffusion length (probably associated to voids at half the thickness of film and/or at GB`s). The results could also display that a high number of grain boundaries limits the oxygen diffusion towards the CISe surface. Hence, more defects in bulk could be passivated in samples with high number of grain boundaries (i.e. those deposited at 250ºC) rather than films with low grain boundaries (i.e. those deposited at 400ºC).

Figure 5.41 shows the quantum efficiency (QE) measurements of the corresponding solar cells. As the 1st-sage substrate temperature increases, the 1h air-annealed samples showed a continuous lowering of efficiencies in comparison with the corresponding CISe references. The CISe-250ºC and -325ºC 24h-annealed cells displayed a clear decrease in QE in the range of ~510-1300 nm, which indicates an incomplete collection of photogenerated carriers probably due to low carrier diffusion length and/or high recombination rates. The incomplete collection confirms the observed in the J(V) measurements. The CISe-400ºC 24h samples showed a general decrease of the quantum efficiency, which is probably related to an important lowering of carrier diffusion length due to the presence of a crystalline defects (e.g. voids at half the thickness of CISe-400ºC 24h film) or due to bad formation of CdS/CISe interface. Contrary to the 400ºC

sample, the CISe-250ºC and -325ºC solar cells exhibited a similar QE signal at ~340-510 nm range, denoting a similar ZnO/CdS/CISe interface formation for both samples.

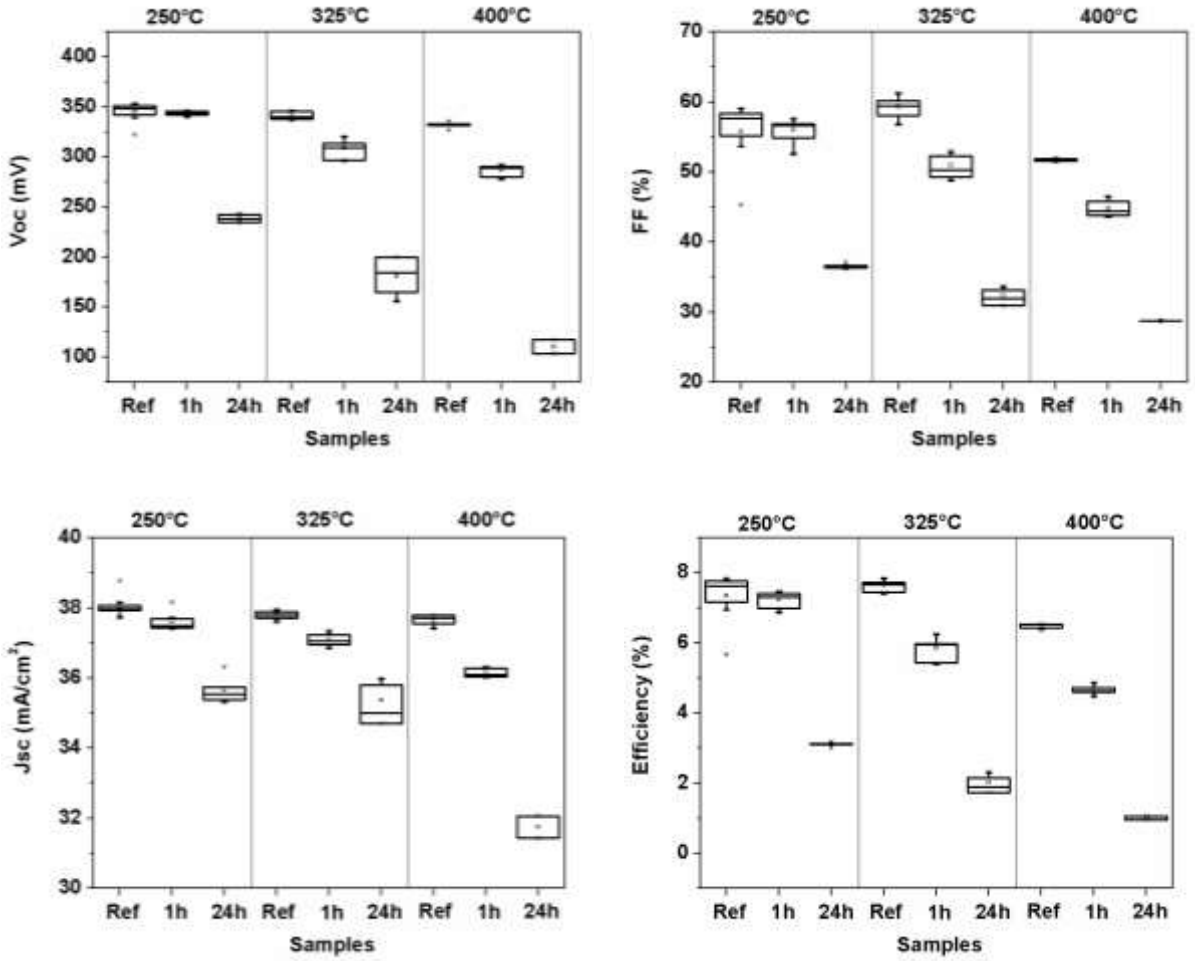

Figure 5.40 Current-voltage measurements of solar cells based on the CISe absorbers grown from Na-free In_2Se_3-250ºC, -325ºC and -400ºC precursor films un-annealed (Reference), 1h and 24h air-annealed. The graph shows the minimum, maximum, median and mean values.

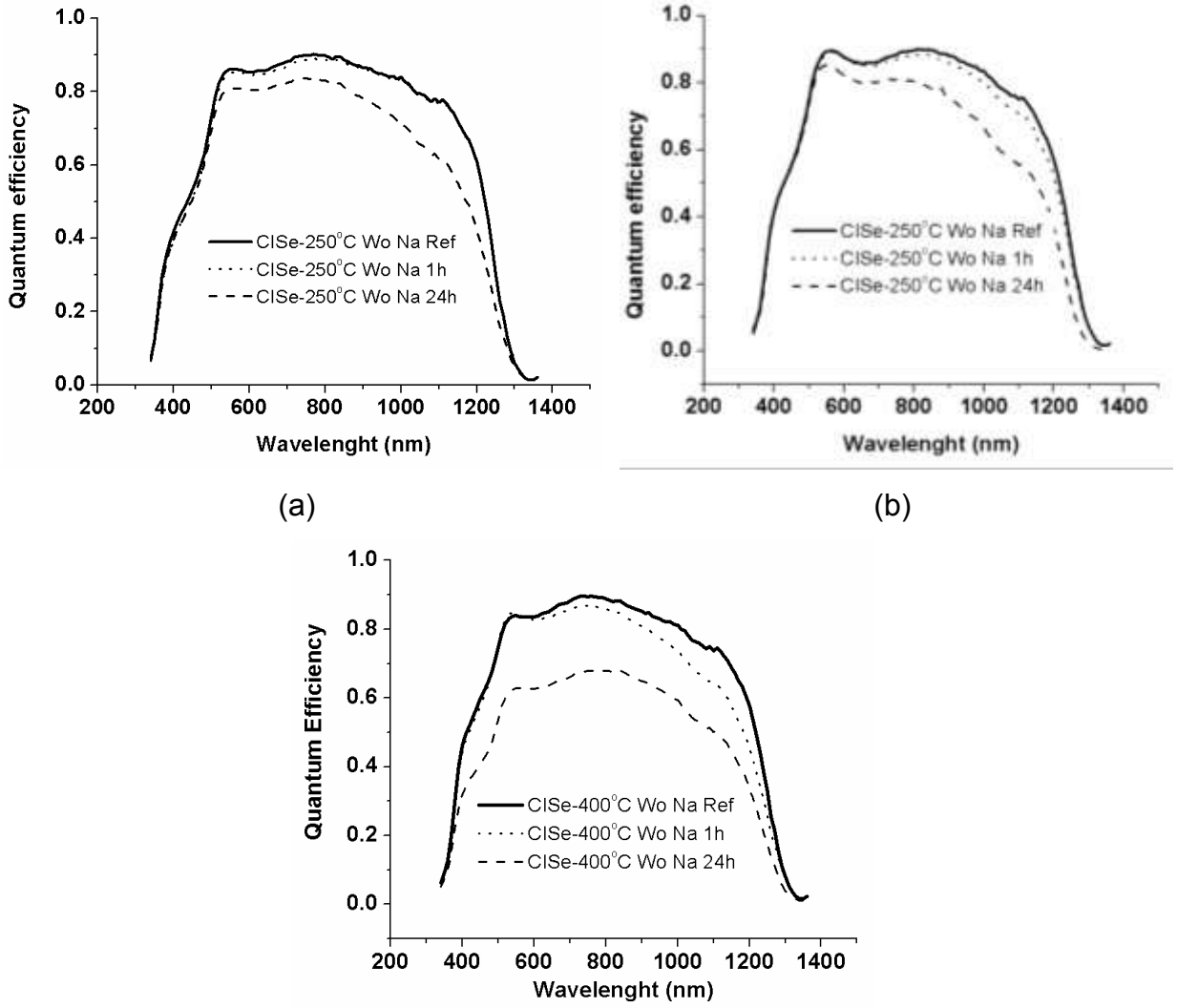

Figure 5.41 Quantum efficiency measurements of solar cells based on the CISe absorbers grown from the In_2Se_3-250ºC (a), -325ºC (b) and -400ºC (c) precursor films reference, 1h and 24h air-annealed.

Considering the above results, it is possible observe that the Na-free CISe films with high grain boundary densities, i.e. those expected in samples deposited at 250ºC (see section 5.1.1, 5.1.2.2), are more resilient to the exposure of oxygen in comparison with low GB density absorbers (i.e. CISe-400ºC). The high number of GB's could minimize the diffusion of oxygen to the CISe surface and thus diminish the negative effects of oxygenation. This last again confirms that the 1st-stage deposition temperature is indeed an important factor participating in the oxygenation of CISe solar cells.

With the aim of improving the observed performance of CISe solar cells exposed to oxygen, the surface modification of In2Se3 precursor films is needed. This treatment is intended to reduce the quantity of surface species related to oxygen and decrease its negative effects on the electronic properties of devices. The next section describes the effect of chemical etching on In2Se3 surfaces and the properties of CISe absorbers.

5.1.2.4 A first approach to the surface treatments of oxygenated CuInSe2 films

To have a clearer idea on a way to improve the efficiency of CISe-based devices exposed to oxygen, four In_2Se_3 precursors were deposited at a substrate temperature of 400ºC. One In_2Se_3 film was used as reference sample and the remaining were exposed to oxygen during 24h at 300ºC. From the oxygenized absorbers, one film was immersed into 2.5 M ammonia (NH_3) solution and another one was dipped in 0.5 M hydrochloric acid (HCl) solution for 5 minutes each one. After all theses treatments, the deposition process was completed to get the $CuInSe_2$ final films. The selection of the NH_3 and HCl chemical treatments is based on their use for removal of surface oxides related to indium material [74–76]. As observed in the XPS results (see section 5.1.2.1.3 and 5.1.2.3.3), the oxygenized In_2Se_3 surface presents the formation of indium oxides and hydroxides back-boned to the film by selenium atoms. The ammonia treatment of oxygenized surface is reported to completely remove indium oxides and Na compounds, leaving few traces of hydroxides (fraction of a monolayer) [75,77]. From this treatment, Se dangling surface bonds are generated as observed in Figure 5.42. The HCl treatment also removes indium and its related compounds from In_2Se_3 oxygenized-films surface, leaving a surface completely clean of indium oxides and a slightly selenium-rich [76,78]. The probable etching reactions are:

$$In_2O_3 + 2NH_3 \rightarrow 2InN + 3H_2O \qquad \text{(eq. 5.2)}$$

$$In_2O_3 + 2HCl \rightarrow 2InCl + H_2O + O_2 \qquad \text{(eq. 5.3)}$$

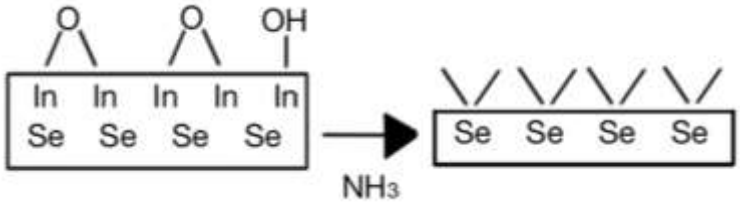

Figure 5.42 Etching of In_2O_3 with NH_3 chemical surface treatment.

Figure 5.43 shows the current-voltage measurements (J(V)) of the solar cell based on surface chemically treated CISe absorbers with and without sodium. The results present 8 cells per box-and-whisker plot. The figure shows an improvement in the Voc and Jsc of the chemical treated oxygenized-CISe samples (both with and without Na), being the HCl etched films which exhibited the best recovery. As a matter of fact, the Voc and Jsc reached the values presented by reference solar cells. This improvement could be related to the restoration of CISe surface band bending and an increase of diffusion length, both effects promoted by the removal of oxygen from the In2Se3 precursor film surface. Comparing to the NH3 treatment, the better recovery of electrical characteristics values using HCl solution as etching agent could be related to a stronger removal of oxides from the In_2Se_3 surface. It might be also associated to the presence of chlorine impurities (see equation 5.3), which increase the overall acceptor concentration and helps to the improvement of Voc and FF [79]. In contrast, the nitrogen impurities (probably present during the NH3 etching, see equation 5.2), are reported to act as a donor impurity [78]. This impurities might compensate certain number of majority charge carriers in the absorber films, and thus promote a lower recovery of the electrical properties. Additionally, the fill factor improved after chemical etching, but in a minor scale as compared to Voc and Jsc.

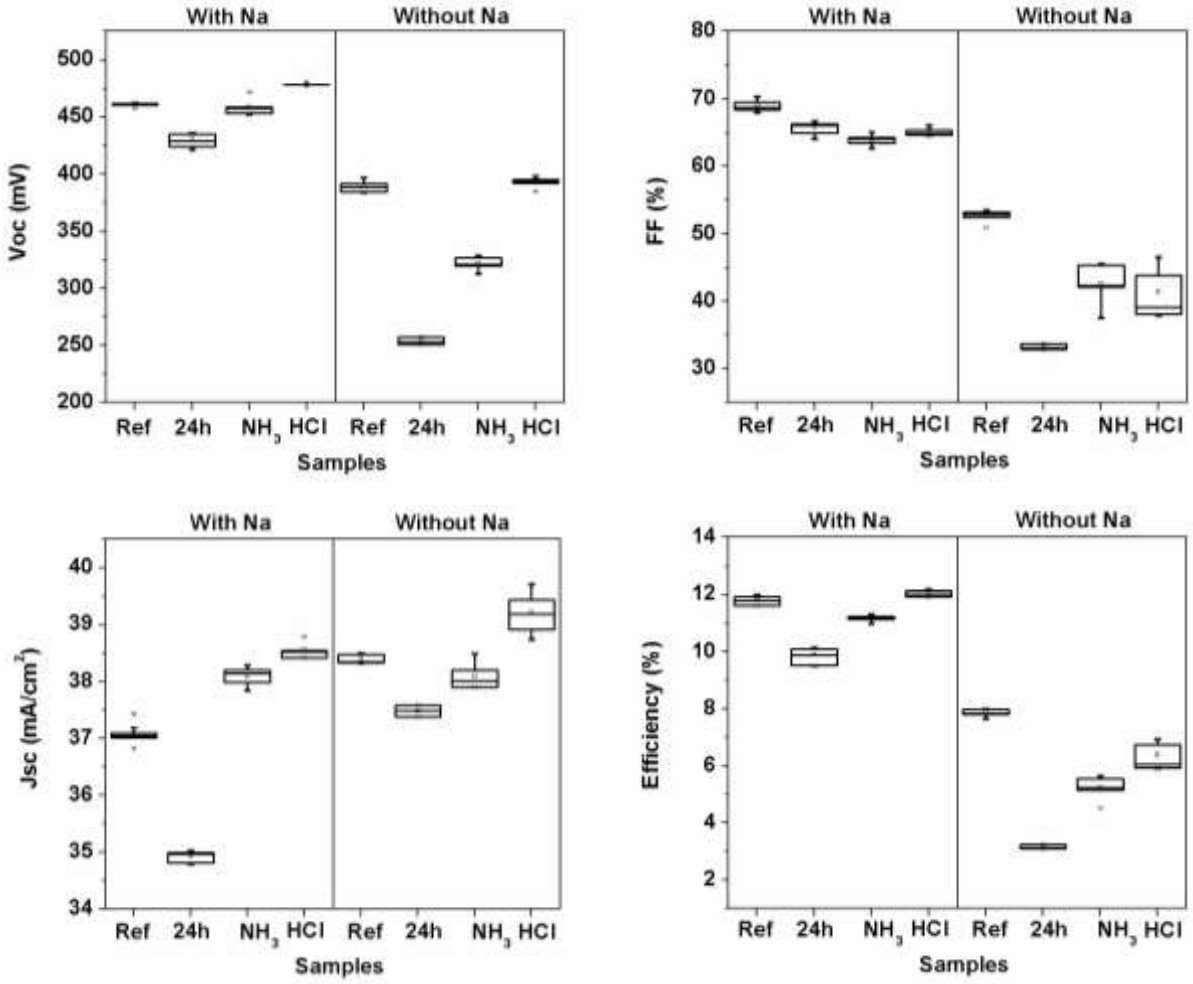

Figure 5.43 Current-voltage measurements (J(V)) of the solar cell based on CISe absorbers grown from In_2Se_3-400ºC precursor films: un-annealed (reference), 24h air-annealed, etched with 2.5 M ammonia (NH3) and 0.5 M hydrochloric acid (HCl) solutions. The graph shows the minimum, maximum, median and mean values.

Figure 5.44 shows the quantum efficiency (QE) measurements of the corresponding solar cells. Indeed, this figure displays the degradation of the 24h oxygenized sample and the its further recovery by NH3 and HCl chemical treatments. The recovery took place especially in the range of 650-1300 nm (approximately), denoting an improved carrier collection related to an increase in effective carrier diffusion length in the absorbers. The improvement in collection confirms the observed in the J(V) measurements of Figure 5.43.

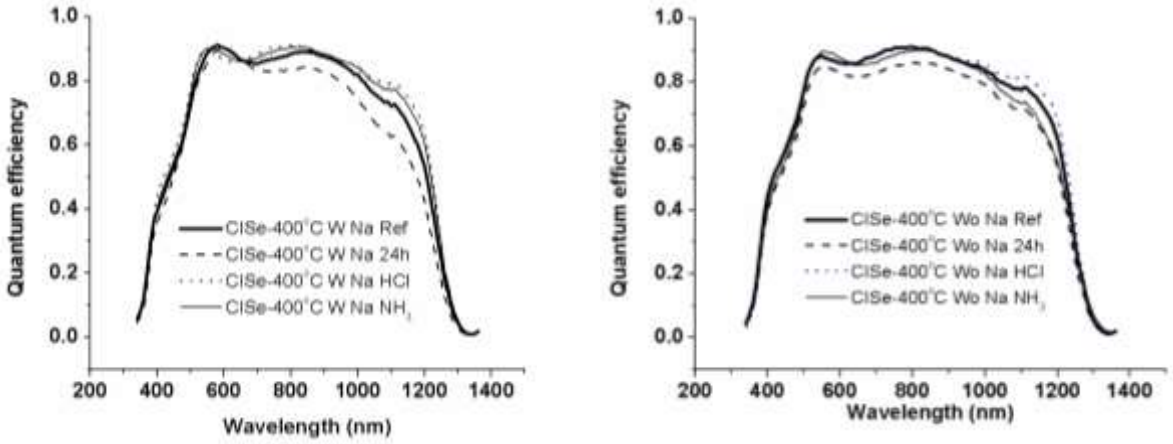

(a) (b)

Figure 5.44 Quantum efficiency measurements of the solar cell based on CISe absorbers grown from In_2Se_3-400ºC precursor films: un-annealed (reference), 24h air-annealed, etched with 2.5 M ammonia (NH3) and 0.5 M hydrochloric acid (HCl) solutions.

Figure 5.45 exhibits the cross-section SEM images of the solar cell based on surface chemically treated CISe films with and without sodium. From the figure it is possible to observed that the surface chemical treatment reduces the voids formation and visible defects located approximately at the middle of CISe thickness. The HCl treatment almost fully restore the morphology, meanwhile the NH3 etching still leaves some traces of defects. The last denotes that the HCl treatment is indeed a stronger etchant in comparison with NH3, at least in terms of oxygen exposure done in this work. The stronger effect of HCl etching exhibited in SEM images match with the recovery observed in the J(V) and QE measurements of Figure 5.43 and 5.44. The change in morphology after chemical etching (specially after HCl treatment) could further confirm the elimination of oxides from In2Se3 films, which indeed promote voids and other defects in final CISe absorbers (observed early in this chapter).

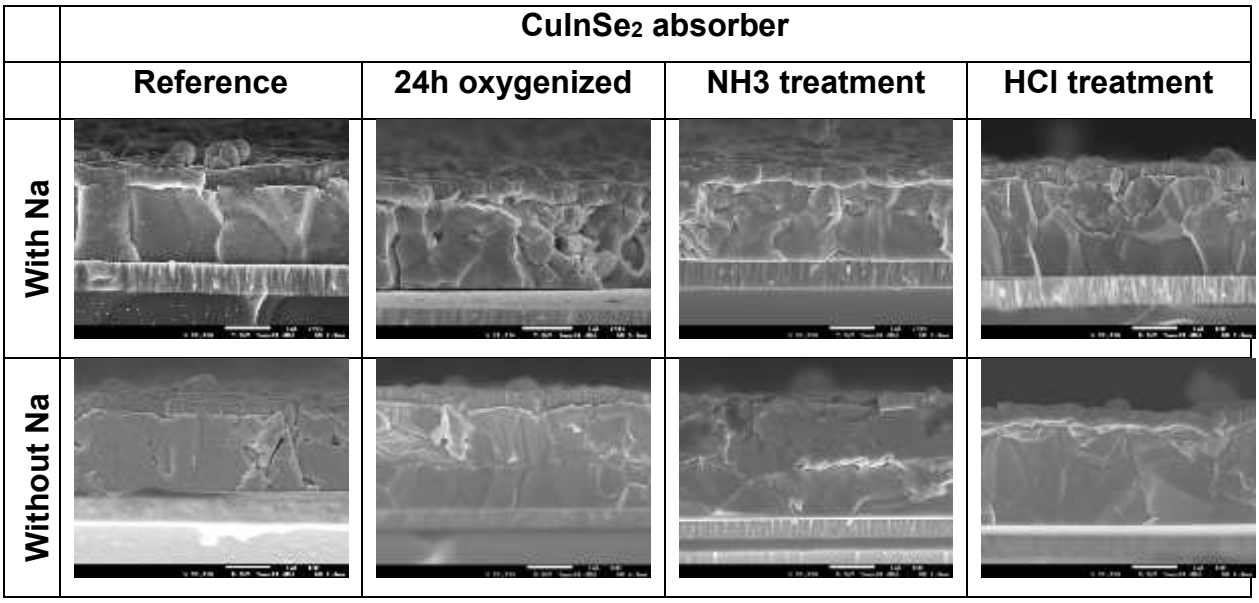

Figure 5.45 SEM cross-section images of the solar cell based on CISe absorbers grown from In_2Se_3-400ºC precursor films: un-annealed (reference), 24h air-annealed, etched with 2.5 M ammonia (NH3) and 0.5 M hydrochloric acid (HCl) solutions.

The previous results show that the electrical and morphological effects of oxygenation treatment on CISe evaporated absorber films are reversible by the chemical surface etching of In2Se3 precursor layers. This reversion is indistinct to the presence or not of sodium in the absorbers. The ammonia and hydrochloric acid treatments eliminate the oxides from films formed during the oxygenation process. The elimination of oxides by NH3 and HCl is also reported elsewhere [75–78]. The removal of oxides after the surface treatments is demonstrated by the improvement of CISe films morphologies and electrical properties of solar cells. Among the used treatments, the HCl etching exhibited the best improvements, probably due to a stronger removal of oxides. The improvement in electrical properties of solar cells after elimination of oxides could be attributed to the restoration of CISe surface band bending and/or the increase of effective carrier diffusion length, this last promoted by the elimination of defects in CISe films.

5.1.3 Conclusion

Growth process of $CuInSe_2$ films

The growth of CuInSe2 absorber films by 3-stage process shows a significant improvement in morphological (e.g. grain size increase) and structural (e.g. decrease of FWHM values) properties of the films during the transition from γ-In_2Se_3 to α-$CuInSe_2$ phase. Indeed, the properties of the CISe absorbers strongly depends on the growth process. To illustrate this, Figure 5.46 shows CISe films deposited by 3-stage and single-stage (see Chapter 2) co-evaporated process. Even though both CISe films has similar final composition in terms of Cu/In~0.9, the quality of the layers significantly differs, being the 3-stage-based film the layer with a better quality (along with an improved solar cell performance). The 3-stage process sequential approach consists in firstly grow a precursor In_2Se_3 layer at a rather low substrate temperature. Secondly supply Cu and Se to In_2Se_3 until the nominal composition of the growing film is Cu-rich (*i.e.* Cu/In>1). Finally, indium is further supplied together with selenium until the nominal composition returns Cu-poor (*i.e.* Cu/In<1), which is a necessary condition to achieve good device performance. The high-quality 3-stage CISe films are attributed to the recrystallization phenomenon occurred during the Cu-poor/Cu-rich transition in the 2^{nd}-stage. The recrystallization involves a reconstruction of the initial layer, which changes its structure from small to large grains while minimizing crystalline defects that may act as recombination centers [22–25]. Thus, the recrystallization of films can dramatically improve the crystalline quality of the precursor layer even if the In2Se3 starting precursor layer have an inferior quality as compared to final films. This last is one of the principal characteristics that promote the 3-stage CIS-based solar cells to yield high conversion efficiencies [21,26].

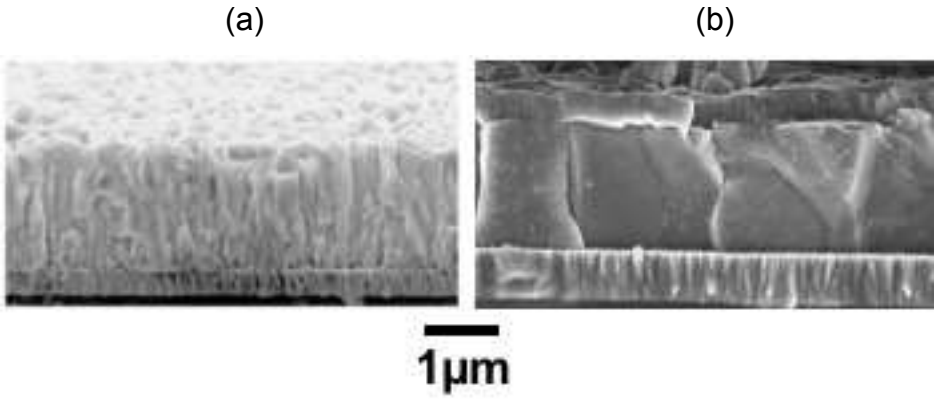

Figure 5.46 SEM cross-section images of the CISe absorbers grown by single-stage (a) and 3-stage (b) process.

An important observation is that the grain size before the recrystallization (i.e. that of the In2Se3 precursor layer) is a factor that affects the extent of changes (e.g. structural, morphological) during the reconstruction of the film. Indeed, the precursor film composed of the smallest grains (e.g. the one deposited at 250°C) is the layer that suffered the greatest grain size increase in comparison to the CISe films obtained from precursors with larger grains (i.e. those deposited at 400°C). Barreau et al. [21] has reported the small-to-large grain transition as a result of the growth of low energetic grains by the consumption of the higher energetic ones, which gives an epitaxial-like growth. This kind of grain growth could be attributed to a grain boundary migration process (GBM) which implicates the transfer of atoms from a consumed grain to a growing grain through a grain boundary [21,30] and originates from the total system energy decrease. Another parameters that affect the morphology and structure of the CISe films are the deposition rate, the excess of copper during the 2nd stage, the selenium evaporation rate, among others [35–37]. The performances of the CISe-based solar cells are also affected by the change of structural and morphological properties of CISe films promoted by the variation of the 1st-stage substrate deposition temperature during the 3-stage growth process. Although the crystalline quality of the films is an important factor, there are other factors that determines the achievement of high-efficiency solar cells such as the presence of sodium and oxygen in the absorber layer. The sodium in the CISe film improves the cell efficiency (mainly by increasing Voc and FF), increases the p-type conductivity, affects

the grain size and preferred orientation [41,42]. The oxygen in CISe layers enhance the net p doping of the absorber, reduces grain boundary recombination, improves the intergrain transport [43,44]. Furthermore, the sodium and oxygen interact each other from a catalytic role that sodium has for the surface oxidation of CISe grains [45].

The effect of oxygen in $CuInSe_2$-based solar cells

Considering the oxygenation of the CISe samples, the air-annealing of In_2Se_3 precursor films has an impact in the morphological (e.g. voids formation) and structural (e.g. change of preferred orientation) properties of the final CISe layers. The FWHM values and the grain size obtained after the recrystallization of the layers seem not to be importantly affected by the annealing process. The XPS results showed the relation between the O1s and Na1s signals, where the higher the sodium signal, the higher the of oxygen peak. This relation can be an evidence of the catalytic effect between oxygen and sodium reported by Kronik et al. [45]. Among the most important species formed during oxygenation process, it is possible to find the In_2O_3, elemental selenium, Na_2SeO_3. The presence of In_2O_3 compound may be related to the passivation of Se vacancies (V_{Se}^{++}), which might be beneficial or detrimental to solar cell operation depending on its location [44,60]. The elemental selenium in CISe has been identified as a detrimental factor leading to the reduction of open voltages and fill factors [61]. The interaction between the Na and O is an important aspect since this promotes the passivation of grain boundaries and create a reservoir of Se for the film to growth [45,51]. The XPS measurements of the also showed that the oxygen, sodium, and the related species, are mostly located on the surface of the layers (within few nanometers).

Considering the catalytic effect between sodium and oxygen, there are two important aspects to consider. In one hand, is has been reported that sodium and oxygen are preferentially transported through grain boundaries [39]. On the other hand, the capacity of Na and O_2 to passivate defects may depend on how well these elements are distributed along the films. As a matter of fact, a proper distribution of theses elements could decouple the GB's beneficial and CISe/CdS interface detrimental passivation.

The crystallinity of the CISe films do not significantly change after the annealing process (same phase, similar FWHM). Nevertheless, a change in preferred orientation is observed, being the films grown at high 1st-stage substrate temperatures the most affected (i.e. 400ºC).

Considering the electrical measurements, it is possible to conclude that the CISe films obtained from In2Se3 films with a “medium” grain boundary densities, i.e. those observed in samples deposited at 250ºC and 325ºC, are more resilient to moderate exposure to oxygen (i.e. one-hour annealing) in comparison with low GB density absorbers. The grain boundaries are indeed an important factor participating in the diffusion of oxygen and sodium. Nevertheless, this is not the only factor affecting the distribution of these elements. In fact, the sodium-oxygen catalytic relation itself is a vital aspect during the passivation of defects.

Role of sodium in the oxygenation of CuInSe2 films

The sodium does not have any impact on the morphological neither structural properties of air-annealed In_2Se_3 precursor films. the influence of Na on the growth of $CuInSe_2$ is taking place only after the deposition of Cu+Se (i.e. 2nd and 3rd stage of 3-stage process).

The XPS spectrums show that the species formed on films without sodium after 24h annealing are mainly related to In_2O_3, $In(OH)_3$, Se^0 and SeO_2. Additionally, it is apparent that the absence of sodium promotes a higher content of In-O compounds (most probably In_2O_3). These compounds are probably accommodated on the In_2Se_3 film near surface region, rather than in the bulk of the precursor films. The oxygen will passivate the dangling bonds related to Se vacancies ($V_{Se,}$ donor defects) and form In_2O_3 compounds on the surface where the CdS/CISe interface will be formed [44,45]. Oxygen passivation at the CdS/CISe interface states can have detrimental or beneficial effects.

The oxygenation of the solar cells prepared with films without sodium (Figure 5.38) showed a greater degradation of its characteristics in comparison with CISe Na-containing cells. It is possible to infer that a probable higher content of oxygen on the surface of the Na-free annealed CISe film could further promote the detrimental effect of the CdS/CISe interface passivation (surpassing the beneficial GB's passivation). Another reason for the detrimental solar cell characteristics can be the related to the junction formation and recombination of charge carriers at the grain boundaries and/or at voids located at half of the CISe film thickness.

From the previous results, it is possible to realize that the presence of sodium in CISe films is vital to minimize the adverse effects of air-annealing treatment (e.g. reduction of positive interface charge, Cu removal) and maximize the beneficial ones (e.g. grain boundary passivation).

It is possible to observe that the Na-free CISe films with high grain boundary densities, i.e. those expected in samples deposited at 250ºC (see section 5.1.1, 5.1.2.2), are more resilient to the exposure of oxygen in comparison with low GB density absorbers (i.e. CISe-400ºC). The high number of GB's could minimize the diffusion of oxygen to the CISe surface and thus diminish the negative effects of oxygenation. This last again confirms that the 1st-stage deposition temperature is indeed an important factor participating in the oxygenation of CISe solar cells.

Finally, the electrical and morphological effects of oxygenation treatment on CISe evaporated absorber films are reversible by the chemical surface etching of In2Se3 precursor layers. This reversion is indistinct to the presence or not of sodium in the absorbers. Among the used treatments, the HCl etching exhibited the best improvements, probably due to a stronger removal of oxides. The improvement in electrical properties of solar cells after elimination of oxides could be attributed to the restoration of CISe surface band bending and/or the increase of effective carrier diffusion length, this last promoted by the elimination of defects in CISe films.

In this work, the highest solar cell efficiency (~12-13%) is achieved with an (110)-oriented γ- In_2Se_3 film precursor with grain size of around 1 μm, obtained at a 1st-stage substrate temperature of 400°C. The use of this precursor results in high-quality (112)-oriented α-CISe film with grains sizes of ~2 μm. Nevertheless, when the absorbers are exposed to oxygen, the γ- In_2Se_3-400°C film is probably not the best option. In case the sample is submitted to an oxygenation process, a viable option could be the use of a In2Se3 film grown at moderate substrate temperatures of 250ºC or 325ºC, which are proven to be more resilient to O_2. Furthermore, in presence of oxygen, precursor films with sodium has to be used in case operative solar cell are needed.

As mentioned in Chapter 1, the advance of Cu(In,Ga)Se2 technology importantly depends (but not only) on addressing the "fundamental" research to develop technology for industrial application. On the other hand, to develop CIGSe technology, it is compulsory to try to reduce the production cost. Taking into consideration all the previous results, this work attempts to develop an alternative CIGSe thin film growth process proposal which try to address low-cost non-vacuum and high efficiency vacuum deposition techniques, the use of less pure precursors materials (cheap and easy to store) and envisage an increase of material-utilization. In next section of this Chapter, the proposal of the alternative growth method is exposed.

5.2 Growth of $CuInSe_2$ films by hybrid process

As mentioned previously, the 3-stage growth process implies a abrupt mean grains size expansion (recrystallization) of the growing film during Cu-poor to Cu-rich transition at the end of the 2nd stage [24,25]. The recrystallization phenomenon is essential for the achievement of high efficiency. In this phenomenon the most stable grains grow at the expense of least stable ones, which are consumed through grain boundary motion [21]. As a consequence, the crystalline and electrical properties of the CIGSe layers are drastically changed during Cu-poor to Cu-rich transition. This suggests that the characteristics of the initial film (precursor) could be highly improved at the end of the

growth process, which highlight the existence of a wide window of structural and electrical properties of the In_2Se_3 precursor films that could result on high-quality CIGSe absorbers.

During the 3-stage process, the Cu-poor/Cu-rich transition occurs when at least 50 % of the total thickness of the absorber is already deposited. Considering the integration of the 3-stage process to a low-cost concept, the last signifies that 50 % of the layer could be deposited very fast, as already proposed by Painchaud et al. [80], or by using another growth technique different than co-evaporation, such as non-vacuum deposition. Moreover, if the effect of the recrystallization phenomenon on the improvement of structural and electrical properties of precursor layers is considered, a range of opportunities for new deposition processes development is created.

The hybrid approach proposed in this work, combines chemical spray pyrolysis (non-vacuum) and co-evaporation (vacuum) deposition techniques, offering opportunities to use of less pure precursors materials, probably increase material-utilization with future possibilities of increasing production throughputs in comparison with the conventional co-evaporation technique. The chemical spray pyrolysis deposition represents a good option for this hybrid process since it possesses the advantages of low-cost equipment, high material-utilization efficiency, and easy scale-up. The co-evaporation deposition also denotes a great choice considering the recrystallization phenomenon occurred during the growth of films and the resulting high efficiencies of the resulting solar cells. In this work, the study of hybrid process is primary focused on the co-evaporation growth conditions, keeping fixed deposition conditions for the chemical spray pyrolysis technique.

5.2.1 Details of the study

In this study, the chemical spray pyrolysis (CSP) has been used to deposit In_2Se_3 precursor films on SLG/Mo substrates. The experimental setup mainly consists of a substrate heater (molten tin bath), a precursor solution container, an atomizer (gas and solution outlet nozzle) and a temperature control system (temperature controller, thermocouple). The In_2Se_3 deposited by CSP were grown at a substrate temperature of

380 °C. The substrate temperature was monitored by a thermocouple located on the backside of the glass substrate. The sprayed solutions contain $InCl_3$ (0.0015 M) and N-N-dimethyl-selenourea (DMSeU, 0.0055 M) diluted in ethanol aqueous solution (20 vol.%). Excess DMSeU compared to the stoichiometric composition (1:2) was provided to compensate eventual losses due to the volatile nature of selenium in the deposition conditions (e.g. high substrate temperature). The desired pH (4-5) of the solution was achieved through the addition of HCl. The total volume of the solution was sprayed at a rate of 6.5 ml/min with nitrogen as the carrier gas with a flow rate of 1.5 l/min and a nozzle-to-substrate distance of 20 cm. These parameters yield films thickness of ~1 µm after 90 min of deposition. It is important to point out that the deposition speed was not the issue in this work. These layers are referenced to as CSP- In_2Se_3 in the following.

Additionally, In_2Se_3 films have also been thermally co-evaporated on a SLG/Mo substrate. The In_2Se_3 films were deposited at a substrate temperature of 380 °C under high vacuum (10^{-4} Pa). The SLG/Mo substrates were heated with the help of halogen lamps, and the temperature was controlled by a thermocouple at the backside of the glass substrate. During the evaporation process, the temperature of In and Se sources were kept at 1010 °C and 285 °C, respectively. The metals, as well as selenium, were evaporated from elemental sources heated by Joule effect; the elements fluxes were indirectly controlled by the temperature of the effusion cells. These layers are referenced to as PVD-In_2Se_3 in the following.

The 1st-stage-equivalent CSP-In_2Se_3 and PVD-In_2Se_3 layers was introduced into the high-vacuum co-evaporation chamber to complete the CISe synthesis by performing the 2nd (i.e. Cu + Se flux) and 3rd (i.e. In + Se flux) stages. The substrates temperature during these 2nd and 3rd steps was 500 °C. It is important to highlight that the CSP-In_2Se_3 layers were exposed to Se-flux for 30 min at 400 °C before the realization of 2nd and 3rd stages. The resulting $CuInSe_2$ layers are referenced to as CSP/PVD and PVD/PVD absorbers relative to the In_2Se_3 deposition technique. In this work, the PVD/PVD process could be considered as a suspended 3-stage procedure, whose purpose is to serve as a reference

representing a situation close to the occurred in the hybrid deposition method (also an interrupted process).

Additionally, $CuInSe_2$ layers were grown following the conventional 3-stage process, with a substrate temperature of 380 °C and 550 °C during 1st and 2nd/3rd stages (respectively), and referenced to as 3-stage-$CuInSe_2$. For all kinds of absorbers, the end-point detection method was used to detect Cu-poor/Cu-rich and Cu-rich/Cu-poor transitions.

The impact of the substrate temperature at the initial growth stage is described at the absorbers level and solar cells through the scanning electron microscopy (SEM), X-ray diffraction (XRD), voltage-current (J-V) and external quantum efficiency (QE) measurements. The end-point detection method was used to detect Cu-poor/Cu-rich and Cu-rich/Cu-poor transitions and final ratios subsequently were measured by energy dispersive spectroscopy (EDS). Figure 6.12 shows the EPD signal (Output Power vs deposition time) of the 2nd and 3rd stage of the deposition process. The thicknesses of final films were obtained with a profilometer equipment.

5.2.2 Morphological and structural properties of In_2Se_3 precursor film deposited by chemical spray deposition

Table 5.15 Composition analysis of as-prepared and selenized CSP-In_2Se_3 and PVD-In_2Se_3 thin films and the respective Se/In relative ratio without considering the oxygen content.

Sample	In (at%)	Se (at%)	Se/In
Selenized CSP-In_2Se_3	43.26 (±1.13)	56.74 (±0.57)	1.31
As-prepared CSP-In_2Se_3	44.44 (±1.28)	55.57 (±0.56)	1.25
PVD-In_2Se_3	42.91 (±1.08)	57.08 (±0.66)	1.33

Table 5.15 shows the mean chemical composition of CSP- and PVD-In_2Se_3 precursor films determined by energy dispersive spectroscopy. During the deposition, both samples were prepared in the sense of having the same Se/In ratio of 1.5. Even though the measurements of both films revealed similar indium and selenium values, a slight decrease of Se content in the CSP- In_2Se_3 film is observed. This decrease is due to the re-evaporation of highly-volatile Se from the heated substrate to the open-air atmosphere during the chemical spray deposition. The PVD- In_2Se_3 layers exhibited higher Se content but the overall compositions are slightly deviated from the desired stoichiometry (Se/ In=3/2). Thus, considering the re-evaporation of selenium, is possible to assume the formation of more Se vacancies (V_{Se}) in the CSP films in comparison with PVD precursor layers.

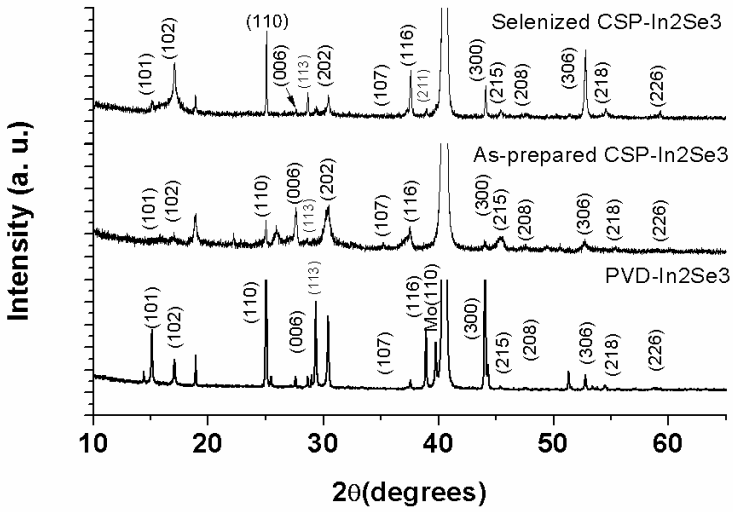

Figure 5.47 X-ray diffraction pattern of PVD-In_2Se_3, CSP-In_2Se_3 as-prepared and selenized CSP-In_2Se_3 precursor films.

The crystalline properties of both types of films were studied by XRD. Figure 5.47 shows the diffractogram of the PVD-In_2Se_3 along with the as-prepared and selenized CSP-In_2Se_3 thin films grown on Mo/SLG. The CSP and PVD films exhibited diffraction peaks related to polycrystalline γ-In_2Se_3 phase with a hexagonal structure (JCPDS #40-1407) [7]. Table 5.16 shows the textures of the measured films determined through Lotgering factors. In this work, eight planes namely (101), (112), (103), (211), (220), (204), (312)

and (116) were considered for the calculation. Films with *F(112)* ≤ |0.2| and *F(220/204)* ≤ |0.2| are deemed to have a random texture. The PVD- In_2Se_3 films have shown (110) preferential orientation (Table 5.16) with weak (006) line. The full width at half maximum (FWHM) of the (110), (006) and (300) peaks were 0.07º, 0.09º and 0.10º, respectively. The as-prepared CSP-In_2Se_3 films (figure 5.47) exhibited a random orientation (see Table 5.16) with a strong (006) line and weak (110) and (300) lines. The FWHM of the corresponding (110), (006) and (300) peaks were 0.10 º, 0.20 º and 0.15º, respectively. The XRD patterns of both, CSP and PVD samples reveal changes in crystal orientation with random and (110)-oriented films, respectively. One reason for the change in preferential orientation could be related to a lower growth temperature in the CSP deposition as compared to the PVD. It has been reported that during the CSP deposition, the substrate temperature in the vicinity of the front surface is lower (ΔT=50 °C/mm) than the back of the substrate where the thermocouple is located [81]. This decrease is due to the difference in temperature of the sprayed precursor solution (room temperature) and the substrate temperature (380 °C). Thus, the substrate temperature during CSP deposition is lower than 380 °C. This lower substrate temperature condition during CSP deposition decreases the surface diffusion of the adsorbed atoms, promoting the formation of a high density of nuclei and thus resulting in a fined grain material with a tendency to a (006) preferred orientation. Mise et al. [3] have reported a similar behavior of $(In,Ga)_2Se_3$ films prepared by PVD at low deposition substrate temperatures. A difference in temperature is also observed in the PVD process, but this is lower than in CSP deposition, owing to the elevated temperatures of the evaporated materials reaching the substrate (T_{In}=1010 °C and T_{Se}=285 °C). Due to this higher substrate temperature, the surface mobility of adsorbed atoms is superior for PVD films in comparison to CSP layers. This higher surface mobility will allow to obtain large columnar grains of an (110) preferred orientation. Another reason for the change in preferred orientation could be the presence of extrinsic impurities incorporated into the In_2Se_3 material during the CSP deposition (e.g. oxygen, sodium). These impurities could promote the formation and stabilization of fined grain structures and certain changes in preferred orientations through faceted nuclei formation [42,82]. In fact, a previous work [83] reported the incorporation of sodium and oxygen extrinsic impurities into the In_2Se_3 films during the CSP deposition.

Moreover, in the same work, it was found a higher Na and O content in CSP films compared to PVD layers. In the CSP-In_2Se_3 films, sodium and oxygen could promote the formation of fine-grained and random oriented layers.

Table 5.16 Lotgering factors *F*(110), *F*(006) and *F*(300) of CSP- and PVD- In_2Se_3 precursor films.

Sample	*F*(110)	*F*(006)	*F*(300)	Texture
Selenized CSP-In_2Se_3	0.126	-0.147	-0.12	Random
As-prepared CSP-In_2Se_3	0.034	0.102	-0.152	Random
PVD- In_2Se_3	0.47	-0.115	0.108	(110)

Cahen and Noufi [43] have reported the passivation of Se vacancies (surface dangling bonds) in the presence of oxygen. The passivation could be attributed to a vacant Se site occupied by negatively charged oxygen atoms. The oxygen bonds to indium and forms an In_2O_3 compound on the surface of the films (including grain boundaries). The passivation of grain boundaries (GB's), among other effects, has a detrimental impact on devices due to enhancing of interface recombination at the CdS/CISe heterojunction [43]. Furthermore, a high concentration of In_2O_3 in GB's could affect the recrystallization of the CISe films [84]. Barreau et al. [21] suggested the hindering of grain boundary migration of CISe films caused by the presence of impurities at the GB's at certain concentrations. Thus, to have a successful recrystallization of the CISe material, it is desirable to reduce or eliminate the impurities present at grain surfaces. It has been reported that the In_2O_3 could be reduced or removed by a heat treatment under highly toxic H_2Se [85] or Se atmosphere [86]. The figure 5.47 shows the XRD pattern of the CSP-In_2Se_3 film after selenization treatment at 400 ºC for 30 min. As observed in CSP-In_2Se_3 as-prepared film, the selenized layer also exhibited diffraction peaks related to γ-In_2Se_3 crystalline phase (JCPDS #40-1407). In this pattern, it is also possible to observe the crystallization of the selenized CSP-In_2Se_3 film. The crystallization is denoted by the FWHM decrease of the (110), (006) and (300) peaks (0.08º, 0.11º, 0.12º, respectively) compared to the CSP as-

prepared layers (0.10º, 0.20º, 0.15º, respectively). Nevertheless, there was no a change of preferred orientation, with a remained randomly oriented film, with a possible tendency to a more (110)-oriented selenized layer. Emziane et al. [87] also observed the crystallization and change in orientation of γ -In_2Se_3 films thermally treated under selenium atmosphere at substrate temperatures of 400 ºC for 30 min. It should be noticed that in a 3-stage-based process, the preferred orientation of final $CuInSe_2$ absorber film could be affected by the orientation of the In_2Se_3 precursor layer and the availability of Na during the growth [3,21].

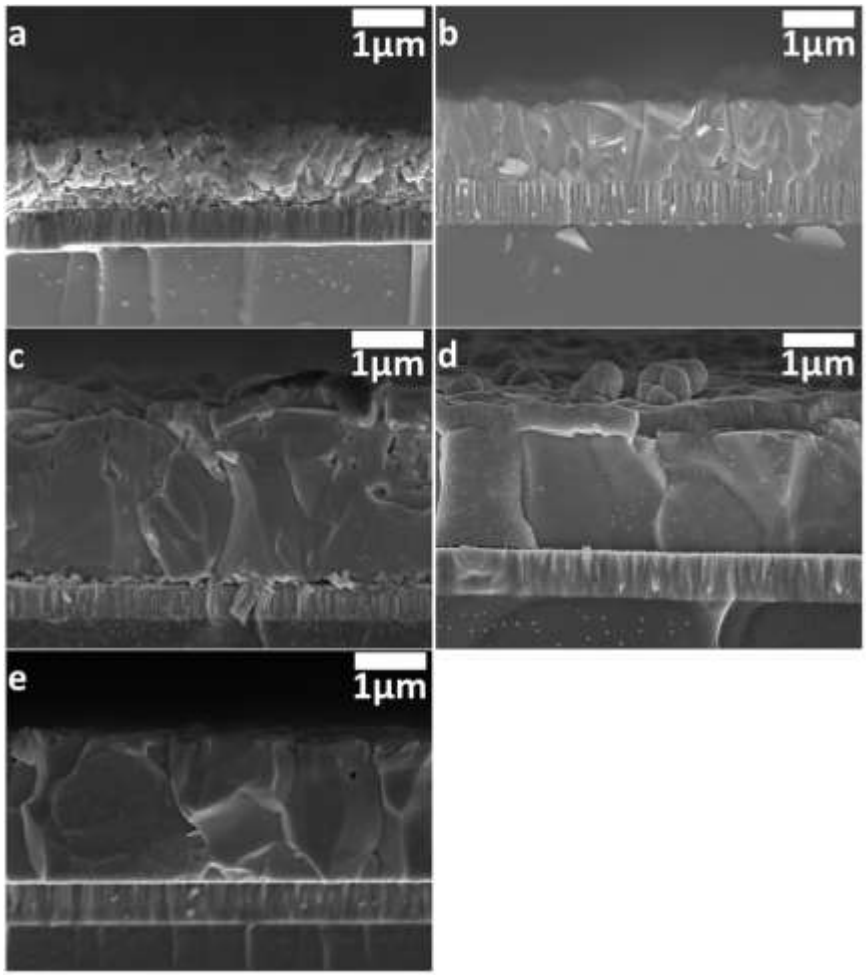

Figure 5.48 SEM cross section images of

(a) Mo/CSP-In_2Se_3

(b) Mo/PVD-In_2Se_3

(c) CSP/PVD-$CuInSe_2$ based solar cell

(d) PVD/PVD-$CuInSe_2$ based solar cell

(e) 3-stage-$CuInSe_2$ grown on SLG/Mo

Figure 5.48a and 5.48b show scanning electron microscopy (SEM) cross-section images of PVD- and selenized CSP-In_2Se_3 samples. The selenized layer exhibits smaller grains (<0.6 µm) and more voids than the PVD-In_2Se_3 reference film. This fine-grained film structure is in agreement with the discussed in the XRD section. The CSP deposition conditions are such that the surface diffusion of atoms is limited. Thus, the film structure is obtained from a high density of new nuclei created on the top of the already created ones, such that the grain growth of the first-layer nuclei does not take place. The voids in CSP film could be related to the impurities (e.g. sodium, vacancies) within the layer, which could agglomerate during the deposition and post-deposition thermal treatment. It is also possible to observe even smaller grains close to the Mo back contact of the selenized CSP-In_2Se_3 film. Its origin is still not clearly identified but could be related to the formation of impurities (e.g. oxides) at the beginning of the spray pyrolysis deposition [88] and/or incomplete propagation of Se during the thermal treatment [84]. This selenized film is used later on in the hybrid deposition process.

Even though the composition of the selenized CSP- In_2Se_3 ayer is closer to the one of the PVD layer, this is still slightly Se-deficient compared to the expected stoichiometry (Table 5.15). The composition of the PVD-In_2Se_3 is also Se-deficient although the SEM cross section (figure 5.48b) exhibits well-defined densely packed columnar structure with grains height in the order of the layer thickness.

5.2.2.1 Formation and recrystallization of $CuInSe_2$ layer

Figure 5.48c and 5.48d show SEM cross-sections of the completed solar cells with CSP/PVD-$CuInSe_2$ and PVD/PVD-$CuInSe_2$ absorbers, respectively. Notably, both absorber layers are made of large and packed grains similar to those of the 3-stage-$CuInSe_2$ shown in figure 5.48e. The grains of CSP/PVD absorber are remarkably much bigger than what they were in CSP-In_2Se_3 precursor film, and no more voids are visible. The volume expansion of grains is an evidence of the thin film recrystallization. This change in morphology supports the fact that the recrystallization is effectively a key step

of the 3-stage process and that the hybrid process approach (non-vacuum/vacuum) is relevant, at least concerning films morphology. The CSP/PVD- $CuInSe_2$ (figure 5.48c) also reveals the presence of fine-grained thin layer (100 nm thick) close to the Mo back contact, as in the case of the CSP-In_2Se_3. Selenized CISe absorbers deposited by different non-vacuum processes also showed such fine-grained layer [84,88]. In these studies, the layer could be attributed to the presence of impurities (e.g. oxides) or incomplete propagation of Se during the treatment. Despite the formation of this fine-grained layer, no adhesion problems were observed in CSP/PVD CISe films, being this comparable to PVD/PVD absorbers. Simichi et al. reported similar adhesion results of CISe films deposited on Mo-O compounds [89]. The compositions of absorbers films (Table 5.16) did not reveal obvious differences that could shade light on the nature of the fine-grained interface layer. All films have a Cu to In atomic ratio between 0.8 and 0.9 and Se content very close to that expected by the 1:1:2 stoichiometry of the chalcopyrite phase.

Figure 5.49a and 5.49b show the Raman scattering spectra acquired from Mo surfaces after peeling off the 3-stage-$CuInSe_2$ and CSP/PVD-$CuInSe_2$ films, respectively. Figure 5.49a shows the typical spectra of the $MoSe_2$ compound, formed in the 3-stage as well as in the PVD/PVD samples, which is commonly found in high efficiency CISe-based solar cells. The presence of oxygen at the back-contact surface was confirmed for the CSP/PVD sample (figure 5.49b). The spectra peaks reveal the formation of MoO_2 compound, which opens the possibility of the formation of a CISe/MoO_2/Mo interface. This interface promotes the construction of a Schottky-type barrier [90] which limits the reachable conversion efficiency by reducing the open circuit voltage of the solar cell [91,92].

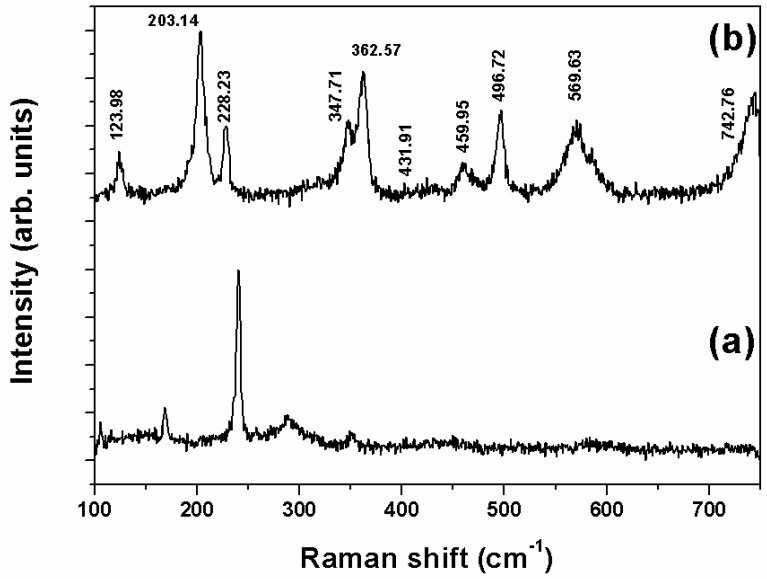

Figure 5.49 Raman spectrum of the molybdenum surfaces corresponding to the (a) 3-stage-$CuInSe_2$ and (b) CSP/PVD- $CuInSe_2$ solar cells.

With the goal to foreground the structural properties of the CISe film prepared by the hybrid process, figure 5.50 shows the XRD pattern of CSP/PVD-$CuInSe_2$ layer. The figure testifies the complete phase transformation during the hybrid deposition process from γ-In_2Se_3 (CSP) to α-$CuInSe_2$ (CSP/PVD) without any clear evidence of secondary phases (JCPDS #40-1487). The FWHM of the (112) peak is 0.06 and 0.05 for the CSP/PVD and 3-stage films, respectively. The $FWHM_{(112)}$ of the 3-stage and PVD/PVD CISe layers are quite similar. The main difference between the CSP/PVD layer XRD pattern and those of the $CuInSe_2$ films fully co-evaporated (3-stage and PVD/PVD, not showed here) concerns the preferential orientation of the grains. Table 5.17 lists the textures of the measured films determined through Lotgering factors. The orientation factor of CSP/PVD-CISe film for the (112) plane is closer to 1, resulting in an (112)-preferred orientation. Furthermore, the *F(hkl)* factor for the (112) plane of the 3-stage-CISe film importantly decreases, culminating in a randomly oriented film. These results reveal that the final orientation of CISe films strongly depends on the type of In_2Se_3 precursor layers used during the growth process, either deposited by chemical spray pyrolysis or co-evaporation technique. These

differences in the texture of the final CISe films are mainly related to the preferential orientation of CSP- and PVD- In_2Se_3 films and the presence of impurities (e.g. sodium) in the CISe layers [3,21]. Effectively, the highly (112)-oriented CSP/PVD CISe could be due to a higher Na content coming from the CSP-based layers[83] and promoted by the presence of O during the spray of In_2Se_3 in air (Na-O catalytic effect) [45].

Table 5.17 Lotgering factors *F*(112), *F*(220) and *F*(204) and texture of CSP/PVD and 3-stage-$CuInSe_2$ absorber films.

Sample	Cu (at%)	In (at%)	Se (at%)	Cu/In
CSP/PVD-$CuInSe_2$	24.98 (±0.58)	26.69 (±1.49)	48.34 (±0.41)	0.93
PVD/PVD-$CuInSe_2$	23.63 (±0.62)	27.76 (±1.24)	48.60 (±0.50)	0.85
3-stage-$CuInSe_2$	23.01 (±0.77)	28.37 (±1.67)	48.61 (±0.62)	0.81

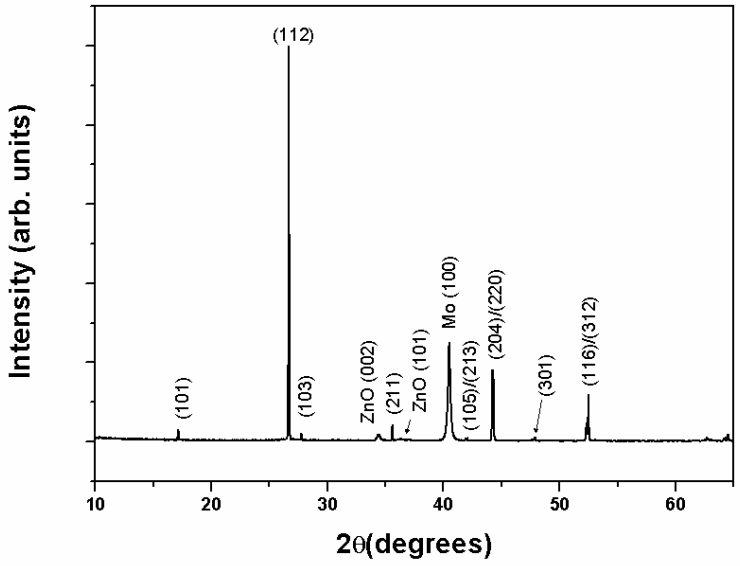

Figure 5.50 X-ray diffraction pattern of CSP/PVD- $CuInSe_2$ absorber film.

5.2.2.2 $CuInSe_2$-based solar cells

Solar cells have been prepared from all of these SLG/Mo/$CuInSe_2$ structures. Figure 5.51a shows the $J(V)$ curves under illumination (AMG1.5, 100 mW/cm², 25 °C) of the best cells achieved within the frame of this study (without anti-reflective coating). The respective external quantum efficiencies are plotted in figure 5.51b. The efficiency reached by the cells with CSP/PVD absorber is 11.1 %, which is very close to those reached by PVD/PVD (12.0 %) and 3-stage absorbers (13.1 %). The main difference between these cells parameters concerns their open circuit voltage (V_{oc}) and fill-factor (FF), whereas the short-circuit current densities (J_{sc}) are similar. The previous results suggested a high Na concentration (related to the Kronik model) denoted by a highly (112)-oriented CSP/PVD-CISe absorber. Thus, the carrier concentration (i.e. acceptor concentration) of the CSP/PVD absorber is likely to be higher than that of PVD/PVD and 3-stage CISe films. Therefore, a higher V_{oc} of CSP/PVD-CISe solar cell is expected. However, the current-voltage measurements (figure 5.51) showed the lowest V_{oc} of the three solar cells. In order to further explore the possible origins of reduced V_{oc} and FF, the $J(V)$ curves of figure 5.51a have been fitted using the one-diode model. Calculation using an algorithm under Matlab platform allows the evaluation of the diode saturation current (J_0) and ideality factor (A), as well as series and shunt resistances; the values are given in Table 5.18.

Table 5.18 Diode saturation current (J_0), ideality factor (A), series (R_s) and shunt (R_{sh}) resistances determined from the fit of the J(V) curves under standard conditions of testing

	J_0 [A/m²]	A	R_s [Ωcm²]	R_{sh} [Ωcm²]
CSP/PVD	1.9 E-7	1.40	6.1 E-1	360
PVD/PVD	8.7 E-10	1.02	7.7 E-1	220
3-stage	3.8 E-9	1.13	6.7 E-1	638

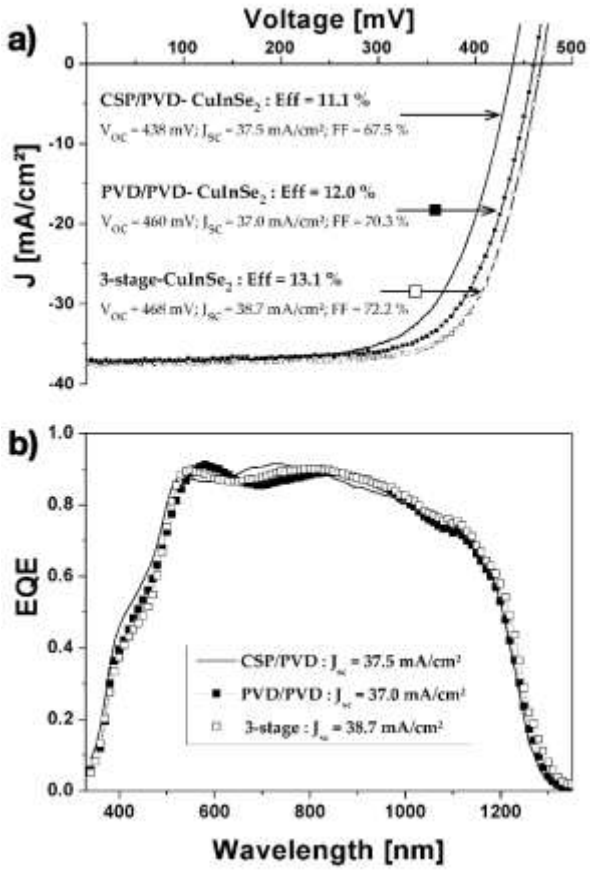

Figure 5.51 (a) Current-voltage and (b) external quantum efficiency of the best cells investigated in this study.

These results suggest higher J_0 and A in the case of the CSP/PVD-$CuInSe_2$ compared to the others, whereas series and shunt resistances are similar. To understand the relation of these values with the results showed in the current-voltage measurements (figure 5.51), is important to consider the diode equation 5.4 for a circuit solar cell model, [93]

$$J = J_0 exp\left[\frac{q}{nKT}(V - RJ)\right] + GV - J_{IL} \qquad \text{(eq. 5.4)}$$

were J is the diode current density, V is the diode voltage, J_0 is the diode saturation current density, n is the diode quality factor, q is the electron charge, k is the Boltzmann constant, T the temperature, R is the series resistance, G is the shunt conductance, and J_{IL} is the photocurrent density. From equation (5.4) and considering a $J_{IL} \sim J_{sc}$ (were Jsc is the short-

circuit current density) and that $GV_{oc}<<J_{sc}$, it is possible to obtain an approximation for the V_{oc} such that [93]

$$V_{oc} \approx \frac{nkT}{q} ln\left(\frac{J_{sc}}{J_0}\right) \qquad \text{(eq. 5.5)}$$

From equations (5.4) and (5.5), it is possible to observe that *n* and J_0 are limiting elements for the increase of the solar cell performance. The lower V_{oc} value of the CSP/PVD-CISe solar cell could be related to the higher J_0 value (2-3 orders of magnitude) compared to the PVD/PVD and 3-stage devices. The J_0 could be considered as [93]:

$$J_0 = qN_C N_V \left(\frac{1}{N_A}\sqrt{\frac{D_n}{\tau_n}} + \frac{1}{N_D}\sqrt{\frac{D_p}{\tau_p}}\right) exp\left(\frac{-E_g}{kT}\right) \qquad \text{(eq. 5.6)}$$

were $N_{C,V}$ are the conduction and valence band density of states, $N_{D,A}$ are the donor and acceptor concentrations, $D_{n,p}$ are the electron and hole diffusion coefficients and $\tau_{n,p}$ are the electron and hole minority-carrier lifetimes in the p and n side of the junction, respectively. Considering the values of table 5.18 and the J_0 value of the CSP/PVD solar cell, it could be proposed that the change in the physical properties of the CSP/PVD-CISe material (e.g. $N_{D,A}$ in/or near the buried pn junction, change in τ_n due to defects) or a different recombination mechanism compared to the fully co-evaporated devices are probably the reason for the lowered V_{oc}. This can be further interpreted as less suitable grain material and/or grain boundary characteristics for photovoltaic applications of the CSP/PVD layer compared to the layers grown by co-evaporation exclusively.

Considering the recombination mechanisms, it is necessary to considerer the diode quality factor (*n*). Values of n close to 1 indicate a recombination in the neutral regions, values close to 2 represent space-charge region (SCR) recombination and *n* values grater than 2 indicates a tunneling recombination mechanisms. It is found that for the CISe solar cells, the efficiency improvement is related to the decrease of the *n* values (e.i. SCR recombination decreases). The higher *n* value of the CSP/PVD-CISe solar cell could

indicate a stronger trend to have SCR recombination (thus lower performance) compared to the fully evaporated devices.

The lower performance of CSP/PVD devices, could be related to the increase in defect density, stronger SCR recombination, changes in physical properties of the CISe and/or in the pn junction. These conditions open new rooms for the improvement of efficiencies of this hybrid deposition approach, through the enhance of the absorber crystalline quality (optimization of deposition process), the development of surface treatments and the study of the Na-O_2 relation

5.2.3 Conclusion

This work has for the first time demonstrated the opportunity of growing $CuInSe_2$ absorbers on SLG/Mo following a hybrid approach combining non-vacuum and vacuum techniques. This process consists in firstly forming an In_2Se_3 layer (*i.e.* 1st-stage) using chemical spray pyrolysis performed in ambient atmosphere and secondly in completing the $CuInSe_2$ film by co-evaporation under vacuum (*i.e.* 2nd- and 3rd-stage). The In_2Se_3 precursor layers with same crystalline structure could be obtained by both CSP and PVD techniques. However, the films were differentiated by its own preferential orientation and morphology. This difference is related to the different growth rate limit step (stablished mostly by temperature, pressure and supersaturation) existing in each deposition technique and the possible extrinsic impurities introduced into the film. The growth rate in CSP-In_2Se_3 film deposition is limited by surface diffusion, showing a fine-grained structure. The growth in PVD- In_2Se_3 film is also limited by diffusion but to a lesser extent, exhibiting a columnar-grained structure. Another important issue in differentiating the morphology and orientation of the films is the presence of sodium (from substrate) and oxygen (from atmosphere), which definitely has an impact on nucleation and grain growth. The final absorber layer exhibited a relation with the precursor layers. The most noted relation is the highly (112)-oriented CISe films prepared with the CSP precursors, which in turn have higher content of oxygen and sodium. Further investigations on the growth

conditions could enlighten how the extrinsic impurities impact on the final absorber layer and device. The proposed hybrid process has demonstrated its relevance since devices prepared with such hybrid-absorber layer have reached outstanding conversion efficiency of 11.1 %. The performance appears still limited in comparison to the $CuInSe_2$ absorbers grown by the regular 3-stage process. Further works are needed to fully understand the limitations of these devices and improve their performance. These results highlight the possibility of using precursor layers deposited by different non-vacuum techniques, focusing in the improvement of the deposition process (e.g. material utilization efficiency).

References

[1] A.M. Gabor, J.R. Tuttle, D.S. Albin, M.A. Contreras, R. Noufi, A.M. Hermann, High-efficiency $CuIn_xGa_{1-x}Se_2$ solar cells made from $(In_x,Ga_{1-x})_2Se_3$ precursor films, Appl. Phys. Lett. 65 (1994) 198–200. doi:10.1063/1.112670.

[2] S. Nishiwaki, T. Satoh, S. Hayashi, Y. Hashimoto, T. Negami, T. Wada, Preparation of $Cu(In,Ga)Se_2$ thin films from In-Ga-Se precursors for high-efficiency solar cells, J. Mater. Res. 14 (1999) 4514–4520. doi:10.1557/JMR.1999.0613.

[3] T. Mise, T. Nakada, Microstructural properties of $(In,Ga)_2Se_3$ precursor layers for efficient CIGS thin-film solar cells, Sol. Energy Mater. Sol. Cells. 93 (2009) 1000–1003. doi:10.1016/j.solmat.2008.11.028.

[4] S. Ishizuka, A. Yamada, P. Fons, S. Niki, Texture and morphology variations in $(In,Ga)_2Se_3$ and $Cu(In,Ga)Se_2$ thin films grown with various Se source conditions, Prog. Photovoltaics Res. Appl. 21 (2013) 544–553. doi:10.1002/pip.1227.

[5] B.A. Movchan, A. V. Demshishin, Study of the structure and properties of thick vacuum condensates of nickel, titanium, tungsten, aluminium oxide and zirconium dioxide, Phys. Met. Met. (Engl. Trans.). 28 (1969) 83–90.

[6] F.K. Lotgering, Topotactical reactions with ferrimagnetic oxides having hexagonal crystal structures, J. Inorg. Nucl. Chem. 9 (1959) 113–123. doi:10.1016/0022-1902(59)80070-1.

[7] A. Likforman, Structure Cristalline du Seleniure d ' Indium In2Se3, Acta Crystallogr. 34 (1978) 1–5.

[8] A. Likforman, P.H. Fourcroy, M. Guittard, J. Flahaut, R. Poirier, N. Szydlo, Transitions de la forme de haute temperature de In_2Se_3, de part et d'autre de la temperature ambiante, J. Solid State Chem. 33 (1980) 91–97. doi:10.1016/0022-4596(80)90551-4.

[9] H.D. Lutz, M. Fischer, H.P. Baldus, R. Blachnik, Zur polymorphie des In_2Se_3, J. Less-Common Met. 143 (1988) 83–92. doi:10.1016/0022-5088(88)90033-1.

[10] F. Hergert, S. Jost, R. Hock, M. Purwins, A crystallographic description of experimentally identified formation reactions of $Cu(In,Ga)Se_2$, J. Solid State Chem. 179 (2006) 2394–2415. doi:10.1016/j.jssc.2006.04.033.

[11] J.-B. Li, M.-C. Record, J.-C. Tedenac, A Thermodynamic Assessment of the In–Se System, Zeitschrift Für Met. 94 (2003) 381–389. doi:10.3139/146.030381.

[12] M.A. Contreras, B. Egaas, D. King, A. Swartzlander, T. Dullweber, Texture manipulation of $CuInSe_2$ thin films, Thin Solid Films. 361 (2000) 167–171. doi:10.1016/S0040-6090(99)00778-6.

[13] A. Rockett, Surface analysis of chalcopyrite materials for photovoltaics, Prog. Photovoltaics Res. Appl. 20 (2012) 575–581. doi:10.1002/pip.2205.

[14] C. Lei, a. Rockett, I.M. Robertson, W.N. Shafarman, M. Beck, Void formation and surface energies in $Cu(InGa)Se_2$, J. Appl. Phys. 100 (2006) 73518. doi:10.1063/1.2357422.

[15] J.S. Chen, E. Kolawa, C.M. Garland, M.A. Nicolet, R.P. Ruiz, Microstructure of polycrystalline $CuInSe_2$/Cd(Zn)S heterojunction solar cells, Thin Solid Films. 219 (1992) 183–192. doi:10.1016/0040-6090(92)90741-S.

[16] C. Li, C. Lei, I. Robertson, A. Rockett, Microstructural and microchemical analysis of chalcopyrite $Cu(In,Ga)Se_2$ films, MRS Proc. 763 (2003) 1–6. http://journals.cambridge.org/abstract_S1946427400133305.

[17] A. Werner, I. Luck, J. Bruns, J. Klaer, K. Siemer, D. Bra, Investigation of the influence of silver on the crystal growth of $CuInS_2$ thin films, Thin Solid Films. 362 (2000) 88–92.

[18] T.B. Massalski, Binary Alloy Phase Diagrams, 1990.
[19] H. Rau, A. Rabenau, Vapour pressure measurements in the copper-selenium system, J. Solid State Chem. 1 (1970) 515–518. doi:10.1016/0022-4596(70)90135-0.
[20] F. Couzinié-Devy, N. Barreau, J. Kessler, Re-investigation of preferential orientation of Cu(In,Ga)Se_2 thin films grown by the three-stage process, Prog. Photovolt Res. Appl. 19 (2011) 527–536. doi:10.1002/pip.
[21] N. Barreau, T. Painchaud, F. Couzinié-Devy, L. Arzel, J. Kessler, Recrystallization of CIGSe layers grown by three-step processes: A model based on grain boundary migration, Acta Mater. 58 (2010) 5572–5577. doi:10.1016/j.actamat.2010.06.025.
[22] J.R. Tuttle, M. Contreras, A. Tennant, D. Albin, R. Noufi, High efficiency thin-film Cu(In,Ga)Se_2-based photovoltaic devices:Progress towards a universal approach to absorber fabrication, (1993).
[23] J. Kessler, C. Chityuttakan, J. Lu, J. Sch??ldstr??m, L. Stolt, J. Schöldström, L. Stolt, Cu(In,Ga)Se_2 thin films grown with a Cu-poor/rich/poor sequence: Growth model and structural considerations, Prog. Photovoltaics Res. Appl. 11 (2003) 319–331. doi:10.1002/pip.495.
[24] H. Rodriguez-Alvarez, N. Barreau, C.A. Kaufmann, A. Weber, M. Klaus, T. Painchaud, H.W. Schock, R. Mainz, Recrystallization of Cu(In,Ga)Se_2 thin films studied by X-ray diffraction, Acta Mater. 61 (2013) 4347–4353. doi:10.1016/j.actamat.2013.04.006.
[25] H. Rodriguez-Alvarez, A. Weber, J. Lauche, C.A. Kaufmann, T. Rissom, D. Greiner, M. Klaus, T. Unold, C. Genzel, H.W. Schock, R. Mainz, Formation of $CuInSe_2$ and $CuGaSe_2$ thin-films deposited by three-stage thermal co-evaporation: A real-time X-ray diffraction and fluorescence study, Adv. Energy Mater. 3 (2013) 1381–1387. doi:10.1002/aenm.201300339.
[26] P. Jackson, D. Hariskos, R. Wuerz, O. Kiowski, A. Bauer, T.M. Friedlmeier, M. Powalla, Properties of Cu(In,Ga)Se_2 solar cells with new record efficiencies up to 21.7%, Phys. Status Solidi - Rapid Res. Lett. 9 (2015) 28–31. doi:10.1002/pssr.201409520.
[27] T. Negami, T. Wada, M. Nishitani, Composition monitoring method in CuInSe, thin film preparation, 258 (1995) 313–316.
[28] J. Kessler, J. Schöldström, L. Stolt, Rapid Cu(In,Ga)Se_2 growth using “end point detection,” Conf. Rec. IEEE Photovolt. Spec. Conf. 2000–Janua (2000) 509–512. doi:10.1109/PVSC.2000.915883.
[29] A. Fahrenbruch, R. Bube, Fundamentals of solar cells: Photovoltaic Solar Energy Conversion, Academic Press, 1983.
[30] M. Hillert, On the theory of normal and abnormal grain growth, Acta Metall. 13 (1965) 227–238. doi:10.1017/CBO9781107415324.004.
[31] T. Painchaud, Mécanismes de croissance des couches minces de Cu(In,Ga)Se_2 co-évaporées : vers des synthèses rapides et à basse température, (2010).
[32] H. Ruckh, D. Schmid, M. Kaiser, R. Schaffler, T. Walter, H.W. Schock, Influence of substrates on the electrical properties of Cu(In,Ga)Se_2 thin films, in: 1st World Conf. Photovolt. Energy Convers., 1994: pp. 156–159. doi:10.1109/WCPEC.1994.519831.
[33] E.P. Zaretskaya, V.F. Gremenyuk, V.B. Zalesski, V.A. Ivanov, I. V Viktorov, V.I. Kovalevski, O. V Ermakov, T.P. Leonova, The properties of $CuInSe_2$ films obtained by selenation of Cu–In layers, 45 (2000) 1371–1373.
[34] J. Kessler, C. Chityuttakan, J. Schöldström, L. Stolt, Growth of Cu(In,Ga)Se_2 films using a Cu-poor/rich/poor sequence: Substrate temperature effects, Thin Solid Films. 431–432 (2003) 1–5. doi:10.1016/S0040-6090(03)00222-0.
[35] D. Abou-Ras, R. Caballero, C.A. Kaufmann, M. Nichterwitz, K. Sakurai, S. Schorr, T. Unold, H.W. Schock, Impact of the Ga concentration on the microstructure of $CuIn_{1-x}Ga_xSe_2$, Phys. Status Solidi – Rapid Res. Lett. 2 (2008) 135–137. doi:10.1002/pssr.200802059.

[36] D. Abou-Ras, M.A. Contreras, R. Noufi, H.W. Schock, Impact of the Se evaporation rate on the microstructure and texture of Cu(In,Ga)Se_2 thin films for solar cells, Thin Solid Films. 517 (2009) 2218–2221. doi:10.1016/j.tsf.2008.10.133.
[37] N. Barreau, J. Lähnemann, F. Couzinié-Devy, L. Assmann, P. Bertoncini, J. Kessler, Impact of Cu-rich growth on the $CuIn_{1-x}Ga_xSe_2$ surface morphology and related solar cells behaviour, Sol. Energy Mater. Sol. Cells. 93 (2009) 2013–2019. doi:10.1016/j.solmat.2009.08.004.
[38] U. Rau, H.W. Schock, Electronic properties of Cu(In,Ga)Se_2 heterojunction solar cells-recent achievements, current understanding, and future challenges, Appl. Phys. A Mater. Sci. Process. 69 (1999) 131–147. doi:10.1007/s003390050984.
[39] A. Laemmle, R. Wuerz, T. Schwarz, O. Cojocaru-mir, P. Choi, M. Powalla, Investigation of the diffusion behavior of sodium in Cu(In,Ga)Se_2 layers, J. Appl. Phys. 154501–1/1 (2014).
[40] D. Rudmann, Effects of sodium on growth and properties of Cu(In,Ga)Se_2 thin films and solar cells, Dissertation, Swiss Federal Institute of Technology, Zürich, 2004.
[41] K. Granath, M. Bodegård, L. Stolt, The effect of NaF on Cu(In,Ga)Se_2 thin film solar cells, Sol. Energy Mater. Sol. Cells. 60 (2000) 279–293. doi:10.1016/S0927-0248(99)00089-6.
[42] D. Rudmann, G. Bilger, M. Kaelin, F.J. Haug, H. Zogg, A.N. Tiwari, Effects of NaF coevaporation on structural properties of Cu(In,Ga)Se_2 thin films, Thin Solid Films. 431 (2003) 37–40. doi:10.1016/s0040-6090(03)00246-3.
[43] D. Cahen, R. Noufi, Defect chemical explanation for the effect of air anneal on CdS/$CuInSe_2$ solar cell performance, Appl. Phys. Lett. 54 (1989) 558–560. doi:10.1063/1.100930.
[44] L. Kronik, U. Rau, J.F. Guillemoles, D. Braunger, H.W. Schock, D. Cahen, Interface redox engineering of Cu(In,Ga)Se_2-based solar cells: Oxygen, sodium, and chemical bath effects, Thin Solid Films. 361 (2000) 353–359. doi:10.1016/S0040-6090(99)00768-3.
[45] B.L. Kronik, D. Cahen, H.W. Schock, Effects of Sodium on Polycrystalline Cu(In,Ga)Se_2 and Its Solar Cell Performance, Adv. Mater. 10 (1998) 31–36. doi:10.1002/(SICI)1521-4095(199801)10:1<31::AID-ADMA31>3.0.CO;2-3.
[46] R. Würz, M. Rusu, T. Schedel-niedrig, M.C. Lux-steiner, I. Chemistry, F. Mpg, In-situ X-ray photoelectron spectroscopy study of the oxidation of $CuGaSe_2$, Surf. Sci. 580 (2005) 80–94. doi:10.1016/j.susc.2005.01.054.
[47] E.G. Michel, J.E. Ortega, E.M. Oellig, M.C. Asensio, J. Ferrón, R. Miranda, Early stages of the alkali-metal-promoted oxidation of silicon, Phys. Rev. B. 38 (1988) 13399–13406. doi:10.1103/PhysRevB.38.13399.
[48] A.J. Muscat, A. Rjeb, D. Roy, Oxidation of Si(111) 7×7 using alkali metal atoms: evidence for local promotion mechanisms, Surf. Sci. 302 (1994) L256–L262. doi:10.1016/0039-6028(94)91085-5.
[49] D.W. Niles, Na impurity chemistry in photovoltaic CIGS thin films: Investigation with x-ray photoelectron spectroscopy, J. Vac. Sci. Technol. A Vacuum, Surfaces, Film. 15 (1997) 3044. doi:10.1116/1.580902.
[50] N. Kohara, T. Negami, M. Nishitani, Y. Hashimoto, T. Wada, Electrical properties of Na-incorporated $Cu(In_{1-x}Ga_x)_3Se_5$ thin films, Appl. Phys. Lett. 71 (1997) 835. doi:10.1063/1.119661.
[51] D. Braunger, D. Hariskos, G. Bilger, U. Rau, H.W. Schock, Influence of sodium on the growth of polycrystalline Cu(In,Ga)Se_2 thin films, Thin Solid Films. 361 (2000) 161–166. doi:10.1016/S0040-6090(99)00777-4.
[52] N.I. of S. and Technology, Wagner plots, (2000). http://srdata.nist.gov/xps/WagnerPlot.aspx.
[53] P.V. Galiy, A.V. Musyanovych, X-ray photoelectron spectroscopy of the interface phase on cleavage surfaces of the layered semiconductor In_4Se_3 crystals, Funct. Mater. 12

(2005) 467–475.
[54] C.D. Wagner, W.M. Riggs, L.E. Davis, J.F. Moulder, G.. Muilenberg, Handbook of X-ray photoelectron spectroscopy, Perkin-Elmer Corporation, 1979.
[55] R. Würz, A. Meeder, D. Fuertes Marrón, T. Schedel-Niedrig, A. Knop-Gericke, K. Lips, Native oxidation of $CuGaSe_2$ crystals and thin films studied by electron paramagnetic resonance and photoelectron spectroscopy, Phys. Rev. B - Condens. Matter Mater. Phys. 70 (2004) 1–10. doi:10.1103/PhysRevB.70.205321.
[56] M.K. Bahl, R.L. Watson, K.J. Irgolic, LMM Auger spectra of selenium and some of its compounds, J. Chem. Phys. 72 (1980) 4069. doi:10.1063/1.439634.
[57] D.A. Magdas, D. Maestre, A. Cremades, L. Gregoratti, J. Piqueras, Study of microstructured indium oxide by cathodoluminescence and XPS microscopy, Superlattices Microstruct. 45 (2009) 429–434. doi:10.1016/j.spmi.2008.10.002.
[58] D.Y. Zemlyanov, E. Savinova, A. Scheybal, K. Doblhofer, R. Schlögl, XPS observation of OH groups incorporated in an Ag(111) electrode, Surf. Sci. 418 (1998) 441–456. doi:10.1016/S0039-6028(98)00728-6.
[59] X. Song, R. Caballero, R. Félix, D. Gerlach, C.A. Kaufmann, H.-W. Schock, R.G. Wilks, M. Bär, Na incorporation into $Cu(In,Ga)Se_2$ thin-film solar cell absorbers deposited on polyimide: Impact on the chemical and electronic surface structure, J. Appl. Phys. 111 (2012) 34903. doi:10.1063/1.3679604.
[60] CAHEN, NOUFI, Surface Passivation of Polycristalline, Chalcogenide Based Photovoltaic Cells, Sol. Cells, 30 53-59. 30 (1991) 53–59.
[61] J. Lindahl, U. Zimmermann, P. Szaniawski, T. Torndahl, A. Hultqvist, P. Salomé, C. Platzer-Björkman, M. Edoff, Inline $Cu(In,Ga)Se_2$ co-evaporation for high-efficiency solar cells and modules, IEEE J. Photovoltaics. 3 (2013) 1100–1105. doi:10.1109/JPHOTOV.2013.2256232.
[62] C. Heske, G. Richter, Z. Chen, R. Fink, E. Umbach, W. Riedl, F. Karg, Influence of Na and H_2O on the surface properties of Cu(In,Ga)Se2 thin films, J. Appl. Phys. 82 (1997) 2411–2420. doi:10.1063/1.366096.
[63] J.H.W. De Wit, Structural aspects and defect chemistry in In_2O_3, J. Solid State Chem. 20 (1977) 143–148. doi:10.1016/0022-4596(77)90061-5.
[64] Y. Oishi, W.D. Kingery, Self-diffusion of oxygen in single crystal and polycrystalline aluminum oxide, J. Chem. Phys. 33 (1960) 480. doi:10.1063/1.1731170.
[65] U. Rau, D. Braunger, R. Herberholz, H.W. Schock, J.-F.F. Guillemoles, L. Kronik, D. Cahen, Oxygenation and air-annealing effects on the electronic properties of $Cu(In,Ga)Se_2$ films and devices, J. Appl. Phys. 86 (1999) 497–505. doi:10.1063/1.370758.
[66] D. Cahen, P.J. Ireland, L.L. Kazmerski, F.A. Thiel, X-ray photoelectron and Auger electron spectroscopic analysis of surface treatments and electrochemical decomposition of CuInSe2 photoelectrodes, J. Appl. Phys. 57 (1985) 4761. doi:10.1063/1.335341.
[67] K. Gartsman, L. Chernyak, V. Lyahovitskaya, D. Cahen, V. Didik, V. Kozlovsky, R. Malkovich, E. Skoryatina, V. Usacheva, Direct evidence for diffusion and electromigration of Cu in CuInSe2, J. Appl. Phys. 82 (1997) 4282. doi:10.1063/1.366252.
[68] I.-J.J. Lee, C. Yu, T.-B. Hur, H.-K. Kim, C.-O. Kim, J.-Y. Kim, Observation of complete oxidation of InN to In_2O_3 in air at elevated temperatures by using X-ray photoemission spectroscopy, 49 (2006) 2176–2179. http://inis.iaea.org/search/search.aspx?orig_q=RN:43039866\npapers2://publication/uuid/1DD5DD51-0F34-49C4-91F4-CA31744CD7F6.
[69] M.A. Contreras, B. Egaas, P. Dippo, J. Webb, J. Granata, K. Ramanathan, S. Asher, A. Swartzlander, R. Noufi, On the role of Na and modifications to $Cu(In,Ga)Se_2$ absorber materials using thin-MF (M=Na, K, Cs) precursor layers, in: 26th IEEE Photovolt. Spec. Conf., 1997: pp. 359–362. doi:10.1109/PVSC.1997.654102.

[70] A.J. Nelson, D.W. Niles, D. Rioux, R. Patel, H. Höchst, H. Höchst, Soft x-ray photoemission investigation on the effect of In doping in CdS/$CuInSe_2$ heterojunction formation, J. Appl. Phys. 72 (1992) 5888–5891. doi:10.1063/1.351895.
[71] K. Granath, L. Stolt, M.Bodegard, Growth of Cu(In,Ga)Se_2 thin films by coevaporation using alkaline precursors, Thin Solid Films 362 (2000) 9-16. doi: 10.1016/S0040-6090(99)00828-7.
[72] R.J. Matson, J.E. Granata, S.E. Asher, M.R. Young, Effects of substrate and Na concentration on device properties, junction formation, and film microstructure in $CuInSe_2$ PV devices, AIP Conf. Proc. 542 (1999) 542–552. doi:10.1063/1.57921.
[73] T. Nakada, H. Ohbo, M. Fukuda, A. Kunioka, Improved compositional flexibility of CIGS-based thin film solar cells by sodium control technique, Sol. Energy Mater. Sol. Cells. 49 (1997) 261–267.
[74] B. Canava, J. Vigneron, A. Etcheberry, D. Guimard, J. Guillemoles, D. Lincot, XPS and electrical studies of buried interfaces in Cu(In,Ga)Se_2 solar cells, 404 (2002) 425–431.
[75] Y. Okano, T. Nakada, A. Kunioka, XPS analysis of CdS/$CuInSe_2$ heterojunctions, Sol. Energ. Mat. Sol. C. 50 (1998) 105–110. doi:10.1016/S0927-0248(97)00129-3.
[76] C.. Huang, Y.. Su, S.. Wu, The effect of solvent on the etching of ITO electrode, Mater. Chem. Phys. 84 (2004) 146–150. doi:10.1016/j.matchemphys.2003.11.021.
[77] R. Hunger, T. Schulmeyer, Removal of the surface inversion of $CuInSe_2$ absorbers by NH_3 etching, in: 3rd World Conference on Photovoltaic Energy Conversion (2003) 566–569.
[78] M. Kauk, K. Ernits, K. Timmo, A. Jagomagi, M. Grossberg, J. Krustok, T. Varema, E. Mellikov, Chemical etching of $CuInSe_2$ absorber surface for monograin layer solar cell application, 20th Eur. Photovolt. Sol. Energy Conf. (2005) 1811–1815.
[79] M. Kauk, M. Altosaar, J. Raudoja, K. Timmo, T. Varema, M. Danilson, M. Grossberg, E. Mellikov, The influence of doping with donor type impurities on the properties of $CuInSe_2$, Phys. Status Solidi. 5 (2008) 609–611. doi:10.1002/pssc.200776831.
[80] T. Painchaud, N. Barreau, L. Arzel, J. Kessler, Fast Cu(In,Ga)Se_2 precursor growth: Impact on solar cell, Thin Solid Films. 519 (2011) 7221–7223. doi:10.1016/j.tsf.2011.01.098.
[81] J.C. Vigui, J. Spitz, Chemical Vapor Deposition at Low Temperature, J. Electrochem. Soc.Solid-State Sci. Technol. 122 (1975) 585–588.
[82] W.A. Bryant, The fundamentals of chemical vapour deposition, J. Mater. Sci. 12 (1977) 1285–1306. doi:10.1007/BF00540843.
[83] P. Reyes, S. Velumani, Structural and optical characterization of mechanochemically synthesized copper doped CdS nanopowders, Mater. Sci. Eng. B. 177 (2012) 1452–1459. doi:10.1016/j.mseb.2012.03.002.
[84] M. Kaelin, D. Rudmann, F. Kurdesau, T. Meyer, H. Zogg, A.N. Tiwari, CIS and CIGS layers from selenized nanoparticle precursors, Thin Solid Films. 431–432 (2003) 58–62. doi:10.1016/S0040-6090(03)00194-9.
[85] W. Wang, S.-Y. Han, S.-J. Sung, D.-H. Kim, C.-H. Chang, 8.01% $CuInGaSe_2$ solar cells fabricated by air-stable low-cost inks, Phys. Chem. Chem. Phys. 14 (2012) 11154. doi:10.1039/c2cp41969f.
[86] F.A. Pulgarín-Agudelo, S. López-Marino, A. Fairbrother, M. Placidi, V. Izquierdo-Roca, P.J. Sebastián, F. Ramos, B. Pina, A. Pérez-Rodríguez, E. Saucedo, A thermal route to synthesize photovoltaic grade $CuInSe_2$ films from printed CuO/In_2O_3 nanoparticle-based inks under Se atmosphere, J. Renew. Sustain. Energy. 5 (2013). doi:10.1063/1.4826197.
[87] M. Emziane, R. Le Ny, Crystallization of In_2Se_3 semiconductor thin films by post-deposition heat treatment ., J. Phys. D. Appl. Phys. 32 (1999) 1319–1328.
[88] T. Magorian Friedlmeier, P. Mantilla Pérez, I. Klugius, P. Jackson, O. Kiowski, E. Ahlswede, M. Powalla, Optoelectronic characterization of co-evaporated and low-cost

$Cu(In,Ga)Se_2$ solar cells, a comparison, Thin Solid Films. 535 (2013) 92–96. doi:10.1016/j.tsf.2012.11.108.
[89] H. Simchi, B.E. McCandless, T. Meng, W.N. Shafarman, Structure and interface chemistry of MoO3 back contacts in $Cu(In,Ga)Se_2$ thin film solar cells, J. Appl. Phys. 115 (2014). doi:10.1063/1.4862404.
[90] D. Schmid, M. Ruckh, H.W. Schock, A comprehensive characterization of the interfaces in Mo/CIS/CdS/ZnO solar cell structures, Sol. Energy Mater. Sol. Cells. 41–42 (1996) 281–294. doi:10.1016/0927-0248(95)00107-7.
[91] P.E. Russell, O. Jamjoum, R.K. Ahrenkiel, L.L. Kazmerski, R.A. Mickelsen, W.S. Chen, Properties of the Mo-$CuInSe_2$ interface, Appl. Phys. Lett. 40 (1982) 995–997. doi:10.1063/1.92955.
[92] S.J. Park, E. Lee, H.S. Jeon, J. Gwak, M.-K. Oh, B.K. Min, Oxidation effects on $CuIn_xGa_{1-x}Se_yS_{2-y}$ thin film growth by solution processes, Thin Solid Films. 520 (2012) 3048–3053. doi:10.1016/j.tsf.2011.10.162.
[93] S.M. Sze, Physics of Semiconductor Devices, 2nd ed., Wiley, 1981.

General conclusion

The objective of this study was to study the deposition of Cu(InGa)Se2 films by co-evaporation and hybrid processes. An approach was used to study the characteristics of the two absorbers produced by the two proposed methods.

A first work on the synthesis of the CIGSe layers by 3-stage process was carried out in order to determine the deposition parameters that vary the properties of the absorber. Special attention was given to the 1st-stage deposition temperature, which has an effect on the grain size and the preferential orientation of the synthesized layers. A fundamental role of the sodium and oxygen was also demonstrated in oxygenized samples. These two elements have a important role specially in the electrical characteristics of the solar cells. This optimization of CISe properties made possible to set up ,at a laboratory level, a standard 3-stage bitherme protocol which made it possible to produce cells with yields close to 12%.

A work of development of a hybrid deposition process of CuInSe2 was then carried out. This process consists in firstly forming an In_2Se_3 layer (*i.e.* 1st-stage) using chemical spray pyrolysis performed in ambient atmosphere and secondly in completing the $CuInSe_2$ film by co-evaporation under vacuum (*i.e.* 2nd- and 3rd-stage). The study of the structural properties of films has shown the possibility of an important improvement in the structure as well as in the morphology of the In2Se3 precursor films. The proposed hybrid process has demonstrated its relevance since devices prepared with such hybrid-absorber layer have reached outstanding conversion efficiency of 11.1 %. A comparative study of the hybrid method with fully evaporated deposition (3-stage process) showed that still there is room for improvement of absorbers films at structural, morphological and electrical level. Further electrical properties measurements are needed in order to better understand the hybrid method.

As future work to further improve the presented results, we need to:

- Investigate the effects of other deposition parameters (Cu excess, Se pressure, among others) on the properties of CISe films and solar cells.
- Study the surface of CISe to identify possible oxide species (XPS, SIMS).
- Develop and study a hybrid deposition using a different co-evaporation “recipe” (other than 3-stage process). Different precursors.
- Avoid the incorporation of oxides from the spray pyrolysis deposition by carrying out the growth inside a bell jar glass.
- Deposition of precursors by other non-vacuum techniques, which could represent an improvement in the material, utilization, higher yields.
- Try the hybrid deposition in bigger deposition areas.

List of figures

List of tables